Time-Domain Macromodeling and Variability Analysis of Electronic and Photonic Circuits

Macromodelleren en variabiliteitsanalyse in het tijdsdomein van elektronische en fotonische circuits

Yinghao Ye

Promotoren: prof. dr. ir. T. Dhaene, prof. dr. ir. W. Bogaerts
Proefschrift ingediend tot het behalen van de graad van
Doctor in de ingenieurswetenschappen: elektrotechniek

UNIVERSITEIT
GENT

Vakgroep Informatietechnologie
Voorzitter: prof. dr. ir. B. Dhoedt
Faculteit Ingenieurswetenschappen en Architectuur
Academiejaar 2018 - 2019

ISBN 978-94-6355-227-1
NUR 950
Wettelijk depot: D/2019/10.500/35

GHENT UNIVERSITY

Ghent University
Faculty of Engineering and Architecture
Department of Information Technology

imec

imec
Internet Technology and Data Science Lab

Examination Board:

em. prof. Daniël De Zutter (chair)
prof. Tom Dhaene (supervisor)
prof. Wim Bogaerts (supervisor)
prof. Guillaume Crevecoeur
prof. Nobby Stevens
prof. Andrea Melloni
prof. Dirk Deschrijver
dr. Domenico Spina
dr. Martin Fiers

FACULTY OF ENGINEERING AND ARCHITECTURE

Dissertation for acquiring the grade of
Doctor of Electrical Engineering

Dankwoord

Since I came to Belgium for my PhD research four years ago, a lot of amazing things have happened in both my personal life and professional career. I wish to thank all the people who have greatly inspired and supported me throughout my research.

First and foremost I thank my supervisor Prof. Tom Dhaene for offering the opportunity to do research at Ghent University. I would also like to thank my co-supervisor Prof. Wim Bogaerts for leading me into the photonics world. I am very grateful for their support, encouragement and guidance during my PhD. I learned from them not only the knowledge, but also the methodology of doing research and rigorous scientific attitude, which are definitely very valuable in my following career. I feel fortunate that I have worked under their guidance and could not expect a better and friendlier supervisor.

I would like to thank Prof. Daniël De Zutter for accepting my request to chair my PhD examination board and for his support during the examination process. Also, I would like to take this opportunity to thank jury members Prof. Dirk Deschrijver, Prof. Guillaume Crevecoeur, Prof. Nobby Stevens, Prof. Andrea Melloni, Dr. Domenico Spain and Dr. Martin Fiers for being a part of my PhD jury and for providing valuable feedback to improve the quality of my PhD thesis.

I am grateful to Dr. Domenico Spina for his help and guidance throughout my PhD and for providing a good foundation to build my research on. During the first days when I was here, my English was quite limited and his patience helped me a lot. I had the pleasure of working with him on many research topics. My sincere thanks also goes to Prof. Dirk Deschrijver for the valuable discussions about the Vector Fitting techniques.

In my daily life, it would not have been pleasant without the amazing colleagues. I would like to thank Dr. Prashant Singh for receiving me on my first day in Ghent and introducing me to the pasta in the Vooruit, which was my first experience with the “incredible cheese”. I appreciate Nicolas Knudde’s help for making the effort to translate my PhD summary in dutch. Dr. Ivo Couckuyt, Dr. Selvakumar Ulaganathan, Dr. Joachim van der Herten, Dr. Joeri Ruyssinck, Dr. Leen De baets, Dr. Arun Kaintura, Roberto Medico, Diego Nieves Avendaño, Kyle Foss, Tom Van Steenkiste, Anthony Faustine and Geethika Bhavanasi; Thank you everyone for being part of my PhD journey and for the good time. I will never

forget the wonderful experience with some of you in Amsterdam. I also appreciate that my colleagues and Prof. Eric Laermans never lost their patience explaining "western culture" to me during our daily lunch talks.

I express my thanks to Arun for his support during my stay in Ghent and taking wedding photos for me and my wife. You started your PhD two months before me, and became the perfect person who I could ask for all kinds of instructions about work related formalities, including all the procedures of the PhD defense. We also learned a lot from each other from those heavy after-work discussions followed by delicious Chinese meals sometimes. You are a very friendly person and I really had good time with you. One day, I will visit your home by crossing the Himalayas.

I am also thankful to my colleagues in the photonic group. Yufei Xing, Mi Wang and Dr. Umar Khan helped me a lot in our cooperation. I also had a very good time with Dr. Ang Li, Antonio Ribeiro, Xiangfeng Chen, Lukas VanIseghem, Hong Deng, Dr. Banafsheh Abasahl and Dr. Iman Zand. They are all kind and helpful.

I am thankful to the technical and administrative staff of IDLAB, the international admissions office, and the department of personnel and organization for helping me carry out all of the administrative formalities during my stay in Ghent. I am thankful to Simon, Martine Buysse, Davinia Stevens, Joke Staelens and Bernadette Becue from the administration.

My sincere thanks also goes to my friend Luk Brazle. He helped correct and improve my English in the past four years, which is a very long period of time. I had a lot of fun on the parties he organized and I still miss the barbecue in his yard. I would like to give my thanks to my friends Dr. Wei Liu, Dr. Zhuo Cui, Yuting Shi, Haolin Li, Yuhui Wu, Mandy Lam, Cécile Gombeaud, Hélène Goutermanoff, Benoît Goutermanoff.

There are many other individuals not named here who have rendered their help for the execution of this work, to them I express my gratefulness.

I also give my special thanks to my wife for supporting me, encouraging me, and eventually marrying me, which makes me feel my four years' frequent travel between Gent and Paris was well spent. You are such a beautiful, smart and kind lady. I always feel I hit the jackpot when I met you, and it will always be exciting to spend the rest of my life with you. I am deeply grateful beyond words to my parents, parents-in-law and my brother for being an unwavering support in my life.

Gent, February 2019
Yinghao Ye

Table of Contents

List of Figures

List of Tables

List of Acronyms

ADS	Advanced Design System
BER	Bit Error Rate
BW	Bandwidth
CDF	Cumulative Distribution Function
CMOS	Complementary Metal Oxide Semi-conductors
CVF	Complex Vector Fitting
DVF	Delayed Vector Fitting
DUV	Deep Ultraviolet
FFT	Fast Fourier Transform
EM	Electromagnetic
EDA	Electronic Design Automation
FIR	Finite Impulse Response
GP	Galerkin Projection
IC	Integrated Circuit
IFFT	Inverse Fast Fourier Transform
IIR	Infinite Impulse Response
I/O	Inputs/Outputs
KCL	Kirchhoff's Current Law
KVL	Kirchhoff's Voltage Law
LF	Lattice Filter

MC	Monte Carlo
MNA	Modified Nodal Analysis
MOR	Model Order Reduction
MOSFET	Metal-Oxide-Semiconductor Field-Effect Transistor
MWP	Microwave Photonics
MZI	Mach-Zehnder Interferometer
ODE	Ordinary Differential Equation
PC	Polynomial Chaos
PDF	Probability Density Function
PIC	Photonic Integrated Circuit
QAM	Quadrature Amplitude Modulation
RLC	Resistor-Inductor-Capacitor
RLGC	Resistance-Inductance-Capacitance-Conductance
RR	Ring Resonator
SC	Stochastic Collocation
SOI	Silicon-On-Insulator
SPICE	Simulation Program with Integrated Circuit Emphasis
SI	Signal Integrity
ST	Stochastic Testing
VF	Vector Fitting
WDM	Wavelength Division Multiplexing

Samenvatting

Tegenwoordig spelen elektronische geïntegreerde circuits (ICs) een onvervangbare rol in bijna elke tak van de industrie vanwege hun hoge performantie en alsmaar kleiner formaat. Een groot nadeel van ICs is echter de hoge kost van ontwerp en de productie van de nodige lithografische maskers, en van het complexe productieproces. De kost van één chip kan enkel voldoende gedrukt worden om competitief te zijn wanneer deze in massa worden geproduceerd gedurende 24u per dag. Het is dus cruciaal om deze circuits te kunnen ontwerpen vóór de productie. Het risico van mislukte ontwerpen kan drastisch worden gereduceerd door enerzijds het gebruik van circuitsimulatoren, die de performantie schatten, en anderzijds verificatie in gesofisticeerde electronic design automation (EDA) software. De nauwkeurigheid van de simulatie hangt vooral af van de modelleringstechnieken van de verscheidene componenten in ICs.

Terwijl de integratie en miniaturisatie van ICs continu verbeterd zijn, hebben de productietoleranties van geometrische en elektrische parameters steeds meer een niet-verwaarloosbare invloed op de werking van ICs, vooral in de sub-100nm schaal. In dit scenario, varieert de performantie van chip tot chip en is deze niet in overeenstemming met het originele ontwerp. Als resultaat degradeert de werking door variaties in het productieproces wat zich kan uiten in een onverwacht yield loss, zelfs wanneer deze ICs werden geverifieerd met behulp van EDA software. Het is dus cruciaal om deze toleranties reeds in rekening te brengen gedurende de ontwerpfase, en ontwerpen op te stellen die minder gevoelig zijn aan deze toleranties.

In de meeste situaties waar men toleranties in rekening wil brengen, gebruikt men Monte Carlo (MC) methoden om de variaties in het productieproces te schatten. Dit vooral omdat deze methoden robuust, accuraat en simpel te implementeren zijn. Een groot nadeel van deze methoden is dat ze een groot aantal simulaties nodig hebben door hun trage convergentie, en simulaties van huidige ICs dikwijls computationeel intensief zijn.

Hoofdstuk 2 en 3 van deze doctoraatsthesis stellen nieuwe en efficiënte aanpakken voor macromodelleren van elektronische circuits voor, onderhevig aan fabricagetoleranties. Hierbij wordt een stochastisch macromodel gedefinieerd als een wiskundig model van een algemeen systeem die het gedrag van het echte systeem beschrijft in de vorm van input/output (I/O) poorten, terwijl een of meerdere van de

systeemparameters onderhevig zijn aan variaties. De voorgestelde aanpak begint van het bouwen van stochastische modellen van alle lineaire en niet-lineaire componenten om deze modellen vervolgens te connecteren met als doel het extraheren van stochastische informatie van het volledige circuit via één enkele simulatie. In vergelijking met MC methoden, is de voorgestelde aanpak efficiënter terwijl ze een vergelijkbare accuraatheid bereikt.

De tweede uitdaging die deze thesis bestudeert is het macromodelleren van lineaire en passieve geïntegreerde fotonische circuits in silicium. Om de toenemende vraag naar snelle transmissie en verwerking van grote volumes aan data tegemoet te komen zijn fotonische circuits belangrijk. De drijvende kracht die achter silicium fotonica chips zit, is de mogelijkheid om CMOS-compatibele productieprocessen aan te wenden, resulterend in hoog volume en lage kost; meer nog, het hoge contrast in refractieve index tussen het geleidende silicium en de cladding laat golfgeleiders op sub-micron schaal toe en een hoge integratie densiteit.

Vergelijkbaar met het design van elektronische ICs, maakt de hoge fabricagekost het essentieel om het design vooraf correct te kunnen vastleggen. Echter, in tegenstelling tot elektronische circuits, dewelke al extensief bestudeerd zijn in de laatste decennia, staat de ontwikkeling van fotonische circuits nog steeds in zijn kinderschoenen, en zijn er nog veel uitdagingen om te komen tot een hoge integratiegraad en massaproductie. Een van de uitdagingen is het definiëren van geschikte modellering en simulatie technieken voor fotonische circuits. Deze dissertatie focust op lineaire passieve fotonische componenten en circuits wiens functie ruwweg in twee categorieën vallen: het distribueren/transporteren van licht (e.g. waveguides), en het filteren van optische golflengten voor applicaties in de spectroscopie, golflengtemultiplexing (WDM) of fotonica op microgolfschaal.

Een veelgebruikte aanpak is het berekenen van analytische modellen, die steunen op de kennis van de werkprincipes van de beschouwde component. Echter, in de praktijk kunnen analytische modellen enkel opgesteld worden voor simpele fotonische systemen en is hun accuraatheid beperkt in het geval van complexe niet-ideale karakteristieken. Daarenboven worden de meeste systemen beschreven als frequentiedomein modellen, terwijl tijdsdomein modellen nodig zijn wanneer het tijdsgedrag in grotere systemen wordt bestudeerd (e.g., transient, bit error, eye diagram).

Een nieuwe modelleringstechniek voor lineaire fotonische circuits beschreven door scattering parameters wordt gepresenteerd in Hoofdstuk 4. Het modelleringsproces is gebaseerd op de robuuste Vector Fitting (VF) techniek en laat efficiënte en accurate tijdsdomein simulatie van algemene, lineaire en passieve fotonische circuits via geschikte complexe toestandsvergelijkingen toe. De voorgestelde techniek wordt basisband modelleren genoemd. Echter, de complexwaardige modellen kunnen enkel gesimuleerd worden in simulatoren die complexe getallen aankunnen. Om deze reden breidt Hoofdstuk 4 de basisband modellering uit en worden reëelwaardige basisband modellen afgeleid, dewelke alle voordelen van hun complex-waardig equivalent bezitten. In de praktijk wordt deze methodologie meer geschikt voor simulaties die beide het optische en elektronische eigenschappen gedrag bestuderen. In Hoofdstuk 5 wordt een alternatieve basisband modelle-

ring besproken voor lineair, fotonische circuits die op het Complex Vector Fitting (CVF) algoritme gebaseerd is. Vergelijkbaar met de aanpak in Hoofdstuk 4, kan deze methode modellen construeren die slechts de helft in grootte zijn, en vormt dus een grote verbetering in efficiëntie voor simulaties in het tijdsdomein. Het is belangrijk om op te merken dat stabiliteit en passiviteit van de modellen bij alle basisband gebaseerde aanpakken, gegarandeerd worden.

Een andere uitdaging voor fotonische circuits is dat de performantie degradeert door fabricagefouten, nog meer dan in het elektronische geval. Doordat de propagatie van licht volledig afhangt van de geometrie en van de materialen zijn fotonische componenten heel gevoelig aan variaties in geometrische parameters en de omgeving. Het hoge contrast in brekingsindex van silicium-op-isolator (SOI) in silicium gebaseerde fotonicachips laten een hogere confinement toe en een grote integratiedensiteit, maar maken de component ook gevoeliger aan fabricagefouten. Het is dus cruciaal om in het ontwerpstadium de degradatie door productiefouten te kwantificeren, zoals voor elektronische circuits. Hoofdstuk 6 stelt een aanpak voor accurate en efficiënte tijdsdomein variabiliteitsanalyse van algemene, lineaire fotonische circuits voor, gebaseerd op expertise vergaard tijdens mijn studie van macromodellering en basisband modellering.

Zoals hierboven beschreven werden accurate, efficiënte en robuuste technieken voor tijdsdomeinmodellering ontwikkeld voor simulatoren voor lineaire en passieve fotonische circuits. Daarenboven zijn efficiënte, stochastische technieken voor macromodellering ontwikkeld voor variabiliteitsanalyse in het tijdsdomein van elektronische en fotonische circuits die onderhevig zijn aan productietoleranties.

Summary

Nowadays, electronic integrated circuits (ICs) play an irreplaceable role in almost every industrial field in the society due to their high performance combined with a miniaturized size. However, the main disadvantage of ICs is the high cost to design them and fabricate the required photomasks, and of the complex manufacturing process. Indeed, the cost of a single chip can be driven down to a competitive price only by mass production and a 24-hours production cycle. Hence, it is crucial to design the circuits to be as close to the intended specifications as possible before they are fabricated. The risk of failed designs can be largely reduced by circuit simulations which provide circuit performance estimation and verification in sophisticated electronic design automation (EDA) tools. The accuracy of the simulation mainly depends on the accuracy of the modeling techniques for different components in ICs, which are well established and highly standardized.

However, while integration and miniaturization level of ICs has been continuously improved, the fabrication variations of geometrical or electrical parameters impose a considerable influence on the performance of ICs, especially in sub-100 nm technologies. In this scenario, the behaviors of the fabricated ICs vary from chip to chip, and are not consistent with the original designs. As a result, even if the ICs are correctly designed and verified by EDA tools, the performance degradation due to the fabrication variations could still cause unexpected yield loss. Hence, it is crucial to take into account the fabrication variations when estimating the performance of ICs during the design phase, thereby generating optimum designs which are more robust.

In this framework, the Monte Carlo (MC) method is considered the standard approach to estimate the effects of the variations of the manufacturing process (also referred to as variability analysis), since it is robust, accurate, and easy to implement. However, it requires a large number of simulations to obtain reliable results, due to its slow convergence rate, and the simulations of modern ICs are often computationally expensive, which, in practice, constitutes a severe limitation for designers.

Chapters 2 and 3 of this PhD thesis propose novel and efficient stochastic macromodeling approaches for electronic circuits subject to manufacturing variations. In this PhD thesis, a stochastic macromodel is defined as a mathematical model of a generic system which describes the system behavior as seen from its

inputs/outputs (I/O) ports, while one or more of the system parameters are subject to fabrication variations. The proposed approach starts with building suitable stochastic models of both linear and nonlinear systems and then properly connects these models for extracting stochastic information of the overall circuit via a single simulation. Compared to the MC method, the proposed approach is much more efficient while providing comparable accuracy.

The second challenge this thesis addresses is the macromodeling of linear and passive silicon photonic integrated circuits. To deal with the increasing demand of fast transmission and processing of large volume data, silicon based photonic integrated circuits (referred to as silicon photonics) is widely accepted as a key technology in the next-generation communications systems and data interconnects. The key driving force behind silicon photonics is the ability to use CMOS-compatible fabrication processes, resulting in a high-volume production at low cost; furthermore, the high material index contrast between the guiding silicon and the cladding permits sub-micron waveguides and a high integration density.

Similar to the design of electronic ICs, the high manufacturing cost makes it essential to guarantee first-time-right design. However, unlike electronic circuits, which have been extensively studied and developed in the last several decades, silicon photonics is still at early development stage and there are many challenges on the way heading to high integration and mass production. One of these challenges is defining suitable modeling and simulation techniques for photonic circuits, which are still not well established. This work focuses on linear passive photonic devices and circuits whose functions roughly fall into two categories: distributing/transporting light (e.g. waveguides), and optical wavelength filtering for applications such as spectroscopy, *wavelength division multiplexing* (WDM) or *microwave photonics* (MWP) applications.

A common approach is to compute analytic models, which rely on the knowledge of the working principles of the device under study. However, in practice, analytic models can be derived only for simple photonic systems and there is a limit in their accuracy when describing complex non-ideal characteristics of the system under study (i.e. backscattering and undesired dispersion effects). Furthermore, most of these models are generally described as frequency- (wavelength) domain models, whereas time-domain models are needed when used in a larger system to evaluate the time-domain behaviors, such as transient, bit error rate (BER) and eye diagrams.

A novel modeling approach for linear photonic circuits described by scattering parameters is presented in Chapter 4. The modeling process leverages on the robust Vector Fitting (VF) technique and allows for efficient and accurate time-domain simulations of general, linear and passive photonic circuits via a suitable complex-valued state-space representation. The proposed technique is referred to as the baseband modeling approach. However, the complex-valued models can only be simulated in simulators able to handle complex numbers. Note that circuits simulators can often not handle complex numbers. Hence, Chapter 4 then extends the baseband modeling approach and derives real-valued baseband models, which inherit all the advantages of their complex-valued counterparts and can

be simulated in a broad range of simulators. In particular, this novel methodology becomes more suitable for optical-electronic co-simulations. Chapter 5 presents an alternative baseband modeling technique for linear photonic circuits which leverages on the Complex Vector Fitting (CVF) algorithm. Compared to the modeling approach in Chapter 4, the novel method is able to generate half-size models for the same applications, thereby achieving a major improvement in the efficiency of the time-domain simulations. It is important to remark that stability and passivity of the models computed with all the proposed baseband approaches, which are fundamental properties for time-domain simulations, can be guaranteed.

Another challenge for silicon photonic circuits is that the performance degradation due to fabrication variations is even more critical than the electronic case. Since the propagation of light is entirely determined by the geometry for certain materials, photonic devices on a chip are very sensitive to variations in geometrical parameters and environment. The high refractive index contrast of silicon-on-insulator (SOI) platforms for silicon photonics allows for tighter confinement of light and a high integration density, but also makes the device more sensitive to process variations. Hence, it is crucial to quantify in the design stage the performance degradation due to fabrication process, as it is done for electronic circuits. Chapter 6 proposes an accurate and efficient time-domain variability analysis approach for general, linear photonic circuits, which leverages on the expertise in both stochastic macromodeling and baseband modeling techniques built up during my research.

To conclude, accurate, efficient, and robust time-domain modeling approaches are proposed for circuit simulations of linear and passive photonic circuits. Furthermore, efficient stochastic macromodeling techniques are developed for time-domain variability analysis of electronic and photonic circuits subject to fabrication variations.

1 Introduction

1.1 Stochastic macromodeling of electronic circuits

Integrated electronic circuits (also referred to as ICs, or chips) were born thanks to the mid-20th-century technology advancements in semiconductor device fabrication. Since their birth, driven by continuous technical advances, chips have progressed enormously in terms of circuit size, speed and capacity: a modern chip may have many hundred million of transistors in an area the size of a human fingernail.

Nowadays, many electronic design automation (EDA) tools (e.g. Mentor, Cadence, ADS, Synopsys) have been developed and are widely used in the industry for ICs design. One of the major functions that EDA tools provide is design verification and performance estimation via circuit simulations, which confirm that the functionality of a designed circuit conforms to the intended or specified behavior.

There are two essential requirements to run circuit simulations: accurate models for each device in the circuit and a suitable software platform where these models can be connected and computed, and a great deal of effort has been invested in this direction by the research community in the past half century. The most well known and sophisticated platform is SPICE (abbreviation for Simulation Program with Integrated Circuit Emphasis), which was developed by Laurence Nagel in 1970s at the Electronics Research Laboratory of the University of California, Berkeley [1]. As an open-source electronic circuit simulator, SPICE was widely distributed, improved, and used in both academia and industry. Nowadays, simu-

lating integrated circuits with SPICE-like programs is the industry-standard way to verify circuit operation at transistor level before committing to manufacturing an integrated circuit. Meanwhile, SPICE-compatible models for different IC components have also been developed and included in SPICE, which range from basic elements (such as resistors, capacitors and inductors), to independent and controlled sources, ideal transmission lines and MOSFET models. In order to standardize these models so that a set of model parameters may be used in different SPICE-like circuit simulators, an industry working group was formed: the Compact Model Council (now the Compact Model Coalition) [2], aiming to choose, maintain and promote the use of standard models. The standard models today include BSIM4, BSIMSOI, PSP, HICUM, and MEXTRAM [3].

Nowadays, for electronic ICs, the attention of the research community is focused on new challenges, such as quantifying the degradation of IC performance due to manufacturing variations. In the past decades, the steady down-scaling of device dimensions along with the integration of more components on a single chip have been the major sources of growth for modern integrated electronic circuits. This growth is in adherence to the Gordon Moore prediction, also known as Moore's Law, stating that the available memory and calculation speed of microprocessors would have an exponential growth doubling every year [4], and it still stands with the correction of doubling every 18 months [5]. However, in sub-100 nm technologies, it is becoming increasingly difficult for the device tolerances to track the scaling rate of the minimum feature sizes [6]. The impact of geometrical or electrical parameters variability on the performance of modern ICs is becoming increasingly problematic [7–9]. There are different sources of variability, like routing/layout uncertainties and changes of the devices operation conditions due to temperature fluctuation, but the manufacturing variations rank among the major ones. Moreover, different manufacturing phases introduce process variations, such as etching, lithography and polishing [10]. As a result, mismatches are introduced between the fabricated ICs that are designed to be the same, which can significantly degrade the performance of both digital and analog circuits [10, 11]. Therefore, it is critical to estimate during the design phase of ICs the effect of the variations of the manufacturing process on the circuit performance, in order to avoid that a large amount of fabricated ICs fail to satisfy the design specifications.

A traditional approach to address this challenge is corner analysis. The idea is to first simulate the circuit under study at all the worst-case parameter corners (e.g. ± 3 sigma of the parameters), and then obtain the worst corners of the performance measures. For example, conventionally, four worst-case performance corners are typically evaluated for ICs: slow NMOS and slow PMOS (SS), fast NMOS and fast PMOS (FF), fast NMOS and slow PMOS (FS), slow NMOS and fast PMOS (SF), with regard to multiple parameters [12]. The corner analysis gives pass/-fail results of a design, depending that if the obtained worst corners still satisfy

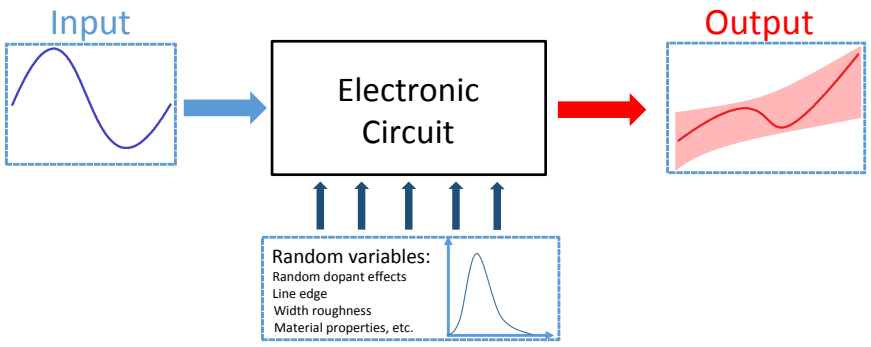

Figure 1.1: Example of the effect of parameters variations on a circuit response. In the presence of variations, the response to a deterministic stimulus is not deterministic anymore: the red line denotes the nominal response, while the pink area indicates its fluctuation.

the design specifications. However, given the continuously decreasing minimum feature sizes, corner analysis has been considered as inadequate, since reliance on corner analysis is usually based on overly pessimistic assumptions and could end up rejecting a valid design [12, 13].

Alternatively, statistical analysis has been proposed as a new family of design techniques. In this framework, the response of modern ICs is considered as a stochastic process with regard to the parameters affected by fabrication process, as shown in Fig. 1.1. While the corner analysis only makes binary decision by evaluating the corners of the parameter space, statistical analysis can estimate the likelihood of circuit response and predict the yield (the percentage of chips that can function correctly) at a expense of evaluating more samples in the parameter space.

The standard approach for statistical analysis is the Monte Carlo (MC) method, which is widely used, robust and easy to implement, but very time consuming. It is essentially a sampling-based approach: first a large set of samples is drawn for the electrical and geometrical parameters under stochastic effects, then a circuit simulation is performed for each sample obtained. Finally, relevant statistical matrix is computed using all the simulation results. However, due to its slow convergence rate, thousands of simulations are usually required for the MC method to give accurate results [14]. Since circuit simulations are time consuming, given the complexity of modern ICs, this method can hardly be applied to large and complex designs or when computationally expensive analysis (such as full wave electromagnetic simulations) are required.

More recently, there has been an increasing interest in applying stochastic spectral methods as an efficient alternative to the computationally cumbersome MC-based techniques for variability analysis of electronic circuits: such as the

polynomial chaos (PC) expansion [15, 16], stochastic collocation (SC) methods [17, 18], and stochastic reduced order models (SROMs) [19, 20]. Among the different techniques presented in the literature, PC-based methods have attracted great interest in the research community for three main reasons [21]:

- the capability to tackle variability analysis problems defined in the frequency and time domain considering different types of systems (i.e., linear and nonlinear ones), and involving random variables of different distributions, even in the presence of correlation;
- the efficiency in estimating stochastic moments (i.e., the mean and standard deviation can be computed via suitable analytical formulas);
- the ease of integration in modern EDA tools via non-intrusive approaches or via the calculation of suitable equivalent circuits describing the variability of the system under study.

In this thesis, novel PC-based stochastic macromodeling approaches will be proposed to characterize the variations in the time domain efficiently, which are elaborated in Chapters 2 and 3.

1.2 Compact macromodeling of photonic circuits

1.2.1 The rise of silicon photonics

With the boom of internet and smartphone usage, our society has entered into the "big data" era and massive amount of data is generated each day via social media, online business, digital content (e.g. photos and videos), internet of things, etc. It is expected that the amount of the data will continuously and more rapidly increase in the future, which defines a new challenge to transmit and process these data with the current electronic circuits.

The solution to increase data process capability is to improve system performance, which depends on either raising clock frequencies or on increasing instruction, thread, and program parallelism [22]. While clock rate speedup has reached power and complexity limits, an increase in parallelism require a corresponding increase in the number of transistors to enable heavily cached, speculative, multicore and/or multithreaded architectures. However, increasing transistor counts by simply assembling multiple chips together on a printed circuit board does not efficiently improve performance, because connecting different chips presents fundamental performance bottlenecks, even when used with high-speed and high-power serializer-deserializer (SerDes) circuits. In particular, transmission of such high speed signals in copper faces two main problems: first, the high speed oscillating signal induces stray currents in the printed circuit boards conductors that

increase the power consumption; second, induced currents inside the wire itself push electrons to the surface of the metal, reducing the effective cross-section of the wire and thus raising its resistance, leading to raising the losses incurred in the data transmission. For example, approximately 50% of microprocessor power was consumed by the interconnect at the 130 nm technology node, and this is expected to rise to 80% [23]. The higher the operating frequency, that is the clock rate of the signal, the greater the losses will be. When linking together the multiple multi-processing modules of a massively parallel computer across boards or racks, the copper bandwidth and power dissipation bottleneck becomes particularly severe.

In this scenario, photonic integrated circuits (PICs), which integrate multiple photonic function blocks on chips, are expected to address this challenge. The major difference between PICs and electronic ICs is that the former process signals at optical wavelengths typically in the visible spectrum or near infrared (corresponding to a wavelength of 850 nm - 1650 nm). The PICs market today is shared by different materials, such as group IV semiconductors (silicon and germanium) [24, 25], compound III-V semiconductors (indium phosphide and gallium arsenide) [26, 27], silica planar lightwave circuits [28], silicon nitride (with flavors such as TriPlex) [29], different polymers [30], and more exotic materials [31]. Among these, group IV semiconductor-based photonics, often called silicon photonics, has become a prominent technology for PICs since its potential was recognized in the first studies of waveguides in silicon-on-insulator (SOI) wafer structures in 1985 [32–34]. Silicon photonics enables high density PICs by means of CMOS-compatible fabrication process technology in a CMOS fab, resulting in complex optical functionality on a compact chip at low cost. Note that the high material index contrast between the guiding silicon and the cladding permits sub-micron waveguides and a high integration density. The SOI structure and a typical fabricated silicon waveguide are illustrated in Fig. 1.2. The top surface of the waveguide can be either left uncovered and exposed to air (e.g. for sensing applications), or covered with a cladding, typically made of silica. Now, silicon photonics is widely accepted as a key technology in the next-generation communications systems and data interconnects [34].

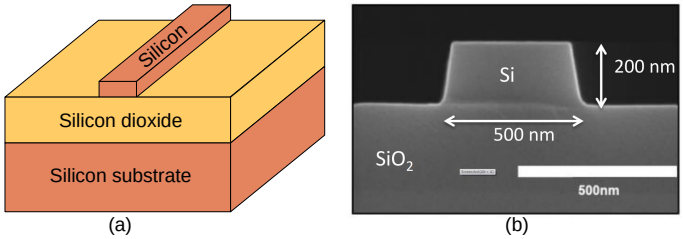

Figure 1.2: (a) The SOI structure; (b) The cross section of a fabricated silicon waveguide.

1.2.2 Challenges in photonic circuit simulation

Similar to the design of electronic ICs, the high manufacturing cost makes it essential to guarantee first-time-right design. However, unlike electronic circuits, which have been extensively studied and developed in the past several decades, silicon photonics is still at early development stage and there are many challenges on the way heading to high integration and mass production [35]. One of these challenges is photonic circuit simulation, which is essential to integrate a large number of complex photonic function blocks into a single chip. Circuit simulations always rely on models and simulators. So far, the modeling and simulation techniques for photonic circuits are far from well established.

Intuitively, the methodologies and even the circuit simulators used in electronics field could be adopted in the photonics field as well. However, several issues appear when it comes to circuit modeling and simulations of photonic systems. Indeed, electronic circuit simulators, such as SPICE, are based on the modified nodal analysis (MNA) method to determine suitable circuit equations by leveraging on the circuits models and Kirchhoff's circuit laws. Both the node voltages and branch currents of the circuit under study can be determined by solving the obtained circuit equations with respect to the time. However, photonic systems are physically described by using wave propagation and scattering formalism (such as bidirectional forward and backward waves). Hence, a MNA-based approach cannot be directly applied to photonic circuits simulations unless the optical waves are converted into a corresponding voltage and current representation. Furthermore, photonic circuits operate at optical frequency range: for example, the bandwidth $[187;\ 200]$ THz, corresponding to a wavelength of $[1.5;\ 1.6]$ μm, is commonly used for telecommunication applications. Performing time-domain simulations on signals defined at such high frequencies is impractical since extremely small time steps have to be used and lead to a high computational cost. Indeed, considering that a sequence signal of 1000 bits with a bit rate of 25 Gbps is modulated on a optical carrier with wavelength 1.55 μm, the total time samples will be 80 million (1000×40 ps/0.5 fs) when a time step of 0.5 fs is adopted. One bit of such modulated optical signal is illustrated in Fig. 1.3. These issues suggest that photonic circuits have to be modeled and simulated in a different way compared to electronic circuits.

A lot of effort has been invested by the research community into developing circuit models for non-linear photonic devices, such as for lasers [36–38], modulators [39–41], photodiodes [42–45]. However, there are very limited existing circuit modeling techniques for linear passive devices and systems, whose functions roughly fall into two categories: distributing/transporting light (e.g. waveguides), and optical wavelength filtering for applications such as spectroscopy, *wavelength division multiplexing* (WDM) or *microwave photonics* (MWP). Especially in the last two applications, an efficient modeling approach of the filters, which is able

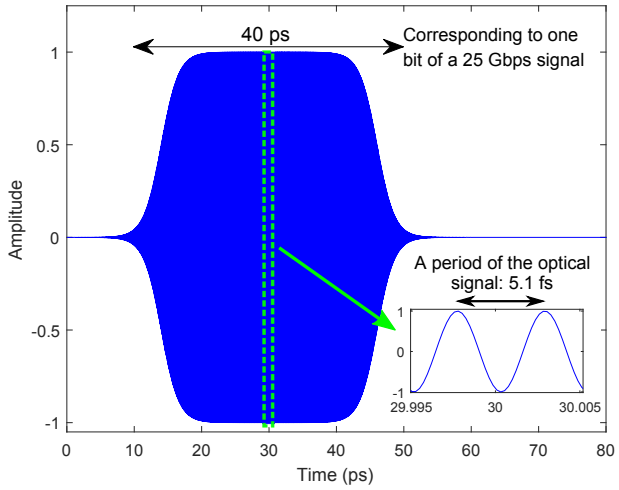

Figure 1.3: A modulated optical signal with carrier wavelength 1.55 μm and a 25 Gbps modulation sequence.

to take into account imperfections such as higher-order dispersion, wavelength-dependent loss, and imperfections in coupling coefficients, is urgently needed.

A common approach is to compute analytic models (or "white box model"), which rely on the knowledge of the working principles of the device under study. Such models are useful in the design phase, because the geometrical or optical parameters (such as length, coupling coefficient, effective index, etc.) are directly related to the performance measures of the device considered. However, in practice, analytic models can be derived only for simple photonic systems and there is a limit in their accuracy when describing complex non-ideal characteristics of the system under study (i.e. backscattering and undesired dispersion effects). Furthermore, most of these models are generally described as frequency- (wavelength) domain models, whereas time-domain models are needed since time-domain simulations are required to evaluate the performance of photonic circuits in a larger system, such as bit error rate and eye diagrams [35, 46]. Actually, for passive devices and circuits, their scattering parameters data are more accessible (e.g. via electromagnetic simulations or measurements) than accurate analytic models. Hence, it is convenient to conduct time-domain simulations starting from the scattering parameters. A typical example is given by the *finite impulse response* (FIR) modeling technique [47], which is based on the scattering parameters representation and is adopted in the photonic simulators Lumerical INTERCONNECT [48], VPIphotonics [49] and PICWave [50]. The built model can be considered as a "black box model" since it only mimics the input and output behaviors and does not reveal

the actual working principle of the circuit under study. The accuracy provided by FIR-based models substantially depends on the design methodology employed and it inherently degrades near the edges of the simulated signal bands [47].

Therefore, to address this problem, novel and accurate macromodeling and simulation techniques for passive photonic circuits have been proposed in this work, which satisfy four requirements:

- the models can be represented in the frequency and time domain;
- the modeling process should be robust;
- the models should be accurate enough with regard to the behaviors of the actual devices, and eventually generate valuable information to guide circuit designs;
- the models must be "compact" to make sure that the circuit simulation is efficient and they should have the potential to be implemented in electronic simulators, such as SPICE and Verilog-A.

This last requirement is important, since there is a dire need of co-simulation of electronic and photonic circuits considering that in some applications they are closely integrated and interact with each other. For example, optoelectronic devices such as detectors, amplifiers, lasers and modulators have both electrical and optical behaviors, and therefore must be simulated in both domains, especially if there are electrical controls or feedback loops.

Another challenge for photonic circuits is to estimate the effect of the manufacturing process variations, since the associated performance degradation is even more problematic than the electronic case [51]. For the best-in-class 193 nm immersion deep ultraviolet (DUV) lithography, the observed waveguide linewidth fluctuations are in the order of 5 nm (as shown in Fig. 1.4) and silicon layer thickness fluctuations of state-of-the-art SOI substrates are in the order of 1 nm [52].

To illustrate this more clearly, let us look at a ring resonator (in Fig. 1.5 (a)) where the resonance condition depends on the optical roundtrip length of the ring waveguide, and this in turn depends on the actual geometry of the waveguide. Small width or height variations will induce a significant shift in the resonance wavelength: for a width change of 1 nm, the wavelength will shift approximately 1 nm (roughly about 130 GHz), which can span more than one channel in a WDM system [53], as shown in Fig. 1.5 (b). Indeed, given that the propagation of light is entirely determined by the geometry for certain materials platform, photonic devices on a chip are very sensitive to variations in geometrical parameters and environment condition. This sensitivity also depends on the materials platform adopted, especially the refractive index contrast between the materials used for waveguide cores and the surrounding cladding. Higher index contrast allows for

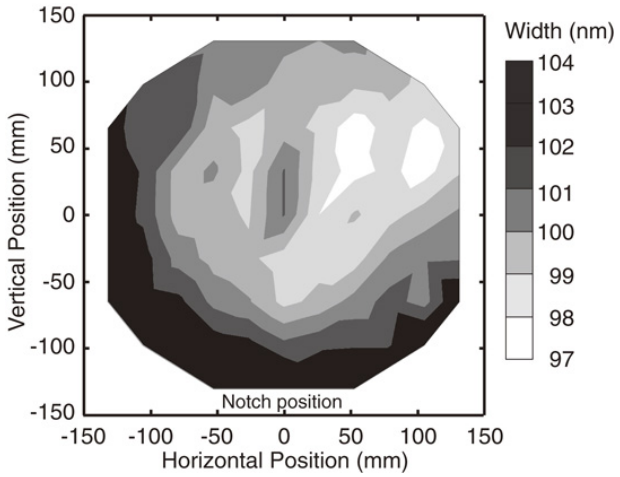

Figure 1.4: Contour map of the widths of a fabricated 100-nm-wide waveguide at 84 points on a 300 mm SOI wafer. The measured widths vary with the locations and have a mean and 3σ (standard deviation) of 100.6 and 5.3 nm, respectively , according to the study in [52].

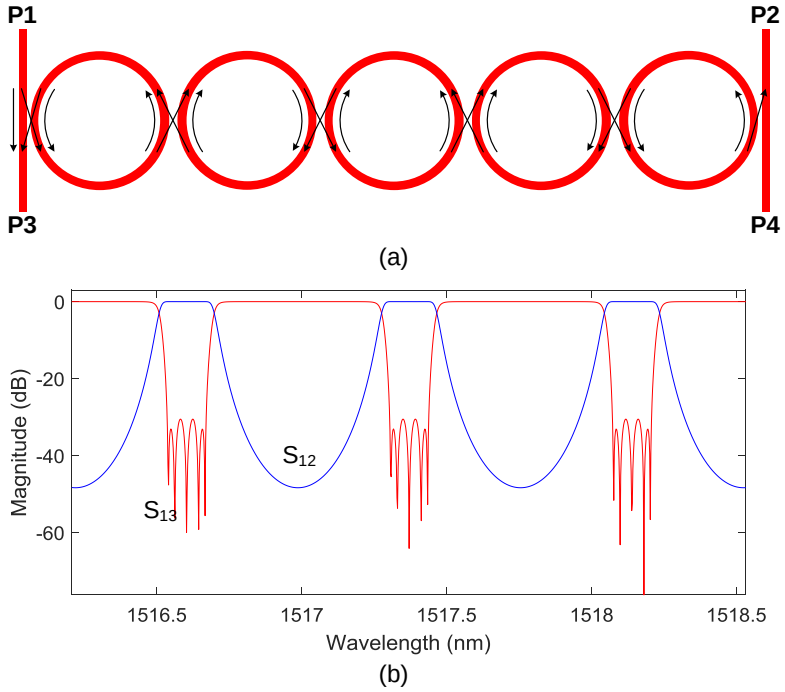

Figure 1.5: (a) Structure of a five-ring resonator. (b) Response of the five-ring resonator.

tighter confinement of light, but this also make the device more sensitive to variations. The issue is particularly prominent in silicon photonics because of its submicron waveguides and extremely large index contrast between the guiding layer and the claddings [35].

Hence, variability analysis is a fundamental tool for photonic circuits design. Recently, variability analysis techniques proposed for electronic circuits have been applied to photonic circuits [54–58]. Most of these works are conducted to quantifying the variations of coupling coefficients [54, 55], 3-dB bandwidth [57, 58], transmission or scattering matrices [56], but no time-domain variability analysis has ever been carried out on the system level, which is crucial for evaluating the overall performance of a photonic circuit (i.e. bit error rate, eye diagrams). In this framework, an accurate and efficient time-domain variability analysis approach for linear photonic circuits is presented in Chapter 6. It leverages on the expertise in stochastic macromodeling and time-domain baseband modeling techniques developed during my entire research.

1.3 Contributions and outline of the thesis

The main contributions of the thesis can be grouped into two parts:

- stochastic macromodeling for electronic circuits (Chapters 2 and 3) and linear photonic circuits (Chapter 6) to quantify the effect of fabrication variations on the time-domain performance;
- compact macromodeling of linear passive (deterministic) photonic circuits for time-domain simulations (Chapters 4 and 5).

Note that the macromodeling techniques of deterministic photonic circuits serves as a foundation for the stochastic ones. The structure of the thesis is illustrated in Fig. 1.6, and the contribution of each chapter is briefly described in the following.

Chapter 1 of this PhD thesis introduces the motivation of variability analysis for both electronic and photonic circuits and the challenges in time-domain modeling and simulation of photonic circuits.

Chapter 2 focuses on linear electronic multiport systems subject to manufacturing variations. Stochastic macromodels are built for linear electronic systems described by different transfer functions: scattering parameters, impedance parameters, and admittance parameters. The physical properties, such as stability and passivity, for the stochastic models are rigorously defined and studied, which is very important for time-domain simulations for the models. Then a parameterized stochastic modeling technique is proposed to deal with linear electronic system with both deterministic parameters and stochastic parameters.

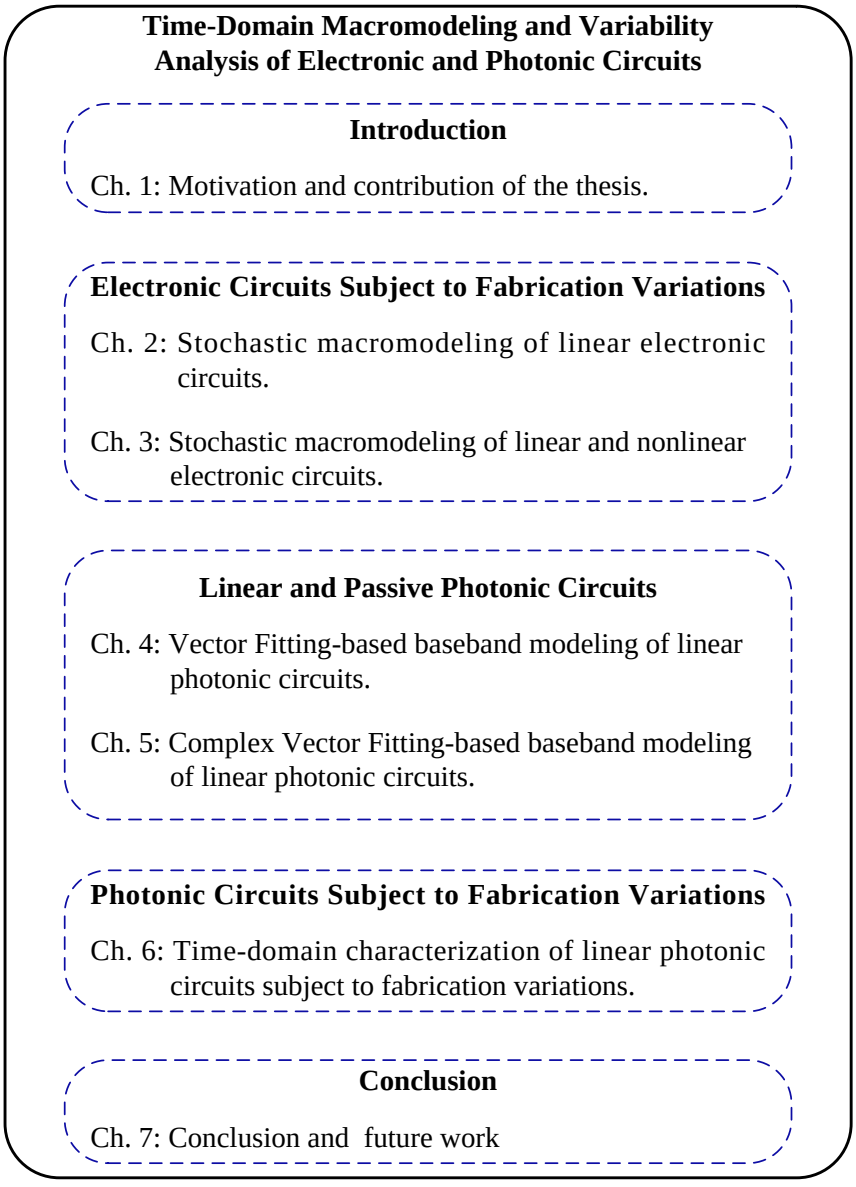

Figure 1.6: The structure of the thesis.

Chapter 3 is for variability analysis of electronic circuits containing both linear and nonlinear devices. Stochastic models can be built for both linear and nonlinear devices separately and then connected in SPICE. Only a single time-domain simulation is required to obtain the stochastic information of outputs of the circuit under study.

While Chapters 2 and 3 study electronic circuits, Chapters 4-6 focus on photonic circuits. As aforementioned, unlike the electronic circuits, which in general already have sophisticated circuit models, photonic circuits are still in the early stage of developing accurate circuit models for time-domain simulations. Especially for the linear devices, they are normally studied in frequency domain and do not have accurate time-domain models which can take into account the nonidealities, such as higher-order dispersion and wavelength-dependent losses. Therefore, time-domain modeling technique of linear (deterministic) photonic circuits are explored in Chapters 4 and 5, and then Chapter 6 performs time-domain variability analysis of photonic circuits subject to fabrication variations.

Chapter 4 proposes an accurate and efficient baseband modeling approach for linear photonic circuits described by scattering parameters. The modeling process leverages on the Vector Fitting (VF) technique which is robust and can build time-domain state-space models from scattering parameters. The built models represent complex-valued systems and can be simulated in the baseband rather than at optical frequency, which dramatically improves the efficiency of time-domain simulations. Since the built models are complex-valued and non-physical, and passivity conditions for physical systems are not applicable, new passivity conditions and fast passivity assessment method are derived for the built non-physical models. Considering the complex-valued models can only be simulated in complex number supported simulators, Chapter 4 then extends the baseband modeling approach and derives real-valued models which not only inherit all the advantages of the complex-valued models but also maintain all properties of linear physical systems. It is more suitable for optical-electronic co-simulations. Chapter 5 presents a novel baseband modeling technique for linear photonic circuits which can build more compact models. Compared to modeling approach in Chapter 4 based on the VF technique, the new modeling approach introduces a novel Complex Vector Fitting (CVF) technique. It can generate a half-size model for the same application, thereby achieving a major improvement in efficiency of the time-domain simulation.

In Chapter 6, time-domain variability analysis of linear photonic circuits subject to manufacturing variations is conducted by leveraging on the stochastic modeling technique in Chapter 2 and baseband modeling technique in Chapters 4 and 5. In future work, the stochastic modeling techniques of Chapters 3 and 6 can be applied to photonic circuits consisting of both linear and nonlinear devices.

Finally in Chapter 7, overall conclusions are drawn and opportunities for future

research directions are briefly described.

1.4 Publications

1.4.1 International journals

- F. Passos, **Y. Ye**, D. Spina, E. Roca, R. Castro-López, T. Dhaene, and F. V. Fernández, "Parametric macromodeling of integrated inductors for RF circuit design," *Microwave and Optical Technology Letters*, vol. 59, no. 9, pp. 1207-1212, Mar. 2017.

- **Y. Ye**, D. Spina, P. Manfredi, D. Vande Ginste, and T. Dhaene, "A comprehensive and modular stochastic modeling framework for the variability-aware assessment of signal integrity in high-speed links," *IEEE Transactions on Electromagnetic Compatibility*, vol. 60, no. 2, pp. 459-467, Apr. 2018.

- **Y. Ye**, D. Spina, Y. Xing, W. Bogaerts, and T. Dhaene, "Numerical modeling of linear photonic systems for accurate and efficient time-domain simulations," *Photonics Research*, vol. 6, no. 6, pp. 560-573, Jun. 2018.

- **Y. Ye**, D. Spina, W. Bogaerts, and T. Dhaene, "Baseband modeling of linear photonic circuits for time-domain simulations," *Journal of Lightwave Technology*, vol. 37, no. 4, pp. 1364-1373, Feb. 2019.

- **Y. Ye**, D. Spina, G. Antonini, and T. Dhaene, "Passivity study on polynomial chaos-based stochastic macromodeling of linear multiport systems," *Under review*.

- **Y. Ye**, D. Spina, D. Deschrijver, W. Bogaerts, and T. Dhaene, "Compact baseband modeling of linear photonic circuits via complex vector fitting," *Under review*.

- **Y. Ye**, M. Wang, D. Spina, W. Bogaerts, and T. Dhaene, "Time-domain characterization of photonic integrated filters subject to fabrication variations," *Under review*.

1.4.2 International conferences

- F. Passos, E. Roca, R. Castro-López, F. V. Fernńdez, **Y. Ye**, D. Spina, and T. Dhaene, "Frequency-dependent parameterized macromodeling of integrated inductors," in the proceedings of the *13th International Conference on Synthesis, Modeling, Analysis and Simulation Methods and Applications to Circuit Design (SMACD)*, Lisbon (Portugal), 2016, pp.1-4.

- **Y. Ye**, D. Spina, T. Dhaene, L. Knockaert, and G. Antonini, "Macromodeling of general linear systems under stochastic variations," in the proceedings of the *IEEE Electrical Design of Advanced Packaging and Systems (EDAPS)*, Honolulu (USA), 2016, pp. 61-63.

- Y. Xing, U. Khan, **Y. Ye**, and W. Bogaerts, "Extracting fabricated geometry on die-Level," in the proceedings of the *IEEE Photonics Scociety Benelux-Annual Symposium*, Netherlands, 2017, pp. 148-151.

- **Y. Ye**, D. Spina, P. Manfredi, D. Vande Ginste, and T. Dhaene, "Time-domain variability analysis of general linear systems terminated with nonlinear devices," in the proceedings of the *IEEE 21st Workshop on Signal and Power Integrity (SPI)*, Baveno (Italy), 2017, pp. 1-4.

- **Y. Ye**, D. Spina, Y. Xing, W. Bogaerts, and T. Dhaene, "Fast and accurate time-domain simulation of passive photonic systems," in the proceedings of the *International Conference on Electromagnetics in Advanced Applications (ICEAA)*, Cartagena des Indias (Colombia), 2018, pp. 396-399.

- **Y. Ye**, D. Spina, G. Antonini, and T. Dhaene, "Parameterized macromodeling of stochastic linear systems for frequency- and time-domain variability analysis," in the proceedings of the *IEEE 22nd Workshop on Signal and Power Integrity (SPI)*, Brest (France), 2018, pp. 1-4.

- Y. Xing, J. Dong, U. Khan, **Y. Ye**, D. Spina, T. Dhaene, and W. Bogaerts, "From parameter extraction, variability models to yield prediction," in the proceedings of the *Latin America Optics and Photonics Conference*, Lima (Peru), 2018, paper W3E.1.

References

[1] L. W. Nagel and D. O. Pederson. *Simulation program with integrated circuit emphasis (SPICE)*. In 16th Midwest Symposium on Circuit Theory, Apr. 1973.

[2] C. C. McAndrew. *SPICE modeling in Verilog-A: Successes and challenges: Invited paper*. In 2017 47th European Solid-State Device Research Conference (ESSDERC), pages 22–25, Sep. 2017.

[3] S. D. Mertens. *Status of the GaN HEMT Standardization Effort at the Compact Model Coalition*. In 2014 IEEE Compound Semiconductor Integrated Circuit Symposium (CSICS), pages 1–4, La Jolla, CA, USA, Oct. 2014.

[4] G. E. Moore. *Cramming more components onto integrated circuits*. Electronics, 38(8):114–117, 1965.

[5] S. B. Dhia, M. Ramdani, and E. Sicard. *Electromagnetic Compatibility of Integrated Circuits: Techniques for Low Emission and Susceptibility*. Springer-Verlag, New York, NJ, USA, 2005.

[6] B. Nikolic, J. Park, J. Kwak, B. Giraud, Z. Guo, L. Pang, S. O. Toh, R. Jevtic, K. Qian, and C. Spanos. *Technology Variability From a Design Perspective*. IEEE Trans. Circuits Syst. I, Reg. Papers, 58(9):1996–2009, Sep. 2011.

[7] S. R. Nassif. *Modeling and analysis of manufacturing variations*. In Proceedings of the IEEE 2001 Custom Integrated Circuits Conference, San Diego, California, USA, pages 223–228, 2001.

[8] D. S. Boning, K. Balakrishnan, H. Cai, N. Drego, A. Farahanchi, K. M. Gettings, D. Lim, A. Somani, H. Taylor, D. Truque, and X. Xie. *Variation*. IEEE Trans. Semicond. Manuf., 21(1):63–71, Feb. 2008.

[9] N. Tega, H. Miki, F. Pagette, D. J. Frank, A. Ray, M. J. Rooks, W. Haensch, and K. Torii. *Increasing threshold voltage variation due to random telegraph noise in FETs as gate lengths scale to 20 nm*. In Symposium on VLSI Technology, Honolulu, HI, USA, pages 50–51, Jun. 2009.

[10] F. Gong, X. Liu, H. Yu, Sheldon X. D. Tan, J. Ren, and L. He. *A Fast Non-Monte-Carlo Yield Analysis and Optimization by Stochastic Orthogonal Polynomials*. ACM T. Des. Automat. El., 17(1):1–23, Jan. 2012.

[11] M. Onabajo and J. Silva-Martinez. *Analog Circuit Design for Process Variation-Resilient Systems-on-a-Chip*. Springer-Verlag New York, NJ, USA, 2012.

[12] S. K. Saha. *Modeling Process Variability in Scaled CMOS Technology*. IEEE Des. Test. Comput., 27(2):8–16, Mar. 2010.

[13] G. Neuberger, G. Wirth, and R. Reis. *Protecting chips against hold time violations due to variability*. Springer, 2014.

[14] G. Fishman. *Monte Carlo: concepts, algorithms, and applications*. Springer Science & Business Media, 2013.

[15] D. Xiu and G. E. Karniadakis. *The Wiener–Askey Polynomial Chaos for Stochastic Differential Equations*. SIAM J. Sci. Comput., 24(2):619–644, 2002.

[16] G. Blatman and B. Sudret. *An adaptive algorithm to build up sparse polynomial chaos expansions for stochastic finite element analysis*. Probabilist Eng. Mech., 25:183–197, Apr. 2010.

[17] J. Tao, X. Zeng, W. Cai, Y. Su, D. Zhou, and C. Chiang. *Stochastic Sparse-grid Collocation Algorithm (SSCA) for Periodic Steady-State Analysis of Nonlinear System with Process Variations*. In In Proceedings Asia and South Pacific Design Automation Conference (ASPDAC), Yokohama, Japan, pages 474–479, Jan. 2007.

[18] J. Silly-Carette, D. Lautru, M. F. Wong, A. Gati, J. Wiart, and V. Fouad Hanna. *Variability on the Propagation of a Plane Wave Using Stochastic Collocation Methods in a Bio Electromagnetic Application*. IEEE Microw. Wireless Compon. Lett., 19(4):185–187, Apr. 2009.

[19] M. Grigoriu. *Reduced order models for random functions. Application to stochastic problems*. Applied Mathematical Modelling, 33(1):161 – 175, 2009.

[20] Z. Fei, Y. Huang, J. Zhou, and Q. Xu. *Uncertainty Quantification of Crosstalk Using Stochastic Reduced Order Models*. IEEE Trans. Electromagn. Compat., 59(1):228–239, Feb. 2017.

[21] A. Kaintura, T. Dhaene, and D. Spina. *Review of Polynomial Chaos-Based Methods for Uncertainty Quantification in Modern Integrated Circuits*. Electronics, 7(3):30, 2018.

[22] A. V. Krishnamoorthy, R. Ho, X. Zheng, H. Schwetman, J. Lexau, P. Koka, G. Li, I. Shubin, and J. E. Cunningham. *Computer Systems Based on Silicon Photonic Interconnects*. Proc. IEEE, 97(7):1337–1361, Jul. 2009.

[23] D. A. B. Miller. *Device Requirements for Optical Interconnects to Silicon Chips*. Proceedings of the IEEE, 97(7):1166–1185, Jul. 2009.

[24] X. Chen, M. M. Milosevic, S. Stankovi, S. Reynolds, T. D. Bucio, K. Li, D. J. Thomson, F. Gardes, and G. T. Reed. *The Emergence of Silicon Photonics as a Flexible Technology Platform*. Proc. IEEE, 106(12):2101–2116, Dec. 2018.

[25] R. Soref. *The past, present, and future of silicon photonics*. IEEE J. Sel. Topics Quantum Electron., 12(6):1678–1687, 2006.

[26] T. L. Koch and U. Koren. *Semiconductor photonic integrated circuits*. IEEE J. Quantum Electron., 27(3):641–653, 1991.

[27] X. Duan, Y. Huang, Y. Cui, J. Wang, and C. M. Lieber. *Indium phosphide nanowires as building blocks for nanoscale electronic and optoelectronic devices*. Nature, 409(6816):66, 2001.

[28] A. Himeno, K. Kato, and T. Miya. *Silica-based planar lightwave circuits*. IEEE J. Sel. Topics Quantum Electron., 4(6):913–924, 1998.

[29] K. Wörhoff, R. G. Heideman, A. Leinse, and M. Hoekman. *TriPleX: a versatile dielectric photonic platform*. Adv. Opt. Mater., 4(2):189–207, 2015.

[30] M. U. Khan, J. Justice, J. Petäjä, T. Korhonen, A. Boersma, S. Wiegersma, M. Karppinen, and B. Corbett. *Multi-level single mode 2D polymer waveguide optical interconnects using nano-imprint lithography*. Opt. Express, 23(11):14630–14639, 2015.

[31] D. Liang and J. E. Bowers. *Recent progress in lasers on silicon*. Nature photonics, 4(8):511, 2010.

[32] R. A. Soref and J. P. Lorenzo. *Single-crystal silicon: a new material for 1.3 and 1.6 μm integrated-optical components*. Electron. Lett., 21(21):953–954, Oct. 1985.

[33] G. T. Reed, W. R. Headley, and CE J. Png. *Silicon photonics: The early years*. In Proc.SPIE, volume 5730, pages 1–19, 2005.

[34] D. Thomson, A. Zilkie, et al. *Roadmap on silicon photonics*. J. Opt., 18(7):073003, Jun. 2016.

[35] Wim Bogaerts and Lukas Chrostowski. *Silicon photonics circuit design: methods, tools and challenges*. Laser Photon Rev., 12(4):1700237, 2018.

[36] P. V. Mena, J. J. Morikuni, S. Kang, A. V. Harton, and K. W. Wyatt. *A comprehensive circuit-level model of vertical-cavity surface-emitting lasers*. J. Lightw. Technol., 17(12):2612–2632, Dec. 1999.

[37] M. Belkin and V. Iakovlev. *Microwave-Band Circuit-Level Semiconductor Laser Modeling*. In 2015 IEEE European Modelling Symposium (EMS), pages 443–445, Oct. 2015.

[38] H. R. Yousefvand. *A Versatile Physics-Based Circuit Model for Mid-Infrared Quantum Cascade Lasers*. J. Lightw. Technol., 34(3):1031–1037, Feb. 2016.

[39] H. Bahrami, H. Sepehrian, C. S. Park, L. A. Rusch, and W. Shi. *Time-Domain Large-Signal Modeling of Traveling-Wave Modulators on SOI*. J. Lightw. Technol., 34(11):2812–2823, Jun. 2016.

[40] S. Tanaka, T. Usuki, and Y. Tanaka. *Accurate SPICE Model of Forward-Biased Silicon PIN Mach-Zehnder Modulator for an Energy-Efficient Multi-level Transmitter*. J. Lightw. Technol., 36(10):1959–1969, May 2018.

[41] B. Wang, C. Li, C. Chen, K. Yu, M. Fiorentino, R. G. Beausoleil, and S. Palermo. *A Compact Verilog-A Model of Silicon Carrier-Injection Ring Modulators for Optical Interconnect Transceiver Circuit Design*. J. Lightw. Technol., 34(12):2996–3005, Jun. 2016.

[42] Y. M. El-Batawy and M. J. Deen. *Analysis, circuit modeling, and optimization of mushroom waveguide photodetector (mushroom-WGPD)*. J. Lightw. Technol., 23(1):423–431, Jan. 2005.

[43] M. Jalali, M. K. Moravvej-Farshi, S. Masudy-Panah, and A. Nabavi. *An Equivalent Lumped Circuit Model for Thin Avalanche Photodiodes With Nonuniform Electric Field Profile*. J. Lightw. Technol., 28(23):3395–3402, Dec. 2010.

[44] M. Piels, A. Ramaswamy, and J. E. Bowers. *Nonlinear modeling of waveguide photodetectors*. Opt. Express, 21(13):15634–15644, Jul. 2013.

[45] D. Dai, M. Piels, and J. E. Bowers. *Monolithic Germanium/Silicon Photodetectors With Decoupled Structures: Resonant APDs and UTC Photodiodes*. IEEE J. Sel. Topics Quantum Electron, 20(6):43–56, Nov. 2014.

[46] C. Sorace-Agaskar, J. Leu, M. R. Watts, and V. Stojanovic. *Electro-optical co-simulation for integrated CMOS photonic circuits with VerilogA*. Opt. Express, 23(21):27180–27203, Oct. 2015.

[47] S. Mingaleev, A. Richter, E. Sokolov, C. Arellano, and I. Koltchanov. *Towards an automated design framework for large-scale photonic integrated circuits*. Proc. SPIE, 9516:951602, 2015.

[48] J. Pond, C. Cone, L. Chrostowski, J. Klein, J. Flueckiger, A. Liu, D. McGuire, and X. Wang. *A complete design flow for silicon photonics*. Proc. SPIE, 9133:913310, 2014.

[49] www.vpiphotonics.com/Tools/PhotonicCircuits/Features/.

[50] www.photond.com/products/fimmprop/fimmprop_features_50.htm.

[51] W. A. Zortman, D. C. Trotter, and M. R. Watts. *Silicon photonics manufacturing*. Opt. Express, 18(23):23598–23607, Nov. 2010.

[52] M. Soma, T. Kita, Y. Tanushi, et al. *Optimum waveguide-core size for reducing device property distribution of Si-wire waveguide devices*. Jpn. J. Appl. Phys., 54(4S):04DG03, Mar. 2015.

[53] W. Bogaerts, M. Fiers, and P. Dumon. *Design Challenges in Silicon Photonics*. IEEE J. Sel. Topics Quantum Electron., 20(4):1–8, Jul. 2014.

[54] T. W. Weng, Z. Zhang, Z. Su, Y. Marzouk, A. Melloni, and L. Daniel. *Uncertainty quantification of silicon photonic devices with correlated and non-Gaussian random parameters*. Opt. Express, 23(4):4242–4254, Feb. 2015.

[55] Y. Xing, D. Spina, A. Li, T. Dhaene, and W. Bogaerts. *Stochastic collocation for device-level variability analysis in integrated photonics*. Photon. Res., 4(2):93–100, Apr. 2016.

[56] A. Waqas, D. Melati, P. Manfredi, and A. Melloni. *Stochastic process design kits for photonic circuits based on polynomial chaos augmented macromodelling*. Opt. Express, 26(5):5894–5907, Mar. 2018.

[57] T. W. Weng, D. Melati, A. Melloni, and L. Daniel. *Stochastic simulation and robust design optimization of integrated photonic filters*. Nanophotonics, 6(1):299–308, 2017.

[58] C. Cui and Z. Zhang. *Uncertainty quantification of electronic and photonic ICs with non-Gaussian correlated process variations*. In Proceedings of the International Conference on Computer-Aided Design, page 97, 2018.

2

Stochastic Macromodeling of Linear Electronic Circuits

Y. Ye, D. Spina, G. Antonini, and T. Dhaene, "Passivity study on polynomial chaos-based stochastic macromodeling of linear multiport systems," Under review at Electronics Letters.

Y. Ye, D. Spina, G. Antonini, and T. Dhaene, "Parameterized macromodeling of stochastic linear systems for frequency- and time-domain variability analysis," in the proceedings of the IEEE 22nd Workshop on Signal and Power Integrity (SPI), Brest (France), 2018, pp. 1-4.

Y. Ye, D. Spina, T. Dhaene, L. Knockaert, and G. Antonini, "Macromodeling of general linear systems under stochastic variations," in the proceedings of the IEEE Electrical Design of Advanced Packaging and Systems (EDAPS), Honolulu (USA), 2016, pp. 61-63.

Abstract

In this chapter, a novel polynomial chaos-based stochastic macromodeling technique for the frequency- and time-domain variability analysis of general linear and passive systems is presented. It can be applied to systems whose transfer func-

tion is described by different representations (namely scattering, impedance and admittance parameters). The properties of the proposed methodology and the relations between stochastic macromodels computed for different transfer function representations are discussed in details. In particular, the passivity conditions for the stochastic macromodels are rigorously derived. Three suitable numerical examples validate the accuracy and efficiency of the proposed technique.

2.1 Introduction

The performance degradation of integrated circuits (ICs) due to manufacturing variations on high frequency designs has arisen as a crucial problem, due to the increasing integration and miniaturization of modern ICs, which makes it critical to estimate the influence of the inherent parameters variability on the ICs performance, often referred to as variability analysis. The standard variability analysis approach is represented by the Monte Carlo (MC) method; however, due to its slow convergence rate, its computational cost becomes prohibitive when studying complex ICs, especially if electromagnetic (EM) simulations are required to describe the distributed elements in the circuit.

The polynomial chaos (PC) expansion [1, 2] has attracted great attention in recent years as an alternative approach to this problem, thanks to its ability to perform variability analysis of complex ICs with high accuracy and efficiency as compared to MC-based methods [3–14]. In particular, the PC-based techniques presented in the literature are tailored for a specific class of circuits, like lumped-element circuits [3], transmission-line circuits with different types of terminations [4–6], general passive linear systems [7–10] or nonlinear circuits described by means of modified nodal equations [11–14]. Especially, the PC-based approach proposed in [9, 10] allows one to compute a suitable macromodel for the time-domain variability analysis of generic linear multiport systems which often involves EM full-wave simulation. Such technique is based on the PC expansion of the scattering parameters of the system under study, and employs the Galerkin projection (GP) method and the Vector Fitting (VF) algorithm to compute a deterministic, stable and passive state-space model describing the relation between the PC coefficients of the system port signals. Pertinent statistical information of the entire system can be computed by means of only one time-domain simulation of such model, which can be readily converted into an equivalent SPICE-compatible circuit, thanks to suitable macromodeling synthesis techniques [15–17]. In the PC jargon, models of such type are usually referred to as “augmented”, since their number of ports is higher with respect to the corresponding system under stochastic variations.

However, the macromodeling approach presented in [9, 10] can be applied only to linear systems described by their scattering parameters for time-domain analy-

sis. In Section 2.2, we overcome this limitation via generalizing the technique in [9, 10] to linear passive stochastic systems represented by their impedance, admittance parameters, and present a detailed breakdown of the computational cost of the modeling technique. Section 2.3 presents a rigorous study on the passivity definition and condition for such "augmented" macromodels for admittance and impedance representations. Then the relations between such "augmented" macromodels computed for different transfer function representations of the same system is derived in Section 2.4. In Section 2.5, we demonstrate an approach to parameterize the augmented systems with regard to design parameters and stochastic parameters, which is very useful when time- or frequency-domain variability analysis of the system under study must be repeated for different nominal values of the random parameters considered, such as designing systems robust to manufacturing variations. The validation of the proposed methods in this chapter is performed in Section 2.6, while conclusions are presented in Section 2.7.

2.2 Stochastic macromodeling for general linear and passive multiport systems

In the following, we will assume that the linear system under study is subjected to the effect of stochastic variations: suitable geometrical or electrical parameters can be considered as random variables, collected in the vector $\boldsymbol{\xi}$ in the stochastic space $\boldsymbol{\Omega}$. As a result of this variability, both the transfer function and the voltages and currents at the input/output ports of such system are random quantities, which can be described by means of the PC expansion as:

$$\boldsymbol{H}(s,\boldsymbol{\xi}) \approx \sum_{j=0}^{M_H} \boldsymbol{H}_j(s)\varphi_j(\boldsymbol{\xi}) \tag{2.1a}$$

$$\boldsymbol{v}(t,\boldsymbol{\xi}) \approx \sum_{j=0}^{M_v} \boldsymbol{v}_j(t)\varphi_j(\boldsymbol{\xi}) \tag{2.1b}$$

$$\boldsymbol{i}(t,\boldsymbol{\xi}) \approx \sum_{j=0}^{M_i} \boldsymbol{i}_j(t)\varphi_j(\boldsymbol{\xi}) \tag{2.1c}$$

where the vectors $\boldsymbol{v}$ and $\boldsymbol{i}$ collects the ports voltage and currents, respectively, the matrix $\boldsymbol{H}$ represents the system transfer function expressed by means of the chosen representation (scattering, impedance or admittance parameters), φ_j are the PC basis functions, which depend on the joint distribution of the random parameters considered, $\boldsymbol{H}_j$, $\boldsymbol{v}_j$ and $\boldsymbol{i}_j$ are the corresponding PC coefficients with the total numbers M_H+1, M_v+1, and M_i+1 respectively, $s=2\pi f$ is the Laplace variable and t the time. Note that, in general, different stochastic quantities in a

system may require different number of PC coefficients (and basis functions) to achieve the PC models (2.1a) - (2.1c) with acceptable accuracy. But in practice same number of PC coefficients can be chosen for simplicity, which would be $\max(M_H+1, M_v+1, M_i+1)$ in this case. The main feature of the PC expansion is the efficient representation of the variability of the quantity under study [1, 2]: for example, stochastic moments such as mean and variance of the impedance matrix can be analytically computed from its PC coefficients. More complex statistical functions, such as the probability density function (PDF) or the cumulative distribution function (CDF), can be calculated via the (inexpensive) sampling of (2.1a) - (2.1c).

The interested reader may consult [1–14] for an extensive reference to PC theory. Note that only the case of independent random variables will be discussed in the rest of the contribution, for simplicity, even though the novel method presented is general and can be extended to correlated random variables. Indeed, correlation among the random parameters considered does not influence the proposed modeling framework, but has only an impact on the calculation of PC expansion in the form (2.1a) - (2.1c) [1, 2], which is the starting point of our stochastic modeling technique. Without loss of generality, the discussion in this chapter is limited to the case of linear terminations only, as for [9, 10], while the general circuits containing both linear and nonlinear devices will be studied in Chapter 3. Finally, throughout this chapter, PC models in the form (2.1a) - (2.1c) will be based on orthonormal PC basis functions φ_j which has the property

$$\langle \varphi_i(\boldsymbol{\xi}), \varphi_j(\boldsymbol{\xi}) \rangle = \int_{\boldsymbol{\Omega}} \varphi_i(\boldsymbol{\xi}) \varphi_j(\boldsymbol{\xi}) W(\boldsymbol{\xi}) d\boldsymbol{\xi} = \delta_{ij} \tag{2.2}$$

where δ_{ij} is the Kronecker delta while $W(\boldsymbol{\xi})$ is a weighting factor corresponding to the normalized joint PDF of $\boldsymbol{\xi}$. In the following sections, the superscript ^{T} denotes transpose, while * stands for complex conjugate, and ^{H} represents transpose conjugate.

2.2.1 Calculation of augmented systems based on impedance and admittance parameters

A stable, passive and linear macromodel describing the stochastic variations for systems represented by admittance or impedance parameters can be obtained by following a similar procedure as the one presented in [9, 10]. In the following, such methodology is described in details for the impedance representation only, since the corresponding procedure for admittance parameters is straightforward.

When a generic linear system described by its impedance representation computed over suitable frequency values f_r for $r = 1, \ldots, R$ (or Laplace variable $s_r = j2\pi f_r$) is subjected to stochastic effects, the following relation holds:

$$\boldsymbol{V}(s_r, \boldsymbol{\xi}) = \boldsymbol{Z}(s_r, \boldsymbol{\xi}) \boldsymbol{I}(s_r, \boldsymbol{\xi}) \tag{2.3}$$

where $\boldsymbol{Z}$ is the impedance parameter matrix of the stochastic linear system under study, $\boldsymbol{V} \in \mathbb{C}^{N\times 1}$ and $\boldsymbol{I} \in \mathbb{C}^{N\times 1}$ are the frequency-domain port voltages and currents, respectively, and N is the number of ports of the linear system. Note that any existing frequency sampling technique valid for deterministic systems can be adopted to choose the element s_r, for $r = 1, \ldots, R$, such as linear, logarithmic or adaptive sampling, and even measured transfer function data can be used.

As mentioned before, the PC model of such impedance matrix can be written as:

$$\boldsymbol{Z}(s_r, \boldsymbol{\xi}) \approx \tilde{\boldsymbol{Z}}(s_r, \boldsymbol{\xi}) = \sum_{j=0}^{M} \boldsymbol{Z}_j(s_r)\varphi_j(\boldsymbol{\xi}) \tag{2.4}$$

where the basis function $\varphi_j(\boldsymbol{\xi})$ are orthonormal polynomials depending only on the joint distribution of the random variables $\boldsymbol{\xi}$, while $\boldsymbol{Z}_j(s_r)$ for $j = 0, \ldots, M$ are the corresponding PC coefficients which must be computed. Note that the PC coefficients in (2.4) can be obtained via any non-intrusive PC-based approach, such as linear regression-, numerical integration- [2], or stochastic testing (ST)-based techniques [11].

Now, by expressing the elements in (2.3) by means of the corresponding PC models leads to

$$\sum_{j=0}^{M} \boldsymbol{V}_j(s_r)\varphi_j(\boldsymbol{\xi}) = \sum_{j=0}^{M}\sum_{k=0}^{M} \boldsymbol{Z}_j(s_r)\boldsymbol{I}_k(s_r)\varphi_j(\boldsymbol{\xi})\varphi_k(\boldsymbol{\xi}) \tag{2.5}$$

where $\boldsymbol{V}_j(s_r)$ and $\boldsymbol{I}_j(s_r)$ are the PC coefficients of $\boldsymbol{V}(s_r, \boldsymbol{\xi})$ and $\boldsymbol{I}(s_r, \boldsymbol{\xi})$, respectively. Projecting (2.5) on the $p-$th PC basis function via GP [1, 2] gives

$$\boldsymbol{V}_p(s_r) = \sum_{j=0}^{M}\sum_{k=0}^{M} \boldsymbol{Z}_j(s_r)\boldsymbol{I}_k(s_r)\langle\varphi_j(\boldsymbol{\xi})\varphi_k(\boldsymbol{\xi}), \varphi_p(\boldsymbol{\xi})\rangle \tag{2.6}$$

Next, by computing relations in the form (2.6) for each basis functions $p = 0, \ldots, M$ and by organizing the results obtained as shown in [9, 10], it is possible to describe the relationship between the PC coefficients of the port voltages and currents as:

$$\boldsymbol{V}_{PC}(s_r) = \boldsymbol{Z}_{PC}(s_r)\boldsymbol{I}_{PC}(s_r) \tag{2.7}$$

where the vectors $\boldsymbol{V}_{PC}(s_r), \boldsymbol{I}_{PC}(s_r) \in \mathbb{C}^{(M+1)N\times 1}$ collect the (deterministic) PC coefficients of the corresponding port voltages and currents, respectively, whereas $\boldsymbol{Z}_{PC}(s_r) \in \mathbb{C}^{(M+1)N\times(M+1)N}$ is a deterministic matrix, obtained by suitable combination of the PC coefficients of the impedance matrix in (2.4). Indeed, the block element of $\boldsymbol{Z}_{PC}(s_r)$ can be written as:

$$[\boldsymbol{Z}_{PC}(s_r)]_{ij} = \sum_{k=0}^{M} \boldsymbol{Z}_k(s_r)\langle\varphi_k(\boldsymbol{\xi})\varphi_j(\boldsymbol{\xi}), \varphi_i(\boldsymbol{\xi})\rangle \tag{2.8}$$

Note that, the symmetry of $\boldsymbol{Z}_{PC}(s_r)$ and, therefore, its reciprocity is preserved by using orthonormal PC basis functions [10].

Now, equation (2.7) describes a new system represented by $\boldsymbol{Z}_{PC}(s_r)$, whose port voltages and currents are the PC coefficients of the port voltage and current of the original stochastic system: $\boldsymbol{Z}_{PC}(s_r)$ is $M+1$ times larger than the original system under study in terms of ports number, and is referred to as the augmented system. It is important to note that $\boldsymbol{Z}_{PC}(s_r)$ can still be seen as an impedance matrix with respect to the PC coefficients of the port voltages and currents: its passivity conditions are the same as for deterministic impedance parameters, as it will be discussed in detail in Section 2.3. At this point, a continuous frequency-dependent rational model of $\boldsymbol{Z}_{PC}(s)$ can be built by means of the VF technique [18, 19]

$$\boldsymbol{Z}_{PC}(s) = \sum_{l=1}^{L} \frac{\boldsymbol{R}_l}{s - p_l} + \boldsymbol{D}_{Z_{PC}} \tag{2.9}$$

where $\boldsymbol{R}_l$ are the residue matrices and p_l are the poles. A pole-flipping scheme allows one to enforce stability, while passivity assessment and enforcement can be accomplished by using robust standard techniques [20, 21]. Next, it is straightforward to convert such rational model into a corresponding state-space representation as

$$\begin{cases} \dfrac{\mathrm{d}\boldsymbol{x}_{PC}(t)}{\mathrm{d}t} = & \boldsymbol{A}_{Z_{PC}}\boldsymbol{x}_{PC}(t) + \boldsymbol{B}_{Z_{PC}}\boldsymbol{i}_{PC}(t) \\ \boldsymbol{v}_{PC}(t) = & \boldsymbol{C}_{Z_{PC}}\boldsymbol{x}_{PC}(t) + \boldsymbol{D}_{Z_{PC}}\boldsymbol{i}_{PC}(t) \end{cases} \tag{2.10}$$

where $\boldsymbol{A}_{Z_{PC}}$, $\boldsymbol{B}_{Z_{PC}}$, $\boldsymbol{C}_{Z_{PC}}$, and $\boldsymbol{D}_{Z_{PC}}$ are the state-space matrices of $\boldsymbol{Z}_{PC}(s)$, and $\boldsymbol{x}_{PC}$ is the corresponding state-vector. Finally, such state-space model can be converted into a SPICE-like equivalent circuit via suitable synthesis techniques [15–17]. A flowchart of calculating thus model of $\boldsymbol{Z}_{PC}(s)$ is illustrated in Fig. 2.1. This procedure can also be applied to admittance parameters $\boldsymbol{Y}(s, \boldsymbol{\xi})$, deriving the augmented system $\boldsymbol{Y}_{PC}(s)$.

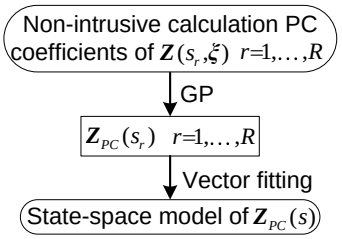

Figure 2.1: Flowchart of the proposed modeling approach for $\boldsymbol{Z}_{PC}(s)$.

2.2.2 Extracting frequency-domain stochastic information from the augmented systems

The augmented systems defined in [9, 10] have been presented only for the variability analysis in the time domain. In the following, the frequency-domain variability analysis based on such augmented systems is discussed.

Given that the VF rational model (2.9) are continuous models with respect to the frequency, it is straightforward to compute the impedance matrix of the augmented system for any value $s_i \in [s_1, s_R]$. Note that $[s_1, s_R]$ is the frequency range used to compute the PC model of the impedance matrix. However, it is not intuitive to directly observe the relation between $\boldsymbol{Z}_{PC}(s)$ and the system variability in the frequency domain. In this work, it is demonstrated that the first block row and block column of $\boldsymbol{Z}_{PC}(s)$ are the $M+1$ PC coefficients $\boldsymbol{Z}_j(s)$ of the impedance $\boldsymbol{Z}(s, \boldsymbol{\xi})$, which means the PC coefficients of the impedance parameters can be directly extracted from the augmented system for frequency-domain variability analysis. Indeed, computing (2.8) for $i = 0$ gives

$$[\boldsymbol{Z}_{PC}(s)]_{0j} = \sum_{k=0}^{M} \boldsymbol{Z}_k(s) \langle \varphi_k(\boldsymbol{\xi}) \varphi_j(\boldsymbol{\xi}), \varphi_0(\boldsymbol{\xi}) \rangle \tag{2.11}$$

Since $\varphi_0(\boldsymbol{\xi})$ is a constant number and equal to 1 for orthonormal basis functions, equation (2.11) becomes

$$[\boldsymbol{Z}_{PC}(s)]_{0j} = \sum_{k=0}^{M} \boldsymbol{Z}_k(s) \langle \varphi_k(\boldsymbol{\xi}) \varphi_j(\boldsymbol{\xi}) \rangle \tag{2.12}$$

Due to the orthonormality of the PC basis functions, equation (2.12) becomes

$$[\boldsymbol{Z}_{PC}(s)]_{0j} = \boldsymbol{Z}_j(s) \tag{2.13}$$

which indicates that the first block row elements in $\boldsymbol{Z}_{PC}(s)$ are the PC coefficients of $\boldsymbol{Z}(s, \boldsymbol{\xi})$. A similar procedure can be adopted for the first block column by choosing $j = 0$ in (2.8). Therefore, the variability analysis of the impedance matrix $\boldsymbol{Z}(s, \boldsymbol{\xi})$ of the system under study can be estimated for any frequency value in the range $s \in [s_1, s_R]$ by first calculating $\boldsymbol{Z}_{PC}(s)$ at the desired frequency values by means of its rational model (see (2.9)), then collecting the corresponding PC coefficients in (2.4) from the first block row or block column of $\boldsymbol{Z}_{PC}(s)$. Now, the frequency-domain variability analysis of the system under study can be performed with accuracy and efficiency thanks to the properties of the PC expansion [1, 2]. Similar relations hold for the augmented systems $\boldsymbol{S}_{PC}(s)$ and $\boldsymbol{Y}_{PC}(s)$ which are based on scattering matrix $\boldsymbol{S}(s, \boldsymbol{\xi})$ and admittance matrix $\boldsymbol{Y}(s, \boldsymbol{\xi})$ respectively. Hence, it is always possible to obtain the PC coefficients of the system transfer function from its corresponding augmented system representation. This property will be exploited in the numerical examples in Section 2.6.

2.2.3 Efficiency analysis of the proposed stochastic macromodeling method

The proposed modeling framework, shown in Fig. 2.1, offers a high degree of flexibility, since it can be applied to a large range of microwave systems, different non-intrusive PC techniques can be adopted to compute the PC coefficients of the transfer function of the system under study, and any macromodeling synthesis technique can be used to import the stochastic macromodel in different SPICE-like circuit simulators. In the following, a detailed breakdown of the computational cost of the proposed method will be presented, where the different factors influencing the modeling efficiency will be discussed.

The starting point of the proposed technique is the calculation of the PC model of the transfer function of the system under study: the corresponding impedance, admittance or scattering parameters must be evaluated over a set of points in the stochastic space $\boldsymbol{\xi}_k$ for $k = 1, \ldots, K$. The sampling strategy depends on the specific non-intrusive method used to compute the PC coefficients, such as linear regression-, numerical integration- [2], or ST-based techniques [11]: for example, by using the approach in [11] leads to $K = M + 1$, where $M + 1$ is given by (2.32). Next, for each sample in the stochastic space, the system transfer function can be evaluated via electromagnetic simulations or measurements, which computational cost is influenced by the number of frequency samples considered and bandwidth of the system. Note that, the sampling strategy in the frequency domain depends only on the accurate description of the transfer function behavior in the chosen frequency range: any existing sampling technique valid for deterministic systems can be adopted (i.e. equally spaced linear/logarithmic sampling or adaptive sampling methods). One requirement is the adoption of the same samples s_r for $r = 1, \ldots, R$ for all K points in the stochastic space, in order to obtain the corresponding PC model by non-intrusive PC techniques [10]. Now, the desired augmented system ($\boldsymbol{Z}_{PC}$ or $\boldsymbol{Y}_{PC}$) can be easily computed as shown in Section 2.2.1 for all the frequency values s_r considered.

Next, a stable and passive state-space model of the augmented system can be computed via the VF algorithm, which computational cost depends on the size of the system, the number of poles needed in the rational model [18] and the specific passivity assessment and enforcement algorithms used among the ones presented in the literature, such as [20, 21]. For example, the passivity enforcement via the approach in [20] has a computational complexity of $O\left(n^3 N^3\right)$, where n is the number of poles and N the number of ports of the system under study. Hence, the passivity assessment and enforcement of the rational model of the augmented scattering parameters matrix via the VF algorithm can become computationally expensive, if the microwave system under the effect of stochastic variations has a high number of ports and depends on several random parameters. Indeed, the size of the augmented system is $(M + 1) N$, where the number of PC basis functions

$M+1$ depends on the number of random parameters and on the PC expansion order as shown in (2.32). A possible solution to reduce such modeling complexity is to adopt sparse PC expansion [22, 23], leading to augmented matrices with a high degree of sparsity [10].

Finally, the macromodel obtained so far can be converted into an equivalent circuit, which can be simulated in any SPICE-like program, via suitable macromodeling synthesis techniques, such as [15–17]. Giving a detailed overview of the different synthesis techniques presented in the literature is outside of the scope of this contribution; however, adopting methods employing a limited number of controlled sources (or none) in the equivalent circuit, see for example [16, 17], can lead to increased efficiency in the corresponding time-domain simulations with respect to circuit realizations relying on multiple controlled sources, such as [15].

2.3 Passivity study on augmented systems

In Section 2.2.1 the augmented systems $\boldsymbol{Z}_{PC}(s)$ and $\boldsymbol{Y}_{PC}(s)$ are defined as equivalent impedance and admittance matrices, respectively, with respect to the port signals formed by the PC coefficients of the port voltages and currents of the stochastic system under study. Hence, it is possible to compute a stable and passive macromodel via the VF method as is also the case for their deterministic counterpart.

In the following, a rigorous definition of the passivity for augmented systems is given and it is shown under what conditions, starting from a generic linear and passive system described by its transfer function, the corresponding augmented system is guaranteed passive as well.

A linear time-invariant system is passive if it absorbs no or more energy than it can generate at any time: the equivalent mathematical representation is [24]

$$\int_{-\infty}^{\tau} \boldsymbol{v}^T(t,\boldsymbol{\xi})\boldsymbol{i}(t,\boldsymbol{\xi})dt \geq 0 \tag{2.14}$$

Note that, equation (2.14) must hold in any point of the stochastic space $\boldsymbol{\Omega}$ under study, where $\boldsymbol{\xi} \in \boldsymbol{\Omega}$.

Now, the port voltages and currents are *exactly* represented by their corresponding PC expansions, if such expansions are not truncated to a limited number of basis function [2] as

$$\boldsymbol{v}(t,\boldsymbol{\xi}) = \sum_{j=0}^{\infty} \boldsymbol{v}_j(t)\varphi_j(\boldsymbol{\xi}) \tag{2.15a}$$

$$\boldsymbol{i}(t,\boldsymbol{\xi}) = \sum_{j=0}^{\infty} \boldsymbol{i}_j(t)\varphi_j(\boldsymbol{\xi}) \tag{2.15b}$$

Then, replacing $\boldsymbol{v}(t,\boldsymbol{\xi})$, $\boldsymbol{i}(t,\boldsymbol{\xi})$ in (2.14) with (2.15a) and (2.15b) gives

$$\int_{-\infty}^{\tau} \sum_{i=0}^{\infty} \boldsymbol{v}_i^T(t)\phi_i(\boldsymbol{\xi}) \sum_{j=0}^{\infty} \boldsymbol{i}_j(t)\phi_j(\boldsymbol{\xi})dt \geq 0 \tag{2.16}$$

By integrating (2.16) in the stochastic space $\boldsymbol{\Omega}$ leads, after simple manipulations, to

$$\int_{-\infty}^{\tau} \left(\int_{\boldsymbol{\Omega}} \sum_{i=0}^{\infty} \sum_{j=0}^{\infty} \boldsymbol{v}_i^T(t)\boldsymbol{i}_j(t)\phi_i(\boldsymbol{\xi})\phi_j(\boldsymbol{\xi})W(\boldsymbol{\xi})d\boldsymbol{\xi} \right) dt \geq 0 \tag{2.17}$$

where $W(\boldsymbol{\xi})$ is the joint PDF of $\boldsymbol{\xi}$. Now, due to the orthonormality of the PC basis functions, equation (2.17) can be simplified into

$$\int_{-\infty}^{\tau} \sum_{j=0}^{\infty} \boldsymbol{v}_j^T(t)\boldsymbol{i}_j(t)dt \geq 0 \tag{2.18}$$

By defining the vectors $\boldsymbol{v}_{PC\infty}^T(t)$ and $\boldsymbol{i}_{PC\infty}^T(t)$, which collect the PC coefficient of the voltages and currents, respectively, leads to

$$\int_{-\infty}^{\tau} \boldsymbol{v}_{PC\infty}^T(t)\boldsymbol{i}_{PC\infty}(t)dt \geq 0 \tag{2.19}$$

Now, the non-truncated PC coefficients $\boldsymbol{v}_j$, $\boldsymbol{i}_j$ can be considered as the port signals of a system with an infinite number of ports, and (2.19) indicates that such system is passive. Hence, despite the PC model of the port signals is a mathematical representation, its coefficients retain a physical meaning. It is important to remark that this conclusion is general and independent on the proposed augmented system-based modeling approach. Indeed, equation (2.18) is derived by leveraging only on the passivity definition and the expression of the port voltages and currents via a PC expansion with an infinite number of terms.

However, in practice it is not possible to compute an infinite number of PC coefficients and (2.15a) must be truncated to a finite number of terms [2, 5, 10, 25]. Given that a truncated PC expansion converges to (2.15a) when a sufficiently high number of terms is considered, intuitively the corresponding truncated equations (2.18) and (2.19) can be expected to hold as well. Hence, it is reasonable to assume that, for passive stochastic circuits it is possible to compute a corresponding passive PC-based augmented system, which can then be used for efficient time-domain variability analysis [10, 25]. In the following, a rigorous criterion will be defined to assess the passivity of PC-based augmented systems describing the variability of general linear and passive circuits.

Given the results obtained so far, $\boldsymbol{Z}_{PC}(s)$ can be considered as an actual impedance matrix. Hence, the passivity conditions defined in the Laplace domain for deterministic impedance matrices are applicable to $\boldsymbol{Z}_{PC}(s)$ as well [26]:

- Each element of $\boldsymbol{Z}_{PC}(s)$ is analytic in $\mathrm{Re}\{s\} > 0$;
- $\boldsymbol{Z}_{PC}^{H}(s)+\boldsymbol{Z}_{PC}(s)$ is a nonnegative-definite matrix for all s such that $\mathrm{Re}\{s\} > 0$;
- $\boldsymbol{Z}_{PC}^{*}(s) = \boldsymbol{Z}_{PC}(s^{*})$.

Now, since $\boldsymbol{Z}(s,\boldsymbol{\xi})$ is passive (impedance matrix of a passive system), its PC model $\tilde{\boldsymbol{Z}}(s,\boldsymbol{\xi})$ defined in (2.4) always meets the first and third passivity conditions, as well as its PC coefficients $\boldsymbol{Z}_j(s)$ for $j = 0,\ldots,M$. Since $\boldsymbol{Z}_{PC}(s)$ is constructed via linear combinations of the PC coefficients $\boldsymbol{Z}_j(s)$, see (2.8), it complies with the first and third condition as well. The second condition requires that

$$\boldsymbol{\alpha}^{H}[\boldsymbol{Z}_{PC}^{H}(s) + \boldsymbol{Z}_{PC}(s)]\boldsymbol{\alpha} \geq 0 \tag{2.20}$$

holds for every non-zero column vector $\boldsymbol{\alpha} \in \mathbb{C}^{(M+1)N\times 1}$. It is important to note that $\boldsymbol{Z}_{PC}^{H}(s) + \boldsymbol{Z}_{PC}(s)$ is a real symmetric matrix if $\boldsymbol{Z}(s,\boldsymbol{\xi})$ represents a reciprocal system, leading to real-valued $\boldsymbol{\alpha}$.

By writing (2.8) as

$$[\boldsymbol{Z}_{PC}(s)]_{ij} = \langle \tilde{\boldsymbol{Z}}(s,\boldsymbol{\xi})\varphi_j(\boldsymbol{\xi}), \varphi_i(\boldsymbol{\xi})\rangle \tag{2.21}$$

allows one to write

$$\begin{aligned}\boldsymbol{\alpha}^{H}\boldsymbol{Z}_{PC}(s)\boldsymbol{\alpha} &= \sum_{i=0}^{M}\sum_{j=0}^{M}\boldsymbol{\alpha}_i^{H}\langle\tilde{\boldsymbol{Z}}(s,\boldsymbol{\xi})\varphi_j(\boldsymbol{\xi}),\varphi_i(\boldsymbol{\xi})\rangle\boldsymbol{\alpha}_j \\ &= \langle\sum_{i=0}^{M}\boldsymbol{\alpha}_i^{H}\varphi_i(\boldsymbol{\xi}), \tilde{\boldsymbol{Z}}(s,\boldsymbol{\xi})\sum_{j=0}^{M}\boldsymbol{\alpha}_j\varphi_j(\boldsymbol{\xi})\rangle \end{aligned}\tag{2.22}$$

where $\boldsymbol{\alpha}_j$ is the j-th block of vector $\boldsymbol{\alpha}$. Define

$$\boldsymbol{\beta}(\boldsymbol{\xi}) = \sum_{j=0}^{M}\boldsymbol{\alpha}_j\varphi_j(\boldsymbol{\xi}) \tag{2.23}$$

which is a non-zero vector given by a suitable linear combination of the basis function $\varphi_j(\boldsymbol{\xi})$. Hence, (2.20) can be written as

$$\langle\boldsymbol{\beta}^{H}(\boldsymbol{\xi}), [\tilde{\boldsymbol{Z}}^{H}(s,\boldsymbol{\xi}) + \tilde{\boldsymbol{Z}}(s,\boldsymbol{\xi})]\boldsymbol{\beta}(\boldsymbol{\xi})\rangle \geq 0 \tag{2.24}$$

which is equivalent to

$$\int_{\Omega}\boldsymbol{\beta}^{H}(\boldsymbol{\xi})[\tilde{\boldsymbol{Z}}^{H}(s,\boldsymbol{\xi}) + \tilde{\boldsymbol{Z}}(s,\boldsymbol{\xi})]\boldsymbol{\beta}(\boldsymbol{\xi})W(\boldsymbol{\xi})d\boldsymbol{\xi} \geq 0 \tag{2.25}$$

Note that, $W(\boldsymbol{\xi})$ is a nonnegative value in the entire stochastic space Ω since it is the joint PDF. Hence, if $\tilde{\boldsymbol{Z}}^{H}(s,\boldsymbol{\xi}) + \tilde{\boldsymbol{Z}}(s,\boldsymbol{\xi})$ is nonnegative-definite for all $\boldsymbol{\xi}$ in $\boldsymbol{\Omega}$,

i.e., that the approximation (2.4) preserves the passivity property of the original system, then it follows

$$\boldsymbol{\beta}^H(\boldsymbol{\xi})[\tilde{\boldsymbol{Z}}^H(s,\boldsymbol{\xi}) + \tilde{\boldsymbol{Z}}(s,\boldsymbol{\xi})]\boldsymbol{\beta}(\boldsymbol{\xi})W(\boldsymbol{\xi}) \geq 0 \tag{2.26}$$

As a result, (2.24) always holds, since the integral of a nonnegative quantity is always nonnegative. Hence, a *sufficient, but not necessary, condition* for the passivity of the augmented system $\boldsymbol{Z}_{PC}(s)$ is that the corresponding PC model of the impedance matrix $\boldsymbol{Z}(s,\boldsymbol{\xi})$ is passive over the entire stochastic space $\boldsymbol{\Omega}$ considered. If the latter condition holds, not only the PC coefficients of $\boldsymbol{v}(t,\boldsymbol{\xi})$ and $\boldsymbol{i}(t,\boldsymbol{\xi})$ meet the corresponding passivity condition (2.19), since they are the port signals of $\boldsymbol{Z}_{PC}$, but it is also possible to compute them via a single time-domain simulation of a suitable macromodel of $\boldsymbol{Z}_{PC}$, by following the same approach described in [10] for scattering parameters representations. Note that, condition (2.24) can still be satisfied even if $\tilde{\boldsymbol{Z}}(s,\boldsymbol{\xi})$ is not passive for some $\boldsymbol{\xi}$ in the stochastic space $\boldsymbol{\Omega}$ (condition (2.26) is sufficient, but not necessary). Finally, it is straightforward to verify that the same conclusions can be drawn for $\boldsymbol{Y}_{PC}(s)$, by following a similar procedure.

2.4 Relations among augmented systems for different transfer function representations

At this point, by following the proposed stochastic macromodeling strategy and the one described in [9, 10], it is possible to compute equivalent matrices and state-space models describing the relations between the PC coefficients of the signals at the port of the system under study, in terms of equivalent scattering, impedance and admittance parameters. In the following, the relations between augmented models computed for different transfer function representations will be studied. Indeed, it is possible to convert an augmented system and the corresponding state-space model computed starting from the PC coefficient of a specific transfer function representation (i.e. impedance parameters) into the equivalent one for a different representation (admittance parameters, for example), by using *the same relations valid for their deterministic counterpart*. For example the augmented matrix for the scattering parameters can be expressed as [27]

$$\boldsymbol{S}_{PC} = (\boldsymbol{Z}_{PC} - Z_{REF}\boldsymbol{U})\,(\boldsymbol{Z}_{PC} + Z_{REF}\boldsymbol{U})^{-1} \tag{2.27}$$

where Z_{REF} is the reference impedance at each system port, which is typically assumed equal to $50\ \Omega$ for all the ports. Furthermore, the transformation can be performed at state-space level: for example, the state-space representation of the

impedance matrix can be written as [27]

$$\boldsymbol{A}_{Z_{PC}} = \boldsymbol{A}_{S_{PC}} + \boldsymbol{B}_{S_{PC}} \left(\boldsymbol{U} - \boldsymbol{D}_{S_{PC}}\right)^{-1} \boldsymbol{C}_{S_{PC}} \tag{2.28}$$

$$\boldsymbol{B}_{Z_{PC}} = \boldsymbol{B}_{S_{PC}} \left(\boldsymbol{U} - \boldsymbol{D}_{S_{PC}}\right)^{-1} Z_{REF} \tag{2.29}$$

$$\boldsymbol{C}_{Z_{PC}} = 2 \left(\boldsymbol{U} - \boldsymbol{D}_{S_{PC}}\right)^{-1} \boldsymbol{C}_{S_{PC}} \tag{2.30}$$

$$\boldsymbol{D}_{Z_{PC}} = \left(\boldsymbol{U} + \boldsymbol{D}_{S_{PC}}\right) \left(\boldsymbol{U} - \boldsymbol{D}_{S_{PC}}\right)^{-1} Z_{REF} \tag{2.31}$$

Figure 2.2 shows the relations between the scattering, admittance and impedance parameters and their corresponding augmented representations.

However, the augmented systems have a unique characteristic: their size depends on the number of PC basis functions $M+1$, which is related to the total order of polynomial basis functions P and the number or random variables Q as [1]:

$$M + 1 = \frac{(Q+P)!}{Q!P!} \tag{2.32}$$

Indeed, different representations ($\boldsymbol{S}$, $\boldsymbol{Y}$ or $\boldsymbol{Z}$) of the transfer function of the same system vary differently in the frequency domain with respect to the random variables, as shown in Section 2.6, Fig. 2.11. Hence, PC expansions of different orders could be needed for the *same frequency value* s_r to accurately express the variability of the corresponding transfer function representation ($\boldsymbol{S}(s_r)$, $\boldsymbol{Y}(s_r)$ or $\boldsymbol{Z}(s_r)$) leading to PC models with a different number of polynomial basis functions, see equation (2.32).

It is important to note that, in order for the transformations (between $\boldsymbol{S}_{PC}$, $\boldsymbol{Z}_{PC}$, $\boldsymbol{Y}_{PC}$) shown in Fig. 2 to be valid, it is necessary that the corresponding augmented systems are all passive and computed with the same number of basis functions. Now, let us assume that a PC model of order P_S has been computed for the system scattering parameters evaluated over the entire frequency samples of interest s_r for $r = 1, \ldots, R$, which gives accurate frequency-domain variability

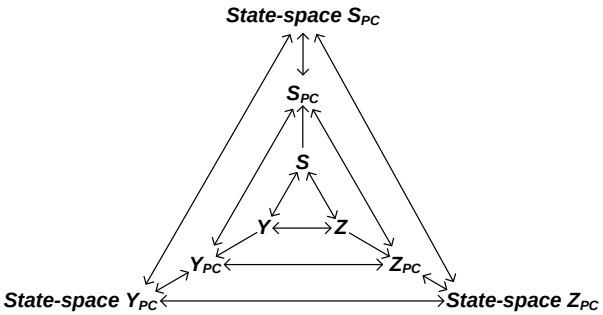

Figure 2.2: Transformation between deterministic $\boldsymbol{S}/\boldsymbol{Y}/\boldsymbol{Z}$ and augmented $\boldsymbol{S}_{PC}/\boldsymbol{Y}_{PC}/\boldsymbol{Z}_{PC}$, and their state-space models.

analysis results, and a PC model of order P_Y is needed instead to compute an accurate PC model describing the variation of the admittance parameters representation on the same frequency samples, with $P_S < P_Y$. The corresponding augmented models are $\boldsymbol{S}_{PC} \in \mathbb{C}^{(M_S+1)N\times(M_S+1)N}$ and $\boldsymbol{Y}_{PC} \in \mathbb{C}^{(M_Y+1)N\times(M_Y+1)N}$, where $M_S + 1 < M_Y + 1$ according to (2.32). When one augmented system representation with smaller size is converted to another representation which is supposed to have larger size, some PC coefficients (in the first row or column block of the matrix, see (2.13)) are missing, leading to an inaccurate estimation of the stochastic variations in the frequency domain, such as in our case, the PC coefficients for polynomials of degree $P_S < P \leq P_Y$. Hence, the variability analysis in the frequency domain of a suitable representation ($\boldsymbol{S}$, $\boldsymbol{Y}$ or $\boldsymbol{Z}$) of the system transfer function should be performed by directly computing the augmented system for the specific representation under study ($\boldsymbol{S}_{PC}$, $\boldsymbol{Z}_{PC}$, $\boldsymbol{Y}_{PC}$) rather via transformations, to avoid the situation described above, since it is not possible to estimate upfront if PC models of different transfer function representations need different PC expansion orders or not.

However, the time-domain variability analysis of the port signals can be performed accurately by transforming PC-based augmented system as described in Fig. 2.2, by construction. Indeed, augmented systems such as $\boldsymbol{S}_{PC}$, $\boldsymbol{Y}_{PC}$ and $\boldsymbol{Z}_{PC}$ are defined as equivalent scattering, impedance or admittance matrices with respect to the PC coefficients of the system port voltages and currents [10]. Now, converting an augmented system computed for a particular representation, for example $\boldsymbol{S}_{PC}$, to another one, let us say admittance parameters, means computing an admittance matrix $\hat{\boldsymbol{Y}}_{PC}$ *giving the same port signals* as $\boldsymbol{S}_{PC}$. Indeed, if a PC model of order P_S gives an accurate representation of the port signals variability, using a higher order P_Y will also lead to an accurate estimation of stochastic variations. Note that all the PC coefficients of the port signals up to order $P = P_S$ are the same for the PC models of order P_S and P_Y, since the PC basis functions are the same (and orthonormal) [1, 2]. Therefore, the transformations in Fig. 2.2 are recommended for variability analysis only in the time domain rather than in the frequency domain.

2.5 Variability analysis via parameterized stochastic macromodeling

The modeling technique presented so far can efficiently perform the variability analysis in the time and frequency domain for a specific nominal value of the random variables in the stochastic space. However, in order to find a design configuration robust to the effects of manufacturing variations, the variability analysis can be carried out for different nominal values of the chosen random parameters.

Since the method presented here offers the unique characteristic of describing the system under study by means of an equivalent augmented transfer function representation, it is possible to build a suitable parameterized macromodel describing the stochastic variations of the system under study for all the possible nominal values of interest of the random parameters considered.

This possibility is interesting because it allows one to define a unique framework to model deterministic and stochastic parameters altogether, as it will be shown in the following, and to individuate the area of the design space for the nominal value of the random parameter under study which are robust to the variations of the manufacturing process. However, the downside of such a stochastic parameterized macromodeling approach is that the computational cost to build the model can be higher than calculating the corresponding augmented system, described in Section 2.2, only for the nominal values of interest for the specific problem at hand. Hence, this approach is efficient only if the number of random parameters considered is limited.

In the rest of the contribution, the parameterized macromodeling approach presented in [28] together with the sequential sampling algorithm proposed in [29] are adopted, since they guarantee a high degree of automation in the model building procedure and the stability and passivity of the parameterized macromodel, fundamental properties for time-domain simulations, can be preserved. However, any parameterized macromodeling technique for deterministic transfer function representations can be adopted to model also the corresponding augmented systems described in Section 2.2. It is important to note that, since the augmented systems described in Section 2.2 can be considered as deterministic scattering, impedance and admittance matrix, the computational cost of a parameterized stochastic macromodel is the same as applying the chosen parameterized macromodeling technique to a deterministic system of size $(M+1)\,N \times (M+1)\,N$, with one difference: K evaluations of the system transfer function are now required to compute an augmented system for a specific nominal value of the parameters considered, where K depends on the particular technique adopted to compute the PC expansion, as discussed in Section 2.2.3.

In the following, in order to provide a complete characterization of the system under study, first the parameterized macromodel of the scattering parameters is built, denoted as PM_S, which describes the performance of the system for the nominal values of the random parameters under study. Next, a parameterized macromodel of the augmented system $\boldsymbol{S}_{PC}$, which is denoted as PM_S_{PC}, can be built based on the scattering parameters generated from PM_S or EM simulators. Note that building the model PM_S_{PC} does not necessarily rely on the model PM_S. Finally, it is important to remark that

- the size of the augmented systems depends on the number of the PC basis functions as $N \times (M+1)$. Starting from a set of different nominal values

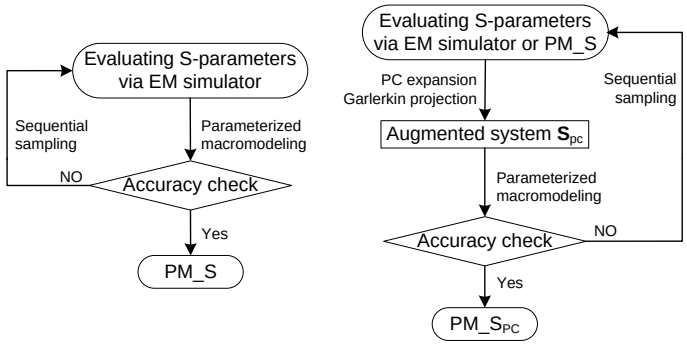

Figure 2.3: Flow chart of the deterministic (left) and stochastic (right) parameterized macromodeling technique.

for the chosen random variable in the design space, an accurate PC model with $M_i + 1$ basis functions is built separately for each point in the design space. The highest M_i is chosen to build the corresponding parameterized macromodel PM_S$_{PC}$.

- if PM_S is used as a simulator for building PM_S$_{PC}$, the design space of PM_S should be larger than that of PM_S$_{PC}$ by Δ for each design parameter since information around the nominal value of the random parameters are needed to build the augmented system. Δ depends on the distribution of corresponding random variable and the method chosen to compute the PC coefficient (i.e. linear regression, numerical integration), for instance
  - Gaussian distribution: $\mathcal{N}(\mu, \sigma^2)$: $\Delta = 6\sigma$
  - Uniform distribution: $U(a, b)$: $\Delta = b - a$

Figure 2.3 describes the flowchart of this modeling process. Similar parameterized macromodeling techniques can be adopted for admittance or impedance representations.

2.6 Numerical examples

The simulations shown in this section are performed with MATLAB and Advanced Design System (ADS) on a computer with Intel Core i3 processor and 8 GB RAM. In the following numerical examples, the total number of samples chosen for the MC analysis represents a trade off between accuracy and associated computational cost in estimating not only simple stochastic moments, like mean and standard deviation, but also complex stochastic quantities like the PDF and CDF.

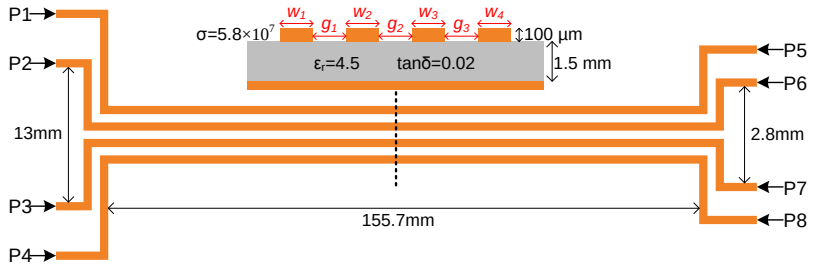

Figure 2.4: Example 2.6.1. Geometry of the nonuniform coupled transmission lines.

2.6.1 Multiple coupled transmission lines

In this example, the nonuniform coupled transmission lines shown in Fig. 2.4 are studied. The width of the four traces (w_1 to w_4) are assumed as independent Gaussian random variables, having a nominal value 250 μm and a standard deviation of 25 μm. The center of each trace is assumed to be fixed as result of the manufacturing process, leading to variations in the gaps (g_1, g_2, g_3), which have a nominal value 250 μm, and can be determined by the trace width values. The scattering parameters of the transmission lines are evaluated in ADS for 251 frequency points in the range $[0$ kHz ~ 4 GHz$]$, 151 of which are used to compute the desired augmented system. The remaining samples are used for evaluation: to verify the accuracy of the rational model of $\boldsymbol{S}_{PC}$ at frequencies not used during the model building phase. Next, a PC order $P = 2$ is chosen according to the method in [8], leading to $M + 1 = 15$ basis functions according to (2.32). By adopting the non-intrusive ST technique [11, 13], only 15 samples of the random variables (w_1, w_2, w_3, w_4) are required to accurately compute the PC coefficients of the system scattering parameters. Next, the augmented system $\boldsymbol{S}_{PC} \in \mathbb{C}^{120\times 120}$ can be calculated for each one of the 151 frequency samples considered. A similar approach can be adopted to compute $\boldsymbol{Z}_{PC}$ and $\boldsymbol{Y}_{PC}$, starting from the impedance and admittance parameters of the transmission lines.

To verify the relations illustrated by Fig. 2.2, the augmented systems for the impedance and admittance parameters obtained by conversion of $\boldsymbol{S}_{PC}$ are denoted as $\hat{\boldsymbol{Z}}_{PC}$ and $\hat{\boldsymbol{Y}}_{PC}$, respectively. For comparison, a MC analysis is also performed by using 10000 samples of the random variables (w_1, w_2, w_3, w_4). Figures 2.5 and 2.6 show the standard deviation of the imaginary part of the admittance and impedance parameters, respectively, computed directly or via conversion, and the MC method. The results obtained show an excellent agreement between all the different approaches.

Next, a stable and passive rational model of $\boldsymbol{S}_{PC}$ is computed via the VF algorithm, by targeting a maximum absolute error threshold of -50 dB, and the

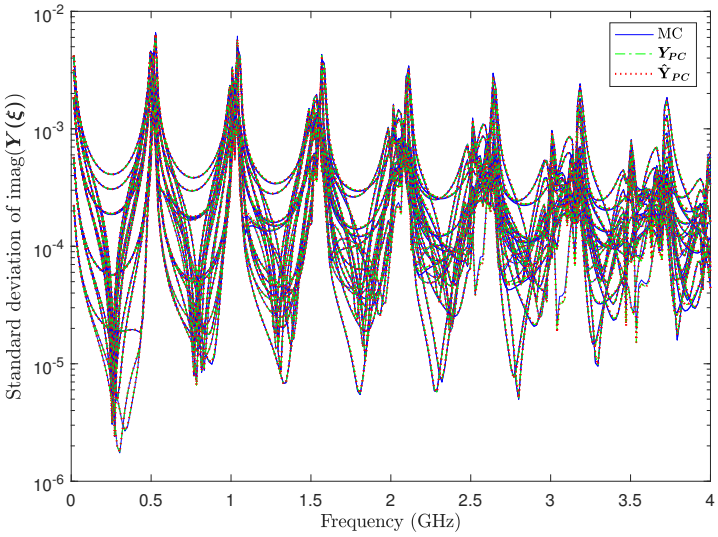

Figure 2.5: Example 2.6.1. Standard deviation of imaginary part of all upper triangular elements in $\boldsymbol{Y}(\boldsymbol{\xi})$ calculated via MC method (full black line), $\boldsymbol{Y}_{PC}$ (green dashed line), $\hat{\boldsymbol{Y}}_{PC}$ (red dotted line).

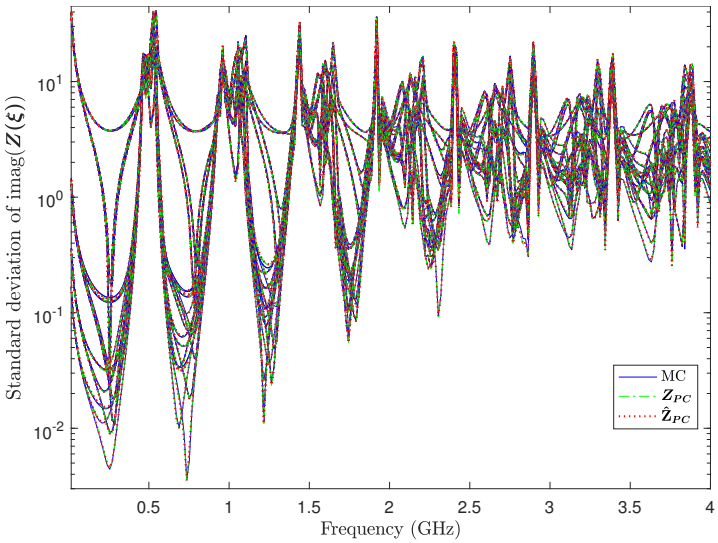

Figure 2.6: Example 2.6.1. Standard deviation of imaginary part of all upper triangular elements in $\boldsymbol{Z}(\boldsymbol{\xi})$ calculated via MC method (full black line), $\boldsymbol{Z}_{PC}$ (green dashed line), $\hat{\boldsymbol{Z}}_{PC}$ (red dotted line).

model accuracy is verified for all the 251 frequency samples considered. Finally, the state-space representation of such rational model, computed with 47 poles, is converted into the corresponding ones for admittance and impedance representation, as shown in Fig. 2.2. In the time domain, the coupled transmission lines are excited at port $P1$ by a smooth voltage pulse with amplitude 1 V, rise/fall times 0.35 ns, width 2 ns, initial delay 6.5 ns and internal resistance $R_S = 50\ \Omega$, and are terminated on a $R_L = 50\ \Omega$ resistor. Then, the time-domain variability analysis is performed by simulating the macromodels obtained for $\boldsymbol{S}_{PC}$, $\hat{\boldsymbol{Y}}_{PC}$ and $\hat{\boldsymbol{Z}}_{PC}$. The mean and mean $\pm$ 3 times of standard deviation of the voltage at ports $P3$ and $P5$ are shown in Fig. 2.7 and 2.8, respectively, where a comparison with respect to the MC analysis is presented as well.

Figure 2.9 shows the PDF and CDF of the current at port $P2$ for the time instant t=7.51 ns obtained by means of the MC method, and time-domain simulation of the state-space model of $\boldsymbol{S}_{PC}$, $\hat{\boldsymbol{Y}}_{PC}$, $\hat{\boldsymbol{Z}}_{PC}$: a high accuracy between the different methods can be observed. Similar results can be obtained for the other port signals as well. Furthermore, the proposed technique shows a great efficiency when compared to the MC analysis, as indicated in details in Table 2.1. The computational time of $\hat{\boldsymbol{Y}}_{PC}$, $\hat{\boldsymbol{Z}}_{PC}$ is similar with that of $\boldsymbol{S}_{PC}$ presented in Table 2.1.

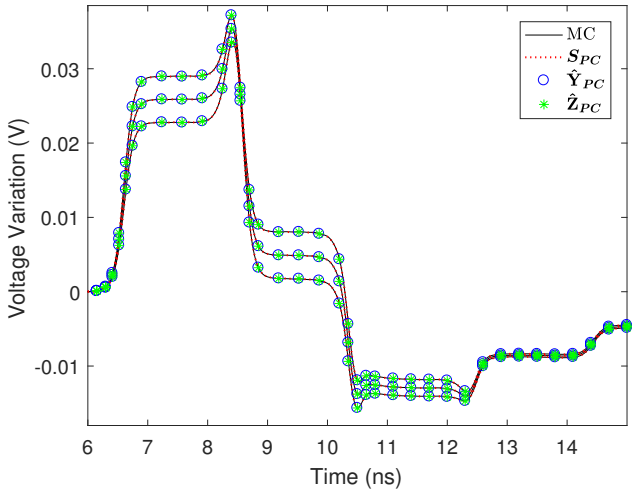

Figure 2.7: Example 2.6.1. The mean and mean $\pm$ 3 times of standard deviation of the voltage at port $P3$ obtained by means of MC analysis (full black line), based on 10000 (w_1, w_2, w_3, w_4) samples, and a single time-domain simulation of the state-space model of $\boldsymbol{S}_{PC}$ (red dashed line), $\hat{\boldsymbol{Y}}_{PC}$ (blue circles), $\hat{\boldsymbol{Z}}_{PC}$ (green asterisk).

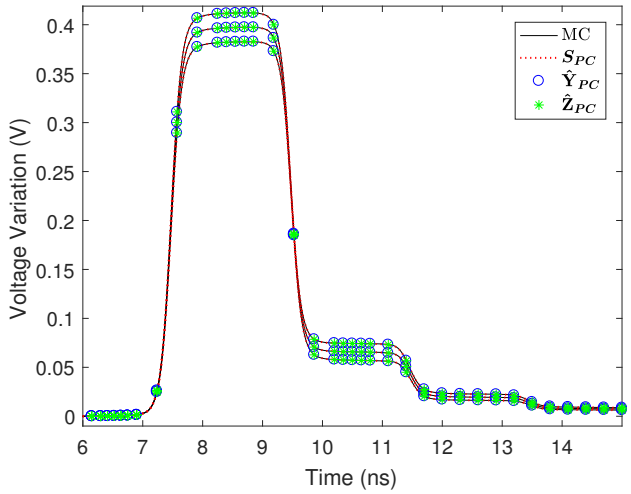

Figure 2.8: Example 2.6.1. The mean and mean $\pm$ 3 times of standard deviation of the voltage at port $P5$ obtained by means of MC analysis (full black line), based on 10000 (w_1, w_2, w_3, w_4) samples, and a single time-domain simulation of the state-space model of $\boldsymbol{S}_{PC}$ (red dashed line), $\hat{\boldsymbol{Y}}_{PC}$ (blue circles), $\hat{\boldsymbol{Z}}_{PC}$ (green asterisk).

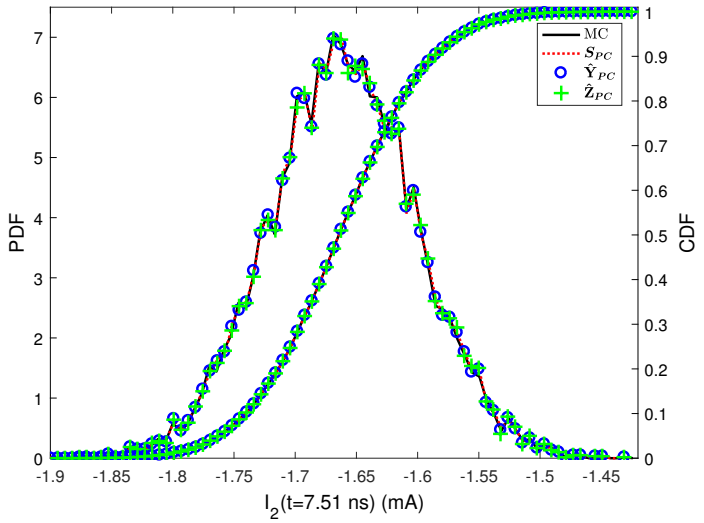

Figure 2.9: Example 2.6.1. PDF and CDF of the current at port $P2$ for the time instant $t = 7.51$ ns obtained by means of the MC analysis (full black line), based on 10000 (w_1, w_2, w_3, w_4) samples, and the time-domain simulation of the state-space model of $\boldsymbol{S}_{PC}$ (red dashed line), $\hat{\boldsymbol{Y}}_{PC}$ (blue circles), $\hat{\boldsymbol{Z}}_{PC}$ (green plus).

MC computational time	
Full wave simulation of 10000 $(w_1 - w_4)$ samples	18 d 17 h 16 m
Calculation of corresponding state-space models	7 h 49 m
Time-domain simulations	2 h 17 m
PC-based method computational time	
Full wave simulation of 15 $(w_1 - w_4)$ samples	40 m 26 s
Computing augmented system	21 s
Building corresponding state-space model	15 m 55 s
Time-domain simulation	8 m 35 s
Speedup time compared with MC	422

Table 2.1: Example 2.6.1. Efficiency analysis of the proposed technique.

2.6.2 Zigzag filter

A zigzag narrow bandpass filter, based on the design proposed in [30] and shown in Fig. 2.10, is studied over the frequency range [1 kHz $\sim$ 4.5 GHz]. The substrate is 0.5 mm thick with a relative dielectric constant $\varepsilon_r = 2.2$ and a loss tangent $tan\delta = 0.003$. The gap G among the horizontal conductor is 0.3 mm, and the width of the both horizontal and vertical conductors is 0.4 mm. This bandpass filter has a very narrow-band response around 2.5 GHz, and its passband and center frequency are very sensitive to its geometric layout. The distance D and the length L of the two coupling parts are assumed as Gaussian distributed random variables, with $D \sim \mathcal{N}(0.85 \text{ mm}, \sigma^2)$ and $L \sim \mathcal{N}(19.2 \text{ mm}, \sigma^2)$, where σ is the standard deviation and equals 60 μm.

With scattering parameters at 49 samples (D, L) chosen over a 7×7 regular grid, the augmented systems $\boldsymbol{S}_{PC}$, $\boldsymbol{Y}_{PC}$, and $\boldsymbol{Z}_{PC}$ are built with 15 PC basis functions, which are sufficient to compute accurate PC models for all the different representations considered, leading to augmented systems with 30 ports. In Fig. 2.11, the standard deviation of the real part of S_{11}, Y_{11}, Z_{11} calculated

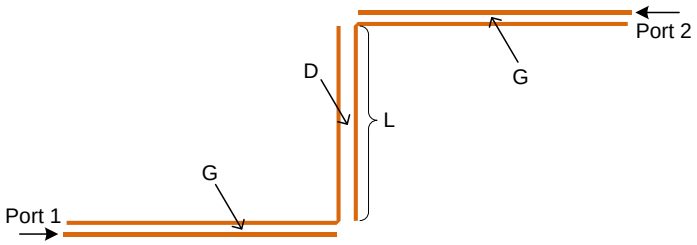

Figure 2.10: Example 2.6.2. Geometry of the zigzag bandpass filter.

from corresponding augmented systems is compared with that from MC analysis based on 10000 (D, L) samples. Furthermore, the same variability analysis result computed via augmented models obtained by conversion of $\boldsymbol{S}_{PC}$, as described in Section 2.4, are shown and indicated with the symbols $\hat{\boldsymbol{Y}}_{PC}$ and $\hat{\boldsymbol{Z}}_{PC}$. All the different stochastic macromodels show a good accuracy with respect to the MC analysis.

In the time domain, the filter is excited at port one (input) by a smooth voltage pulse with amplitude 1 V, rise/fall times 0.13 ns, width 1.8 ns, initial delay 3 ns and internal resistance $R_S = 50\ \Omega$, while port two (output) is terminated on a $R_L = 50\ \Omega$ resistor. Then the state-space models of the augmented systems $\boldsymbol{S}_{PC}$, $\boldsymbol{Y}_{PC}$, and $\boldsymbol{Z}_{PC}$ are built with 20, 25, 27 poles respectively. Time-domain simulations with these built models are performed, and the results are compared with the corresponding MC analysis, as shown in Fig. 2.12. Similar results can be obtained from the simulation of the macromodels $\hat{\boldsymbol{Y}}_{PC}$ and $\hat{\boldsymbol{Z}}_{PC}$. In this case, the model building process and time-domain simulations of $\boldsymbol{S}_{PC}$, $\boldsymbol{Y}_{PC}$, and $\boldsymbol{Z}_{PC}$ take 50 min 20.5 s, 50 min 55.5 s, and 50 min 50 s, respectively, while the MC analysis of 10000 samples requires 171 h 27 min.

Next, we will describe how the approach presented in Section 2.5 can tackle deterministic and stochastic parameters altogether. In particular, the gap is now assumed as deterministic parameter varying in the range $G \in [0.3, 0.5]$ mm, while the nominal values of the two Gaussian random variables considered are defined in the range $D \in [0.8, 1.0]$ mm and $L \in [19.1, 19.3]$ mm, respectively. Figure 2.13 shows an example of the filter scattering parameters with respect to (G, D, L).

Following the steps shown in Fig. 2.3, first PM_S is built starting from the filter scattering parameters, computed by ADS over 151 frequency samples ranging from 1 kHz to 4.5 GHz in the design space $G \in [0.3, 0.5]$ mm, $D \in [0.62, 1.18]$ mm, $L \in [18.92, 19.48]$ mm. The mean absolute value of the difference of scattering parameters between model and EM simulator is chosen as error measure to build the parameterized macromodel PM_S, due to the sharp variations of the passband frequency response [29], with -55 dB as error threshold. Next, the parameterized augmented matrix $\boldsymbol{S}_{PC}$, based on a PC model with 10 basis functions, is calculated by using PM_S instead of ADS, in order to reduce the stochastic macromodel computational time. Finally, the desired PM_S_{PC} is built by adopting a maximum absolute error threshold -45 dB for the VF algorithm.

As shown in Fig. 2.14, the frequency-domain accuracy of proposed technique is validated by comparison with the results of MC analysis over 64 samples for the nominal values of (G, D, L), computed on a $(4 \times 4 \times 4)$ regular grid in the design space, which have not been used to build the model. In particular, the MC method results shown in Fig. 2.14 are based on PM_S to calculate the scattering parameters for 10000 (D, L) samples for each of the 64 nominal values considered, due to the high computational time associated for their computation via ADS.

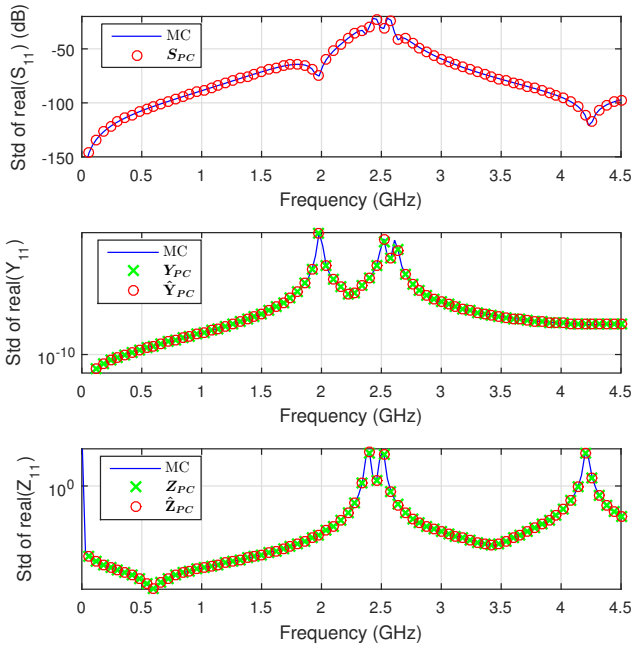

Figure 2.11: Example 2.6.2. Top: standard deviation (std) of the real part of S_{11} calculated via $\boldsymbol{S}_{PC}$ and MC. Center: std of the real part of Y_{11} obtained by $\boldsymbol{Y}_{PC}$, $\hat{\boldsymbol{Y}}_{PC}$ and MC. Bottom: std of the real part of Z_{11} computed via $\boldsymbol{Z}_{PC}$, $\hat{\boldsymbol{Z}}_{PC}$ and MC.

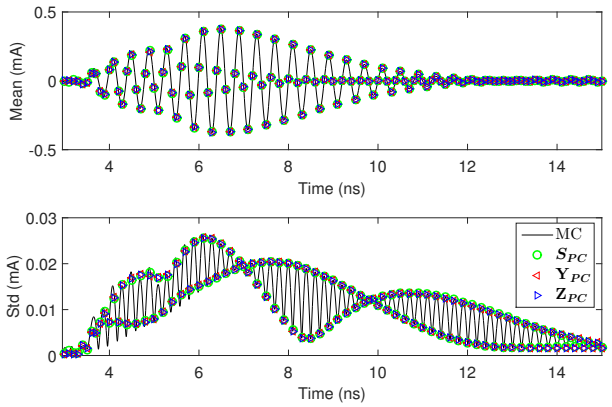

Figure 2.12: Example 2.6.2. Mean and standard deviation (std) of the filter output current obtained by MC method based on 10000 (D, L) samples and by one time-domain simulation of the augmented systems $\boldsymbol{S}_{PC}$, $\boldsymbol{Y}_{PC}$, and $\boldsymbol{Z}_{PC}$.

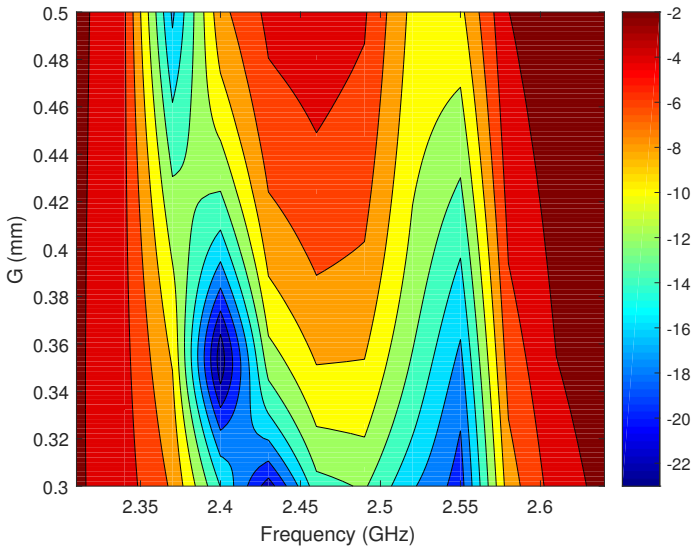

Figure 2.13: Example 2.6.2. Magnitude (dB) of $S_{11}(f, G)$ for $(D, L) = (0.62, 19.48)$mm.

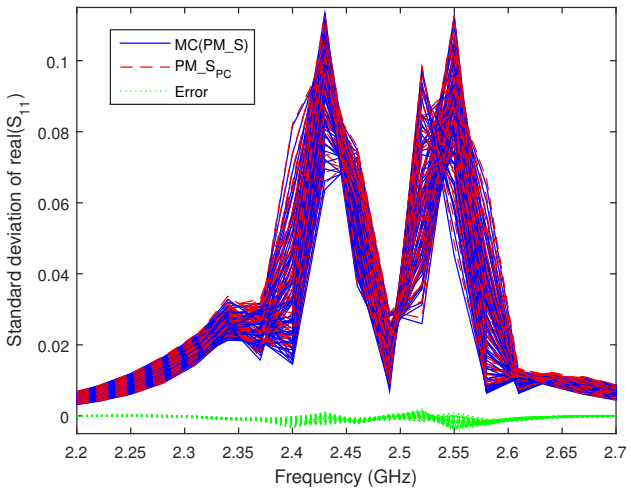

Figure 2.14: Example 2.6.2. Standard deviation of the element S_{12} calculated by means of MC and PM_S_{PC} for 64 (G, D, L) values.

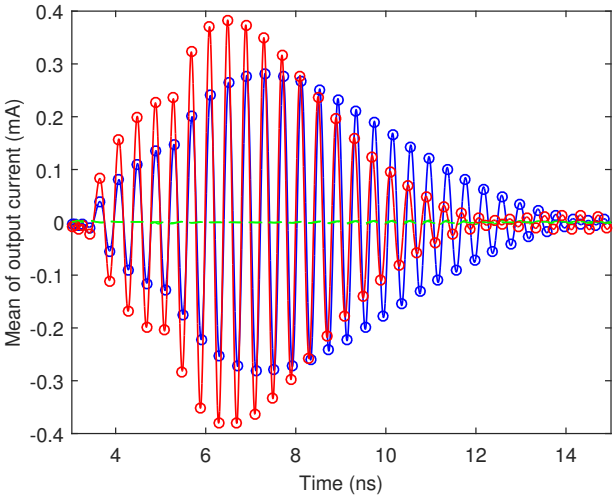

Figure 2.15: Example 2.6.2. Mean of the filter output current for two samples in the design space (G, D, L)=(0.475, 0.975, 19.25) mm and (0.325, 0.825, 19.15) mm: the solid lines are the results from the MC method based on ADS; the marker $\circ$ represents that from the built PM_S$_{PC}$; and the dash lines indicate error in between.

Time-domain simulations are performed with the same setting described above and Fig. 2.15 shows the mean of output current for two (G, D, L) samples in the design space: the output current is a signal with frequency shifting around 2.5 GHz and its shapes varies in the design space. In Fig. 2.16, the time-domain variability analysis result of the output current at the sample (G, D, L)=(0.41, 0.92, 19.22) mm is obtained from the proposed method, and compared with the MC analysis, which shows very good agreement.

Table 2.2 presents the computational cost of the time-domain variability analysis via different approaches for five (G, D, L) values in the design space, namely: the proposed parameterized stochastic macromodeling technique and the MC analysis based on ADS and on PM_S. Note that, the evaluation of the filter scattering parameters via ADS is computationally expensive: the MC analysis based on the EM simulator requires more than 7 days for each of the five (G, D, L) values in the design space, while the same analysis can be performed more efficiently via the PM_S model, which requires around 1 h and 16 min to perform the same task. However, since the proposed macromodeling technique directly computes the PC coefficients of the port signals via a single time-domain simulation, less than 2 min are required for each one of the chosen (G, D, L) values. Finally, one additional consideration: computing the parametric macromodels PM_S and PM_S$_{\text{PC}}$ is expensive in this case, since the evaluation of the filter scattering parameters

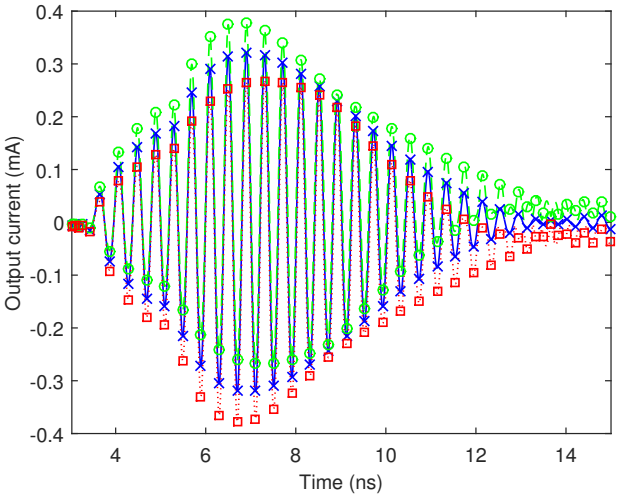

Figure 2.16: Example 2.6.2. The mean μ and the range $\mu \pm 3\sigma$ of the output current of the zigzag filter at (G, D, L)=(0.41, 0.92, 19.22) mm: the (solid, dash, dot) lines are the results computed by the MC method based on ADS; the symbols ($\times$,$\circ$,$\square$) represent the same quantities obtained from PM_S$_{PC}$.

Models		Computational time	
PM_S		10 h 13 min	
PM_S$_{PC}$		6 h 6 min	
Computational time of time-domain simulation			
Sample	MC(EM)	MC(PM_S)	Proposed technique
1	171 h 28 min	1 h 16 min	1 min 3.3 s
2	171 h 27 min	1 h 16 min	1 min 21.3 s
3	171 h 27 min	1 h 16 min	1 min 0.9 s
4	171 h 27 min	1 h 17 min	1 min 1.0 s
5	171 h 31 min	1 h 18 min	1 min 1.5 s

Table 2.2: Example 2.6.2. Efficiency of the parameterized stochastic macromodeling of the zigzag filter.

via ADS is time-consuming and the filter frequency response is very dynamic. In particular, the MC analysis based on PM_S is more efficient than PM_S$_{PC}$ when less than five (G, D, L) values are considered, since the model building phase of PM_S$_{PC}$, based on the scattering parameters evaluated through PM_S, requires more than 6 hours. However, when variability analysis information are required in more than five points in the design space, the proposed parameterized macromod-

eling approach shows significant efficiency compared with the others. An alternative approach is to perform the time- and frequency-domain variability analysis by computing the corresponding augmented system only for the (G, D, L) nominal values of interest, as described in Section 2.2. Such multi-point variability analysis approach allows one to avoid the 6 hours long computation of PM_S_{PC}, but it gives relevant statistical information only for specific values of the parameters considered. Depending on the designer goals, both approaches can represent a valid methodology.

2.6.3 Microstrip lowpass filter

The microstrip lowpass filter shown in Fig. 2.17 and described in [31] is analyzed over the frequency range $[1 - 7]$ GHz. The filter scattering parameters are evaluated in Matlab via a quasi-analytical model [32]. The width W of the three microstrips varies in the range $[9 - 15]$ mm and is assumed as a deterministic parameter, since the filter performance is not sensitive to its variation caused by the manufacturing process; the height of the substrate H is considered as a Gaussian distributed random variable with nominal values in the range $[1.5 - 3.5]$ mm and standard deviation 75 μm; the relative permittivity of the substrate ϵ_r is a Gaussian random variable with fixed nominal value 4.2 and standard deviation 0.067: once the substrate material is chosen, the variations of ϵ_r only depend on the manufacturing process.

Following the approach described in Section 2.2, ten PC basis functions are used to compute the desired model, leading to twenty-port augmented system. The non-intrusive ST sampling method [11, 13] is used to minimize the number of samples required for computing the desired PC coefficients. As a result, the augmented system can be built by evaluating the scattering parameters at $K = 10$ samples of the chosen parameters around each nominal value.

Next, a parameterized macromodel PM_S_{PC} is built by assuming a maximum absolute error threshold of -45 dB between the model response and the computed augmented systems.

Figure 2.18 shows the modeling accuracy in the frequency domain: the results of the proposed macromodel for 36 points spreading over the design space (not used to build the model) are compared with the MC analysis performed for 5000 (W, H, ϵ_r) samples. The accuracy is good for all the points considered.

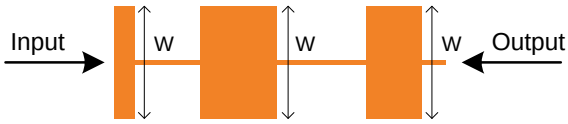

Figure 2.17: Example 2.6.3. Geometry of the microstrip lowpass filter under study.

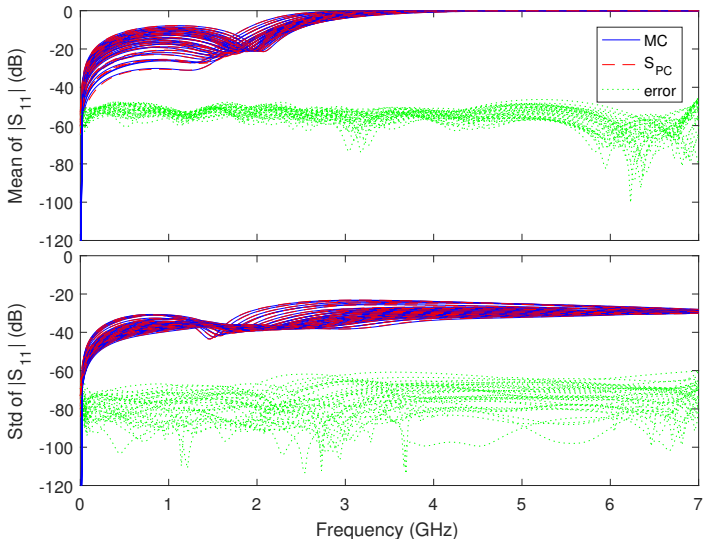

Figure 2.18: Example 2.6.3. The mean and standard deviation (std) of the magnitude of $S_{11}(s, \boldsymbol{\xi})$ for 36 nominal values of (W, H, ϵ_r). The blue lines indicate the MC analysis, the red dash lines are results of the proposed model, while the green dotted lines shows the corresponding absolute error.

Time-domain simulations are performed with the following settings: the filter is excited by a source with $50\ \Omega$ internal resistance and is terminated on a $50\ \Omega$ resistor. The source generates a windowed sinc function voltage pulse with rectangular shape spectrum from DC to 5.2 GHz. Note that the parameterized model PM_S_{PC} is stable and passive: it can be directly adopted for time-domain simulations. Six samples equally spaced along each diagonal of the two dimensional design space (W, H) are chosen for accuracy assessment of the model (note that the nominal value of ϵ_r is constant), while the time-domain MC analysis at the same samples is also conducted as a benchmark. In particular, a state-space model is built via the VF algorithm for each sample used in the MC analysis. The corresponding mean and standard deviation of the output voltage are shown in Figs. 2.19 and 2.20. It is interesting that all the mean values in Fig. 2.19 are quite similar, while the corresponding standard deviations present noticeable differences, which indicates that some samples are more robust than others with regard to the variations of the random parameters. Instead, for the points at the other diagonal both the mean and standard deviation are quite sensitive to the parameters variations as Fig. 2.20 shows. These results show the capability of the proposed method of giving a comprehensive analysis of the filter performance in the entire design space.

Furthermore, complex stochastic moments such as the PDF and CDF can also

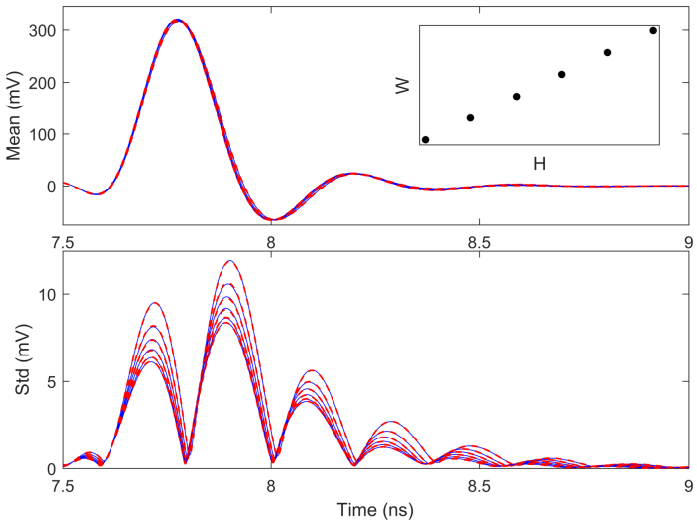

Figure 2.19: Example 2.6.3. Mean and standard deviation (std) of the output voltage for six samples equally spaced along one diagonal of the design space: from $(W = 9.25,\ H = 1.55)$*mm to* $(W = 14.75,\ H = 3.45)$*mm. The blue lines indicate the MC analysis and red dash lines are obtained via the proposed model.*

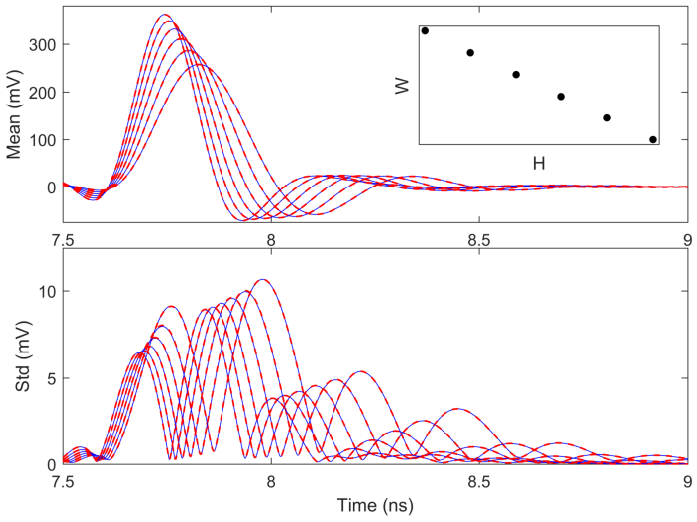

Figure 2.20: Example 2.6.3. Mean and standard deviation (std) of the output voltage for six samples equally spaced along one diagonal of the design space: from $(W = 14.75,\ H = 1.55)$*mm to* $(W = 9.25,\ H = 3.45)$*mm. The blue lines indicate the MC analysis and red dash lines are obtained via the proposed model.*

be computed via the (inexpensive) sampling of the corresponding PC model in the frequency and time domain [10].

The model building process is completed in 9 hours and 29 minutes. However, the frequency- and time-domain variability analysis via the computed model require 2.5 s and 30 s, respectively, for each nominal value of the parameters considered. Note that a single time-domain MC analysis requires about 4 hours 30 minutes, on average. Hence, the proposed approach is more efficient than the MC method if more than two design points are considered.

2.7 Conclusion

The stochastic macromodeling technique presented in this contribution extended the method presented in [9, 10] to generic linear and passive systems, whose transfer function can be described by means of different representations (namely scattering, impedance and admittance parameters). The passivity of the augmented macromodels and the relations between such macromodels computed for different transfer function representations were discussed in details. Furthermore, two possible approaches were presented when the variability analysis needs to be carried out for different nominal values of the chosen random parameters, based on the proposed stochastic macromodeling technique: a multi-point and a parameterized macromodeling approach. The accuracy, efficiency and flexibility of the proposed method were validated with three suitable numerical examples where comparison with the MC analysis was carried out in both frequency and time domain.

References

[1] D. Xiu and G. E. Karniadakis. *The Wiener-Askey Polynomial Chaos for Stochastic Differential Equations*. SIAM J. Sci. Comput., 24(2):619–644, Apr. 2002.

[2] M. S. Eldred. *Recent advances in non-intrusive polynomial-chaos and stochastic collocation methods for uncertainty analysis and design*. In Proc. 50th AIAA/ASME/ASCE/AHS/ASC Structures, Structural Dynamics, and Materials Conference, pages 1–37, Palm Springs, California, May 2009.

[3] K. Strunz and Q. Su. *Stochastic Formulation of SPICE-type Electronic Circuit Simulation with Polynomial Chaos*. ACM Trans. Model. Comput. Simul., 18(4):15:1–15:23, September 2008.

[4] P. Manfredi, D. Vande Ginste, D. De Zutter, and F. G. Canavero. *Uncertainty Assessment of Lossy and Dispersive Lines in SPICE-Type Environments*. IEEE Trans. Compon., Packag., Manuf. Technol., 3(7):1252–1258, Jul. 2013.

[5] T. A. Pham, E. Gad, M. S. Nakhla, and R. Achar. *Decoupled Polynomial Chaos and Its Applications to Statistical Analysis of High-Speed Interconnects*. IEEE Trans. Compon., Packag., Manuf. Technol., 4(10):1634–1647, Oct. 2014.

[6] A. Biondi, D. Vande Ginste, D. De Zutter, P. Manfredi, and F. G. Canavero. *Variability Analysis of Interconnects Terminated by General Nonlinear Loads*. IEEE Trans. Compon., Packag., Manuf. Technol., 3(7):1244–1251, Jul. 2013.

[7] D. Spina, F. Ferranti, G. Antonini, T. Dhaene, and L. Knockaert. *Efficient Variability Analysis of Electromagnetic Systems Via Polynomial Chaos and Model Order Reduction*. IEEE Trans. Compon., Packag., Manuf. Technol., 4(6):1038–1051, Jun. 2014.

[8] D. Spina, F. Ferranti, T. Dhaene, L. Knockaert, and G. Antonini. *Polynomial chaos-based macromodeling of multiport systems using an input-output approach*. Int. J. Numer. Model., 28(5):562–581, Sep./Oct. 2015.

[9] Y. Ye, D. Spina, T. Dhaene, L. Knockaert, and G. Antonini. *Macromodeling of general linear systems under stochastic variations*. In Proc. IEEE Electrical Design of Advanced Packaging and Systems (EDAPS), pages 61–63, Hawaii, USA, Dec. 2016.

[10] D. Spina, T. Dhaene, L. Knockaert, and G. Antonini. *Polynomial Chaos-Based Macromodeling of General Linear Multiport Systems for Time-Domain Analysis*. IEEE Trans. Microw. Theory Techn., 65(5):1422–1433, May 2017.

[11] Z. Zhang, T. A. El-Moselhy, I. M. Elfadel, and L. Daniel. *Stochastic Testing Method for Transistor-Level Uncertainty Quantification Based on Generalized Polynomial Chaos*. IEEE Trans. Comput.-Aided Design Integr. Circuits Syst., 32(10):1533–1545, Oct. 2013.

[12] M. R. Rufuie, E. Gad, M. Nakhla, and R. Achar. *Generalized Hermite Polynomial Chaos for Variability Analysis of Macromodels Embedded in Nonlinear Circuits*. IEEE Trans. Compon., Packag., Manuf. Technol., 4(4):673–684, Apr. 2014.

[13] P. Manfredi, D. Vande Ginste, D. De Zutter, and F. G. Canavero. *Generalized Decoupled Polynomial Chaos for Nonlinear Circuits With Many Random Parameters*. IEEE Microw. Wireless Compon. Lett., 25(8):505–507, Aug. 2015.

[14] A. K. Prasad and S. Roy. *Accurate Reduced Dimensional Polynomial Chaos for Efficient Uncertainty Quantification of Microwave/RF Networks*. IEEE Trans. Microw. Theory Techn., 65(10):3697–3708, Oct. 2017.

[15] R. Neumayer, F. Haslinger, A. Stelzer, and R. Weigel. *Synthesis of SPICE-compatible broadband electrical models from n-port scattering parameter data*. In Proc. IEEE Electromagnetic Compatibility (EMC), pages 469–474, Minneapolis, USA, Aug. 2002.

[16] G. Antonini. *SPICE equivalent circuits of frequency-domain responses*. IEEE Trans. Electromagn. Compat., 45(3):502–512, Aug. 2003.

[17] J. F. Villena and L. M. Silveira. *Circuit Synthesis for Guaranteed Positive Sparse Realization of Passive State-Space Models*. IEEE Trans. Circuits Syst. I, Reg. Papers, 64(6):1576–1587, Jun. 2017.

[18] B. Gustavsen and A. Semlyen. *Rational approximation of frequency domain responses by Vector Fitting*. IEEE Trans. Power Del., 14(3):1052–1061, Jul. 1999.

[19] D. Deschrijver and T. Dhaene. *Broadband macromodelling of passive components using orthonormal vector fitting*. Electron. Lett., 41(21):1160–1161, Oct. 2005.

[20] B. Gustavsen. *Fast Passivity Enforcement for Pole-Residue Models by Perturbation of Residue Matrix Eigenvalues*. IEEE Trans. Power Del., 23(4):2278–2285, Oct. 2008.

[21] D. Deschrijver and T. Dhaene. *Fast Passivity Enforcement of S-Parameter Macromodels by Pole Perturbation*. IEEE Trans. Microw. Theory Techn., 57(3):620–626, Mar. 2009.

[22] G. Blatman and B. Sudret. *Adaptive sparse polynomial chaos expansion based on least angle regression*. J. Comput. Phys, 230(6):2345 – 2367, 2011.

[23] J Peng, J Hampton, and A Doostan. *A weighted ℓ_1-minimization approach for sparse polynomial chaos expansions*. J. Comput. Phys, 267:92 – 111, 2014.

[24] M. R. Wohlers. *Lumped and Distributed Passive Networks*. Academic Press, New York, 1969.

[25] P. Manfredi, D. Vande Ginste, D. De Zutter, and F. G. Canavero. *On the Passivity of Polynomial Chaos-Based Augmented Models for Stochastic Circuits*. IEEE Trans. Circuits Syst. I, Reg. Papers, 60(11):2998–3007, Nov. 2013.

[26] P. Triverio, S. Grivet-Talocia, M. S. Nakhla, F. G. Canavero, and R. Achar. *Stability, Causality, and Passivity in Electrical Interconnect Models*. IEEE Trans. Adv. Packaging, 30(4):795–808, Nov. 2007.

[27] C. P. Coelho, J. R. Phillips, and L. M. Silveira. *Passive constrained rational approximation algorithm using Nevanlinna-Pick interpolation*. In Proc. Design, Automation and Test in Europe Conference and Exhibition, pages 923–930, Paris, France, Mar. 2002.

[28] Francesco Ferranti, Luc Knockaert, Tom Dhaene, and Giulio Antonini. *Parametric macromodeling based on amplitude and frequency scaled systems with guaranteed passivity*. Int. J. Numer. Model., 25(2):139–151, Mar./Apr. 2012.

[29] K. Chemmangat, F. Ferranti, T. Dhaene, and L. Knockaert. *Scalable models of microwave system responses using sequential sampling on unstructured grids*. Int. J. Numer. Model., 27(1):122–137, Jan./Feb. 2014.

[30] D. Puttadilok, D. Eungdamrong, and W. Tanacharoenwat. *A study of narrowband and compact size microstrip bandpass filters for wireless communications*. In Proc. SICE Annual Conference 2007, pages 1418–1421, Takamatsu, Japan, Sep. 2007.

[31] B. Omid and R. Arman. *Design, Simulation and Construction a Low Pass Microwave Filters on the Micro Strip Transmission Line*. Int. J. Comput. Theory Eng., 4(5):784–787, Oct. 2012.

[32] K. C. Gupta, Ramesh Garg, Inder Bahl, and Prakash Bhartia. *Microstrip Lines and Slotlines, 2nd Edition*. Norwood, MA: Artech House, Inc., 1996.

3

Stochastic Macromodeling of Linear and Nonlinear Electronic Circuits

Y. Ye, D. Spina, P. Manfredi, D. Vande Ginste, and T. Dhaene, "A comprehensive and modular stochastic modeling framework for the variability-aware assessment of signal integrity in high-speed links," IEEE Transactions on Electromagnetic Compatibility, vol. 60, no. 2, pp. 459-467, Apr. 2018.

Abstract

This chapter presents a comprehensive and modular modeling framework for stochastic signal integrity analysis of complex high-speed links. Such systems are typically composed of passive linear networks and nonlinear, usually active, devices. The key idea of the proposed contribution is to express the signals at the ports of each of such system elements or subnetworks as a polynomial chaos expansion. This allows one to compute, for each block, equivalent deterministic models describing the stochastic variations of the network voltages and currents. Such models are synthesized into SPICE-compatible circuit equivalents, which are readily connected together and simulated in standard circuit simulators. Only a single circuit simulation of such an equivalent network is required to compute the pertinent statistical information of the entire system, without the need of running a large number of time-consuming electromagnetic-circuit co-simulations. The accuracy

and efficiency of the proposed approach, which is applicable to a large class of complex circuits, are verified by performing signal integrity investigations of two interconnect examples.

3.1 Introduction

In recent years, a great deal of attention has been devoted to study the effects of geometrical and/or electrical parameter variations on the performance of various electronic circuits. Indeed, circuit performance is nowadays largely affected by the variations of the manufacturing process, due to the increasing integration and miniaturization. In this context, uncertainty quantification methods become a critical resource for the signal integrity (SI) assessment of high-speed designs. The Monte Carlo (MC) method is robust, accurate and easy to implement, and it is considered as the standard approach for variability analysis. However, its high computational cost often prohibits its application to the analysis of complex designs. Therefore, more efficient techniques for stochastic simulations are needed.

Many techniques based on the polynomial chaos (PC) method [1, 2] have been recently developed to tackle this problem [3–14], and are able to perform variability analysis with high accuracy and efficiency compared to MC-based approaches. Each method is tailored for a specific class of circuits, like lumped-element circuits [3], transmission-line circuits [4, 5], arbitrary passive linear systems [6–8], or nonlinear circuits [9–14]. However, a general and comprehensive modeling framework, capable of including heterogeneous stochastic components appears yet to be missing. Indeed, modern interconnect designs consist of a combination of circuit-level components, behavioral macromodels, and 3D structures. The present chapter aims at covering the aforementioned gap by proposing a comprehensive and modular approach that allows the inclusion of any linear passive structure (possibly characterized by means of full-wave EM simulations) or nonlinear component (either at physical or behavioral level). The point of departure is the technique presented in [8], which was recently proposed to compute a stable and passive PC-based macromodel of a generic linear, passive and frequency-dependent stochastic system. It is a flexible and reliable modeling approach, but it is limited to passive linear systems.

In order to overcome this limitation, we integrate the technique proposed in [13], which can create a deterministic equivalent circuit model of any stochastic nonlinear component at both the physical or behavioral level, thus yielding a novel and powerful framework for the variability-aware SI analysis of complex high-speed circuit designs. The models for each linear and nonlinear subpart are computed separately, with the desired (or most convenient) level of modularity, and then connected together in a SPICE-type environment. Within the novel modeling framework, only a single time-domain simulation of the entire system is required

to perform the variability analysis, thus avoiding expensive repeated (EM-)circuit (co)-simulations. As will be shown in Section 3.3, complete interconnect links can as such be analyzed very efficiently.

The chapter is organized as follows. Section 3.2 describes the novel proposed approach, while its validation is carried out in Section 3.3 by means of two pertinent numerical examples. Conclusions are drawn in Section 3.4.

3.2 Stochastic modeling of complex links

Modern high-speed links consist of a combination of nonlinear, possibly active components (e.g., diodes, drivers and receivers) and passive linear structures (e.g., transmission lines, power distribution networks, vias, packages, etc.). While the former are defined by nonlinear relations between their port signals, which can be defined in different ways (for example analytical formulas or behavioral models), the latter are completely defined by their transfer function, which can be expressed in several forms (i.e., impedance, admittance or scattering representations) and may require time-consuming EM simulations to be determined.

In the following, we assume that the linear parts of the system under study depend on some geometrical or electrical random parameters collected in the vector $\boldsymbol{\xi}$, while the nonlinear elements are influenced by the vector of random variables $\hat{\boldsymbol{\xi}}$. As a result of this variability, the voltages and currents at each port of such linear and nonlinear components depend on both the random variables $\hat{\boldsymbol{\xi}}$ and $\boldsymbol{\xi}$, as illustrated in Fig. 3.1.

According to the PC theory, such port signals are represented as a truncated summation of basis functions with suitable coefficients:

$$v(\hat{\boldsymbol{\xi}}, \boldsymbol{\xi}, t) \approx \sum_{i=0}^{M} v_i\,(t)\,\varphi_i(\hat{\boldsymbol{\xi}}, \boldsymbol{\xi}) \tag{3.1}$$

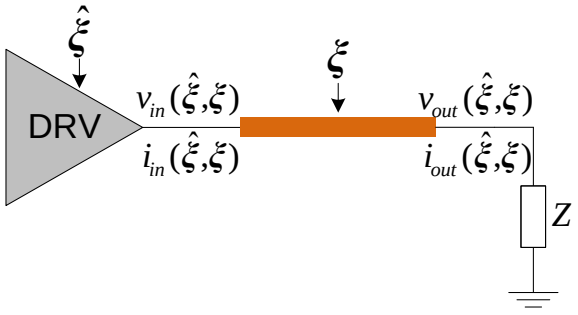

Figure 3.1: Example of a link subject to stochastic variations affecting a (nonlinear) driver (DRV), a transmission line and a lumped termination.

where $v(\hat{\boldsymbol{\xi}}, \boldsymbol{\xi}, t)$ denotes a generic voltage within the system (currents are treated in a similar fashion), the basis functions $\varphi_i(\hat{\boldsymbol{\xi}}, \boldsymbol{\xi})$ are orthogonal polynomials depending on the joint distribution of the random variables $\boldsymbol{\xi}$ and $\hat{\boldsymbol{\xi}}$, and $v_i\,(t)$ are the corresponding $M+1$ coefficients to be determined.

The key idea of the proposed approach is to describe the stochastic variations of both the linear and nonlinear system subnetworks via suitable PC models, which will simultaneously account for all the random variables $\boldsymbol{\xi}$ and $\hat{\boldsymbol{\xi}}$. Specifically, the procedure foresees the computation of equivalent and *deterministic circuit models* describing the time-domain behavior of the PC coefficients of the port voltages and currents, starting from the original stochastic system, which are then connected together according to the original circuit topology. In the PC jargon, such models are usually referred to as "augmented" [8], since their number of ports is higher with respect to the corresponding stochastic elements. However, as the model is deterministic, a single transient circuit simulation (e.g., in SPICE) allows determining all the PC expansion coefficients in (3.1) and hence the desired statistical information.

At this point, it is important to stress two important features offered by the advocated modeling strategy to circuit designers:

- The equivalent models can be constructed with the desired level of modularity. For example, subparts that have already a circuit-level description can still be modeled using the approaches for lumped and distributed elements in [10] and [4], respectively. However, if the stochastic behavior of their inner voltages and currents is not of interest, they can be encompassed in a larger macromodel.

- Circuit-EM co-simulations are avoided, as every block is synthesized into a SPICE-compatible equivalent circuit network.

The method adopted for the modeling of linear networks is detailed in Section 3.2.1, while Section 3.2.2 addresses the modeling of the nonlinear components. For the sake of simplicity, in the remainder of this chapter we will describe only the case of independent random variables, even though it is possible to extend the proposed method to the case of correlated random variables [1, 2]. Furthermore, only orthonormal PC basis functions will be considered. Please note that discussing the properties of the PC expansion is outside the scope of this contribution. The interested reader may consult [1]– [13] for an extensive reference to PC theory.

3.2.1 Stochastic modeling of general passive linear systems

When a generic linear system is subjected to stochastic effects caused by random variations of geometric or electrical parameters, here denoted by $\boldsymbol{\xi}$, the pertinent

scattering matrix will be $\boldsymbol{\xi}$ dependent. If such a system is embedded in a network that is also affected by the random variables $\hat{\boldsymbol{\xi}}$, the incident and reflected waves will in general depend on both $\boldsymbol{\xi}$ and $\hat{\boldsymbol{\xi}}$ (see Fig. 3.1). The scattering relations can therefore be expressed as

$$\boldsymbol{b}(\boldsymbol{\xi}, \hat{\boldsymbol{\xi}}, s) = \boldsymbol{S}(\boldsymbol{\xi}, s)\boldsymbol{a}(\boldsymbol{\xi}, \hat{\boldsymbol{\xi}}, s) \tag{3.2}$$

where $\boldsymbol{S}$ is the scattering parameter matrix of the stochastic linear system, s is the Laplace variable, and $\boldsymbol{a} \in \mathbb{C}^{N\times 1}$ and $\boldsymbol{b} \in \mathbb{C}^{N\times 1}$ are the incident and reflected waves, respectively, with N the number of ports of the system.

The starting point of the proposed method is the computation of a PC model of the system scattering parameters over a discrete set of frequency values f_l for $l = 1, \ldots, L$ (or the Laplace variable $s_l = j2\pi f_l$) as:

$$\boldsymbol{S}(\boldsymbol{\xi}, s_l) \approx \sum_{i=0}^{M_S} \boldsymbol{S}_i\,(s_l)\,\varphi_i(\boldsymbol{\xi}) \tag{3.3}$$

where $M_S + 1$ is the number of basis functions depending only on $\boldsymbol{\xi}$. Any non-intrusive PC-based approach can be used for this purpose: the PC coefficients in (3.3) can be obtained via linear regression-, numerical integration- [2], or stochastic testing (ST)-based techniques [14], for example.

Now, it is easy to express (3.3) with respect to all the random variables considered $\left(\hat{\boldsymbol{\xi}}, \boldsymbol{\xi}\right)$ as

$$\boldsymbol{S}(\hat{\boldsymbol{\xi}}, \boldsymbol{\xi}, s_l) \approx \sum_{i=0}^{M} \boldsymbol{S}_i\,(s_l)\,\varphi_i(\hat{\boldsymbol{\xi}}, \boldsymbol{\xi}) \tag{3.4}$$

since $\varphi_i(\boldsymbol{\xi})$ for $i = 0, \ldots, M_S$ are a subset of $\varphi_i(\hat{\boldsymbol{\xi}}, \boldsymbol{\xi})$ for $i = 0, \ldots, M$, thanks to the property that, for independent random variables, the PC basis functions in (3.4) are the product combination of the basis functions for each random variable considered [1, 2]. Hence, all the PC coefficients in (3.4) for basis functions depending on $\hat{\boldsymbol{\xi}}$ are zero.

Nevertheless, a full expression of the PC expansion in the form (3.4) is required to properly account for the additional variability introduced by the rest of the network.

Now, by following the approach presented in [8], it is possible to apply Galerkin projections (GP) [1] to (3.2) and describe the relationship between the PC coefficients of the incident and reflected waves as:

$$\boldsymbol{b}_{PC}(s_l) = \boldsymbol{S}_{PC}(s_l)\boldsymbol{a}_{PC}(s_l) \quad \text{for } l = 1, \ldots, L \tag{3.5}$$

where the vectors $\boldsymbol{a}_{PC}, \boldsymbol{b}_{PC} \in \mathbb{C}^{(M+1)N\times 1}$ collect the (deterministic) PC coefficients of the corresponding incident and reflected wave, respectively, with $M + 1$ the total number of the PC basis functions, whereas $\boldsymbol{S}_{PC} \in \mathbb{C}^{(M+1)N\times(M+1)N}$ is

a deterministic matrix, obtained by suitable combination of the PC coefficients of the scattering matrix in (3.4).

Equation (3.5) describes a new system, whose port voltages and currents are the PC coefficients of those of the original stochastic system. Note that $\boldsymbol{S}_{PC}$ is $M+1$ times larger than the original system in terms of number of ports. Furthermore, the matrices $\boldsymbol{S}_{PC}(s_l)$ for $l = 1, \ldots, L$ are sparse by construction [8], since in (3.4) some PC coefficients are zero, as discussed above. Finally, in [8] it is proven that $\boldsymbol{S}_{PC}$ can still be regarded as a scattering parameter matrix, now relating the PC coefficients of the incident and reflected waves: its passivity conditions are therefore the same as for deterministic scattering parameters.

At this point, a rational model of $\boldsymbol{S}_{PC}$ is built by means of the Vector Fitting (VF) technique [15], where a pole-flipping scheme is used to enforce stability, while passivity assessment and enforcement are accomplished by using standard and robust techniques [16]. Then, it is straightforward to convert such a rational model into a corresponding state-space representation [15], which can be converted into an equivalent circuit via a suitable synthesis technique [17].

A key step in any modeling process is adopting a suitable error measure and error threshold. The maximum absolute model error (MER) between the elements of the scattering parameter augmented matrix $\boldsymbol{S}_{PC}^{i,j}$ and the corresponding VF model response $\boldsymbol{H}_{PC}^{i,j}$ in the entire frequency range is chosen in [8] to compute the desired rational model of $\boldsymbol{S}_{PC}$:

$$MER = max_{i,j,l}\left(|\boldsymbol{S}_{PC}^{i,j}(s_l) - \boldsymbol{H}_{PC}^{i,j}(s_l)|\right) \tag{3.6}$$

for $i, j = 1, \ldots, (M+1)\,N$ and $l = 1, \ldots, L$. Note that in [8], the choice of the MER error threshold was left to the designer's expertise, by considering that modeling $\boldsymbol{S}_{PC}$ is similar to modeling a deterministic scattering parameter matrix. Here, a new criterion is provided based on the unique characteristics of the $\boldsymbol{S}_{PC}$ augmented system. Indeed, thanks to the properties of the GP method, it is easy to prove that all the non-null elements of the first $N \times (M+1)\,N$ or $(M+1)\,N \times N$ block of $\boldsymbol{S}_{PC}$ are, by construction, formed by the PC coefficients of the scattering parameter matrix in (3.4).

Since the first two stochastic moments, i.e., the mean $\boldsymbol{\mu}$ and the standard deviation $\boldsymbol{\sigma}$, can be analytically computed from these coefficients [1, 2] in the following the MER error threshold in (3.6) is chosen such that the differences:

$$\begin{cases} error_{mean}(s_l) = & max(|\boldsymbol{\mu}(s_l) - \boldsymbol{\mu}_H(s_l)|) \\ error_{sigma}(s_l) = & max(|\boldsymbol{\sigma}(s_l) - \boldsymbol{\sigma}_H(s_l)|) \end{cases} \tag{3.7}$$

are minimized, where $\boldsymbol{\mu}_H$ and $\boldsymbol{\sigma}_H$ are the mean and standard deviation computed by the VF model of $\boldsymbol{S}_{PC}$ for all the frequency samples considered $l = 1, \ldots, L$. Hence, the MER error threshold in (3.6) is chosen based on the model capability of accurately estimating the stochastic moments (3.7).

Finally, in [8] it is proven that the PC coefficients of the incident and reflected waves at the $k-$th port of the system depend only on the corresponding voltage and current PC coefficients at the same port, as for the original deterministic system. This property allows one to easily connect the model of $\boldsymbol{S}_{PC}$ to the models of the other system subparts, as will be discussed in details in the following.

It is important to point out that the modeling approach outlined in this section readily applies to any general electrical (e.g., circuit or EM) system supporting a scattering representation like (3.2).

3.2.2 Stochastic modeling of nonlinear components

Nonlinear components affected by random variables $\hat{\boldsymbol{\xi}}$ are described by suitable and possibly dynamic relationships between the time-domain counterparts of the port voltages and currents, here denoted as

$$\boldsymbol{i}(\boldsymbol{\xi},\hat{\boldsymbol{\xi}},t)=\boldsymbol{\mathcal{F}}(\boldsymbol{v}(\boldsymbol{\xi},\hat{\boldsymbol{\xi}},t),t,\hat{\boldsymbol{\xi}}) \tag{3.8}$$

where vectors $\boldsymbol{v}(\boldsymbol{\xi},\hat{\boldsymbol{\xi}},t)$ and $\boldsymbol{i}(\boldsymbol{\xi},\hat{\boldsymbol{\xi}},t)$ collect all port voltages and currents, whereas $\boldsymbol{\mathcal{F}}$ is understood to be a vectorized operator whose $k-$th row, $i_k=\mathcal{F}_k(\boldsymbol{v},t,\hat{\boldsymbol{\xi}})$, describes the nonlinear relationship between the $k-$th port current and (all) port voltages. This can be either an explicit nonlinear function or an implicit characteristic imposed by a generic nonlinear component or subcircuit (e.g, diode, transistor, or behavioral model). As already mentioned for the linear components, the port voltages and currents are stochastic as a result of the variability in both the linear and nonlinear parts of the network, and $\boldsymbol{\mathcal{F}}$ is subjected to stochastic effects, but only due to $\hat{\boldsymbol{\xi}}$.

Replacing the port voltages and currents in (3.8) with their PC expansions, and enforcing the resulting equation to hold for $M+1$ values $\{\boldsymbol{\xi}_m,\hat{\boldsymbol{\xi}}_m\}_{m=0}^{M}$ of the random variables, pre-determined via the ST algorithm [9], yields a deterministic system of $M+1$ equations in the voltage and current PC coefficients. For example, for the current at the $k-$th port:

$$\begin{aligned}
&a_{00}i_{k0}(t)+\ldots+a_{0M}i_{kM}(t)=\mathcal{F}_k(a_{00}\boldsymbol{v}_0(t)+\ldots+a_{0M}\boldsymbol{v}_M(t),t,\hat{\boldsymbol{\xi}}_0)\\
&\quad\vdots\qquad\qquad\qquad\qquad\qquad\qquad\qquad\vdots\\
&a_{M0}i_{k0}(t)+\ldots+a_{MM}i_{kM}(t)=\mathcal{F}_k(a_{M0}\boldsymbol{v}_0(t)+\ldots+a_{MM}\boldsymbol{v}_M(t),t,\hat{\boldsymbol{\xi}}_M)
\end{aligned} \tag{3.9}$$

where a_{mi} are mere scalar coefficients obtained by evaluating the $i-$th PC basis function at the $m-$th ST point:

$$a_{mi}=\varphi_i(\hat{\boldsymbol{\xi}}_m,\boldsymbol{\xi}_m) \tag{3.10}$$

It is important to note that, while the nonlinear characteristic $\mathcal{F}_{\|}$ in (3.9) itself depends solely on the ST points $\hat{\boldsymbol{\xi}}_m$, its inputs depend also on the points $\boldsymbol{\xi}_m$.

In general, even for deterministic nonlinear elements, the voltage and current PC coefficients are coupled, as opposed to the case of deterministic linear components [10, 13].

From (3.9), an explicit relation for the coefficients of the port current is obtained by inverting the system (3.9) in matrix form:

$$\begin{bmatrix} i_{k0}(t) \\ \vdots \\ i_{kM}(t) \end{bmatrix} = \begin{bmatrix} a_{00} \ldots a_{0M} \\ \vdots \ \ddots \ \vdots \\ a_{M0} \ldots a_{MM} \end{bmatrix}^{-1} \times \begin{bmatrix} \mathcal{F}_k(a_{00}\boldsymbol{v}_0(t) + \ldots + a_{0M}\boldsymbol{v}_M(t), t, \hat{\boldsymbol{\xi}}_0) \\ \vdots \\ \mathcal{F}_k(a_{M0}\boldsymbol{v}_0(t) + \ldots + a_{MM}\boldsymbol{v}_M(t), t, \hat{\boldsymbol{\xi}}_M) \end{bmatrix} \tag{3.11}$$

The system (3.11) has a SPICE-compatible circuit interpretation, as described in [13]. It can be inferred from the vector term in the r.h.s. of (3.11) that such an equivalent circuit requires $M + 1$ *deterministic* replicas of the nonlinear component, for which the stochastic parameters are evaluated as defined by the corresponding ST points. The general topology of the circuit model is, however, independent of the specific type of nonlinear element, as long as it has a description of the form (3.8).

3.2.3 Overall network model

The augmented deterministic models described in Sections 3.2.1 and 3.2.2 must be suitably connected together to produce the complete model of the stochastic network under study. This is done in accordance with the original network topology. For example, Fig. 3.2 (a) shows the connection of a 2-port nonlinear device to a 2-port linear network. The two components are subjected to stochastic effects due to two random variables $\hat{\xi}$ and ξ, respectively. For the sake of illustration, we consider a first-order PC expansion, leading to a total of three basis functions. The extension to systems with a higher number of ports and/or of PC basis functions is straightforward.

The SPICE-compatible circuit model for the nonlinear part is shown in Fig. 3.2 (b). It includes three instances $\boldsymbol{\mathcal{F}}(\hat{\xi}_0)$, $\boldsymbol{\mathcal{F}}(\hat{\xi}_1)$, $\boldsymbol{\mathcal{F}}(\hat{\xi}_2)$ of the original stochastic nonlinear component, in which the random parameter $\hat{\xi}$ is set to values $\hat{\xi}_0$, $\hat{\xi}_1$ and $\hat{\xi}_2$, respectively. The required voltages at the ports of these instances are produced by means of controlled voltage sources, with coefficients as in (3.10). Analogously, the correct expression of the currents in the main circuit (3.11) is reproduced by means of controlled current sources, with coefficients

$$\begin{bmatrix} b_{00} & b_{01} & b_{02} \\ b_{10} & b_{11} & b_{12} \\ b_{20} & b_{21} & b_{22} \end{bmatrix} = \begin{bmatrix} a_{00} & a_{01} & a_{02} \\ a_{10} & a_{11} & a_{12} \\ a_{20} & a_{21} & a_{22} \end{bmatrix}^{-1} \tag{3.12}$$

The interested readers may consult [13] for more detailed information about this model.

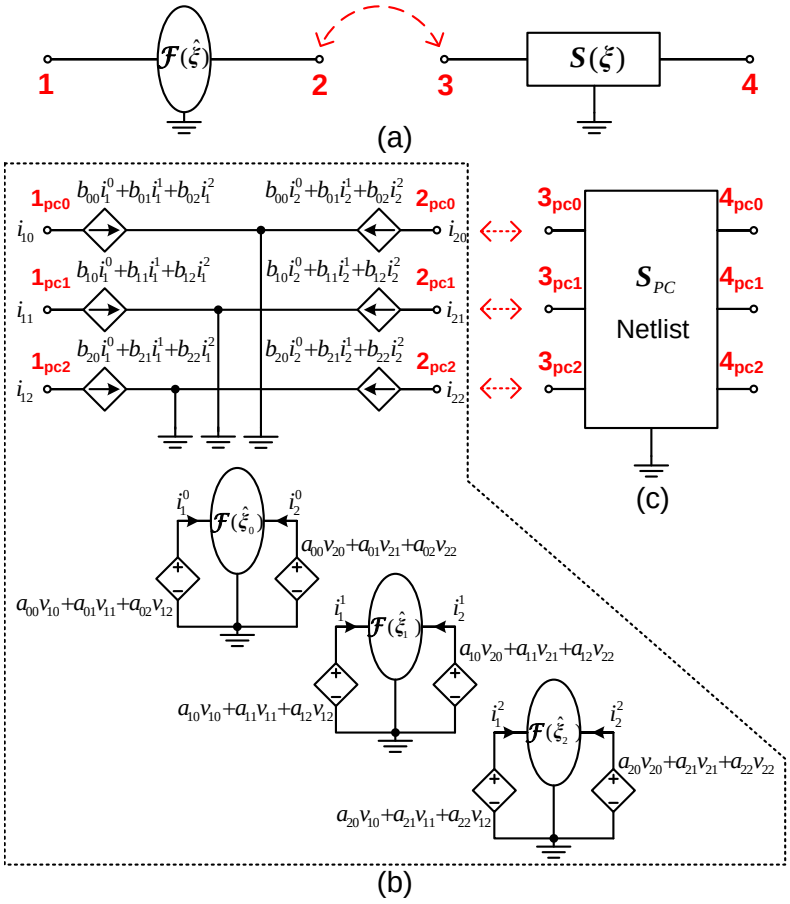

Figure 3.2: (a) Connected nonlinear and linear systems subjected to stochastic effects; (b) and (c) Deterministic equivalent models of the stochastic nonlinear and linear systems.

The model for the linear system in Fig. 3.2 (c) is synthesized into an equivalent SPICE netlist consisting of lumped elements, which suitably describes the augmented system $\boldsymbol{S}_{PC}$ that is obtained as described in Section 3.2.1. It is clear that each port of the original systems is now described by three corresponding ports in the augmented models, one for each PC coefficient of the port voltages and currents. The connectivity between the ports remains consistent for the augmented models, as shown in Fig. 3.2.

The resulting netlist can be readily simulated in a SPICE-type circuit simulator. A single time-domain simulation simultaneously yields all the PC coefficients of the port voltages and currents, which in turn provide comprehensive statistical information. The outlined modeling strategy offers circuit designers a modular

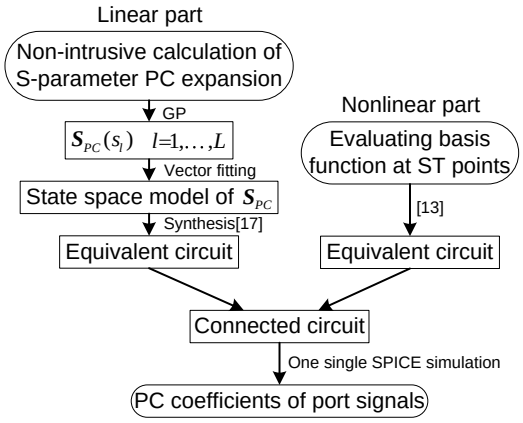

Figure 3.3: Flowchart of the proposed statistical simulation framework.

and powerful tool allowing for the stochastic analysis of a system consisting of an arbitrary combination of passive linear systems and nonlinear components, each possibly affected by variability. The flowchart of the proposed modeling framework is shown in Fig. 3.3.

3.3 Applications and numerical results

This section discusses two application examples, concerning the SI analysis of i) an interconnect tree and ii) a nonuniform differential link. All the time-domain simulations are carried out with HSPICE on a computer with an Intel(R) Core(TM) I3 Processor running at 2.93 GHz and 8 GB of RAM.

3.3.1 Interconnect tree

The first application example concerns the interconnect tree depicted in Fig. 3.4, consisting of both lumped interconnections and microstrip segments, whose cross-section is also indicated in the figure. The tree is driven at the input port by a behavioral macromodel of an I/O transceiver of a 512-Mb Flash memory chip, which produces a pulse with a risetime of 1 ns. The behavioral macromodel is obtained with the techniques in [18–20]. Each of the four output ports is terminated by a pair of diodes with saturation current $I_S = 50$ pA, series resistance $R_S = 5\,\Omega$, and junction capacitance $C_{JO} = 3$ pF. Not shown in Fig. 3.4 is the RL power supply network for the driver, with supply voltage $V_{DD} = 1.8$ V, $R = 10$ mΩ and $L = 2$ nH.

The thickness and relative permittivity of the microstrip substrate are assumed to be affected by process variations and therefore to vary according to a Gaussian distribution with a relative standard deviation of 5% of their nominal values. Moreover, the operating temperature at the receiver side is considered as an additional Gaussian random variable with nominal value 60°C and a standard deviation of 3°C. This temperature fluctuation affects the operation of the diodes. Hence, there are three independent random parameters in the entire network, and a second-order PC expansion is used to describe the variations of the port signals, leading to a total of 10 PC basis functions. Now, in order to stress the versatility of the advocated modeling strategy, we consider the following alternative approaches to model the

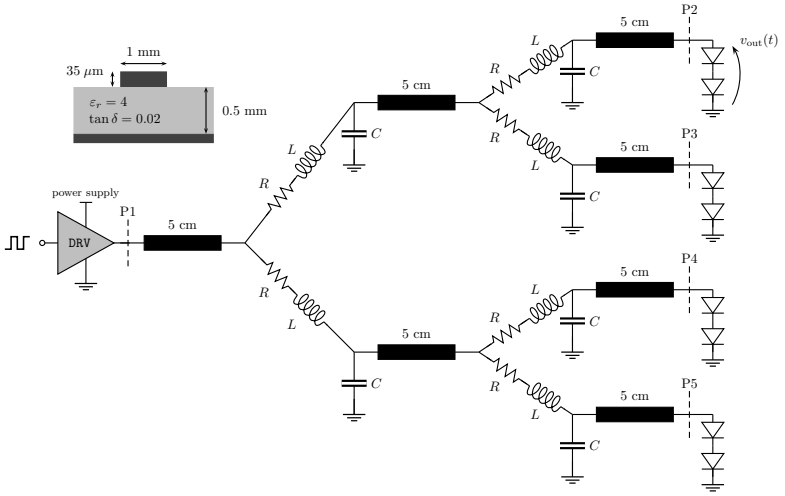

Figure 3.4: Example 3.3.1. Schematic of the interconnect tree, composed of seven identical lossy microstrip transmission lines, driven by a nonlinear I/O transceiver and terminated with diodes.

linear part of the network, based on the procedure outlined in Section 3.2.1:

- the transmission-line elements are modeled as stochastic 2-port devices, the modeling of the remaining deterministic RLC elements being trivial, as discussed later;
- the entire linear part is modeled as a 5-port stochastic network.

In either cases, the linear models are complemented with the pertinent models of the nonlinear (deterministic) driver and (stochastic) diodes to obtain the equivalent PC-based model of the overall network. These two scenarios allow us not only to highlight the modularity of the proposed technique, but also to assess its performance for different modeling choices.

The scattering parameters of both the 5-port linear subnetwork and the 2-port transmission-line elements are evaluated at 561 frequency points in the range [0 - 3.5] GHz, 188 of which are used to build the corresponding $\boldsymbol{S}_{PC}$ models. The remaining samples are used for validation, thus verifying the model accuracy at frequencies that were not used to create the model.

Note that, as a result of the multiplication of the original port numbers by the number of PC basis functions, the model for the entire interconnection has 50 ports, while the model of each transmission-line segment has only 20 ports (see Section 3.2.1). However, in the latter case the models for each transmission line need to be properly connected between each other in order to describe the variation of the entire interconnection. Therefore, an equivalent model of the lumped RLC elements must be generated as well. Yet, since these lumped elements are in this case deterministic, the corresponding model matrix is block diagonal, which means the transmission line models are interconnected by suitable replicas of the original RLC elements in Fig. 3.4 [4].

At this point, two alternative deterministic equivalent models describing the statistical variations of the interconnect in Fig. 3.4 have been computed, one starting from the scattering parameters of the entire interconnection and one from the scattering parameters of the single transmission-line elements. In the following, the results obtained using these two models, synthesized into SPICE-compatible networks, are denoted with "$Simu_I$" and "$Simu_{TL}$", respectively.

Now, the performance of the proposed models is compared not only against the results of a MC analysis, but also with the technique in [4]. Indeed, [4] offers an accurate and efficient reference approach, which can however be used only as long as the transmission lines are uniform, as is the case for the network of Fig. 3.4. On the contrary, the new proposed modeling strategy is applicable to any arbitrary line layout, as will be shown in the second application example.

Figure 3.5 shows the statistical behavior of the voltage v_{out} at any (due to the structure symmetry) of the output ports P2–P5 of the interconnect tree of Fig. 3.4. The thin gray curves are a superposition of 10000 random voltages from the MC

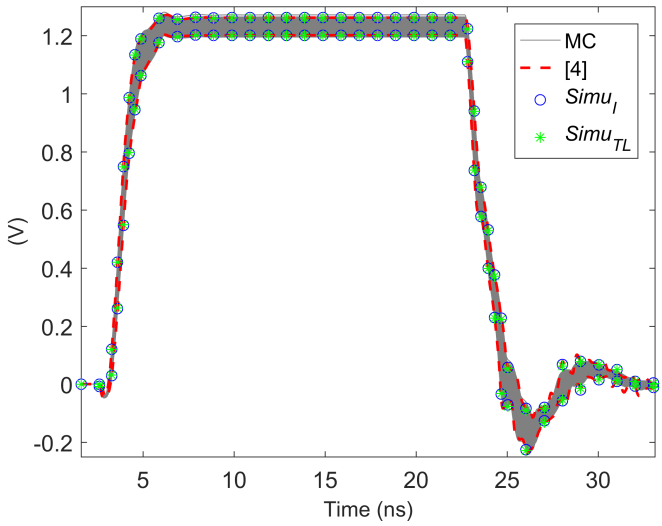

Figure 3.5: Example 3.3.1. Statistical analysis of the output voltage $v_{\rm out}$ in the circuit of Fig. 3.4. The thin gray lines represent 10000 samples from MC analysis; the dashed red lines, and markers $\circ$, $*$ represent the 0.05%–99.95% quantiles obtained with the technique in [4], $Simu_I$, and $Simu_{TL}$, respectively.

analysis, which give a qualitative overview of the spread due to the variability. The dashed red lines and markers $\circ$, $*$ indicate the 0.05% and 99.95% quantiles estimated with the technique in [4], $Simu_I$ and $Simu_{TL}$, respectively.

The PDF and CDF can also be obtained from the PC results. For example, Fig. 3.6 shows the PDF and CDF of the output voltage at the time instant $t = 23.08$ ns, obtained by means of the MC method, as well as with $Simu_I$ and $Simu_{TL}$. The good agreement between these techniques demonstrates the accuracy and flexibility of the proposed approach. It is interesting to note that these results are obtained by using PC models of the same order as for the technique in [4], which relies however on a PC expansion of the transmission-line RLGC parameters rather than of the scattering parameters.

The simulation of 10000 MC samples for the circuit under study required 41248 s, while $Simu_I$, $Simu_{TL}$, and the technique in [4] required 139 s, 91 s, and 45 s, respectively. Hence, the new technique offers a great efficiency with respect to the MC analysis, achieving a speed-up factor of 297$\times$ ($Simu_I$) and 453$\times$ ($Simu_{TL}$). This not only demonstrates the flexibility of the proposed technique, but also shows an alternative and more efficient way to deal with complex systems by modeling their stochastic subnetworks.

On the other hand, it should be noted that the technique in [4] offers an even su-

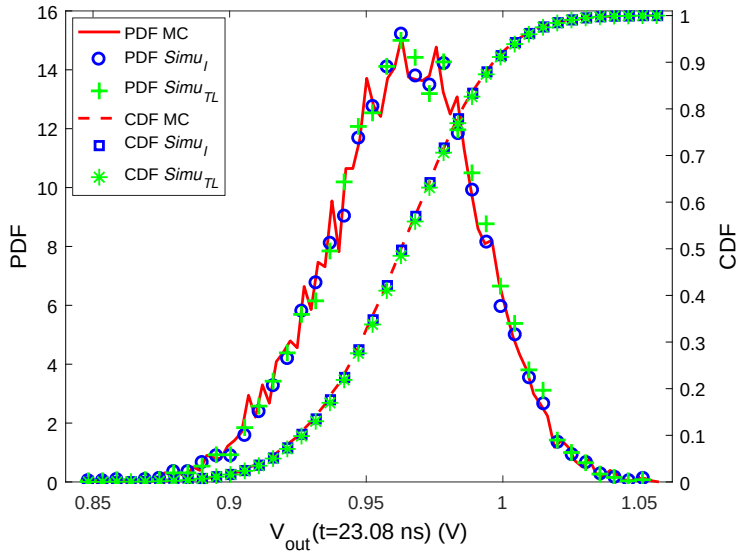

Figure 3.6: Example 3.3.1. PDF and CDF of the output voltage. The solid line, and markers $\circ$, $+$ represent the PDF calculated with the MC method, $Simu_I$, and $Simu_{TL}$, respectively; the dashed line and markers $\square$, $*$ represent the CDF calculated from the MC, $Simu_I$, and $Simu_{TL}$, respectively.

perior efficiency because it directly models the RLGC parameters of the transmission lines. It is well known that VF is not very efficient for modeling electrically-long interconnects, which may lead to an increase of the model complexity with consequent reduction of simulation efficiency as the interconnect length and/or port number is increased. Hence, a lower computational efficiency is to be expected when simulating a network that consists of circuit components only. Nevertheless, as already mentioned, the proposed approach has the considerable advantage of being more general and applicable to any passive linear system, since it is based on a scattering representation.

3.3.2 Nonuniform differential line

Coupled microstrip lines are widely used in modern high-speed digital circuits to transmit differential signals across boards, with higher EM immunity against conducted and radiated noise, lower interference and lower crosstalk. When using such differential line circuits, it is important to minimize the risk of differential-to-common mode conversion. However, layout constraints due to large-scale integration and miniaturization often make line bends unavoidable, which gives rise to such a mode conversion, and lead to a reduction in the spacing between the lines,

which can exacerbate the impact of manufacturing variations, possibly leading to severe signal degradation. Therefore, it is important to quantify the effects of geometrical parameter variations on the SI in the early-stage design of the system.

As an example, the differential microstrip interconnect illustrated in Fig. 3.7 is analyzed in this section. The line exhibits a larger spacing between the traces at the terminal sections, which is reduced in the central part to achieve lower area occupation and lower mode conversion [21], and a 90-degree bend in the middle. As shown in Fig. 3.8, this nonuniform coupled line is differentially driven at the input ports, and it is terminated with clamp diodes to limit voltage over- and undershoots at the receiver side. The driver is implemented using behavioral macromodels of a Texas Instruments transceiver (model name SN74ALVCH16973, power supply voltage $V_{DD} = 2.5$ V). It produces a pseudo-random sequence of 1000 bits, with a bit time of 3 ns and a Gaussian jitter having a standard deviation of 0.15 ns. The diodes have saturation current $I_S = 50$ pA, series resitance $R_S = 1\,\Omega$ and junction capacitance $C_{JO} = 1$ pF.

The values of the geometrical and electrical parameters of the microstrip line are shown in Fig. 3.7. In addition, the trace widths w_1 and w_2 are assumed to be independent Gaussian random variables, having a nominal value 0.625 mm and a relative standard deviation of 5%. It is important to note that, since this interconnection must be studied by means of full-wave electromagnetic simulators and is terminated with nonlinear devices, its stochastic analysis cannot be addressed by previously proposed techniques.

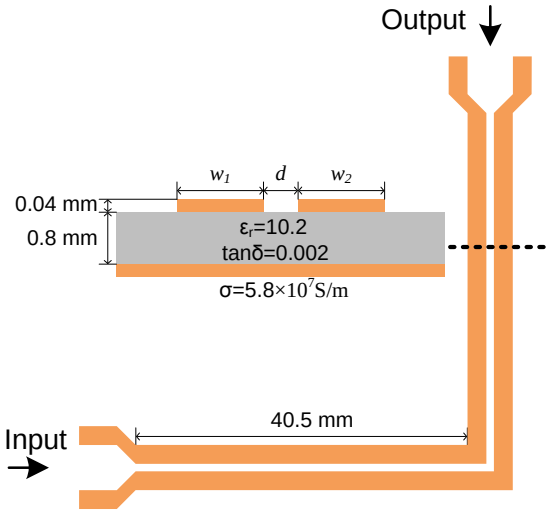

Figure 3.7: Example 3.3.2. Layout and cross-section of the bent microstrip differential line.

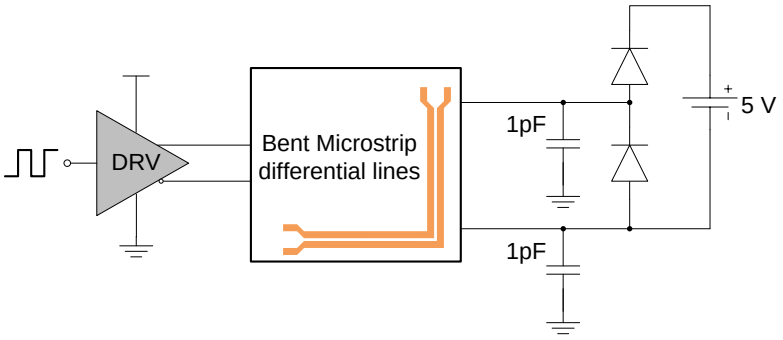

Figure 3.8: Example 3.3.2. Schematic of the complete differential link with driver and terminations.

The scattering matrices of the differential microstrip line are evaluated in ADS[1] at 152 frequency points in the frequency range [0 - 5] GHz: half of them is used to build the desired model, the rest is used for validation. By following the procedure described in Section 3.2.1, the augmented $\boldsymbol{S}_{PC}$ matrix is computed for each frequency sample starting from a PC expansion of order two, leading to six PC basis functions. Next, the equivalent state-space model is computed by means of the VF algorithm and then synthesized into a SPICE-compatible equivalent circuit. This equivalent circuit is complemented with the models for the driver and terminations, which are properly interconnected as discussed in Section 3.2.

At this point, one transient SPICE simulation allows the designer to estimate the PC coefficients of the port signals, from which stochastic information pertaining the common and differential mode voltages are readily calculated.

A similar strategy is also adopted to run the comparative MC analysis. The scattering parameters of the stochastic system are evaluated for 10000 samples of the two random parameters w_1, w_2. For each sample, a stable and passive model is obtained by means of VF and then, via the same synthesis technique [17], converted into an equivalent circuit that is simulated in SPICE.

Figure 3.9 shows the probability of the common mode voltage levels, arising from both the mismatch in line length between the two traces [21] and the asymmetry introduced by the stochastic variations of the cross-sectional geometry [22], over a two-bit span resulting from the superposition of 10000 MC simulations for the entire 1000-bit input stream. The results from MC and PC-based analysis, the latter obtained by inexpensive sampling of the PC expansion (3.1), are compared side by side showing again excellent qualitative agreement.

Another important analysis for SI investigation is the prediction of the eye diagram. Fig. 3.10 shows the eye diagram of the output differential mode (DM) volt-

[1] Advanced Design System (ADS), Keysight Technologies, Santa Rosa, CA.

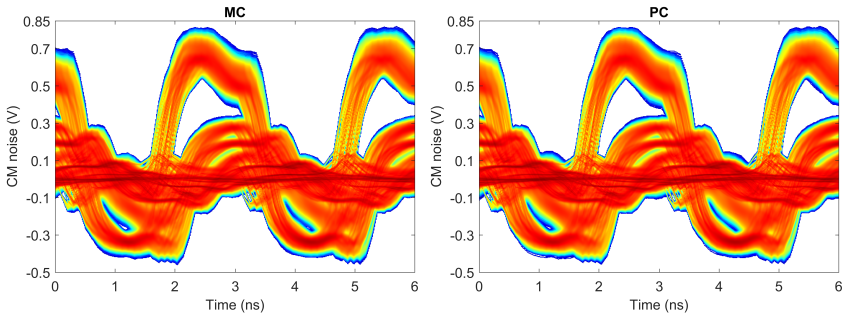

Figure 3.9: Example 3.3.2. Probability of common mode (CM) voltage levels in a two-bit time window calculated from the results of MC (left) and PC-based (right) analyses.

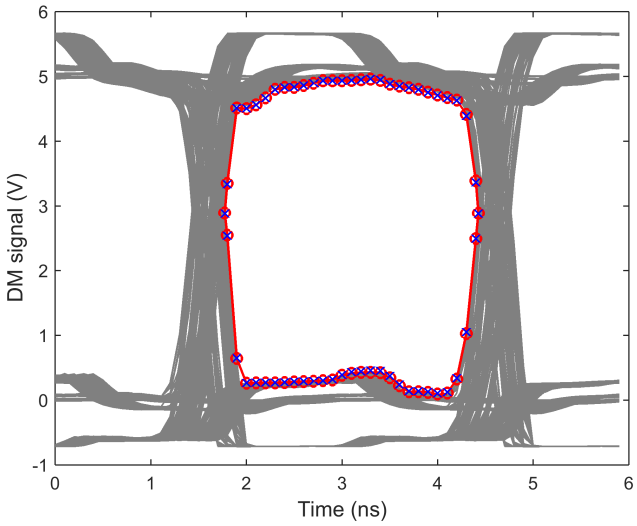

Figure 3.10: Example 3.3.2. Eye diagram of the differential model (DM) signal with inclusion of the eye opening profile computed with a 99% confidence level. Markers $\times$ and $\circ$ indicate the mask obtained from the MC samples and via the proposed technique, respectively.

age for 10000 MC simulations of the bitstream transmission. In addition, markers $\times, \circ$ indicate the profile of the eye opening calculated with a 99% confidence level, which means there is a 1% probability that the stochastic differential mode response lies inside this mask.

Finally, Fig. 3.11 shows the probability distribution of the differential mode voltage obtained from both the MC (left panel) and PC (right panel) results, whereas Fig. 3.12 compares the PDF and CDF of the eye height calculated with the two

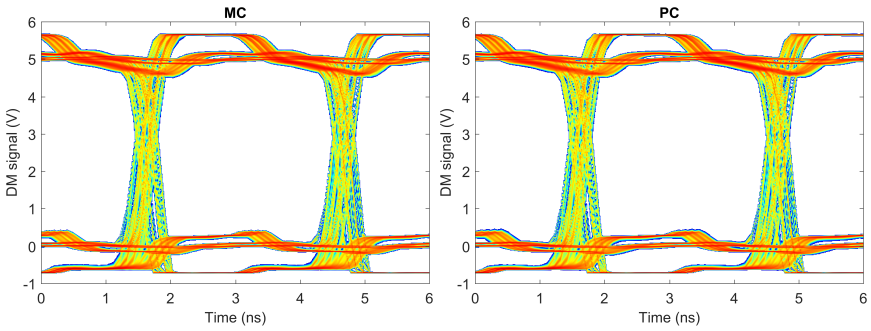

Figure 3.11: Example 3.3.2. Probability of differential mode (DM) voltage levels calculated from the results of MC (left) and PC-based (right) analyses.

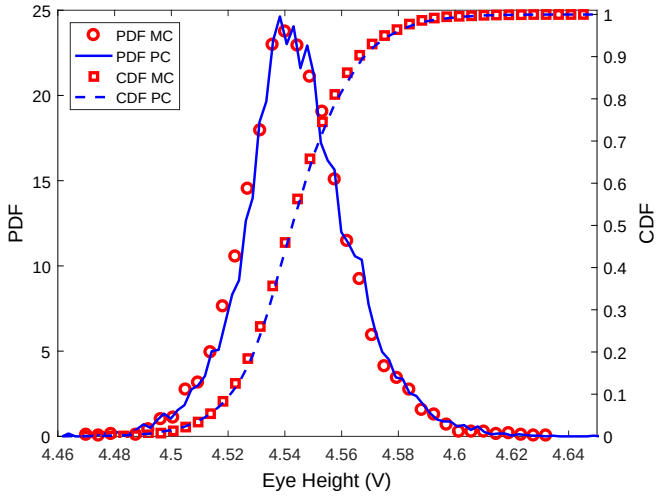

Figure 3.12: Example 3.3.2. PDF (full line) and CDF (dashed line) of the eye height computed using the new proposed technique. Markers ○ and □ indicate the same quantities computed with the MC method.

methods. An excellent agreement between MC and the proposed PC-based technique is once again established.

As far as the computational times are concerned, the MC analysis based on 10000 samples required 5 d 19 h 44 m for the S-parameter extractions, 1 h 1 m for 10000 circuit models building and 22 d 14 h 49 m for the time-domain simulations. In contrast, the new proposed technique required 20 m 58 s, 9.4 s and 1 h 21 m for these three phases, respectively, thus achieving a speed-up of about 400× for each phase.

3.4 Conclusion

The efficient stochastic SI analysis of complex circuits including both passive linear subnetworks and nonlinear components is addressed in this chapter. The proposed framework is based on representing the stochastic port voltages and currents of each component or subsystem as PC expansions. Deterministic augmented models are computed that describe the relationship between the pertinent PC coefficients. Such augmented models are synthesized into equivalent circuits, which are properly interconnected and solved with a single SPICE simulation to retrieve the time-domain behavior of the PC coefficients. From these PC coefficients, relevant statistical information about SI is obtained. The proposed method is modular and applicable to a broad range of systems composed by different elements (lumped, distributed, passive and active ones), thereby significantly expanding the scope of applicability of existing PC-based techniques. The accuracy, efficiency and flexibility of the modeling framework are illustrated by means of relevant numerical examples concerning SI investigations of digital interconnects.

References

[1] D. Xiu and G. M. Karniadakis. *The Wiener-Askey Polynomial Chaos for Stochastic Differential Equations*. SIAM J. Sci. Comput., 24(2):619–644, Apr. 2002.

[2] M. S. Eldred. *Recent advances in non-intrusive polynomial-chaos and stochastic collocation methods for uncertainty analysis and design*. In Proc. 50th AIAA/ASME/ASCE/AHS/ASC Struct., Structural Dynam., Mat. Conf., AIAA-2009-2274, Palm Springs, California, May 2009.

[3] K. Strunz and Q. Su. *Stochastic Formulation of SPICE-type Electronic Circuit Simulation with Polynomial Chaos*. ACM Trans. Model. Comput. Simul., 18(4):15:1–15:23, Sep. 2008.

[4] P. Manfredi, D. Vande Ginste, D. De Zutter, and F. G. Canavero. *Uncertainty Assessment of Lossy and Dispersive Lines in SPICE-Type Environments*. IEEE Trans. Compon., Packag., Manuf. Technol., 3(7):1252–1258, Jul. 2013.

[5] X. Chen, J. E. Schutt-Aine, and A. C. Cangellaris. *Stochastic LIM for Transient Simulations of Printed Circuit Board Transmission Lines with Uncertainties*. In Proc. IEEE 64th Electron. Compon. Technol. Conf., pages 2297–2304, Las Vegas, USA, May 2016.

[6] D. Spina, F. Ferranti, G. Antonini, T. Dhaene and L. Knockaert. *Efficient Variability Analysis of Electromagnetic Systems Via Polynomial Chaos and Model Order Reduction*. IEEE Trans. Compon., Packag., Manuf. Technol., 4(6):1038–1051, Jun. 2014.

[7] D. Spina, F. Ferranti, T. Dhaene, L. Knockaert, and G. Antonini. *Polynomial chaos-based macromodeling of multiport systems using an input-output approach*. Int. J. Numer. Model., 28(5):562–581, Sep./Oct. 2015.

[8] D. Spina, T. Dhaene, L. Knockaert and G. Antonini. *Polynomial Chaos-Based Macromodeling of General Linear Multiport Systems for Time-Domain Analysis*. IEEE Trans. Microw. Theory Techn., 65(5):1422–1433, May 2017.

[9] Z. Zhang, T. A. El-Moselhy, I. M. Elfadel and L. Daniel. *Stochastic Testing Method for Transistor-Level Uncertainty Quantification Based on Generalized Polynomial Chaos*. IEEE Trans. Comput.-Aided Design Integr. Circuits Syst, 32(10):1533–1545, Oct. 2013.

[10] P. Manfredi, D. Vande Ginste, D. De Zutter, and F. G. Canavero. *Stochastic Modeling of Nonlinear Circuits via SPICE-Compatible Spectral Equivalents*. IEEE Trans. Circuits Syst. I, 61(7):2057–2065, Jul. 2014.

[11] M. R. Rufuie, E. Gad, M. Nakhla and R. Achar. *Generalized Hermite Polynomial Chaos for Variability Analysis of Macromodels Embedded in Nonlinear Circuits*. IEEE Trans. Compon., Packag., Manuf. Technol., 4(4):673–684, Apr. 2014.

[12] Z. Zhang, T. A. El-Moselhy, I. M. Elfadel and L. Daniel. *Calculation of Generalized Polynomial-Chaos Basis Functions and Gauss Quadrature Rules in Hierarchical Uncertainty Quantification*. IEEE Trans. Comput.-Aided Design Integr. Circuits Syst, 33(5):728–740, May 2014.

[13] P. Manfredi and F. G. Canavero. *Efficient statistical simulation of microwave devices via stochastic testing-based circuit equivalents of nonlinear components*. IEEE Trans. Microw. Theory Techn., 63(5):1502–1511, May 2015.

[14] P. Manfredi, D. Vande Ginste, D. De Zutter, and F. G. Canavero. *Generalized Decoupled Polynomial Chaos for Nonlinear Circuits With Many Random Parameters*. IEEE Microw. Wireless Compon. Lett., 25(8):505–507, Aug. 2015.

[15] B. Gustavsen and A. Semlyen. *Rational approximation of frequency domain responses by Vector Fitting*. IEEE Trans. Power Del., 14(3):1052–1061, Jul. 1999.

[16] D. Deschrijver, and T. Dhaene. *Fast Passivity Enforcement of S-Parameter Macromodels by Pole Perturbation*. IEEE Trans. Microw. Theory Techn., 57(3):620–626, Mar. 2009.

[17] R. Neumayer, F. Haslinger, A. Stelzer and R. Weigel. *Synthesis of SPICE-compatible broadband electrical models from n-port scattering parameter data*. In Proc. IEEE Int. Symp. on Electromagnetic Compatibility (EMC), Minneapolis, USA, Aug. 2002.

[18] I. S. Stievano, I. A. Maio, and F. G. Canavero. *Mπlog, macromodeling via parametric identification of logic gates*. IEEE Trans. Adv. Packag., 27(1):15–23, Feb. 2004.

[19] G. Signorini, C. Siviero, S. Grivet-Talocia, and I. S. Stievano. *Macromodeling of I/O Buffers via Compressed Tensor Representations and Rational Approximations*. IEEE Trans. Compon., Packag., Manuf. Technol., 6(10):1522–1534, Oct. 2016.

[20] G. Signorini, C. Siviero, M. Telescu, and I. S. Stievano. *Present and future of I/O-buffer behavioral macromodels*. IEEE Electrmagn. Compat., 5(3):79–85, Third Quarter 2016.

[21] C. Gazda, D. Vande Ginste, H. Rogier, R. B. Wu, and D. De Zutter. *A Wideband Common-Mode Suppression Filter for Bend Discontinuities in Differential Signaling Using Tightly Coupled Microstrips*. IEEE Trans. Adv. Packag., 33(4):969–978, Nov. 2010.

[22] F. Grassi, Y. Yang, X. Wu, G. Spadacini, and S. A. Pignari. *On Mode Conversion in Geometrically Unbalanced Differential Lines and Its Analogy With Crosstalk*. IEEE Trans. Electromagn. Compat., 57(2):283–291, Apr. 2015.

4

Vector Fitting-Based Baseband Modeling of Linear Photonic Circuits

Y. Ye, D. Spina, Y. Xing, W. Bogaerts, and T. Dhaene, "Numerical modeling of linear photonic systems for accurate and efficient time-domain simulations," Photonics Research, vol. 6, no. 6, pp. 560-573, Jun. 2018.

Y. Ye, D. Spina, W. Bogaerts, and T. Dhaene, "Baseband modeling of linear photonic circuits for time-domain simulations," Journal of Lightwave Technology, vol. 37, no. 4, pp. 1364-1373, Feb. 2019.

Abstract

In this chapter, a novel modeling and simulation method for general linear, time-invariant, passive photonic devices and circuits is proposed. This technique, starting from the scattering parameters of the photonic system under study, builds a baseband equivalent state-space model which splits the optical carrier frequency and operates at baseband, thereby significantly reducing the modeling and simulation complexity without losing accuracy. Indeed, it is possible to analytically reconstruct the port signals of the photonic system under study starting from the time-domain simulation of the corresponding baseband equivalent model. However, such equivalent models are complex-valued systems and, in this scenario, the conventional passivity constraints are not applicable anymore. Hence, the passivity

constraints for scattering parameters and state-space models of baseband equivalent systems are presented, which are essential for time-domain simulations. Furthermore, the built complex-valued baseband models can be analytically converted to real-valued ones, which preserve all the properties of physical systems and can be simulated in a variety of solvers. Several suitable examples demonstrate the feasibility, accuracy and efficiency of the proposed method.

4.1 Introduction

Over the last decade, *photonic integrated circuits* (PICs), and especially *silicon photonics*, gained a lot of popularity due to their compatibility with the manufacturing processes used in the CMOS industry. Given the rapid development of PICs in terms of complexity and integration scale, *photonic design automation* (PDA) tools for photonic circuit simulations, and photonic-electronic co-simulation [1–4], become of paramount importance.

In this framework, it is fundamental to build compact models which can accurately and efficiently mimic the behavior of photonic devices and circuits, for both frequency-domain and time-domain simulations. In our work, we focus on the modeling of linear passive devices and systems whose functions roughly fall into two categories: distributing/transporting light (e.g. waveguides), and optical wavelength filtering for applications such as spectroscopy, *wavelength division multiplexing* (WDM) or *microwave photonics* (MWP) applications. Especially in the last two applications, an efficient modeling approach of the filters, which is able to take into account imperfections such as higher-order dispersion, wavelength-dependent loss, and imperfections in coupling coefficients, is urgently needed.

A common approach is to compute analytic models, which rely on the knowledge of the working principles of the device under study. Such models are useful in the design phase, because the geometrical or optical parameters (such as length, coupling coefficient, effective index, etc.) are directly related to the performance measures of the device considered. However, in practice, analytic models can be derived only for simple photonic systems and there is a limit in their accuracy when describing complex non-ideal characteristics of the system under study (i.e. backscattering and dispersion effects). Furthermore, most of these models are generally described as frequency- (wavelength) domain models, whereas time-domain models are needed when time-domain simulations are required to evaluate the performance of the PICs, such as bit error rate and eye diagrams [1, 3].

In practice, for passive devices and circuits, their scattering parameters data are more accessible (e.g. via electromagnetic simulations or measurements) than accurate analytic models. Hence, it is convenient to conduct time-domain simulations starting from the scattering parameters. A typical example is given by the *finite impulse response* (FIR) modeling technique [5], which is based on the scat-

tering parameters representation and is adopted in the dedicated photonic simulators Lumerical INTERCONNECT [6], VPIphotonics [7] and PICWave [8]. The accuracy provided by FIR filters substantially depends on the design methodology employed and it inherently degrades near the edges of the simulated signal bands [5].

In the electronic field, a popular compact modeling approach for distributed devices, such as nonuniform transmission lines or microstrip filters, leverages on a frequency-domain system identification technique named *vector fitting* (VF) algorithm [9], which is able to build stable and passive rational models of the scattering parameters of the devices under study. Then, these frequency-domain models can be directly converted to an equivalent state-space representation in the time domain. This technique is widely applied to electronic systems, for example in [9–14].

Since the VF method is developed for linear, time-invariant, passive systems and is based on their transfer function representation (e.g. scattering parameters), it is immediately applicable to passive photonic devices and circuits [15]. However, compared to electronic systems, the frequency range of interest for photonic systems is typically around $[187.5;\ 200]$ THz, corresponding to a wavelength of $[1.5;\ 1.6]$ μm, commonly used for telecommunication applications. Such a wide range at high frequencies has a direct impact on the modeling and simulation processes, which can become very time and/or memory consuming.

To address this problem, a novel modeling method is proposed in this chapter, which is based on baseband equivalent signal and system representation. In particular, the proposed modeling approach computes an accurate baseband equivalent state-space representation, starting from the scattering parameters of the photonic system under study evaluated at optical frequencies. However, such equivalent state-space model is complex-valued, and not physically realizable. Furthermore, the stability and passivity constraints on scattering parameters and state-space models of complex-valued systems, which are fundamental properties for time-domain simulations, appear yet to be missing in literature. In this work, we rigorously discuss these conditions for the proposed baseband equivalent systems based on the classic definitions of stability and passivity to validate the feasibility of the proposed time-domain simulation method. The proposed technique offers two main advantages: 1) the modeling process is based on the scattering parameters, which makes it a widely applicable method for generic linear passive photonic components and circuits; 2) the state-space representation is a continuous time-domain model, which can be efficiently simulated in the time domain without involving convolution, *fast Fourier transform* (FFT), or *inverse fast Fourier transform* (IFFT), thereby making this method robust and accurate.

The remainder of this chapter is organized as follows: Section 4.2 presents an overview of the "standard" modeling approach based on the VF algorithm, while

Section 4.3 introduces the baseband equivalent signals and systems and describes the novel proposed modeling framework. The stability and passivity constraints of such systems are discussed in Section 4.4. A practical guideline for the application of the proposed modeling approach is given in Section 4.5 while Section 4.6 validates the proposed method by means of three pertinent numerical examples. Then, Section 4.7 extends the applicable range of the proposed technique and the real-valued baseband model is derived in Section 4.8. Finally, Section 4.9 presents two suitable examples validating the accuracy and efficiency of the real-valued baseband modeling technique, and conclusions are drawn in Section 4.10.

4.2 Conventional state-space modeling of photonic systems

In both electronics and photonics, the scattering matrix is widely used to describe the behaviors of passive devices and circuits:

$$\boldsymbol{b}(s) = \boldsymbol{S}(s)\boldsymbol{a}(s) \tag{4.1}$$

where s is the Laplace variable, $\boldsymbol{a}(s)$ and $\boldsymbol{b}(s)$ are the forward wave and backward wave, respectively, and $\boldsymbol{S}(s)$ is the scattering matrix of the system under study, which can be obtained through simulations or measurements. The aim of the rational modeling is to find a Laplace-domain model of (4.1) in a pole-residue form as

$$\boldsymbol{S}(s) = \sum_{k=1}^{K} \frac{\boldsymbol{R_k}}{s - p_k} + \boldsymbol{D} \tag{4.2}$$

where $\boldsymbol{D} \in \mathbb{R}^{n\times n}, \boldsymbol{R}_k \in \mathbb{C}^{n\times n}, k = 1, \cdots, K$, n and K being the number of ports of the system under study and the number of poles used to approximate the scattering parameters, respectively. Typically, all the elements $S_{ij}(s)$ of the scattering matrix representation (4.2) use a common denominator polynomial and pole-set $[p_1, p_2, \cdots, p_K]$, where such poles are either real quantities or complex conjugate pairs [9]. The identification of poles p_k and residue matrices $\boldsymbol{R}_k$ can be performed via the VF algorithm [9, 16–19], starting from a set of the scattering parameters under study obtained for $s_r = j2\pi f_r$ with $r = 1, \ldots, R$. It is important to remark that the model (4.2) can be considered as a black-box model and its poles do not necessarily represent the physical poles of the system under study.

However, it is important to note that the sign convention e^{jwt} is commonly used in the electronics field to represent the incident and reflected waves in (4.1), while e^{-jwt} is sometimes adopted in the optics field [20, 21]. Hence, the scattering matrix defined with one sign convention is the complex conjugate of the other. The VF algorithm is based on the assumption that the sign convention e^{jwt} is adopted, since it has been originally developed for electromagnetic problems. In case e^{-jwt}

is used to define the scattering parameters under study, a simple solution is to apply the VF algorithm to the complex conjugate of the scattering matrix.

Then, the rational model (4.2) can be transformed to state-space form by a simple rearrangement [18, 22]

$$\boldsymbol{S}(s) = \boldsymbol{C}(s\boldsymbol{I}_m - \boldsymbol{A})^{-1}\boldsymbol{B} + \boldsymbol{D} \tag{4.3}$$

where $\boldsymbol{A} \in \mathbb{C}^{m\times m}$, $\boldsymbol{B} \in \mathbb{R}^{m\times n}$, $\boldsymbol{C} \in \mathbb{C}^{n\times m}$, $\boldsymbol{D} \in \mathbb{R}^{n\times n}$, $m = nK$ and $\boldsymbol{I}_m$ is the identity matrix of size $m \times m$ in this chapter. In particular, $\boldsymbol{A}$ is a diagonal matrix with all the poles as diagonal elements while $\boldsymbol{C}$ contains all the residues, and they can be always converted to real matrices as long as the poles and residues are real or complex conjugate pairs [18].

Now, it is straightforward to convert (4.3) to an equivalent state-space representation in the time domain [22] as

$$\begin{cases} \dfrac{\mathrm{d}\boldsymbol{x}(t)}{\mathrm{d}t} = & \boldsymbol{A}\boldsymbol{x}(t) + \boldsymbol{B}\boldsymbol{a}(t) \\ \boldsymbol{b}(t) = & \boldsymbol{C}\boldsymbol{x}(t) + \boldsymbol{D}\boldsymbol{a}(t) \end{cases} \tag{4.4}$$

where $\boldsymbol{x}(t) \in \mathbb{R}^{m\times 1}$ is the state vector.

Note that, fundamental properties for time-domain simulations such as the stability and passivity of models in the form (4.4) must be assured [14]. While the stability of VF models can be guaranteed by construction by means of suitable pole flipping schemes [9], their passivity can be checked and, eventually, enforced only after the rational model is computed by adopting passivity enforcement techniques. Indeed, due to the unavoidable numerical approximations, the rational model computed might be non-passive. Several robust passivity enforcement methods have been proposed in the literature, see for example [17–19]. Now, time-domain simulations can be carried out by solving the system of first-order *ordinary differential equations* (ODE) (4.4) via suitable numerical techniques [23, 24]. These approaches iteratively solve (4.4) for a discrete set of values of the time, which are chosen via suitable algorithms (i.e. fixed or adaptive time-step). In particular, the computational cost of solving (4.4) depends on three main elements:

- the bandwidth of the signals considered, which define the maximum time-step Δt_{max} that can be adopted: Δt_{max} must be smaller than the highest frequency component of the signals considered;
- the numerical technique adopted to solve (4.4);
- the number of poles K and of ports n of the system under study, which directly determine the number of states $m = nK$.

The modeling technique described so far allows one to simulate any generic linear and passive system in the time or frequency domain and it has found extensive applications in the electronic engineering problems [9–14]. However, when it

comes to photonic circuits one substantial difference arise with respect to the electronic domain: the range of frequency of interest is, for example, typically around $[187.5;\ 200]$ THz, corresponding to a wavelength of $[1.5;\ 1.6]$ μm, or even higher frequencies for shorter wavelengths. This has a major impact on the modeling and simulation complexity of the approach described so far. Indeed, a high number of poles K can be required to accurately model the scattering parameters in the chosen frequency range and the passivity enforcement phase can become computationally prohibitive. Furthermore, the corresponding ODE (4.4) will have a high number of equations and a small time-step (of the order of femtoseconds) must be adopted to solve it.

In order to tackle these issues, a novel approach based on baseband equivalent state-space models is proposed in this contribution, which can be applied to either a large or relatively small modeling frequency range for time-domain simulations.

4.3 Baseband equivalent state-space models for time-domain simulation of photonic systems

The basic concepts of baseband equivalent signals and systems are first introduced in Section 4.3.1, given their importance in the definition of the proposed modeling approach, which is described in Section 4.3.2.

4.3.1 Baseband equivalent signals and systems

The excitation signal of photonic systems is often an amplitude and/or phase modulated signal with optical carrier and electronic modulating signals, which can be written in the following form

$$u(t) = A(t)\cos(2\pi f_c t + \phi(t)) \tag{4.5}$$

where $A(t)$ is the time-varying amplitude or envelope of the modulated signal, and $\phi(t)$ is the time-varying phase. In electronics or *radio-frequency* (RF) applications, both $A(t)$ and $\phi(t)$ relate to electronic signals, such as voltage, current or electric field. In photonics, the optical carrier frequency f_c is much higher than the bandwidth of $A(t)$ and $\phi(t)$, given that the wavelength of light is much smaller than the one of RF signals, so the representation (4.5) is often called a *bandpass signal*.

An analytic complex-valued representation of the real-valued signal (4.5), called *analytic signal*, is introduced here as [25]

$$u_a(t) = u(t) + j\mathcal{H}(u(t)) = A(t)e^{j(2\pi f_c t + \phi(t))} \tag{4.6}$$

where $\mathcal{H}(u(t))$ is the Hilbert transform of $u(t)$. In the frequency-domain equation (4.6) becomes

$$U_a(f) = 2U(f)Step(f) \tag{4.7}$$

where $U_a(f)$ and $U(f)$ are the Fourier transform of $u_a(t)$ and $u(t)$, respectively, and $Step(f)$ is a unit step function defined by

$$Step(f) = \begin{cases} 1, f > 0 \\ \frac{1}{2}, f = 0 \\ 0, f < 0 \end{cases} \tag{4.8}$$

Now, the corresponding *baseband equivalent signal* of the bandpass signal is defined as

$$u_l(t) = u_a(t)e^{-j2\pi f_c t} = A(t)e^{j\phi(t)} \tag{4.9}$$

$$U_l(f) = 2U(f + f_c)Step(f + f_c) \tag{4.10}$$

which can be considered as the complex envelope optical signal representation and is widely used in photonics and optical fiber communication. The relations between $u(t)$, $\mathcal{H}(u(t))$ and $u_l(t)$ in the time- and frequency-domain are [25]

$$u(t) = \Re[u_l(t)e^{j2\pi f_c t}] \tag{4.11}$$

$$\mathcal{H}(u(t)) = \Im[u_l(t)e^{j2\pi f_c t}] \tag{4.12}$$

$$U(f) = \frac{1}{2}U_l^*(-f - f_c) + \frac{1}{2}U_l(f - f_c) \tag{4.13}$$

where the superscript * denotes complex conjugate operator while $\Re$ and $\Im$ stand for real and imaginary parts, respectively.

In the frequency domain, the concepts of analytic signal and baseband equivalent signal are intuitive: $U(f)$ has a symmetric spectrum with respect to the positive and negative frequencies, while $U_a(f)$ has only a non-zero spectrum in the positive frequencies around the carrier frequency; by shifting the spectrum of $U_a(f)$ in the direction of the negative frequencies of f_c (or equivalently in the time domain by multiplying $u_a(t)$ with $e^{-j2\pi f_c t}$) leads to $U_l(f)$. Such relations are illustrated in Fig. 4.1.

If a system with impulse response $h(t)$ and frequency response $H(f)$ operates in the bandwidth BW around f_c satisfying $f_c >> BW$, then it can be considered as a bandpass system. Now, the corresponding *baseband equivalent system* can be defined by applying the same concepts described for the baseband signals. Thanks to the relations among bandpass signals and systems, and their baseband equivalents, it can be proven that the output signal of a bandpass system can be

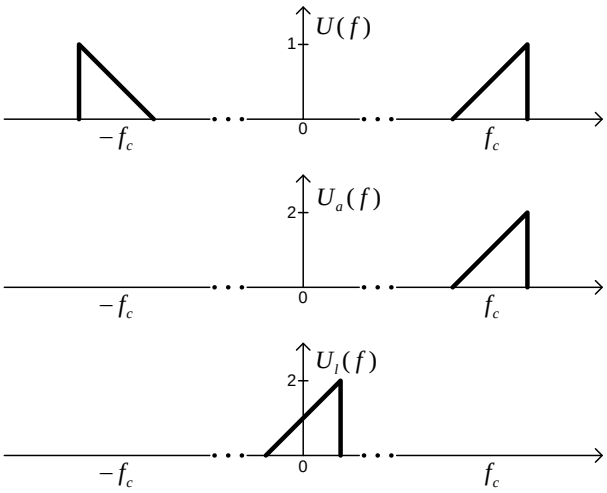

Figure 4.1: Spectrum of bandpass signal $U(f)$, analytic signal $U_a(f)$, and baseband equivalent signal $U_l(f)$.

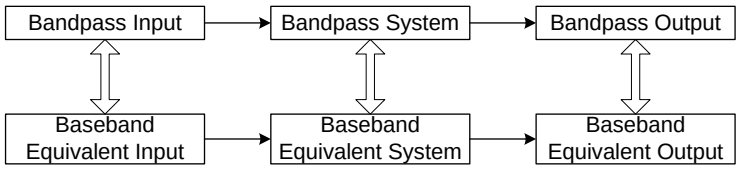

Figure 4.2: Time-domain simulation of bandpass system and baseband equivalent system.

analytically recovered from the output of the corresponding baseband system, as illustrated in Fig. 4.2. A detailed proof is given in Appendix 4.11.1.

It is important to remark that performing time-domain simulations of baseband equivalent systems allows one to efficiently recover the corresponding bandpass signals, thus avoiding expensive time-domain simulations of photonic system at optical frequencies.

4.3.2 Realization of baseband equivalent signals and systems

Baseband equivalent signals $u_l(t)$ can be easily computed with (4.9), where $u_l(t)$ can be a real (amplitude modulation) or a complex signal (when both amplitude and phase modulation are applied). For example, in case of a *quadrature amplitude modulation* (QAM), $u_l(t)$ can be expressed with respect to its in-phase component $I(t) = A(t)\cos\phi(t)$ and quadrature component $Q(t) = A(t)\sin\phi(t)$, as $u_l(t) = I(t) + jQ(t)$.

Note that, baseband equivalent signals and systems are widely used in the sim-

ulation of communication systems to simplify the modulation, demodulation and filtering process [25]. In such a scenario, continuous systems and signals are often first sampled and defined as finite discrete sequences, and then convolution, FFT, or IFFT are adopted for the time-domain simulation of the discrete-time representations of such signals and systems, which could lead to inaccurate results [5].

In this section, the goal is to build stable and passive continuous models for baseband equivalent systems in state-space form, whose time-domain simulation can also capture transient behaviors. However, a readily baseband counterpart for (4.4) does not exist in literature. Indeed, baseband systems have an *asymmetric* frequency response with respect to the positive and negative frequencies (similar to $U_l(f)$ in Fig. 4.1) resulting in a non-physical, complex-valued system, as described in details in Appendix 4.11.1. The VF algorithm [9] is a technique developed for physical systems with a symmetric frequency response, which can be described with real or complex conjugate poles: this situation clearly does not hold for baseband systems and VF cannot be directly applied to the baseband response of the system under study.

In order to reach our goal, the first step is to express $\boldsymbol{a}(t)$, $\boldsymbol{b}(t)$ and $\boldsymbol{x}(t)$ in the system of ODE (4.4) in the form (4.11), which gives

$$\begin{cases} \Re\dfrac{\mathrm{d}\boldsymbol{x_l}(t)e^{j2\pi f_c t}}{\mathrm{d}t} = \boldsymbol{A}\Re[\boldsymbol{x_l}(t)e^{j2\pi f_c t}] + \boldsymbol{B}\Re[\boldsymbol{a_l}(t)e^{j2\pi f_c t}] \\ \Re[\boldsymbol{b_l}(t)e^{j2\pi f_c t}] = \boldsymbol{C}\Re[\boldsymbol{x_l}(t)e^{j2\pi f_c t}] + \boldsymbol{D}\Re[\boldsymbol{a_l}(t)e^{j2\pi f_c t}] \end{cases} \tag{4.14}$$

where $\boldsymbol{a_l}(t)$, $\boldsymbol{b_l}(t)$, and $\boldsymbol{x_l}(t)$ are the baseband equivalents of $\boldsymbol{a}(t)$, $\boldsymbol{b}(t)$, and $\boldsymbol{x}(t)$, respectively. Next, by using the Hilbert transform and the relation (4.12) to represent $\boldsymbol{a}(t)$, $\boldsymbol{b}(t)$ and $\boldsymbol{x}(t)$ in equation (4.4) leads to

$$\begin{cases} \Im\dfrac{\mathrm{d}\boldsymbol{x_l}(t)e^{j2\pi f_c t}}{\mathrm{d}t} = \boldsymbol{A}\Im[\boldsymbol{x_l}(t)e^{j2\pi f_c t}] + \boldsymbol{B}\Im[\boldsymbol{a_l}(t)e^{j2\pi f_c t}] \\ \Im[\boldsymbol{b_l}(t)e^{j2\pi f_c t}] = \boldsymbol{C}\Im[\boldsymbol{x_l}(t)e^{j2\pi f_c t}] + \boldsymbol{D}\Im[\boldsymbol{a_l}(t)e^{j2\pi f_c t}] \end{cases} \tag{4.15}$$

Equations (4.14) and (4.15) allow us to write

$$\begin{cases} \dfrac{\mathrm{d}\boldsymbol{x_l}(t)e^{j2\pi f_c t}}{\mathrm{d}t} = \quad \boldsymbol{A}\boldsymbol{x_l}(t)e^{j2\pi f_c t} + \boldsymbol{B}\boldsymbol{a_l}(t)e^{j2\pi f_c t} \\ \boldsymbol{b_l}(t)e^{j2\pi f_c t} = \quad \boldsymbol{C}\boldsymbol{x_l}(t)e^{j2\pi f_c t} + \boldsymbol{D}\boldsymbol{a_l}(t)e^{j2\pi f_c t} \end{cases} \tag{4.16}$$

After simple mathematical manipulations, (4.16) can be written as

$$\begin{cases} \dfrac{\mathrm{d}\boldsymbol{x_l}(t)}{\mathrm{d}t} = (\boldsymbol{A} - j2\pi f_c \boldsymbol{I}_m)\boldsymbol{x_l}(t) + \boldsymbol{B}\boldsymbol{a_l}(t) \\ \boldsymbol{b_l}(t) = \boldsymbol{C}\boldsymbol{x_l}(t) + \boldsymbol{D}\boldsymbol{a_l}(t) \end{cases} \tag{4.17}$$

which represents a realization of the baseband equivalent system by means of the state-space matrices $(\boldsymbol{A} - j2\pi f_c \boldsymbol{I}_m)$, $\boldsymbol{B}$, $\boldsymbol{C}$ and $\boldsymbol{D}$: in this contribution we define

it as *baseband state-space model*. It is evident that such model can be obtained by directly shifting all the poles of the corresponding state-space model (4.4) of bandpass system by $j2\pi f_c$, considering that $\boldsymbol{A}$ is a diagonal complex-valued matrix with all the poles as diagonal elements, as mentioned in Section 4.2.

It is important to remark one difference between the representation (4.17) and the definition of baseband systems: in (4.17) the entire frequency response of the system under study is shifted into baseband, while for the baseband system introduced in Section 4.3.1 only the frequency response at positive frequencies is shifted into baseband. However, in Appendix 4.11.2 it is rigorously proven that these two representation are equivalent in terms of time-domain simulations. Hence, in the rest of the contribution the expression "baseband equivalent system" does not refer to the classic definition given in Section 4.3.1 and Appendix 4.11.1, but to the new proposed baseband equivalent "shifted" system, where the entire frequency response of the system under study is shifted into baseband.

A similar realization of baseband equivalent systems in the frequency domain, computed by shifting the poles of the transfer function of the corresponding bandpass system by $j2\pi f_c$, has been presented in the electronic domain in [25, 26], but the derivation is not given. Note that the time-domain simulation methods in [25, 26] are substantially different from the one presented here. In [25], once the transfer function of the baseband equivalent system is obtained, it is first sampled and converted to an equivalent discrete system, and then the discrete impulse response is calculated via IFFT. Finally, the time-domain behavior of the baseband equivalent system is simulated by convolution. In [26], first the inverse Laplace transform is adopted to analytically convert the baseband equivalent transfer function to a continuous impulse response, then a recursive convolution technique is used to perform time-domain simulations. In contrast, the time-domain simulation method presented in this chapter directly solves the corresponding ODE, which is more straightforward. However, it is crucial to prove that fundamental properties for time-domain simulations, such as stability and passivity [14], still hold for the proposed baseband equivalent state-space representation.

4.4 Passivity of baseband equivalent systems

The poles and residues of rational models of electronic and photonic systems are always real, or complex conjugate pairs as discussed in Section 4.2. However, for the baseband equivalent state-space model (4.17), the poles do not follow this rule anymore; furthermore the corresponding frequency response is not symmetrical with respect to positive and negative frequencies, which makes the baseband equivalent system a non-physical, complex-valued system. Finally, the most remarkable difference with respect to bandpass systems is that the impulse response of these baseband equivalent systems is not real, and with a real input, they can

generate a complex output.

Then, it is important to verify if such linear, time-invariant complex-valued systems still comply with the passivity conditions of "conventional" real-valued systems, which are listed as follows [27]:

1. Each element of $\boldsymbol{S}(s)$ is analytic in $\Re(s) > 0$;
2. $\boldsymbol{I}_n - \boldsymbol{S}^H(s)\boldsymbol{S}(s)$ is a nonnegative-definite matrix for all s such that $\Re(s) > 0$;
3. $\boldsymbol{S}^*(s) = \boldsymbol{S}(s^*)$.

The superscript ^{H} stands for the transpose conjugate operator. The first condition is related to causality and stability; the second one is basically a bound for $\boldsymbol{S}(s)$; the third ensures that the associated impulse response is real, which requires the system to be real-valued [28]. Evidently, the third condition is not suitable for complex-valued systems anymore. In this section, the passivity constraints for scattering parameters of baseband equivalent systems will be proposed, and a fast assessment of the passivity of the corresponding baseband equivalent state-space model will be presented.

4.4.1 Passivity constraints on scattering parameters of baseband equivalent systems

According to [27, 29, 30], an n-port electronic system is passive if, for any $\tau > -\infty$ and $\boldsymbol{v}(t) \in L_{2n}$ (L_{2n} denotes the space of all vectors whose n components are functions of a real variable t and square integrable over $-\infty < t < \infty$), it holds

$$\Re \int_{-\infty}^{\tau} \boldsymbol{v}^H(t)\boldsymbol{i}(t)dt \geq 0 \tag{4.18}$$

where $\boldsymbol{v}(t)$, $\boldsymbol{i}(t)$ are the voltage and current at the system ports. It is important to note that this definition is given not only for real signals but also for complex ones. By expressing (4.18) in terms of the forward $\boldsymbol{a}(t)$ and backward $\boldsymbol{b}(t)$ waves, the passivity definition becomes [27, 31, 32]

$$\int_{-\infty}^{\tau} \boldsymbol{a}^H(t)\boldsymbol{a}(t) - \boldsymbol{b}^H(t)\boldsymbol{b}(t)dt \geq 0 \tag{4.19}$$

which is more convenient for describing photonic systems.

Following the same proof process as [27], particularly *Theorem 2* and *Theorem 3*, the first and second passivity conditions can be derived from (4.19) for the complex-valued systems studied in this chapter. Alternatively, the same conclusion can be obtained via the approach in *Chapter II* of [31] which gave simpler formal

proofs using the theory of distributions. The interested reader may consult [27] and [31] for a detailed and comprehensive proof.

Therefore, we propose the following passivity constraints on the scattering parameters $\boldsymbol{S}_l(s)$ of the baseband equivalent systems as:

1. $\boldsymbol{S}_l(s)$ is analytic in $\Re(s) > 0$;

2. $\boldsymbol{I}_n - \boldsymbol{S}_l^H(s)\boldsymbol{S}_l(s)$ is a nonnegative-definite matrix for all s such that $\Re(s) > 0$.

Note that real-valued systems need the extra condition $\boldsymbol{S}(s^*) = \boldsymbol{S}^*(s)$, which ensures that the impulse response is real, so that a real input results in a real output, and makes the system physically realizable. Furthermore, it is clearly mentioned in *Section IV* of [27] that this requirement is independent with respect to the passivity definition in (4.18) and (4.19). Therefore this is evidently not required for the passivity of complex-valued systems which are proposed only for simulation purposes.

4.4.2 Fast passivity assessment of baseband equivalent systems

Passivity conditions require both scattering parameters $\boldsymbol{S}(s)$ and their baseband equivalent $\boldsymbol{S}_l(s)$ to be bounded by unity, which implies that all singular values σ of $\boldsymbol{S}_l(s)$ are smaller than unity at all frequencies:

$$\sigma_i(f) < 1, \quad i = 1, \ldots, n \tag{4.20}$$

An efficient and accurate method to assess the passivity properties of state-space models of electronic and photonic systems is based on the Hamiltonian matrix $\boldsymbol{M}$ [18] defined as

$$\boldsymbol{M} = \begin{bmatrix} \boldsymbol{A} - \boldsymbol{B}\boldsymbol{L}^{-1}\boldsymbol{D}^T\boldsymbol{C} & -\boldsymbol{B}\boldsymbol{L}^{-1}\boldsymbol{B}^T \\ \boldsymbol{C}^T\boldsymbol{Q}^{-1}\boldsymbol{C} & -\boldsymbol{A}^T + \boldsymbol{C}^T\boldsymbol{D}\boldsymbol{L}^{-1}\boldsymbol{B}^T \end{bmatrix} \tag{4.21}$$

where $\boldsymbol{A}$, $\boldsymbol{B}$, $\boldsymbol{C}$, $\boldsymbol{D}$ are the state-space matrices in (4.4), while $\boldsymbol{L} = \boldsymbol{D}^T\boldsymbol{D} - \boldsymbol{I}_n$ and $\boldsymbol{Q} = \boldsymbol{D}\boldsymbol{D}^T - \boldsymbol{I}_n$.

A state-space model is passive if its Hamiltonian matrix has no purely imaginary eigenvalues, since any imaginary eigenvalue indicates a crossover frequency where a singular value changes from being smaller to larger than unity, or vice versa. This approach is more reliable and efficient than sweeping the singular values over a set of discrete frequencies, especially for photonic systems which are defined over a large frequency range.

A similar Hamiltonian matrix $\boldsymbol{M}_l$ for baseband equivalent systems $\boldsymbol{S}_l(s)$ can be derived by following the procedure in [18], leading to

$$\boldsymbol{M}_l = \begin{bmatrix} \boldsymbol{A}_l - \boldsymbol{B}_l\boldsymbol{L}_l^{-1}\boldsymbol{D}_l^H\boldsymbol{C}_l & -\boldsymbol{B}_l\boldsymbol{L}_l^{-1}\boldsymbol{B}_l^H \\ \boldsymbol{C}_l^H\boldsymbol{Q}_l^{-1}\boldsymbol{C}_l & -\boldsymbol{A}_l^H + \boldsymbol{C}_l^H\boldsymbol{D}_l\boldsymbol{L}_l^{-1}\boldsymbol{B}_l^H \end{bmatrix} \tag{4.22}$$

where $\boldsymbol{A}_l$, $\boldsymbol{B}_l$, $\boldsymbol{C}_l$, $\boldsymbol{D}_l$ are the complex-valued baseband equivalent state-space matrices, while $\boldsymbol{L}_l = \boldsymbol{D}_l^H \boldsymbol{D}_l - \boldsymbol{I}_n$ and $\boldsymbol{Q}_l = \boldsymbol{D}_l \boldsymbol{D}_l^H - \boldsymbol{I}_n$. The derivation of $\boldsymbol{M}_l$ is shown in Appendix 4.11.3.

One can observe that the only difference between $\boldsymbol{M}$ and $\boldsymbol{M}_l$ is the use of the transpose conjugate operator for the state-space matrices in $\boldsymbol{M}_l$, while only the transpose operator is required in $\boldsymbol{M}$. Indeed, state-space models of general electronic or photonic systems satisfy the conjugacy property $\boldsymbol{S}^*(s) = \boldsymbol{S}(s^*)$: the corresponding scattering parameters do not change if the state-space matrices $\boldsymbol{A}$, $\boldsymbol{B}$, $\boldsymbol{C}$, $\boldsymbol{D}$ are replaced with their conjugate counterparts [18]. Evidently, this is not valid for the baseband equivalent systems.

Note that the eigenvalues of (4.22) can be obtained directly from the eigenvalues of the corresponding bandpass system (4.21). According to (4.17), by replacing $\boldsymbol{A}_l$, $\boldsymbol{B}_l$, $\boldsymbol{C}_l$, $\boldsymbol{D}_l$ in (4.22) with

$$\begin{aligned} \boldsymbol{A}_l &= \boldsymbol{A} - j2\pi f_c \boldsymbol{I}_m \\ \boldsymbol{B}_l &= \boldsymbol{B} \\ \boldsymbol{C}_l &= \boldsymbol{C} \\ \boldsymbol{D}_l &= \boldsymbol{D} \end{aligned}$$

gives

$$\boldsymbol{M}_l = \boldsymbol{M} - j2\pi f_c \boldsymbol{I}_{2m} \tag{4.23}$$

where $\boldsymbol{M}$ is the Hamiltonian matrix of the corresponding bandpass system. Then it is easy to derive (see Appendix 4.11.3)

$$\lambda_{li} = \lambda_i - j2\pi f_c, \qquad \text{for } i = 1, \ldots, 2m \tag{4.24}$$

where $2m$ is the total number of eigenvalues, while λ_i and λ_{li} are the eigenvalues of $\boldsymbol{M}$ and $\boldsymbol{M}_l$, respectively.

Hence, the following properties hold:

- If there are passivity violations in a bandpass state-space model, the corresponding baseband equivalent system (4.17) is not passive either.
- There is an one-to-one correspondence between the frequencies where passivity violations occurs in the state-space models of the bandpass and corresponding baseband equivalent.
- The passivity of baseband equivalent state-space models (4.17) can be guaranteed by applying "standard" passivity enforcement algorithm, such as [19, 33], to the corresponding state-space models of the bandpass systems.

4.5 Proposed modeling framework of photonic system for time-domain simulations

The signals traveling through photonic systems are usually phase and/or amplitude modulated signals over a suitable optical carrier. The modulating signals are electronic ones, whose spectrum bandwidth is normally less than a few hundred gigahertz, while the carrier frequency is usually defined for example in the range $[187.5;\ 200]$ THz, corresponding to a wavelength of $[1.5;\ 1.6]$ μm.

The proposed modeling approach starts from evaluating the scattering parameters of the photonic system under study in the frequency range of interest. Next an accurate rational model is computed via the VF algorithm. Stability is enforced during the model-building phase via suitable pole-flipping schemes [9], while the model passivity is checked and, eventually, enforced as a post-processing step via robust passivity enforcement methods, such as [19, 33]. A baseband equivalent state-space representation (4.17) can now be obtained with guaranteed passivity by (4.24). Such model can be used to efficiently perform time-domain simulations. The flowchart of the proposed modeling framework is shown in Fig. 4.3.

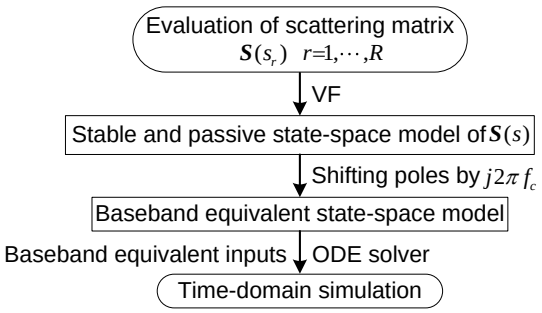

Figure 4.3: Flowchart of the proposed modeling framework for time-domain simulation of photonic systems.

In particular, when it comes to building state-space models of photonic systems for time-domain simulations, there are two options:

1. modeling the frequency range of interest, e.g. $[187.5;\ 200]$ THz, noted as *Model A* (covering a large frequency range);

2. considering only the frequency range corresponding to the spectrum of the optical input signals under study around the carrier frequency, normally a few hundred gigahertz, noted as *Model B* (covering a small frequency range).

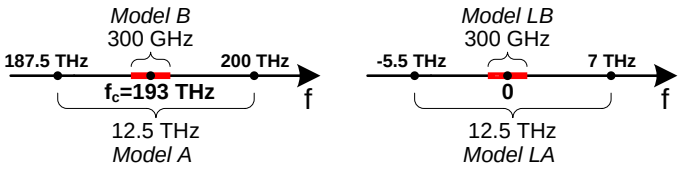

Figure 4.4: Frequency ranges of Model A, LA, B, and LB.

Models	compact	flexible	simulation at baseband
Model A	×	√	×
Model B	√	×	×
Model LA	×	√	√
Model LB	√	×	√

Table 4.1: Comparison of different modeling strategies.

The corresponding baseband equivalent state-space models are indicated as *Model LA* and *Model LB*, respectively. The modeling frequency ranges of these four models are illustrated in Fig. 4.4 when assuming $f_c = 193$ THz and the spectrum of the optical input signal of interest is 300 GHz. Note that *Model A* and *B* can also be used directly to evaluate the behavior of the chosen photonic system in the time domain: such modeling strategies follow the approach outlined in Section 4.2.

It is important to remark that *Model A* and *LA* are likely to require more poles as compared to *Model B* and *LB*, since they are computed over a larger bandwidth: the modeling complexity is higher and the corresponding system of ODE will be larger. If the scattering parameters under study are very dynamic in the range $[187.5;\ 200]$ THz, the modeling process can become prohibitively expensive, making it practically infeasible to build accurate, stable and passive models. However, this approach offers more flexibility since the corresponding models can be used for any value of the carrier frequency in the frequency range $[187.5;\ 200]$ THz, while *Model B* and *LB* must be constructed anew for each value of the carrier frequency considered.

It is important to note that both *Model LA* and *LB* operate at baseband, which means that a relatively large time-step can be used to solve the corresponding ODE for time-domain simulation, thereby saving both computational time and memory storage. Table 4.1 compares the advantages and disadvantages of different approaches considered during the model building and time-domain simulation process.

Finally, no matter which model is used for the time-domain simulation, the

modeling frequency range must be larger than or at least equal to the frequency range of the input signals considered. Indeed, no information on the scattering parameters behavior outside such modeling frequency range is provided to the VF algorithm: the model obtained via the VF approach extrapolates the scattering parameters outside the modeling frequency range. Hence, while the state-space model computed is stable and passive at $[0;\ \infty]$ Hz, it is not possible to guarantee its accuracy outside the modeling frequency range. Therefore, if the input signal is noisy, the spectrum of the noise should also be considered during the model building phase.

4.6 Numerical examples

This section presents three application examples of the proposed modeling and simulation technique. The scattering parameters of the photonic systems under study are evaluated via Caphe [34], while the time-domain simulations are carried out in MATLAB via the routine *lsim* on a personal computer with Intel Core i3 processor and 8 GB RAM.

4.6.1 Mach-Zehnder interferometer

In this example, the *Mach-Zehnder interferometer* (MZI) shown in Fig. 4.5 is studied, which is formed by two identical directional couplers (with coupling coefficient 50/50) and two waveguides with lengths 150 μm (upper one) and 100 μm (lower one). Both waveguides have effective index 2.35 and group index 4.3 at 1.55 μm, and a propagation loss of 200 dB/m. The time-domain simulation is carried out with the conventional modeling technique (in Section 4.2) and the proposed baseband equivalent modeling approach. For comparison, an analytic model for MZI is also built by considering the loss and dispersion of the waveguides. The directional coupler is assumed to be an ideal signal spliter or combiner, which adds a $\pi/2$ phase delay to the cross-coupled signals. The time-domain simulation of this analyitical model is conducted as a benchmark.

The RF modulation signal is a smooth pulse with amplitude 1 V, a rise/fall time of 5.7 ps, width of 32 ps, initial delay of 18 ps, and a spectrum bandwidth of 100 GHz. An optical carrier of frequency $f_c = 193.72$ THz, which is chosen at random in the frequency range $[187.5;\ 200]$ THz, is used to transmit the modulation signal through the MZI. Note that we assume the RF signal is ideally modulated on the carrier via amplitude modulation. Both the modulated signal at optical frequencies and the smooth RF pulse are shown in Fig. 4.6.

Model A is built starting from the MZI scattering parameters in the range $[187.5;\ 200]$ THz, while *Model B* requires only the scattering parameters in $[f_c - \Delta; f_c + \Delta]$, where the choice $\Delta = 150$ GHz allows one to cover the entire spec-

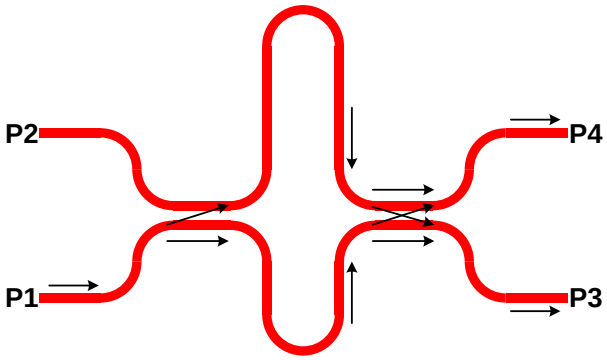

Figure 4.5: Example 4.6.1. The geometric structure of the MZI under study.

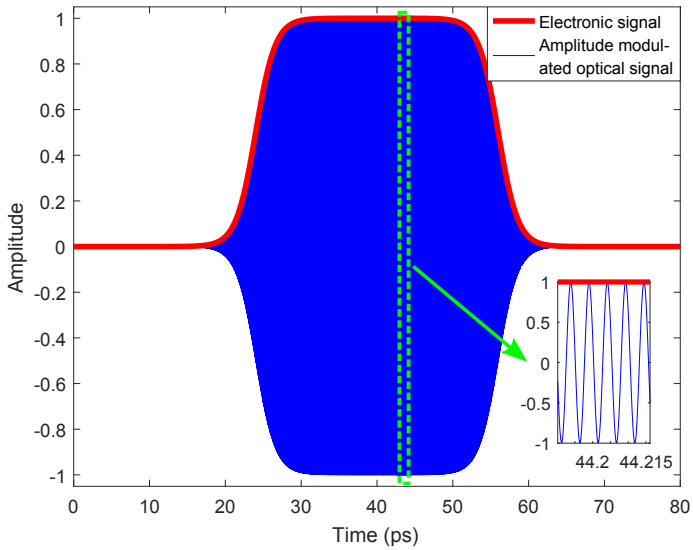

Figure 4.6: Example 4.6.1. The electronic signal and amplitude modulated optical signal for the MZI.

trum of the modulated optical signal. In particular, first the frequency samples have been divided in two groups: one to compute the desired rational model (modeling data) and the other to verify its accuracy (validation data). Then *Model A* and *B* are built via the VF algorithm with 67 poles and 8 poles, respectively, aiming at a maximum absolute error of less than -60 dB between the model and MZI scattering parameters. Finally, *Model LA* and *LB* can be derived analytically from *Model A* and *B*, as shown in Section 4.3.2.

The accuracy of *Model A* and *LB* in the frequency-domain is shown in Fig. 4.7 and Fig. 4.8, respectively, which show both the magnitude and the phase of the MZI scattering parameters obtained by Caphe and by the corresponding state-space models.

Time-domain simulations are carried out with all the four models considered; while for *Model A* and *B* a time-step 0.23 fs is adopted, a time-step of 0.4 ps can be used for *Model LA* and *LB*. Meanwhile, time-domain simulation of the analytic model built according the underlying physical principle of the MZI is performed in Caphe to validate the accuracy of the other models. The outputs at port $P3$ of *Model A*, *Model LB*, and the analytic model are shown in Fig. 4.9. According to Section 4.3, the magnitude of the outputs of *Model LB* is the envelope of the output of *Model A*, and this fact is exactly illustrated by Fig. 4.9. In addition, it is easy to observe that the output of *Model LB* accurately matches the analytic model prediction.

The time for model building and time-domain simulation for all the different models are present in Table 4.2. It clearly shows that modeling only the small frequency range (*Model B* and *LB*) rather than the large frequency range (*Model A* and *LA*) consumes far less time and results in compact models. Note that the time-domain simulation at baseband with compact models, such as *Model LB*, is

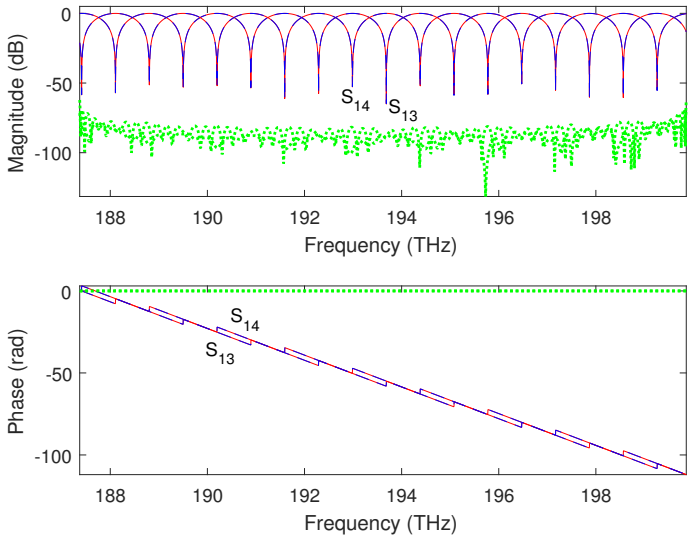

Figure 4.7: Example 4.6.1. Comparison of the magnitude (top) and phase (bottom) of the MZI scattering parameters extracted via Caphe (full blue line) and Model A (red dashed line), where the green dots represent the corresponding absolute error.

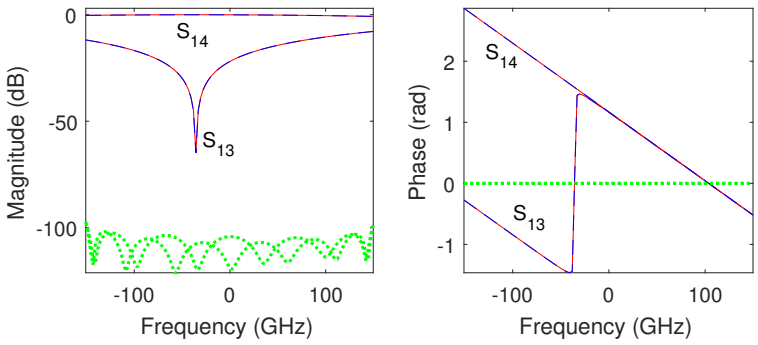

Figure 4.8: Example 4.6.1. Comparison of the magnitude (left) and phase (right) of the MZI scattering parameters extracted via Caphe (full blue line) and Model LB (red dashed line), where the green dots represent the corresponding absolute error.

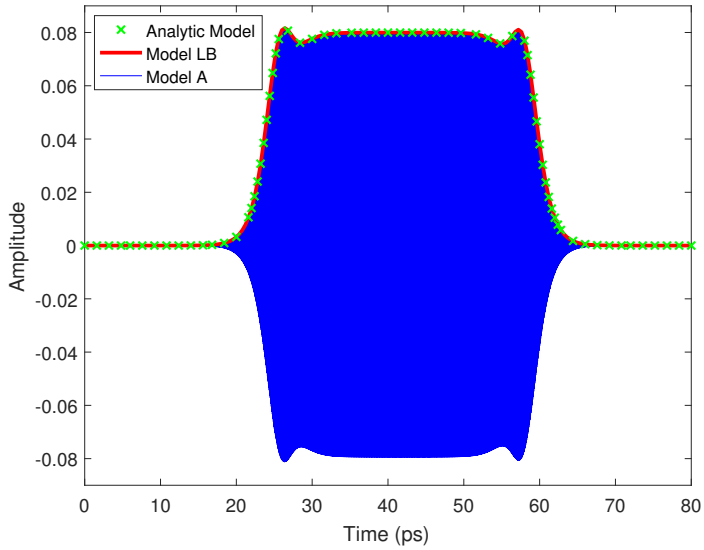

Figure 4.9: Example 4.6.1. The output at port $P3$ of the MZI, the red line is the absolute value of the complex signal obtained by the time-domain simulation of Model LB, the blue line is the corresponding signal from Model A, while the marker $\times$ denotes the same signal from the analytic model.

the most efficient, which is consistent with the analysis in Section 4.5.

Finally, the following test illustrates the importance of choosing the correct modeling frequency range, as mentioned in Section 4.5. Let us assume an electronic pulse signal with width of 1 ps and spectrum in the range $[0; 6]$ THz as the

Models	Time step	Poles number	Model building	Time-domain simulation
Model A	0.23 fs	67	2.10 s	35.66 s
Model B	0.23 fs	8	0.028 s	2.16 s
Model LA	0.4 ps	67	2.10 s	0.49 s
Model LB	0.4 ps	8	0.028 s	0.024 s

Table 4.2: Example 4.6.1. Efficiency comparison of the different modeling strategies.

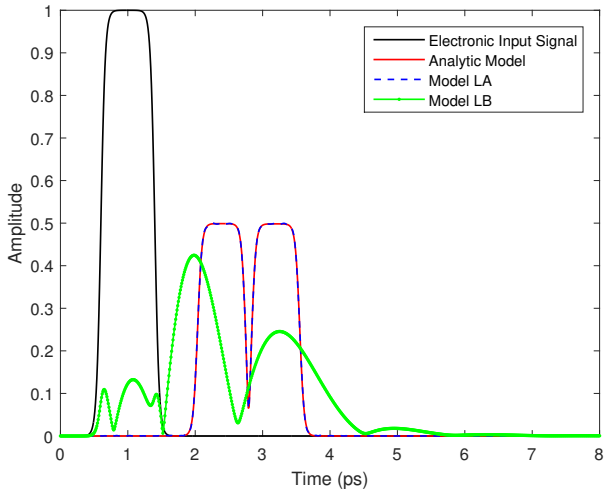

Figure 4.10: Example 4.6.1. Time-domain simulation of Model LA and LB with very narrow pulse input signal. The black line is the electronic input signal, the red solid line is the output at port $P3$ of the analytic model, while the blue dashed line and green dotted line indicate the outputs at the same port of Model LA and LB, respectively.

input signal of *Model LA* and *LB* of the MZI. The corresponding output at port $P3$ is shown in Fig. 4.10: *Model LA* still gives very accurate results compared to the analytic model, while the output of *Model LB* is not even close to the benchmark. The reason is that the modeling frequency range (12.5 THz) of *Model LA* covers the spectrum of the input signal, but this does not hold for *Model LB*.

4.6.2 Ring resonator

In this example, a double ring resonator (RR) is composed of two rings and two waveguides, and designed as a narrow band flat-top filter, as shown in Fig. 4.11. The two rings have different circumferences 20 μm (lower one) and 20.01 μm (upper one), resulting in slightly different R_1 and R_2. The ring waveguides and bus

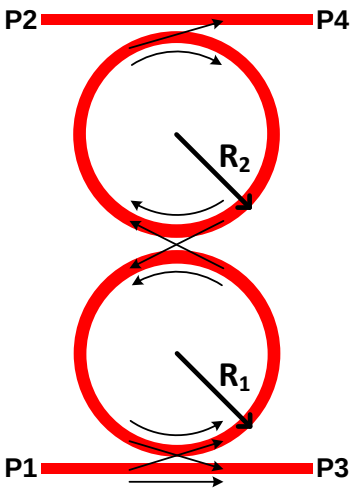

Figure 4.11: Example 4.6.2. The geometric structure of the double ring resonator.

waveguides have effective index 2.35 and group index 4.3 at wavelength 1.55 μm. The coupling coefficient between waveguides and rings is 0.2, while the same parameter (coupling coefficient) between two rings is 0.03.

First, the *Model A* of the ring resonator is built in the range $[187.5;\ 200]$ THz with 22 poles, while *Model B* is computed with 6 poles in the range $[f_c - \Delta;\ f_c + \Delta]$, with $f_c = 195.75$ THz and $\Delta = 450$ GHz. The maximum absolute error of both models is less than -65 dB. Next, *Model LB* is directly derived by shifting the poles of *model B*. Figures 4.12 and 4.13 describe the frequency-domain accuracy for *Model A* and *LB*, respectively. In this example, a 4-QAM (Quadrature phase-shift keying) modulated input signal is applied to $P1$ for time-domain simulations. The in-phase I and quadrature Q parts of the modulating signal are the 4-bits sequences (-1,-1,1,1) and (-1,1,-1,1), respectively, where each bit lasts for 20 ps. As shown in Fig. 4.14, the modulating signals are realistic analog signals, for example affected by overshoot and undershoot. As mentioned in Section 4.3.2, the baseband equivalent of the modulated input signal can be easily calculated, since I and Q are its real and imaginary parts, respectively.

After conducting the proposed time-domain simulation, the outputs of *Model LB* are complex, and their magnitude are the envelopes of the outputs of *Model A* as shown in Fig. 4.15. Note that the outputs of *model A* can be analytically recovered from the outputs of *Model LB*, according to (4.52). Hence, Fig. 4.16 shows a side by side comparison of the output of *Model A* at port $P4$ and the corresponding value recovered from *Model LB*. For a better observation of the accuracy of the recovered signal, Fig. 4.17 shows a zoom of Fig. 4.16 around $t = 45.6$ ps, which demonstrates an excellent agreement.

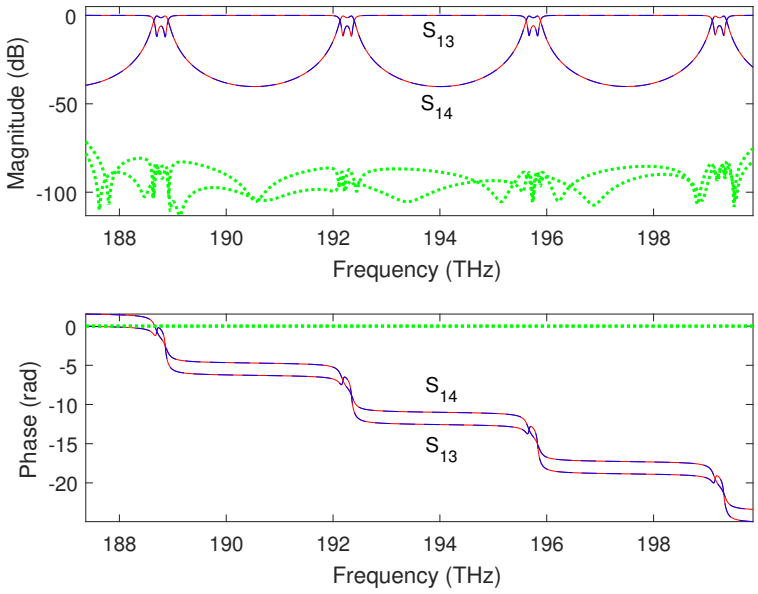

Figure 4.12: Example 4.6.2. Comparison of the magnitude (top) and phase (bottom) of the ring resonator scattering parameters extracted via Caphe (full blue line) and Model A (red dashed line), where the green dots represent the corresponding absolute error.

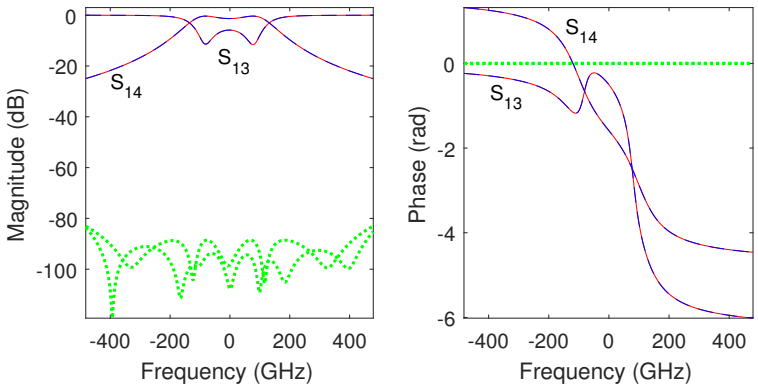

Figure 4.13: Example 4.6.2. Comparison of the magnitude (left) and phase (right) of the ring resonator scattering parameters extracted via Caphe (full blue line) and Model LB (red dashed line), where the green dots represent the corresponding absolute error.

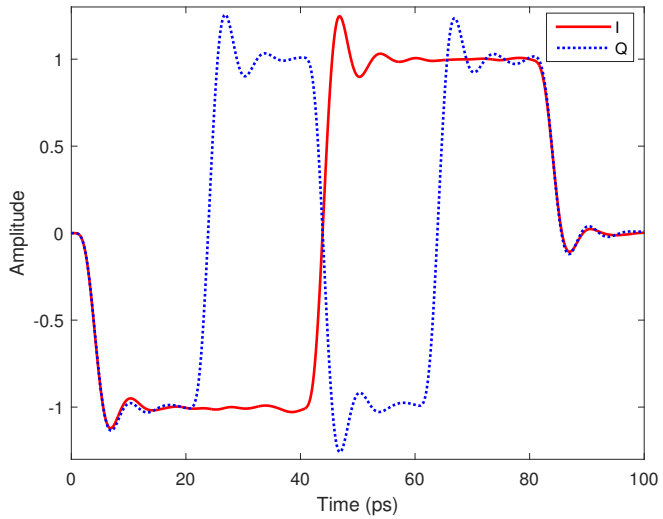

Figure 4.14: Example 4.6.2. The modulating signals: in-phase part I and quadrature part Q.

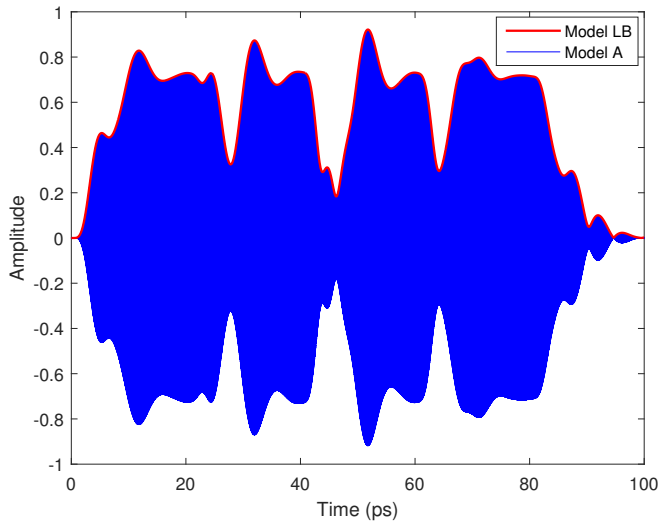

Figure 4.15: Example 4.6.2. The output at port $P4$ of the double ring resonator, the red line is the absolute value of the complex signal obtained by the time-domain simulation of Model LB, while the blue line is the corresponding signal from Model A.

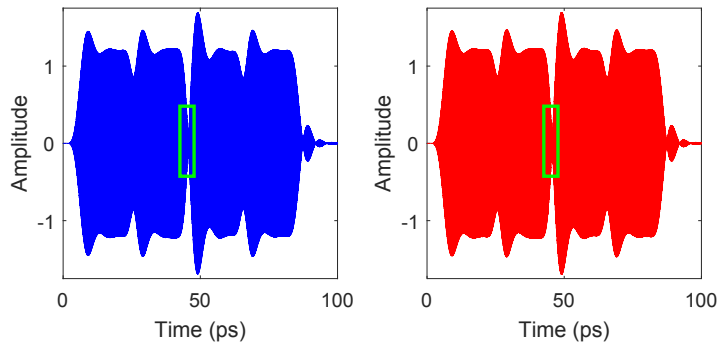

Figure 4.16: Example 4.6.2. The output at port $P4$ of the double ring resonator. Left: the output of Model A. Right: the recovered bandpass output from Model LB.

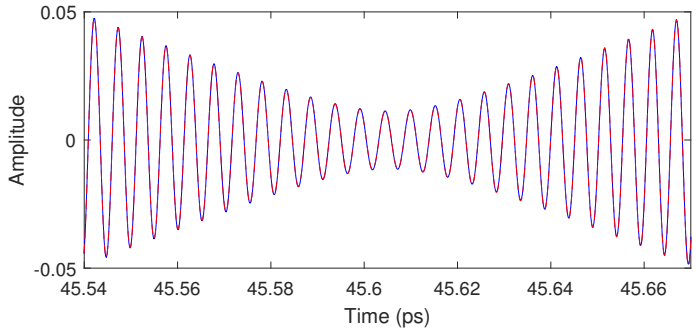

Figure 4.17: Example 4.6.2. A zoom of the output at port $P4$ of the double ring resonator around $t = 45.6$ ps (the green rectangular area in Fig. 4.16). The blue line is used for Model A, while the red dash line is the recovered bandpass output from Model LB.

As far as the computational times are concerned, building the *Model A* and *LB* required 0.28 s and 0.04 s respectively while their time-domain simulations took 9.29 s and 0.05 s, respectively, which clearly demonstrates the superior efficiency of the proposed technique when dealing with amplitude and phase modulated signals.

4.6.3 Lattice filter

A fifth order filter with a Chebyshev window, designed by using a discrete *finite impulse response* (FIR) filter design method [35], is realized via a Mach-Zehnder interferometer lattice filter (LF) [36]. As illustrated in Fig. 4.18, it is formed by six directional couplers with power coupling coefficients of 0.008, 0.067, 0.175, 0.175, 0.067, 0.008, and waveguides with a length difference of 179 μm between

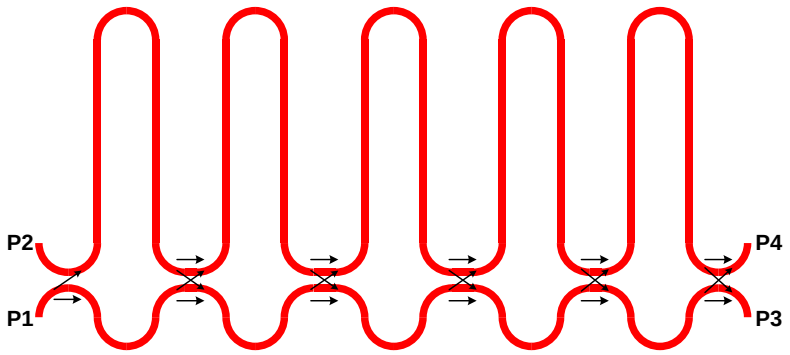

Figure 4.18: Example 4.6.3. The geometric structure of the Mach-Zehnder interferometer lattice filter.

the upper and lower ones, whose effective and group index are 2.30 and 4.18, respectively. In practice, due to process variations, when manufacturing photonic devices geometrical or optical parameters can vary in a relatively small range around their nominal value [37]; which in turn can lead to variations in the device frequency response, such as frequency shifts. In this example, we study the time-domain influence of frequency shifts in the response of the lattice filter via an eye diagram analysis.

For eye diagram analysis, the input signal and time-domain simulation should last a relatively long period of time (long bits sequence), which could make the time-domain simulation of *Model A* and *B* unfeasible. In this example, a pseudo-random sequence of 1000 bits, with a bit time of 30 ps and a Gaussian jitter having a standard deviation of 1.5 ps is used as modulating signal $A(t)$. The amplitude of such signal up to 1 ns is shown in Fig. 4.19. The total number of time-steps required for time-domain simulations of *Model A* and *B* with such input signal is 60 million (30 ns/0.5 fs), while this number reduces to only 30,000 time-steps (30 ns/1 ps) for *Model LA* and *LB*.

The scattering matrices of the lattice filter are computed in the range $[187.5; 200]$ THz. However, due to the dynamic behavior of the filter frequency response in such a wide bandwidth, the modeling complexity of *Model A* (*LA*) is very high. Considering that the efficiency and accuracy of *Model LB* have been already demonstrated in Sections 4.6.1 and 4.6.2, only the time-domain simulation of *Model LB* is performed.

The sequence signal is modulated on $f_c = 195.11$ THz (λ=1.5365 μm), which is chosen as the filter passband center frequency during the design phase. Due to fabrication variations, let us assume that the center frequency can shift to 195.05 THz (λ=1.5370 μm) or 194.98 THz (λ=1.5375 μm), as shown in Fig. 4.20. *Model LB* is built for each one of these three situations, by adopting a pole shift of

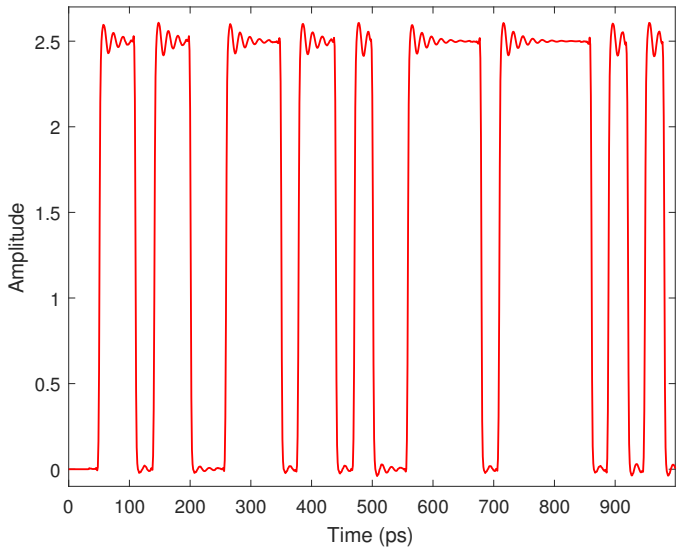

Figure 4.19: Example 4.6.3. Pseudo-random sequence of 1000 bits for $t \in [0;\ 1]$ *ns.*

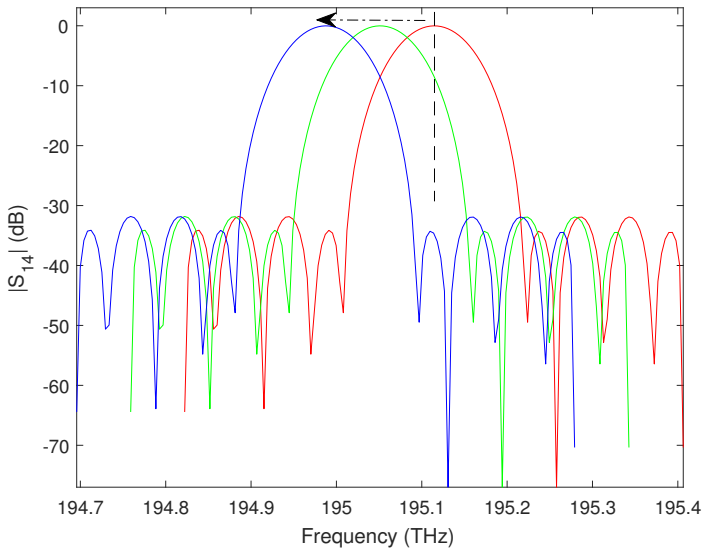

Figure 4.20: Example 4.6.3. Shift of the center frequency of passband of the lattice filter due to the fabrication variations.

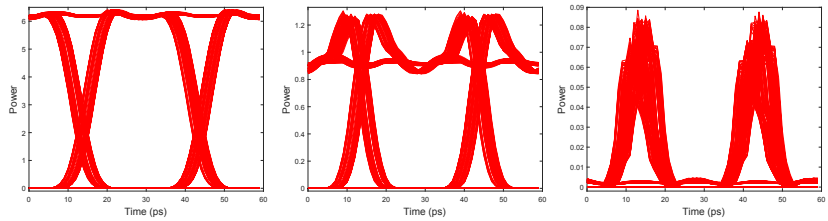

Figure 4.21: Example 4.6.3. The eye diagrams at port $P4$ of the baseband equivalent systems of the lattice filter with passband center frequency 195.11 THz, 195.05 THz, 194.98 THz (from left to right).

$f_c = 195.11$ THz, since the excitation signal is modulated on this frequency. In particular, the models for the three wavelength considered are built with 36 poles achieving a maximum absolute error of -60 dB.

Then, the time-domain simulations can be easily carried out at baseband with the pseudo-random sequence of 1000 bits. Figure 4.21 shows the eye diagram of the power of the complex output signals at port $P4$ of the three baseband equivalent systems, over a two-bit span resulting from the entire 1000-bit input stream. It is evident that the signal is completely distorted when the center frequency shift from 195.11 THz to 194.98 THz. The computational time of the time-domain simulation for generating each eye diagram is 1.09 s while building each model took 1.67 s, which is very efficient. This example shows that expensive time-domain simulations can be efficiently performed via the proposed technique, without a loss in accuracy.

4.7 Extension of the baseband modeling technique

A general linear, passive, and time-invariant physical system can always be described by real-valued state-space models. They are widely used in the electronics and control theory fields where complex models, such as (4.4), are rarely used. Therefore, to make maximum use of such techniques for photonic circuit modeling, it is important to extend the baseband modeling technique to general real-valued state-space representations of linear photonic systems.

Let us assume that a general, linear and passive n-ports photonic system can be represented by a stable and passive state-space model operating at optical frequencies in the form:

$$\begin{cases} \dfrac{\mathrm{d}\boldsymbol{x}(t)}{\mathrm{d}t} = \boldsymbol{A}\boldsymbol{x}(t) + \boldsymbol{B}\boldsymbol{a}(t) \\ \boldsymbol{b}(t) = \boldsymbol{C}\boldsymbol{x}(t) + \boldsymbol{D}\boldsymbol{a}(t), \end{cases} \tag{4.25}$$

where $\boldsymbol{A} \in \mathbb{R}^{m\times m}$, $\boldsymbol{B} \in \mathbb{R}^{m\times n}$, $\boldsymbol{C} \in \mathbb{R}^{n\times m}$, $\boldsymbol{D} \in \mathbb{R}^{n\times n}$. Even though (4.25)

shares the same form of (4.4), It is important to note that $\boldsymbol{A}$, $\boldsymbol{B}$, $\boldsymbol{C}$, $\boldsymbol{D}$ in (4.25) are assumed as matrices with real elements: such model can be obtained by means of the VF algorithm through a suitable conversion of the rational model (4.2) (see, for example, the method described in [18]), but also from other approaches, such as MOR techniques [38], while (4.4) is the particular form of state-space models derived only from the VF technique.

Now, starting from (4.25), it is possible to derive an equivalent complex-valued baseband state-space model by applying the same procedure described in Section 4.3.2. In the following, we define such model as *general complex-valued baseband state-space model* in the form:

$$\begin{cases} \dfrac{\mathrm{d}\boldsymbol{x_l}(t)}{\mathrm{d}t} = (\boldsymbol{A} - j2\pi f_c \boldsymbol{I}_m)\boldsymbol{x_l}(t) + \boldsymbol{B}\boldsymbol{a_l}(t) \\ \boldsymbol{b_l}(t) = \boldsymbol{C}\boldsymbol{x_l}(t) + \boldsymbol{D}\boldsymbol{a_l}(t), \end{cases} \tag{4.26}$$

which demonstrates that the proposed baseband modeling approach is not only applicable to a specific complex realization of the state-space matrices obtained via VF, but also to any general state-space model. It is important to note that the frequency response of the complex-valued model (4.26) is the frequency response of the model (4.25) shifted by the carrier frequency f_c. Indeed, expressing (4.26) into the Laplace domain leads to

$$\begin{aligned} \boldsymbol{S}_l(s) &= \boldsymbol{C}\left((s + j2\pi f_c)\boldsymbol{I}_m - \boldsymbol{A}\right)^{-1}\boldsymbol{B} + \boldsymbol{D} \\ &= \boldsymbol{S}(s + j2\pi f_c), \end{aligned} \tag{4.27}$$

where $\boldsymbol{S}_l(s)$ and $\boldsymbol{S}(s)$ are the transfer functions of the models (4.26) and (4.25) in the Laplace domain, respectively. Hence, the frequency response of the model (4.26) is not symmetrical with respect to positive and negative frequencies, which makes the baseband equivalent model a non-physical, complex-valued system.

The stability and passivity of the model (4.26), which are fundamental properties for time-domain simulations [14], are now investigated. In Section 4.4, a thorough discussion on the definition of the stability and passivity criteria for baseband systems is presented. Here it is sufficient to remark that the same methods to assess the stability and passivity of the state-space models of physical systems can be employed for general baseband models as well. In particular, the stability of a (complex- or real-valued) state-space model can be assessed by the eigenvalues of the matrix $\boldsymbol{A}$: the model is stable if the real part of all the eigenvalues is negative [39]. Now, let us assume that we start off with a realistic system (4.25) that is stable (e.g. any passive linear optical filter circuit), and the corresponding matrix $\boldsymbol{A}$ is diagonalizable, where

$$\boldsymbol{A} = \boldsymbol{T}\boldsymbol{V}\boldsymbol{T}^{-1}, \tag{4.28}$$

and $\boldsymbol{T}$ comprises all the eigenvectors and $\boldsymbol{V}$ is a diagonal matrix whose elements are the corresponding eigenvalues. Note that all the eigenvalues in $\boldsymbol{V}$ have negative

real parts, since the state-space model (4.25) is assumed to be stable. Then, it is easy to derive

$$\boldsymbol{A} - j2\pi f_c \boldsymbol{I}_m = \boldsymbol{T}(\boldsymbol{V} - j2\pi f_c \boldsymbol{I}_m)\boldsymbol{T}^{-1}, \tag{4.29}$$

which indicates that the eigenvalues of the baseband model (4.26) are the ones of the model (4.25) shifted over $j2\pi f_c$ along the imaginary axis in the complex plane. Hence, the baseband model (4.26) is also stable (all the eigenvalues of the matrix $\boldsymbol{A} - j2\pi f_c \boldsymbol{I}_m$, have negative real parts) if the original state-space model (4.25) is stable.

The passivity of stable models can be verified by means of the corresponding Hamiltonian matrix, which for the system (4.26) is

$$\boldsymbol{M}_l = \begin{bmatrix} \boldsymbol{A}_l - \boldsymbol{B}\boldsymbol{L}^{-1}\boldsymbol{D}^H\boldsymbol{C} & -\boldsymbol{B}\boldsymbol{L}^{-1}\boldsymbol{B}^H \\ \boldsymbol{C}^H\boldsymbol{Q}^{-1}\boldsymbol{C} & -\boldsymbol{A}_l{}^H + \boldsymbol{C}^H\boldsymbol{D}\boldsymbol{L}^{-1}\boldsymbol{B}^H \end{bmatrix}, \tag{4.30}$$

where $\boldsymbol{B}$, $\boldsymbol{C}$, $\boldsymbol{D}$ are the real state-space matrices in (4.26), while $\boldsymbol{A}_l = \boldsymbol{A} - j2\pi f_c \boldsymbol{I}_m$, $\boldsymbol{L} = \boldsymbol{D}^H\boldsymbol{D} - \boldsymbol{I}_n$ and $\boldsymbol{Q} = \boldsymbol{D}\boldsymbol{D}^H - \boldsymbol{I}_n$. Note that for real-valued systems the transpose operator ^{T} is used in the Hamiltonian matrix [18], but in a complex-valued system the transpose conjugate operator ^{H} is required according to Section 4.4.2. In particular, a (complex- or real-valued) stable state-space model is passive if its Hamiltonian matrix has no purely imaginary eigenvalues, since any purely imaginary eigenvalue indicates a crossover frequency where a singular value of the scattering matrix changes from being smaller to larger than unity, or vice versa [18]. In the following, it is proven that the general complex-valued baseband state-space model (4.26) is passive by construction if the original model (4.25) is passive as well.

Indeed, the Hamiltonian matrix $\boldsymbol{M}$ for the real-valued model (4.25) is in the form (4.21) [18]. By comparing (4.30) and (4.21), it is clear that

$$\boldsymbol{M}_l = \boldsymbol{M} - j2\pi f_c \boldsymbol{I}_{2m}, \tag{4.31}$$

which describes same the relation as (4.23). Hence, similar conclusion is drawn, the baseband model (4.26) is passive (the Hamiltonian matrix $\boldsymbol{M}_l$ has no purely imaginary eigenvalues) if the original state-space model (4.25) is passive.

The methodology here presented extends the modeling power of the technique, while preserving its main advantages: robustness in the model-building phase and efficiency in time-domain simulations. In particular, the model stability and passivity can be guaranteed by enforcing the same properties on the model (4.25) computed at optical frequencies. If the VF algorithm is adopted, the model stability can be guaranteed by construction and its passivity can be enforced through robust passivity enforcement techniques [16, 19, 33].

4.8 Real-valued baseband state-space models

Baseband state-space models represented by (4.17) and (4.26) are systems of first-order ODE and can be simulated only in solvers which support complex-valued signals and matrices. Whereas this complex system is compact and elegant, many solver techniques are developed and optimized for real-valued systems, such as SPICE, Verilog-A. In this section, a new real-valued baseband state-space model is derived starting from the baseband model (4.26), and its stability and passivity will also be investigated.

4.8.1 Model derivation

Complex baseband equivalent signals can be represented with respect to their real and imaginary parts, such as for $\boldsymbol{a}_l(t)$

$$\boldsymbol{a}_l(t) = \boldsymbol{a}_{l\Re}(t) + j\boldsymbol{a}_{l\Im}(t). \tag{4.32}$$

By expressing all the complex signals in (4.26) in the form of (4.32) and by solving separately with respect to the real and the imaginary parts, lead to:

$$\begin{cases} \dfrac{\mathrm{d}\boldsymbol{x}_{l\Re}(t)}{\mathrm{d}t} = \boldsymbol{A}\boldsymbol{x}_{l\Re}(t) + 2\pi f_c \boldsymbol{x}_{l\Im}(t) + \boldsymbol{B}\boldsymbol{a}_{l\Re}(t) \\ \dfrac{\mathrm{d}\boldsymbol{x}_{l\Im}(t)}{\mathrm{d}t} = \boldsymbol{A}\boldsymbol{x}_{l\Im}(t) - 2\pi f_c \boldsymbol{x}_{l\Re}(t) + \boldsymbol{B}\boldsymbol{a}_{l\Im}(t) \\ \boldsymbol{b}_{l\Re}(t) = \boldsymbol{C}\boldsymbol{x}_{l\Re}(t) + \boldsymbol{D}\boldsymbol{a}_{l\Re}(t) \\ \boldsymbol{b}_{l\Im}(t) = \boldsymbol{C}\boldsymbol{x}_{l\Im}(t) + \boldsymbol{D}\boldsymbol{a}_{l\Im}(t). \end{cases} \tag{4.33}$$

It is important to remark that (4.33), which is a real system of ODE, can only be derived starting from the baseband state-space model (4.26) where $\boldsymbol{A}$, $\boldsymbol{B}$, $\boldsymbol{C}$, $\boldsymbol{D}$ are real matrices: the model (4.17) proposed in Section 4.3.2 cannot be used to obtain (4.33). Then, by defining

$$\hat{\boldsymbol{a}}(t) = \begin{bmatrix} \boldsymbol{a}_{l\Re}(t) \\ \boldsymbol{a}_{l\Im}(t) \end{bmatrix},\ \hat{\boldsymbol{b}}(t) = \begin{bmatrix} \boldsymbol{b}_{l\Re}(t) \\ \boldsymbol{b}_{l\Im}(t) \end{bmatrix},\ \hat{\boldsymbol{x}}(t) = \begin{bmatrix} \boldsymbol{x}_{l\Re}(t) \\ \boldsymbol{x}_{l\Im}(t) \end{bmatrix} \tag{4.34}$$

and

$$\begin{aligned} \hat{\boldsymbol{A}} &= \begin{bmatrix} \boldsymbol{A} & 2\pi f_c \boldsymbol{I}_m \\ -2\pi f_c \boldsymbol{I}_m & \boldsymbol{A} \end{bmatrix}, \quad \hat{\boldsymbol{B}} = \begin{bmatrix} \boldsymbol{B} & \boldsymbol{0} \\ \boldsymbol{0} & \boldsymbol{B} \end{bmatrix}, \\ \hat{\boldsymbol{C}} &= \begin{bmatrix} \boldsymbol{C} & \boldsymbol{0} \\ \boldsymbol{0} & \boldsymbol{C} \end{bmatrix}, \qquad\qquad \hat{\boldsymbol{D}} = \begin{bmatrix} \boldsymbol{D} & \boldsymbol{0} \\ \boldsymbol{0} & \boldsymbol{D} \end{bmatrix}, \end{aligned} \tag{4.35}$$

where $\boldsymbol{0}$ represent the null matrix, equation (4.33) can be written as

$$\begin{cases} \dfrac{\mathrm{d}\hat{\boldsymbol{x}}(t)}{\mathrm{d}t} = \hat{\boldsymbol{A}}\hat{\boldsymbol{x}}(t) + \hat{\boldsymbol{B}}\hat{\boldsymbol{a}}(t) \\ \hat{\boldsymbol{b}}(t) = \hat{\boldsymbol{C}}\hat{\boldsymbol{x}}(t) + \hat{\boldsymbol{D}}\hat{\boldsymbol{a}}(t), \end{cases} \tag{4.36}$$

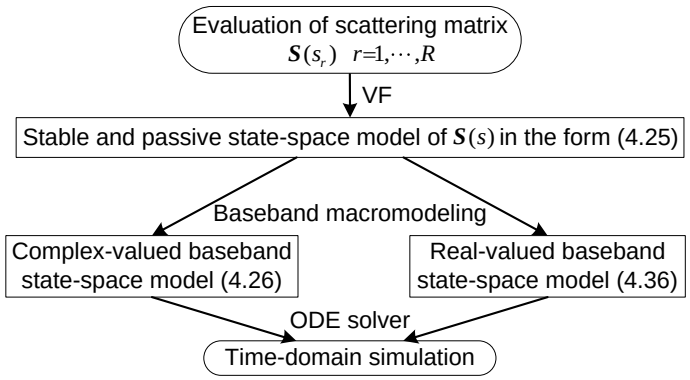

Figure 4.22: Flowchart of the proposed baseband modeling framework for the time-domain simulation of photonic systems.

which is defined as *real-valued baseband state-space model*.

It is important to remark the key difference of the novel representation (4.36) with respect to the complex-valued baseband models (4.17) and (4.26). Indeed, the models (4.17) and (4.26) are pure mathematical representations of the system under study: their frequency response is not symmetrical with respect to positive and negative frequencies, and their impulse response is not real: even with real input signals, they can generate a complex output. The novel macromodel (4.36) has a symmetrical frequency response with respect to positive and negative frequencies and its impulse response, input and output signals are real. Hence, it retains all properties of a physical system. It is defined as real-valued baseband state-space model since it can be simulated at the frequencies of the electronic modulating signal(s) rather than at optical frequencies, as for the complex-valued baseband models (4.17) and (4.26), thus achieving a significant speed-up in terms of efficiency with respect to models of photonic systems in the form (4.4) and (4.25). Furthermore, the novel model (4.36) is a system of first-order *real-valued* ODE, thereby it can be solved in a wider range of simulators than the complex models (4.17) and (4.26), which opens up the possibility of directly simulating passive photonic circuits with electronic ones. As remarked in the introduction, photonic-electronic co-simulations are of paramount importance [1–4, 40, 41]. This topic will be investigated in future contributions.

The novel model (4.36) still represents the same system as (4.26), but all the signals (originally complex) are now split into two real-valued signals representing their real and imaginary parts, which are coupled in the system of ODE (4.36). However, the size of (4.36) is doubled compared to (4.26) in terms of number of ports and state variables, since the signals of (4.36) are the real and imaginary parts of the signals in (4.26). This could have an impact in terms of simulation

efficiency, but the model (4.36) maintains a high level of sparsity as well, as indicated in (4.35). It is important to remark that the novel real-valued baseband model (4.36) has been derived in this section starting from model (4.26). However, it can be directly computed starting from the state-space model (4.25), as indicated in equation (4.35). Hence, the calculation of the complex-valued baseband model (4.26) is not necessary to obtain the model (4.36). The flowchart in Fig. 4.22 shows the proposed baseband modeling framework in the case the VF algorithm is adopted to build the model (4.25).

4.8.2 Stability and passivity analysis of the real-valued baseband models

Since the model (4.36) can be considered as a real, linear, and time-invariant system with real input and output signals, the stability and passivity conditions defined for physical linear systems [39], such as (4.25), still hold for the new model (4.36).

The stability of a state-space model can be assessed by the eigenvalue of the matrix $\boldsymbol{A}$, as indicated in Section 4.7: the model is stable if the real part of all the eigenvalues is negative [39]. Let us indicate the eigenvalues of $\hat{\boldsymbol{A}}$ with the symbol $\hat{V}_k$ for $k = 1, \ldots, 2m$ and the eigenvalues of $\boldsymbol{A}$ with V_k for $k = 1, \ldots, m$. Starting from (4.35), it is proven in Appendix 4.11.4 that

$$\hat{V}_{2k-1,2k} = V_k \pm j2\pi f_c. \tag{4.37}$$

Hence, the real part of the eigenvalues of $\hat{\boldsymbol{A}}$ is the same as the eigenvalues of $\boldsymbol{A}$: the model (4.36) is stable if the original model at optical frequencies is stable.

Then, as indicated in Section 4.7, the passivity of the model (4.36) can be verified by means of its Hamiltonian matrix, which can be written as:

$$\hat{\boldsymbol{M}} = \begin{bmatrix} \hat{\boldsymbol{M}}_{11} & \hat{\boldsymbol{M}}_{12} \\ \hat{\boldsymbol{M}}_{21} & \hat{\boldsymbol{M}}_{22} \end{bmatrix}, \tag{4.38}$$

where

$$\hat{\boldsymbol{M}}_{11} = \begin{bmatrix} \boldsymbol{A} - \boldsymbol{B}\boldsymbol{L}^{-1}\boldsymbol{D}^T\boldsymbol{C} & 2\pi f_c \boldsymbol{I}_m \\ -2\pi f_c \boldsymbol{I}_m & \boldsymbol{A} - \boldsymbol{B}\boldsymbol{L}^{-1}\boldsymbol{D}^T\boldsymbol{C} \end{bmatrix},$$
$$\hat{\boldsymbol{M}}_{12} = \begin{bmatrix} -\boldsymbol{B}\boldsymbol{L}^{-1}\boldsymbol{B}^T & \boldsymbol{0} \\ \boldsymbol{0} & -\boldsymbol{B}\boldsymbol{L}^{-1}\boldsymbol{B}^T \end{bmatrix},$$
$$\hat{\boldsymbol{M}}_{21} = \begin{bmatrix} \boldsymbol{C}^T\boldsymbol{Q}^{-1}\boldsymbol{C} & \boldsymbol{0} \\ \boldsymbol{0} & \boldsymbol{C}^T\boldsymbol{Q}^{-1}\boldsymbol{C} \end{bmatrix},$$
$$\hat{\boldsymbol{M}}_{22} = \begin{bmatrix} -\boldsymbol{A}^T + \boldsymbol{C}^T\boldsymbol{D}\boldsymbol{L}^{-1}\boldsymbol{B}^T & 2\pi f_c \boldsymbol{I}_m \\ -2\pi f_c \boldsymbol{I}_m & -\boldsymbol{A}^T + \boldsymbol{C}^T\boldsymbol{D}\boldsymbol{L}^{-1}\boldsymbol{B}^T \end{bmatrix}.$$

It is not surprising that the Hamiltonian matrix for (4.36) can be expressed in terms of block matrices, given that the state-space matrices for the real-valued baseband state-space model are block matrices as well, as indicated in (4.35).

By performing a similarity transformation, the matrix $\bar{\boldsymbol{M}}$ can be obtained

$$\bar{\boldsymbol{M}} = \boldsymbol{P}\hat{\boldsymbol{M}}\boldsymbol{P}^{-1} = \begin{bmatrix} \boldsymbol{M} & 2\pi f_c \boldsymbol{I}_{2m} \\ -2\pi f_c \boldsymbol{I}_{2m} & \boldsymbol{M} \end{bmatrix}, \tag{4.39}$$

where

$$\boldsymbol{P} = \begin{bmatrix} \boldsymbol{I}_m & \boldsymbol{0} & \boldsymbol{0} & \boldsymbol{0} \\ \boldsymbol{0} & \boldsymbol{0} & \boldsymbol{I}_m & \boldsymbol{0} \\ \boldsymbol{0} & \boldsymbol{I}_m & \boldsymbol{0} & \boldsymbol{0} \\ \boldsymbol{0} & \boldsymbol{0} & \boldsymbol{0} & \boldsymbol{I}_m \end{bmatrix}, \tag{4.40}$$

and $\boldsymbol{M}$ is the Hamiltonian matrix of the system (4.25), described in (4.21). Note that, the similarity transformation (4.39) is equivalent to row and column blocks exchanges and it can be derived by simple algebraic manipulations.

Since similarity transformations of matrices do not change their eigenvalues, $\bar{\boldsymbol{M}}$ and $\hat{\boldsymbol{M}}$ share the same set of eigenvalues Λ_k with $k = 1, \ldots, 4m$. Now, by following the procedure described in Appendix 4.11.4, it is proven that

$$\Lambda_{2i-1,2i} = \lambda_i \pm j2\pi f_c, \tag{4.41}$$

where λ_i with $i = 1, \ldots, 2m$ are the eigenvalues of $\boldsymbol{M}$. Equation (4.41) proves that the eigenvalues of $\bar{\boldsymbol{M}}$ and $\hat{\boldsymbol{M}}$ share the same real parts with the ones of $\boldsymbol{M}$: the model (4.36) is passive ($\hat{\boldsymbol{M}}$ has no purely imaginary eigenvalue) if the model (4.25) is passive.

Hence, this section demonstrates that the stability and passivity of the new model (4.36) are directly determined by the properties of the original model (4.25), and the following statements hold:

- one unstable eigenvalue (whose real part is positive) of (4.25) leads to two unstable eigenvalues of the model (4.36).
- one crossover frequency point where a passivity violation occurs for (4.25) leads to two crossover frequency points for the model (4.36).

4.9 Examples on photonic circuits

This section presents two application examples of the proposed modeling and simulation techniques. The scattering parameters of the photonic systems under study are evaluated via the *Caphe* circuit simulator (Luceda Photonics) and electromagnetic simulations in *FDTD Solutions* (Lumerical), while the time-domain simulations are carried out in Matlab on a personal computer with Intel Core i3 processor

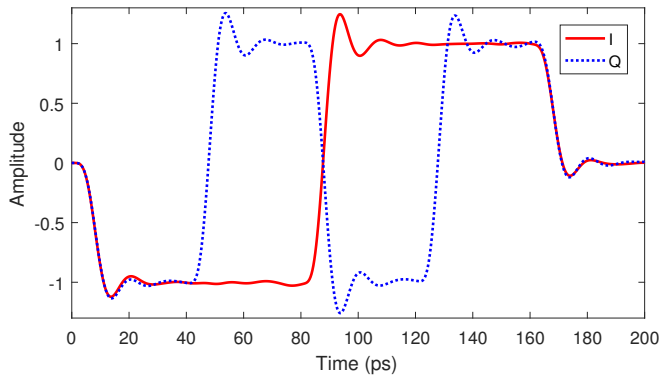

Figure 4.23: Example 4.9.1. The modulating signals: in-phase part $I(t)$ and quadrature part $Q(t)$.

and 8 GB RAM. It is important to remark that, even though Caphe and FDTD Solutions are chosen to estimate the scattering parameters in the proposed examples, there is no limitation on adopting any other simulator.

4.9.1 Lattice filter

In this section, the lattice filter presented in Fig. 4.18 in Section 4.6.3 is studied with the extended baseband modeling techniques.

Let us assume that port $P1$ of the filter is excited by a 4-QAM (*quadrature phase-shift* keying) modulated optical signal with carrier frequency $f_c = 195.11$ THz and the in-phase $I(t)$ and quadrature component $Q(t)$ are four bits sequences (-1, -1, 1, 1) and (-1, 1, -1, 1), respectively, as shown in Fig. 4.23 where overshoot and undershoot are present to mimic realistic RF signals. It is important to remark that any RF signal with generic shape can be adopted here, as long as the chosen modeling frequencies cover the spectrum of the signal.

The scattering parameters of the filter are simulated in Caphe in the frequency range $[f_c - \Delta;\ f_c + \Delta]$, where $\Delta = 380$ GHz, in order to guarantee that the chosen range covers the spectrum of the modulated optical signal. In this example, 181 frequency samples are used and they are uniformly distributed over the frequency range of interest. Adaptive sampling strategies can also be adopted to choose the frequency samples efficiently: more samples are chosen where the frequency response is dynamic, such as resonances, and less are chosen in smooth areas [39]. Next, a state-space model is built with 39 poles via the VF algorithm, achieving a maximum absolute error of less than -50 dB. A standard bottom-up approach is used to select the required number of poles [39, 42]: the initial number of poles is iteratively increased until the desired accuracy of -50 dB is reached. In particu-

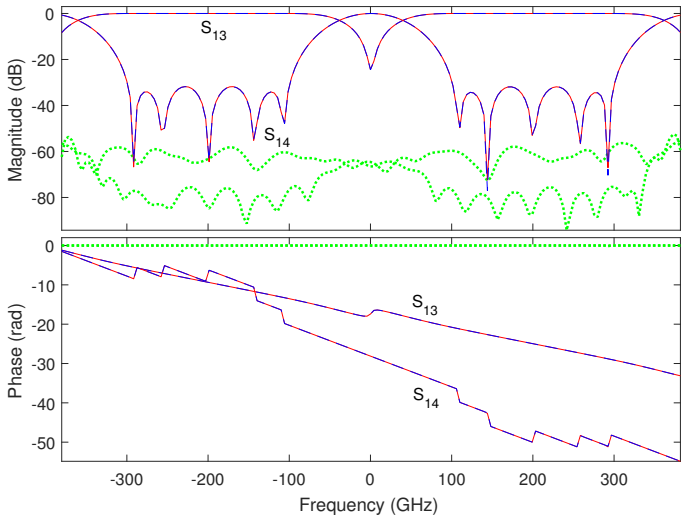

Figure 4.24: Example 4.9.1. Magnitude (top) and phase (bottom) of the lattice filter baseband scattering parameters extracted via Caphe (full blue line) and computed via the complex-valued baseband state-space model (4.26) *(red dashed line), where the green dots represent the corresponding absolute error.*

lar, the state-space model computed is formed only by real-valued matrices, as in (4.25). Note that, the time-domain simulation of this model computed at optical frequencies will be used in the following as a reference to validate the accuracy and the efficiency of the proposed method.

Next, the corresponding complex-valued baseband state-space model in the form (4.26) can be easily computed. The frequency-domain accuracy of such model is illustrated in Fig. 4.24, where a comparison between the model frequency response and the corresponding baseband scattering parameters (obtained by translating the scattering parameters simulated in Caphe into baseband) is shown.

Finally, a real-valued baseband state-space model in the form (4.36) has been computed by following the procedure described in Section 4.8.

The simulations of the three models (namely, (4.25), (4.26), and (4.36)) are carried out with the Matlab routine $lsim$, and require 10 s, 0.12 s and 0.11 s, respectively. The main speed-up factor of the proposed modeling approach is given by the adopted time-step: the model (4.25) requires a time step of 0.25 fs, while the baseband models (4.26) and (4.36) are simulated with a time step of 0.33 ps.

It is important to remark that the output of model (4.26) is a complex signal and its magnitude corresponds to the envelope of the output of model (4.25), as illustrated in Fig. 4.25. Furthermore, it is always possible to analytically reconstruct the port signals of the photonic system under study starting from the time-domain

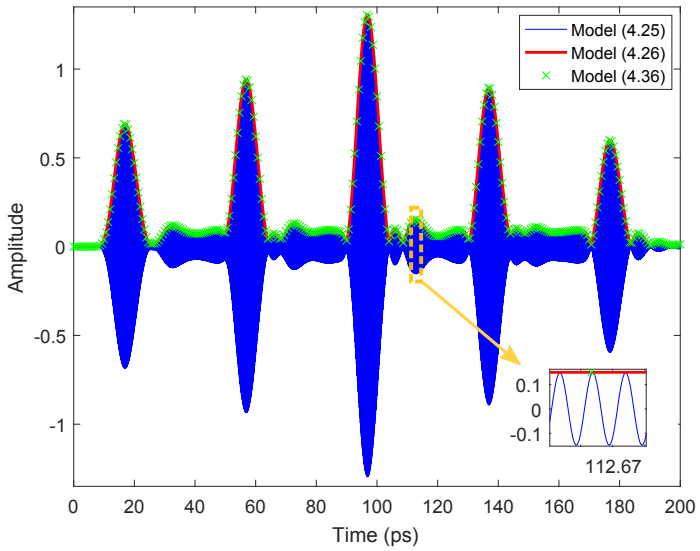

Figure 4.25: Example 4.9.1. Output signal at port $P3$ of the lattice filter. The blue line represents the signal obtained from model (4.25)*, while the red line and green cross represent the the absolute value of the complex signal obtained by the time-domain simulation of* (4.26) *and* (4.36)*.*

simulation of the corresponding baseband equivalent model. Finally, Fig. 4.25 shows the baseband complex signals computed from the outputs of model (4.36), according to (4.32) and (4.33).

It is evident that the time-domain simulation results of the two novel proposed models (4.26) and (4.36) are in excellent agreement with the reference solution obtained via the model (4.25). As additional proof of the accuracy of the proposed modeling strategies, a comparison of the real and imaginary part of the complex baseband signal at port $P4$ obtained by the complex- and real-valued baseband models is shown in Fig. 4.26: the results demonstrate a very good match.

4.9.2 Circuit simulation

The simulation of the photonic circuit shown in Fig. 4.27, formed by two directional couplers and a lattice filter, is described in the following. The lattice filter is the one presented in the previous section, while the two identical directional couplers have 20 μm coupling length, 5 μm bend radius, and 0.15 μm gap between coupling waveguides, whose width is 0.43 μm.

In order to simulate this circuit, the baseband models for each device in Fig. 4.27 are computed first, and then properly connected. Since the 4-QAM modulating

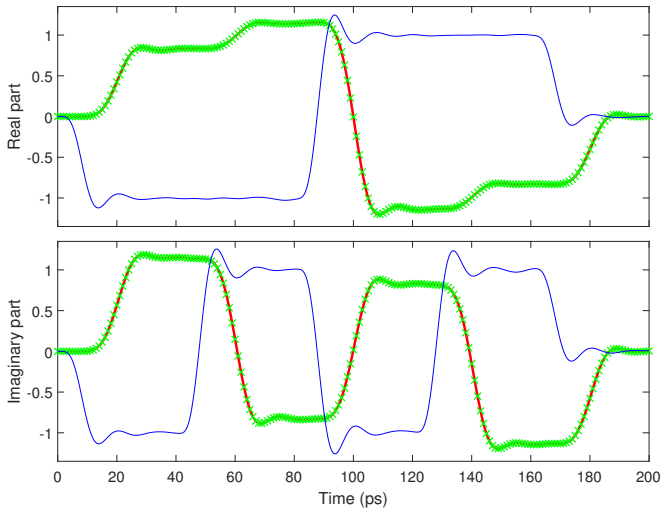

Figure 4.26: Example 4.9.1. Real (top) and imaginary (bottom) parts of the output signal at port $P4$ of the lattice filter obtained via the models (4.26) *and* (4.36)*, where the solid red lines and green crosses represent the results from* (4.26) *and* (4.36)*, respectively, while the blue solid lines are the corresponding real and imaginary parts of the input signal at port P1.*

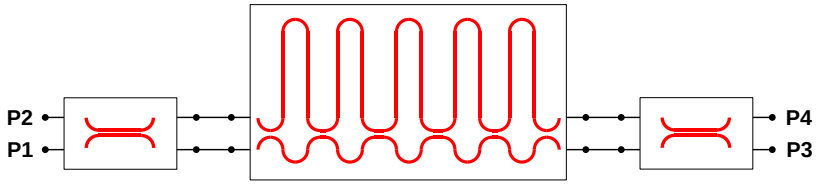

Figure 4.27: Example 4.9.2. The schematic structure of the photonic circuit under study.

signal (with same carrier frequency) described in Section 4.9.1 is used to excite the circuit at port $P1$, the scattering parameters of the directional coupler are evaluated in the Lumerical FDTD solver for the same frequency range used for the lattice filter, namely $[f_c - \Delta;\ f_c + \Delta]$, where $\Delta = 380$ GHz. Considering that the frequency response is rather smooth over the frequency range of interest, only 30 equidistantly spread frequency samples are selected for building the model. It is important to note that the scattering parameters of the lattice filter are evaluated in Caphe and its Caphe model is an ideal model without considering reflections, while the directional coupler is simulated in Lumerical FDTD solver where the reflection at each port is modeled. Figure 4.28 shows the transmissions and reflections characteristics of the whole circuit under study. Then, a state-space model

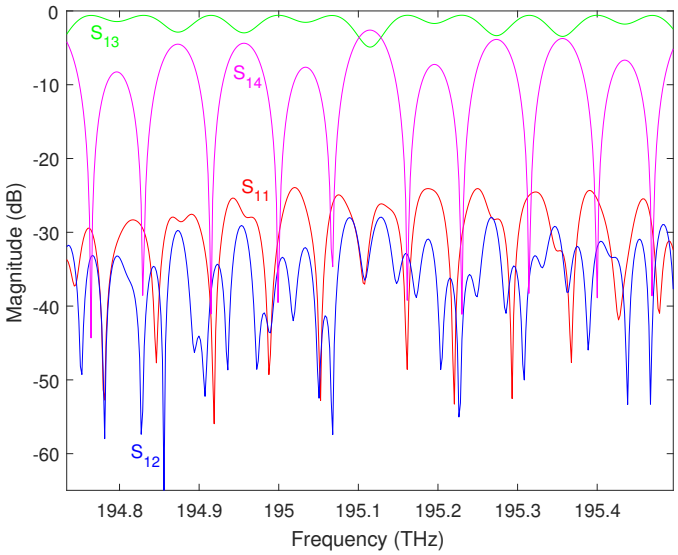

Figure 4.28: Example 4.9.2. Frequency response of the photonic circuit in Fig. 4.27 in the frequency range of interest.

in the form (4.25) is built for the directional coupler via the VF algorithm with 14 poles, achieving an absolute maximum error of less than -50 dB. Finally, the corresponding complex- and real-valued baseband models are computed via the approaches outlined in Sections 4.7 and 4.8, respectively.

Once the models of the lattice filter and directional coupler have been obtained, they can be easily connected in order to describe the input/output behavior of the circuit under study. Figure 4.29 shows an example of the connection of baseband models computed for two-ports devices. It is very intuitive to realize that the forward wave at port 3 in Fig. 4.29 is the backward one for port 2, and vice versa: the corresponding ports of the baseband models must be connected accordingly. The same principle applies to general types of connections (i.e. parallel, feedback, etc.) and for any number of ports. Now, the built complex-valued and real-valued baseband models can be readily connected via the $connect$ routine in Matlab, following the method illustrated in Fig. 4.29, and the time-domain simulation can be performed via the dedicated linear system solver $lsim$. Note that any hierarchical connection can be realized via the $connect$ routine, even if only the cascaded case is shown in this example.

Figure 4.30 shows the magnitude of the complex baseband reflected signal at port $P1$ and transmission signal at port $P3$ obtained with the models (4.26) and (4.36), which again demonstrates the accuracy of the proposed techniques. The

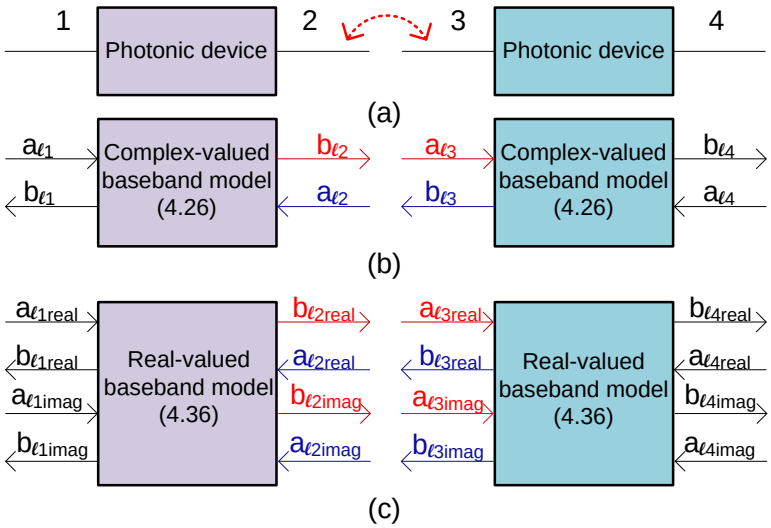

Figure 4.29: Example 4.9.2. Example of the connection of the baseband models of two-ports photonic devices. (a) The physical connection; (b) the connection of the corresponding complex-valued baseband state-space models (4.26)*; (c) the connection of the corresponding real-valued baseband state-space models* (4.36)*.*

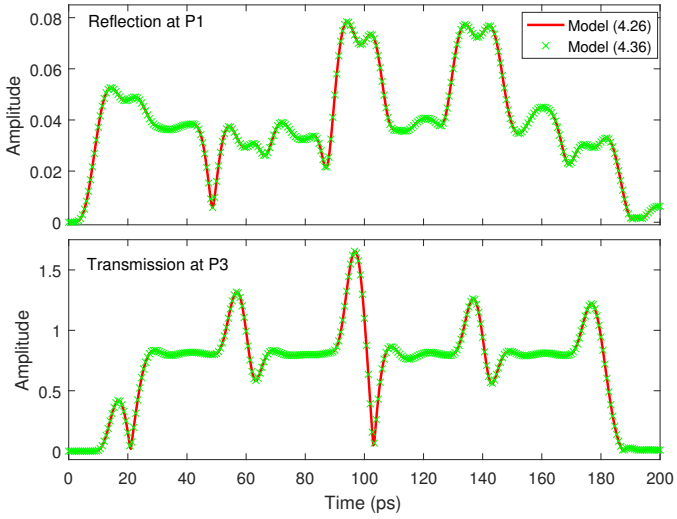

Figure 4.30: Example 4.9.2. The amplitude of the reflected signal at port $P1$ (top) and transmission signal at port $P3$ (bottom) of the circuit obtained from the simulations of the models (4.26) *and* (4.36) *with excitation signal shown in Fig. 4.23.*

simulation of the complex- and real-valued models requires the same time: 0.42 s.

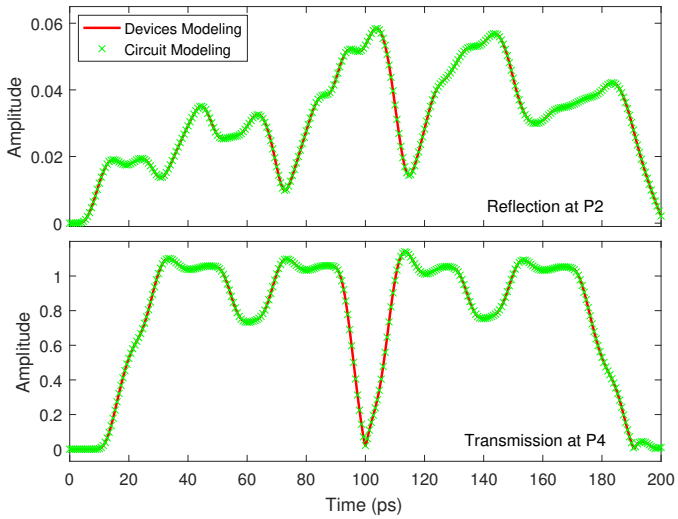

Figure 4.31: Example 4.9.2. The amplitude of the reflected signal at port $P2$ (top) and transmission signal at port $P4$ (bottom) of the circuit obtained by the real baseband model (4.36) *computed via the devices and circuit modeling strategies.*

Rather than modeling each device separately, it is also possible to consider the entire circuit in Fig. 4.27 as a single passive element, described by its scattering parameters. Then, a state-space model in the form (4.25) can be built for the entire circuit with 69 poles via the VF algorithm, achieving a maximum absolute error of less than -50 dB. The corresponding complex- and real-valued baseband models can be calculated as described in Sections 4.7 and 4.8, respectively. Figure 4.31 shows an example of the results of the two modeling strategies considered, namely *devices* and *circuit modeling*: the two approaches are in excellent agreement. This is a remarkable improvement compared with the FIR modeling technique, where the modeling accuracy could decrease significantly when multiples FIR models are connected [5].

The time-domain simulation of the baseband model obtained via the circuit modeling approach requires 0.43 s, a similar computational cost to the devices modeling approach, once again demonstrating the efficiency of the proposed method.

4.10 Conclusion

A novel modeling and simulation technique for general linear and passive photonic components and circuits has been proposed in this chapter, which is flexible, efficient, accurate and robust. Photonics systems can be characterized by the proposed baseband equivalent state-space models via the robust VF algorithm, which

allows for the time-domain simulations to be conducted at baseband rather than at the optical carrier frequency. The outputs of photonic systems can be immediately recovered from the outputs of the corresponding baseband equivalent models, thereby significantly decreasing the simulation time and memory usage. The passivity conditions of the proposed baseband equivalent systems are rigorously discussed and a fast passivity assessment method for the corresponding state-space models is presented in this chapter. For the simulators which can only deal with real-valued models of physical systems, the complex-valued baseband models can now be analytically converted to real-valued ones immediately. The accuracy and efficiency of the proposed approaches are verified by several photonic circuit examples.

4.11 Appendix

4.11.1 Time-domain simulation of baseband equivalent signals and systems

If a system with impulse response $h(t)$ and frequency response $H(f)$ operates in the bandwidth BW around f_c satisfying $f_c >> BW$, then it can be considered as a bandpass system. Now, in a similar manner as with the baseband equivalent signal, a *baseband equivalent system* with impulse response $h_l(t)$ and frequency response $H_l(f)$ can be defined as [25]

$$h_l(t) = \frac{1}{2} h_a(t) e^{-j2\pi f_c} \tag{4.42}$$

$$H_l(f) = H(f + f_c) Step(f + f_c) \tag{4.43}$$

where $h_a(t)$ is the analytic signal of $h(t)$ and is defined in the same way as (4.6).

Compared with the definition of baseband equivalent signals, a factor $1/2$ is introduced into the definition of baseband equivalent systems [25]. Again, the relations between $h(t)$, $\mathcal{H}(h(t))$ and $h_l(t)$ in the time- and frequency-domain are

$$h(t) = 2\Re[h_l(t) e^{j2\pi f_c t}] \tag{4.44}$$

$$\mathcal{H}(h(t)) = 2\Im[h_l(t) e^{j2\pi f_c t}] \tag{4.45}$$

$$H(f) = H_l^*(-f - f_c) + H_l(f - f_c) \tag{4.46}$$

It is important to note that baseband equivalent signals and systems are not physical, but constitute a mathematical representation developed only for simplifying analysis and simulation of bandpass signals and systems, as discussed in the following.

Let us assume that the bandpass input signal, system, and output are $u(t)$, $h(t)$ and $r(t)$, respectively, while their corresponding Fourier transforms are indicated as $U(f)$, $H(f)$ and $R(f)$. Then, the following relations hold

$$\begin{array}{rcl} r(t) & = & h(t) \otimes u(t) \\ R(f) & = & H(f)U(f) \end{array} \tag{4.47}$$

where $\otimes$ represents the convolution operator. Now, the corresponding baseband equivalents of the input signal and system are $u_l(t)$, $h_l(t)$, $U_l(f)$, $H_l(f)$. Hence, the output signal of the baseband equivalent system can be defined as

$$\begin{array}{rcl} r_l(t) & = & h_l(t) \otimes u_l(t) \\ R_l(f) & = & H_l(f)U_l(f) \end{array} \tag{4.48}$$

In the following, it is proven that the output of the baseband equivalent system $r_l(t)$, $R_l(f)$ and the output of the bandpass system $r(t)$, $R(f)$ have the same relations as baseband equivalent and bandpass signals (see (4.11) and (4.13)). Indeed, starting from (4.47) and (4.48), the following relations can be derived [25]:

$$\begin{aligned} R(f) &= \mathscr{F}(r(t)) = H(f)U(f) \\ &= \frac{1}{2}[H_l(f-f_c) + H_l^*(-f-f_c)][U_l(f-f_c) + U_l^*(-f-f_c)] \\ &= \frac{1}{2}[H_l(f-f_c)U_l(f-f_c) + H_l^*(-f-f_c)U_l^*(-f-f_c)] \\ &= \frac{1}{2}[R_l(f-f_c) + R_l^*(-f-f_c)] \\ &= \frac{1}{2}\mathscr{F}(r_l(t)e^{j2\pi f_c t} + r_l^*(t)e^{-j2\pi f_c t}) \\ &= \mathscr{F}(\Re(r_l(t)e^{j2\pi f_c t})) \end{aligned} \tag{4.49}$$

where the symbol $\mathscr{F}$ represents the Fourier transform operator. Equation (4.49) clearly demonstrates that $r_l(t)$ is the complex envelope of the bandpass system output: $r(t)$ can be immediately obtained from $r_l(t)$ [25].

4.11.2 Baseband equivalent "shifted" system

In the following, we prove that the baseband equivalent "shifted" system represented by (4.17) is equivalent to the based equivalent system $h_l(t)$ in (4.42), in the sense of time-domain simulations.

According to Section 4.3.2, the transfer function $\tilde{H}_l(f)$ and impulse response $\tilde{h}_l(t)$ of the proposed baseband equivalent state-space model (4.17) can be described as

$$\tilde{H}_l(f) = H(f+f_c) = H_l(f+2f_c) + H_l(f) \tag{4.50}$$

$$\tilde{h}_l(t) = h(t)e^{-j2\pi f_c t} \tag{4.51}$$

since it is obtained by shifting all the poles of the corresponding state-space model of bandpass system by $j2\pi f_c$, considering that $\boldsymbol{A}$ is a diagonal complex-valued matrix with all the poles as diagonal elements.

By comparing the results obtained in (4.50) and (4.51) to the baseband equivalent system definition given in (4.42) and (4.43), one difference is clear: only the frequency response of $H(f)$ at *positive frequencies* is shifted by f_c in the definitions (4.42) and (4.43), while in (4.50) and (4.51) the *entire* frequency response of the bandpass system considered is shifted. This difference is illustrated in Fig. 4.32.

Then it is proven that the relation (4.49) still holds for baseband equivalent "shifted" systems calculated by means of (4.50) and (4.51). Indeed, the output signals of the bandpass system in the frequency-domain can be written as

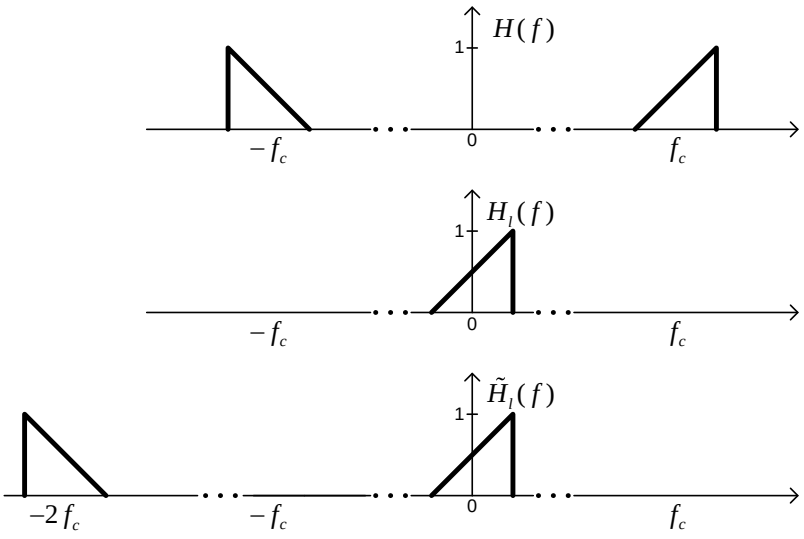

Figure 4.32: Spectrum of bandpass system $H(f)$, baseband equivalent system $H_l(f)$, and baseband equivalent "shifted" system $\tilde{H}_l(f)$.

$$
\begin{aligned}
R(f) &= \mathscr{F}(r(t)) = H(f)U(f) \\
&= \frac{1}{2}\tilde{H}_l(f-f_c)[U_l(f-f_c)+U_l^*(-f-f_c)] \\
&= \frac{1}{2}[\tilde{H}_l(f-f_c)U_l(f-f_c)+\tilde{H}_l^*(-f-f_c)U_l^*(-f-f_c)] \\
&= \frac{1}{2}[H_l(f-f_c)U_l(f-f_c)+H_l^*(-f-f_c)U_l^*(-f-f_c)] \\
&= \frac{1}{2}[R_l(f-f_c)+R_l^*(-f-f_c)] \\
&= \frac{1}{2}\mathscr{F}(r_l(t)e^{j2\pi f_c t}+r_l^*(t)e^{-j2\pi f_c t}) \\
&= \mathscr{F}(\Re(r_l(t)e^{j2\pi f_c t}))
\end{aligned}
\tag{4.52}
$$

where

$$
\begin{aligned}
H(f) &= \tilde{H}_l(f-f_c) \\
H(f) &= H^*(-f) \\
\tilde{H}_l(f-f_c) &= \tilde{H}_l^*(-f-f_c)
\end{aligned}
\tag{4.53}
$$

$$
\begin{aligned}
\tilde{H}_l(f-f_c)U_l(f-f_c) &= H_l(f-f_c)U_l(f-f_c) \\
\tilde{H}_l^*(-f-f_c)U_l^*(-f-f_c) &= H_l^*(-f-f_c)U_l^*(-f-f_c)
\end{aligned}
\tag{4.54}
$$

Note that equation (4.54) holds because $\tilde{H}_l(f-f_c)$ and $\tilde{H}_l^*(-f-f_c)$ have a non-zero frequency response at both positive and negative frequencies, while $U_l(f-f_c)$ and $U_l^*(-f-f_c)$ have a non-zero frequency response only at positive and negative frequencies, respectively.

Finally, equation (4.52) demonstrates that the state-space representation (4.17) of the baseband equivalent "shifted" system can effectively be used to replace the expensive time-domain simulations of the bandpass system.

4.11.3 Hamiltonian matrix of baseband equivalent system

Following the procedure in [18] and assuming that $\boldsymbol{S}_l(s)$ is the scattering matrix of a baseband equivalent system, such system is switching from a non-passive to a passive state (or the other way around) at the frequencies where $\boldsymbol{I}-\boldsymbol{S}_l^H(s)\boldsymbol{S}_l(s)=0$. To identify these frequencies, with input $|\boldsymbol{u}_l|\neq 0$, we write

$$\boldsymbol{w}_l = (\boldsymbol{I}-\boldsymbol{S}_l^H(s)\boldsymbol{S}_l(s))\boldsymbol{u}_l = 0 \tag{4.55}$$

$$\boldsymbol{y}_{l1} = \boldsymbol{S}_l(s)\boldsymbol{u}_l \tag{4.56}$$

$$\boldsymbol{y}_{l2} = \boldsymbol{S}_l^H(s)\boldsymbol{y}_{l1} \tag{4.57}$$

$$\boldsymbol{w}_l = \boldsymbol{u}_l - \boldsymbol{y}_{l2} = 0 \tag{4.58}$$

Let us assume that $\boldsymbol{S}_l(s)$ has state-space parameters $\boldsymbol{A}_l$, $\boldsymbol{B}_l$, $\boldsymbol{C}_l$, $\boldsymbol{D}_l$; while $\boldsymbol{A}_l^H, \boldsymbol{C}_l^H, \boldsymbol{B}_l^H, \boldsymbol{D}_l^H$ are the state-space parameters of $\boldsymbol{S}_l^H(s)$. Then, equations (4.56) and (4.57) can be written in the form

$$j\omega \boldsymbol{x}_{l1} = \boldsymbol{A}_l \boldsymbol{x}_{l1} + \boldsymbol{B}_l \boldsymbol{u}_l \tag{4.59}$$

$$\boldsymbol{y}_{l1} = \boldsymbol{C}_l \boldsymbol{x}_{l1} + \boldsymbol{D}_l \boldsymbol{u}_l \tag{4.60}$$

$$-j\omega \boldsymbol{x}_{l2} = \boldsymbol{A}_l^H \boldsymbol{x}_{l2} + \boldsymbol{C}_l^H \boldsymbol{y}_{l1} \tag{4.61}$$

$$\boldsymbol{y}_{l2} = \boldsymbol{B}_l^H \boldsymbol{x}_{l2} + \boldsymbol{D}_l^H \boldsymbol{y}_{l1} \tag{4.62}$$

which can be simplified as

$$j\omega \begin{bmatrix} \boldsymbol{x}_{l1} \\ \boldsymbol{x}_{l2} \end{bmatrix} = \begin{bmatrix} \boldsymbol{A}_l & 0 \\ -\boldsymbol{C}_l^H \boldsymbol{C}_l & -\boldsymbol{A}_l^H \end{bmatrix} \begin{bmatrix} \boldsymbol{x}_{l1} \\ \boldsymbol{x}_{l2} \end{bmatrix} + \begin{bmatrix} \boldsymbol{B}_l \\ -\boldsymbol{C}_l^H \boldsymbol{D}_l \end{bmatrix} \boldsymbol{u}_l \tag{4.63}$$

$$\begin{bmatrix} \boldsymbol{D}_l^H \boldsymbol{C}_l & \boldsymbol{B}_l^H \end{bmatrix} \begin{bmatrix} \boldsymbol{x}_{l1} \\ \boldsymbol{x}_{l2} \end{bmatrix} = (\boldsymbol{I} - \boldsymbol{D}_l^H \boldsymbol{D}_l)\boldsymbol{u}_l \tag{4.64}$$

Combining (4.63) and (4.64) leads to

$$j\omega \begin{bmatrix} \boldsymbol{x}_{l1} \\ \boldsymbol{x}_{l2} \end{bmatrix} = \begin{bmatrix} \boldsymbol{A}_l - \boldsymbol{B}_l \boldsymbol{L}_l^{-1} \boldsymbol{D}_l^H \boldsymbol{C}_l & -\boldsymbol{B}_l \boldsymbol{L}_l^{-1} \boldsymbol{B}_l^H \\ \boldsymbol{C}_l^H \boldsymbol{Q}_l^{-1} \boldsymbol{C}_l & -\boldsymbol{A}_l^H + \boldsymbol{C}_l^H \boldsymbol{D}_l \boldsymbol{L}_l^{-1} \boldsymbol{B}_l^H \end{bmatrix} \begin{bmatrix} \boldsymbol{x}_{l1} \\ \boldsymbol{x}_{l2} \end{bmatrix} \tag{4.65}$$

where

$$\boldsymbol{L}_l = \boldsymbol{D}_l^H \boldsymbol{D}_l - \boldsymbol{I} \tag{4.66}$$

$$\boldsymbol{Q}_l = \boldsymbol{D}_l \boldsymbol{D}_l^H - \boldsymbol{I} \tag{4.67}$$

Thus, the Hamiltonian matrix of baseband equivalent systems is

$$\boldsymbol{M}_l = \begin{bmatrix} \boldsymbol{A}_l - \boldsymbol{B}_l \boldsymbol{L}_l^{-1} \boldsymbol{D}_l^H \boldsymbol{C}_l & -\boldsymbol{B}_l \boldsymbol{L}_l^{-1} \boldsymbol{B}_l^H \\ \boldsymbol{C}_l^H \boldsymbol{Q}_l^{-1} \boldsymbol{C}_l & -\boldsymbol{A}_l^H + \boldsymbol{C}_l^H \boldsymbol{D}_l \boldsymbol{L}_l^{-1} \boldsymbol{B}_l^H \end{bmatrix} \tag{4.68}$$

and its imaginary eigenvalues $j\omega$ give the angular frequencies ω where (4.55) is satisfied and the matrix $\boldsymbol{I} - \boldsymbol{S}_l^H(s)\boldsymbol{S}_l(s)$ is singular.

Finally, by indicating the eigenvalues of $\boldsymbol{M}_l$ with the symbol λ_{li}, the following equation holds

$$\lambda_{li} \begin{bmatrix} \boldsymbol{x}_{l1} \\ \boldsymbol{x}_{l2} \end{bmatrix} = \boldsymbol{M}_l \begin{bmatrix} \boldsymbol{x}_{l1} \\ \boldsymbol{x}_{l2} \end{bmatrix} \tag{4.69}$$

Now, assuming that exists a matrix $\boldsymbol{M}$ with eigenvalues λ_i satisfying $\boldsymbol{M}_l = \boldsymbol{M} - j2\pi f_c \boldsymbol{I}$, leads to

$$\lambda_i \begin{bmatrix} \boldsymbol{x}_{l1} \\ \boldsymbol{x}_{l2} \end{bmatrix} = \boldsymbol{M} \begin{bmatrix} \boldsymbol{x}_{l1} \\ \boldsymbol{x}_{l2} \end{bmatrix} = \lambda_{li} \begin{bmatrix} \boldsymbol{x}_{l1} \\ \boldsymbol{x}_{l2} \end{bmatrix} + j2\pi f_c \begin{bmatrix} \boldsymbol{x}_{l1} \\ \boldsymbol{x}_{l2} \end{bmatrix} \tag{4.70}$$

which indicates that

$$\lambda_{li} = \lambda_i - j2\pi f_c, \qquad \text{for } i = 1, \ldots, 2m \tag{4.71}$$

4.11.4 Eigenvalues calculation

Indicating one of the eigenvalues of $\hat{\boldsymbol{A}}$ with $\hat{V}_k$ and considering (4.35), the following holds:

$$\left|\hat{\boldsymbol{A}} - \hat{V}_k \boldsymbol{I}_{2m}\right| = \left|\begin{bmatrix} \boldsymbol{A} - \hat{V}_k \boldsymbol{I}_m & 2\pi f_c \boldsymbol{I}_m \\ -2\pi f_c \boldsymbol{I}_m & \boldsymbol{A} - \hat{V}_k \boldsymbol{I}_m \end{bmatrix}\right| = 0, \tag{4.72}$$

where $|\cdot|$ stands for the determinant of a matrix. Thanks to (4.28), equation (4.72) can be written as

$$\left|\begin{bmatrix} \boldsymbol{T}(\boldsymbol{V} - \hat{V}_k \boldsymbol{I}_m)\boldsymbol{T}^{-1} & 2\pi f_c \boldsymbol{I}_m \\ -2\pi f_c \boldsymbol{I}_m & \boldsymbol{T}(\boldsymbol{V} - \hat{V}_k \boldsymbol{I}_m)\boldsymbol{T}^{-1} \end{bmatrix}\right| = 0. \tag{4.73}$$

Since the determinant operator in (4.73) is applied to a block matrix, it is possible to write equation (4.73) as [43]

$$\left|\boldsymbol{T}(\boldsymbol{V} - \hat{V}_k \boldsymbol{I}_m)^2 \boldsymbol{T}^{-1} + (2\pi f_c)^2 \boldsymbol{I}_m\right| = 0, \tag{4.74}$$

leading to

$$\left|\boldsymbol{T}\left((\boldsymbol{V} - \hat{V}_k \boldsymbol{I}_m)^2 + (2\pi f_c)^2 \boldsymbol{I}_m\right)\boldsymbol{T}^{-1}\right| = 0. \tag{4.75}$$

Hence, there must be a diagonal element V_i in $\boldsymbol{V}$ satisfying

$${V_i}^2 - 2V_i\hat{V}_k + \hat{V}_k^2 + (2\pi f_c)^2 = 0. \tag{4.76}$$

Solving (4.76) for $\hat{V}_k$ gives

$$\hat{V}_k = \begin{cases} V_i + j2\pi f_c \\ V_i - j2\pi f_c \end{cases}, \tag{4.77}$$

which indicates that the eigenvalues of $\hat{\boldsymbol{A}}$ can be obtained by shifting the eigenvalues of $\boldsymbol{A}$ along the imaginary axis in the complex plane by $\pm j2\pi f_c$.

References

[1] W. Bogaerts and L. Chrostowski. *Silicon photonics circuit design: methods, tools and challenges*. Laser Photon Rev., 12(4):1700237, 2018.

[2] Z. Zhang, R. Wu, Y. Wang, C. Zhang, E. J. Stanton, C. L. Schow, K. T. Cheng, and J. E. Bowers. *Compact Modeling for Silicon Photonic Heterogeneously Integrated Circuits*. J. Lightw. Technol., 35(14):2973–2980, Jul. 2017.

[3] C. Sorace-Agaskar, J. Leu, M. R. Watts, and V. Stojanovic. *Electro-optical co-simulation for integrated CMOS photonic circuits with VerilogA*. Opt. Exp., 23(21):27180–27203, Oct. 2015.

[4] P. Gunupudi, T. Smy, J. Klein, and Z. J. Jakubczyk. *Self-Consistent Simulation of Opto-Electronic Circuits Using a Modified Nodal Analysis Formulation*. IEEE Trans. Adv. Packag., 33(4):979–993, Nov. 2010.

[5] S. Mingaleev, A. Richter, E. Sokolov, C. Arellano, and I. Koltchanov. *Towards an automated design framework for large-scale photonic integrated circuits*. Proc. SPIE, 9516:951602, 2015.

[6] J. Pond, C. Cone, L. Chrostowski, J. Klein, J. Flueckiger, A. Liu, D. McGuire, and X. Wang. *A complete design flow for silicon photonics*. Proc. SPIE, 9133:913310, 2014.

[7] `www.vpiphotonics.com/Tools/PhotonicCircuits/Features/`.

[8] `www.photond.com/products/fimmprop/fimmprop_features_50.htm`.

[9] B. Gustavsen and A. Semlyen. *Rational approximation of frequency domain responses by Vector Fitting*. IEEE Trans. Power Del., 14(3):1052–1061, Jul. 1999.

[10] G. Antonini. *SPICE equivalent circuits of frequency-domain responses*. IEEE Trans. Electromagn. Compat., 45(3):502–512, Aug. 2003.

[11] A. Chinea, S. Grivet-Talocia, H. Hu, P. Triverio, D. Kaller, C. Siviero, and M. Kindscher. *Signal Integrity Verification of Multichip Links Using Passive Channel Macromodels*. IEEE Trans. Compon. Packag. Manuf. Technol., 1(6):920–933, Jun. 2011.

[12] D. Spina, F. Ferranti, G. Antonini, T. Dhaene, L. Knockaert, and D. Vande Ginste. *Time-Domain Green's Function-Based Parametric Sensitivity Analysis of Multiconductor Transmission Lines*. IEEE Trans. Compon. Packag. Manuf. Technol., 2(9):1510–1517, Sep. 2012.

[13] M. Sahouli and A. Dounavis. *An Instrumental-Variable QR Decomposition Vector-Fitting Method for Modeling Multiport Networks Characterized by Noisy Frequency Data*. IEEE Microw. Compon. Lett., 26(9):645–647, Sep. 2016.

[14] S. Grivet-Talocia and B. Gustavsen. *Black-box macromodeling and its EMC applications*. IEEE Electromagn. Compat. Mag., 5(3):71–78, 3rd Quart. 2016.

[15] L. Chrostowski and M. Hochberg. *Silicon Photonics Design: From Devices to Systems*. Cambridge University Press, 2015.

[16] D. Saraswat, R. Achar, and M. S. Nakhla. *A fast algorithm and practical considerations for passive macromodeling of measured/simulated data*. IEEE Trans. Adv. Packag., 27(1):57–70, Feb 2004.

[17] D. Deschrijver, M. Mrozowski, T. Dhaene, and D. De Zutter. *Macromodeling of Multiport Systems Using a Fast Implementation of the Vector Fitting Method*. IEEE Microw. Compon. Lett., 18(6):383–385, Jun. 2008.

[18] B. Gustavsen and A. Semlyen. *Fast Passivity Assessment for S-Parameter Rational Models Via a Half-Size Test Matrix*. IEEE Trans. Microw. Theory Techn., 56(12):2701–2708, Dec. 2008.

[19] D. Deschrijver, and T. Dhaene. *Fast Passivity Enforcement of S-Parameter Macromodels by Pole Perturbation*. IEEE Trans. Microw. Theory Techn., 57(3):620–626, Mar. 2009.

[20] R. H. Muller. *Definitions and conventions in ellipsometry*. Surf. Sci., 16:14 – 33, 1969.

[21] R. Atkinson and P. H. Lissberger. *Sign conventions in magneto-optical calculations and measurements*. Appl. Opt., 31(28):6076–6081, Oct. 1992.

[22] S. Grivet-Talocia and A. Ubolli. *On the generation of large passive macromodels for complex interconnect structures*. IEEE Trans. Adv. Packag., 29(1):39–54, Feb. 2006.

[23] D. G. Schultz and J. L. Melsa. *State Functions and Linear Control Systems*. McGrawHill, 1967.

[24] J. C. Butcher. *Numerical Methods for Ordinary Differential Equations*. John Wiley and Sons, 2003.

[25] M. C. Jeruchim, P. Balaban, and K. S. Shanmugan. *Simulation of communication systems: modeling, methodology and techniques*. Springer, 2006.

[26] J. B. King and T. J. Brazil. *Time-domain simulation of passband S-parameter networks using complex baseband vector fitting*. In Integrated Nonlinear Microwave and Millimetre-wave Circuits Workshop (INMMiC), pages 1–4, Apr. 2017.

[27] D. Youla, L. Castriota, and H. Carlin. *Bounded real scattering matrices and the foundations of linear passive network theory*. IRE Transactions on Circuit Theory, 6(1):102–124, 1959.

[28] P. Triverio, S. Grivet-Talocia, M. S. Nakhla, F. G. Canavero, and R. Achar. *Stability, Causality, and Passivity in Electrical Interconnect Models*. IEEE Trans. Adv. Packag., 30(4):795–808, Nov. 2007.

[29] R. W. Newcomb. *On the energy in passive systems*. Proc. IEEE, 53(10):1651–1652, Oct. 1965.

[30] R. Nedunuri. *On the Definition of Passivity*. IEEE Trans. Circuit Theory, 19(1):72–72, Jan. 1972.

[31] M. R. Wohlers. *Lumped and Distributed Passive Networks*. Academic, New York, 1969.

[32] S. Boyd and L. O. Chua. *On the passivity criterion for LTI N-ports*. Int. J. Circ. Theor. App., 10(4):323–333, 1982.

[33] B. Gustavsen. *Fast Passivity Enforcement for S-Parameter Models by Perturbation of Residue Matrix Eigenvalues*. IEEE Trans. Adv. Packag., 33(1):257–265, Feb. 2010.

[34] `www.lucedaphotonics.com`.

[35] K. Jinguji and M. Kawachi. *Synthesis of coherent two-port lattice-form optical delay-line circuit*. J. Lightw. Technol., 13(1):73–82, Jan. 1995.

[36] S. Suzuki, Y. Inoue, and T. Kominato. *High-density integrated* 1×16 *optical FDM multi/demultiplexer*. In Proc. IEEE LEOS Conf., volume 2, pages 263–264, Oct. 1994.

[37] Y. Xing, D. Spina, A. Li, T. Dhaene, and W. Bogaerts. *Stochastic collocation for device-level variability analysis in integrated photonics*. Photon. Res., 4(2):93–100, Apr. 2016.

[38] R. Achar and M. S. Nakhla. *Simulation of high-speed interconnects*. Proc. IEEE, 89(5):693–728, May 2001.

[39] S. Grivet-Talocia and B. Gustavsen. *Passive Macromodeling: Theory and Applications*. Hoboken, NJ, USA: Wiley, 2015.

[40] S. Tanaka, T. Usuki, and Y. Tanaka. *Accurate SPICE Model of Forward-Biased Silicon PIN MachZehnder Modulator for an Energy-Efficient Multi-level Transmitter*. J. Lightw. Technol., 36(10):1959–1969, May 2018.

[41] B. Wang, C. Li, C. Chen, K. Yu, M. Fiorentino, R. G. Beausoleil, and S. Palermo. *A Compact Verilog-A Model of Silicon Carrier-Injection Ring Modulators for Optical Interconnect Transceiver Circuit Design*. J. Lightw. Technol., 34(12):2996–3005, Jun. 2016.

[42] N. Stevens, D. Deschrijver, and T. Dhaene. *Fast automatic order estimation of rational macromodels for signal integrity analysis*. In IEEE Workshop on Signal Propagation on Interconnects, pages 89–92, Genova, Italy, May 2007.

[43] P. D. Powell. *Calculating determinants of block matrices*. https://arxiv.org/abs/1112.4379, 2011.

5

Complex Vector Fitting-Based Baseband Modeling of Linear Photonic Circuits

Y. Ye, D. Spina, D. Deschrijver, W. Bogaerts, and T. Dhaene, "Compact baseband modeling of linear photonic circuits via complex vector fitting," Under review.

Abstract

In this chapter, a novel baseband macromodeling framework for linear passive photonic circuits is proposed, able to build accurate and compact models while taking into account the nonidealities, such as higher-order dispersion and wavelength dependent losses of the circuits. Compared to a previous modeling method based on the Vector Fitting (VF) algorithm in Chapter 4, the proposed modeling approach introduces a novel Complex Vector Fitting (CVF) technique. It can generate a half-size state-space model for the same applications, thereby achieving a major improvement in efficiency of the time-domain simulations. The proposed modeling framework requires only measured or simulated scattering parameters as input, which are widely used to represent linear and passive systems. Three photonic circuits are studied to demonstrate the accuracy and efficiency of the proposed technique.

5.1 Introduction

In order to build time-domain models of linear and passive photonic circuits, which take into account the imperfections such as higher-order dispersion and wavelength dependent losses, in Chapter 4 (which is formed of [1, 2]), a baseband modeling approach was proposed to build state-space model from the scattering parameters via the robust *Vector Fitting* (VF) technique [3–5]. Such model is inherently a system of first-order ordinary differential equations (ODEs) and can be efficiently simulated in ODE solvers. In this chapter, a novel alternative approach is presented, called *Complex Vector Fitting* (CVF), which preserves all the advantages of the previous methods in Chapter 4, but generates more compact baseband state-space models that are only half the size of the corresponding models obtained in Chapter 4. Note that this reduces the simulation time by, at least, a factor of two [6]. This is a significant advantage when considering complex systems comprised of a large number of passive components. However, the proposed models are complex-valued systems and can only be adopted in simulators supporting complex-valued signals and matrices. Since many solver techniques are developed and optimized for real-valued systems, such as SPICE and Verilog-A, it is demonstrated that such stable and passive complex-valued baseband model can be directly converted into a corresponding real-valued state-space representation, whose stability and passivity are preserved by construction.

The chapter is organized as follows. Section 5.2 presents an overview on baseband signals and systems. The novel compact baseband modeling approach is presented in Section 5.3, while its passivity assessment and enforcement are studied in Section 5.4. Section 5.5 compares the proposed technique with the previous one in Chapter 4. The real-valued baseband model is derived in Section 5.6 and its properties are rigorously discussed. Finally, Section 5.7 presents three photonic circuits examples, and conclusions are drawn in Section 5.8.

5.2 Problem statement

Photonic circuits are characterized in the optical frequency range: for telecommunication applications, this is typically defined as $[187;\ 200]$ THz, which corresponds to wavelengths in the range of $[1.5;\ 1.6]$ μm. A direct time-domain simulation at this overwhelmingly high frequency range is impractical in terms of computational time and memory requirements [1, 7], especially for large and complex PICs. In particular, the transmitted signals in photonic systems are usually defined as amplitude and/or phase modulated optical signals in the form

$$a(t) = A(t)\cos\left(2\pi f_c t + \phi(t)\right), \tag{5.1}$$

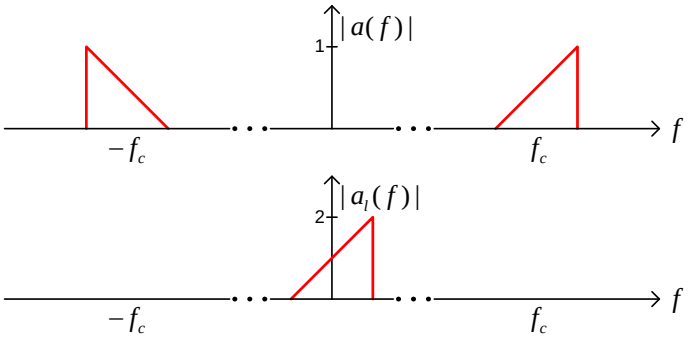

Figure 5.1: Spectrum of the modulated optical signal (top) and its baseband equivalent signal (bottom).

where f_c is the optical carrier frequency, while $A(t)$ and $\phi(t)$ are the time-varying amplitude and phase, respectively, which are radio frequency (RF) modulating signals. Hence, the spectrum of $a(t)$ is centered around the optical carrier frequency and its bandwidth is relatively small compared to f_c. The signals in the form (5.1) are called *bandpass signals* [8]. Analogously, general linear and passive photonic circuits that deal with signals in the form (5.1) can be considered as *bandpass systems*.

In this scenario, time-domain simulations of bandpass photonic circuits have to be carried out with very small time steps due to the large carrier frequency, whereas the *baseband* modeling and simulation approach can adopt relatively large time steps to significantly increase the efficiency without losing accuracy [1, 8]. The main idea is to "remove" the optical carrier frequency from the bandpass signal $a(t)$ by deriving a corresponding baseband equivalent signal $a_l(t)$ as [8]

$$a_l(t) = A(t)e^{j\phi(t)}, \tag{5.2}$$

which represents the complex envelope of the signal $a(t)$. The relation between $a(t)$ and $a_l(t)$ in the frequency domain is more intuitive and is illustrated in Fig. 5.1. The baseband equivalents for bandpass systems can be defined in a similar way, shown in Fig. 5.2, where $S(f)$ is the frequency response of the bandpass system, while $S_l(f)$ is its baseband equivalent. If $a(t)$ is the port signal of the bandpass system $S(f)$, $a_l(t)$ can be considered as the port signal of the baseband equivalent system $S_l(f)$. Interested readers are referred to [8] for more details about the definition and derivation of baseband equivalent signals and systems. One important property of the baseband modeling and simulation approach is that the port signals (in the form (5.1)) of the bandpass photonic circuits can be analytically recovered from their baseband equivalents (in the form (5.2)) [1, 8].

It is easy to observe that $S_l(f)$ is simply equal to $S(f)$ at the positive frequencies shifted by $-f_c$. As shown in Fig. 5.2, $S_l(f)$ is a mathematical representation

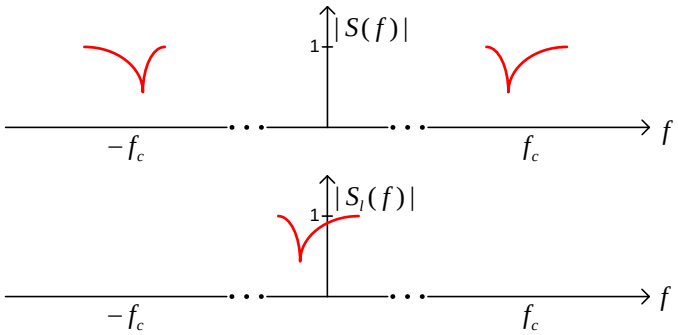

Figure 5.2: Spectrum of bandpass systems (top) and the corresponding baseband equivalent systems (bottom).

of a physical system that has an asymmetric frequency response with regard to the positive and negative frequencies. Therefore, it also has a complex-valued impulse response in the time domain. Directly computing a model of $S_l(f)$ that can be used for time-domain simulation is a challenging problem. In the next two sections, a novel methodology to compute stable and passive baseband models of $S_l(f)$ in state-space form is proposed.

5.3 Pole-residue modeling via Complex Vector Fitting

As described in Section 5.1, the modeling process starts from the scattering parameters in order to take into account non-ideal behaviours such as higher-order dispersion and wavelength dependent losses. Hence, let us assume that the scattering parameters of the photonic circuit under study have been obtained (via simulations or measurements) for a discrete set of frequency values in the bandwidth of interest for the application considered: $\boldsymbol{S}(f_r)$ for $r = 1, \ldots, R$.

Next, shifting $\boldsymbol{S}(f_r)$ towards 0 Hz by the carrier frequency f_c leads to the baseband scattering parameters $\boldsymbol{S}_l(f_i)$, as shown in Fig. 5.3 where $f_i = f_r - f_c$. Then, the CVF algorithm is developed to calculate a pole-residue model of $\boldsymbol{S}_l(f_i)$ as

$$\boldsymbol{S}_l(s) = \sum_{k=1}^{K} \frac{\boldsymbol{R}_k}{s - p_k} + \boldsymbol{D}, \tag{5.3}$$

where $s = j2\pi f$ is the Laplace variable, p_k are the poles, which can be either real or complex, and $\boldsymbol{R}_k$ are the corresponding residues, while $\boldsymbol{D}$ is a real matrix. This form is very similar to pole-residue models that can be computed by the well known VF algorithm [3, 4], which was proposed two decades ago and is

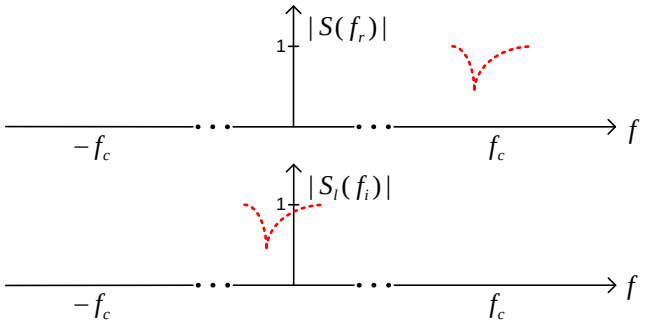

Figure 5.3: The simulated or measured scattering parameters at a set of discrete frequency samples (top) and the corresponding baseband scattering parameters (bottom).

widely used in the electronic field to build pole-residue models for linear passive distributed devices and systems represented by scattering parameters. There are several versions of the VF algorithm, that adopt different modeling strategies [3, 9, 10] and passivity enforcement methods [5, 11–14]. In this work, the CVF is a variant of the VF algorithm available at [15], which implements the techniques in [3–5, 16]. Since VF has been extensively studied in the past two decades, and the proposed CVF shares several similarities with it, only the differences between them that are relevant for our application will be discussed. Interested readers are referred to [3–5, 16] for a thorough understanding of the VF modeling approach.

In particular, both CVF and VF adopt pole-residue models formed by real and complex poles having a negative real part, in order to guarantee the stability of the model [17]. However, the complex poles and the corresponding residues computed via VF must always occur in complex conjugate pairs, for example

$$\begin{aligned} p_k^{VF} &= -\alpha + j\beta, \qquad & p_{k+1}^{VF} &= -\alpha - j\beta \\ \boldsymbol{R}_k^{VF} &= \boldsymbol{\eta} + j\boldsymbol{\gamma}, \qquad & \boldsymbol{R}_{k+1}^{VF} &= \boldsymbol{\eta} - j\boldsymbol{\gamma} \end{aligned} \tag{5.4}$$

where k is the pole and residue index in (5.3), α is a real positive scalar forcing all the poles in left hand side of the complex plane (for stability), β is a (positive or negative) real scalar, while $\boldsymbol{\eta}$ and $\boldsymbol{\gamma}$ are real matrices.

The frequency response of physical linear systems is always symmetric about zero (even amplitude and odd phase). The complex conjugate constraint implemented in VF allows to preserve this property, such that the corresponding impulse response in the time-domain is guaranteed to be real-valued. However, baseband systems are non-physical and have an asymmetric frequency response with respect to 0 Hz by construction. Therefore, VF cannot be applied to model such a system *directly*, as described in Section 5.5.

In order to overcome this problem, the complex conjugate constraint is removed in the CVF algorithm: the corresponding complex poles and residues are

given by

$$\begin{aligned} p_k &= -\alpha + j\beta, \qquad & p_{k+1} &= -\nu + j\rho \\ \boldsymbol{R}_k &= \boldsymbol{\eta} + j\boldsymbol{\gamma}, & \boldsymbol{R}_{k+1} &= \boldsymbol{\zeta} + j\boldsymbol{\xi} \end{aligned} \tag{5.5}$$

where $\alpha, \beta \neq \nu, \rho$ and $\boldsymbol{\eta}, \boldsymbol{\gamma} \neq \boldsymbol{\zeta}, \boldsymbol{\xi}$. Besides this difference, the methodology employed to compute a rational model is the same: the pole flipping scheme [3], relaxed formulation [16] and fast implementation base on QR decomposition [4] used in VF can be directly adopted for CVF.

The idea of removing the complex conjugacy constraint in the VF algorithm was first proposed in [18] in order to design complex infinite impulse response (IIR) filters having asymmetric frequency response. There are two important differences with regard to this work: 1) the $\boldsymbol{D}$ matrix in [18] is assumed to be a complex matrix, whereas it must be real in this work. This physical-base restriction is relevant for our applications, as discussed in Section 5.6.2. 2) The models built in [18] are not used for time-domain simulations: the passivity definition, assessment and enforcement of the complex-valued models are not investigated in [18], while here they are rigorously studied in Section 5.4.

Once a model in the form (5.3) has been obtained via the CVF algorithm, it can be easily converted into a corresponding state-space form [19] as

$$\begin{cases} \dfrac{\mathrm{d}\boldsymbol{x_l}(t)}{\mathrm{d}t} = \boldsymbol{A}\boldsymbol{x_l}(t) + \boldsymbol{B}\boldsymbol{a_l}(t) \\ \boldsymbol{b_l}(t) = \boldsymbol{C}\boldsymbol{x_l}(t) + \boldsymbol{D}\boldsymbol{a_l}(t), \end{cases} \tag{5.6}$$

where $\boldsymbol{a}_l(t) \in \mathbb{C}^{n\times 1}$ and $\boldsymbol{b}_l(t) \in \mathbb{C}^{n\times 1}$ are the input and output signals of the n-port baseband system, respectively, which are the baseband equivalents of the modulated port signals of the original photonic circuit, while $\boldsymbol{x}_l(t) \in \mathbb{C}^{m\times 1}$ with $m = nK$ collects the state variables. The matrices $\boldsymbol{A}$, $\boldsymbol{B}$, $\boldsymbol{C}$, $\boldsymbol{D}$ can be analytically derived from (5.3): $\boldsymbol{A} \in \mathbb{C}^{m\times m}$ is a diagonal matrix with all the poles p_k as diagonal entries, $\boldsymbol{B} \in \mathbb{R}^{m\times n}$ is a matrix containing only ones and zeros, $\boldsymbol{C} \in \mathbb{C}^{n\times m}$ contains all the residues $\boldsymbol{R}_k$, $\boldsymbol{D} \in \mathbb{R}^{n\times n}$ is the same as in (5.3) [19]. The representation (5.6) offers two main advantages:

- fundamental properties for time-domain simulations, such as causality, stability and passivity, are well defined for state-space models;
- state-space models are inherently systems of first-order ODEs: time-domain simulations can be performed by solving the state-space models in a variety of robust ODE solvers with great accuracy and efficiency, for example the Matlab linear state-space system solver *lsim* and its open-source counterpart in Python package *SciPy*.

It is important to remark that the computational time for building a CVF model with K poles is comparable to the time needed to build a VF model with $2K$ poles.

The number of unknowns is the same in both algorithms, considering that the poles and residues in VF are complex conjugated [3].

5.4 Passivity assessment and enforcement of CVF models

Since the baseband model (5.6) will be used for simulations in the time-domain, the model passivity must be checked and, eventually, enforced [17]. In Chapter 4, the passivity definition and conditions for complex-valued linear baseband systems are presented. In particular, there are two passivity constraints that the baseband scattering parameters $\boldsymbol{S}_l(s)$ must satisfy:

1. $\boldsymbol{S}_l(s)$ is analytic in $\Re(s) > 0$;
2. $\boldsymbol{I}_n - \boldsymbol{S}_l^H(s)\boldsymbol{S}_l(s)$ is a nonnegative-definite matrix for all s such that $\Re(s) > 0$.

where $\Re(s)$ represents the real part of the Laplace variable while $\boldsymbol{I}_n$ is the identity matrix of size $n \times n$. Note that such conditions are the same as for physical systems, with the exception that the conjugacy relation $\boldsymbol{S}^*(s) = \boldsymbol{S}(s^*)$ no longer needs to hold for complex-valued systems.

Now, the above passivity conditions require that the maximum singular value of $\boldsymbol{S}_l(s)$ is bounded by unity at all frequencies. In this framework, it has been proven that the Hamiltonian matrix $\boldsymbol{M}$ can be used to assess the model passivity with accuracy and efficiency [1], which is defined as

$$\boldsymbol{M} = \begin{bmatrix} \boldsymbol{M}_{11} & \boldsymbol{M}_{12} \\ \boldsymbol{M}_{21} & \boldsymbol{M}_{22} \end{bmatrix}, \tag{5.7}$$

where

$$\begin{aligned} \boldsymbol{M}_{11} &= \boldsymbol{A} - \boldsymbol{B}\boldsymbol{L}^{-1}\boldsymbol{D}^H\boldsymbol{C}, \\ \boldsymbol{M}_{12} &= -\boldsymbol{B}\boldsymbol{L}^{-1}\boldsymbol{B}^H, \\ \boldsymbol{M}_{21} &= \boldsymbol{C}^H\boldsymbol{Q}^{-1}\boldsymbol{C}, \\ \boldsymbol{M}_{22} &= -\boldsymbol{A}^H + \boldsymbol{C}^H\boldsymbol{D}\boldsymbol{L}^{-1}\boldsymbol{B}^H, \\ \boldsymbol{L} &= \boldsymbol{D}^H\boldsymbol{D} - \boldsymbol{I}_n, \quad \boldsymbol{Q} = \boldsymbol{D}\boldsymbol{D}^H - \boldsymbol{I}_n. \end{aligned} \tag{5.8}$$

Note that $\boldsymbol{M}_{11}$, $\boldsymbol{M}_{21}$, $\boldsymbol{M}_{22}$ are complex matrices, while $\boldsymbol{M}_{12}$ is real, since $\boldsymbol{A}$ and $\boldsymbol{C}$ are complex, while $\boldsymbol{B}$ and $\boldsymbol{D}$ are real. The Hamiltonian matrix for complex-valued systems is very similar to the corresponding one defined for real-valued ones, except that the former employs the conjugate transpose operator ^{H} [1], whereas the latter one can use the transpose operator ^{T} [19], as shown in Section 5.6.2.

In particular, a (complex- or real-valued) stable state-space model is passive if its Hamiltonian matrix has no purely imaginary eigenvalues: any such eigenvalue indicates a crossover frequency where a singular value of the scattering matrix changes from being smaller to larger than unity, or vice versa [1, 19]. Once the crossover frequency points are identified by checking the eigenvalues of (5.7), the local maxima of violating singular values of the scattering matrix can be found [5]. Passivity can be enforced by perturbing the residues such that the violating singular values become smaller than unity [5].

From an algorithmic point of view, the CVF technique offers a robust model building tool and can leverage on powerful passivity assessment and enforcement techniques developed for the VF algorithm, with one exception. Indeed, the half-size passivity test matrix that is proposed in [19] for an efficient passivity assessment of real-valued reciprocal systems, is no longer applicable to the complex-valued systems studied in this chapter, due to the presence of the conjugate transpose operator ^{H} in (5.7). Interested readers are referred to [19] for details.

5.5 Comparison with previous work

The section compares the proposed technique to the VF-based baseband modeling technique presented in Chapter 4 ([1, 2]). The main differences with respect to the proposed modeling framework are outlined in Fig. 5.4. In particular, the approach in Chapter 4 is based on the VF algorithm: first a state-space model $\boldsymbol{S}^{VF}(f)$ of $\boldsymbol{S}(f_r)$ is computed via VF. Then, since $\boldsymbol{S}^{VF}(f)$ operates at optical frequency range, it is converted into a baseband model $\boldsymbol{S}_l^{VF}(f)$, whose time-domain state-space representation is in the form

$$\begin{cases} \dfrac{\mathrm{d}\boldsymbol{x_l}(t)}{\mathrm{d}t} = (\boldsymbol{A}_{VF} - j2\pi f_c \boldsymbol{I})\boldsymbol{x_l}(t) + \boldsymbol{B}_{VF}\boldsymbol{a_l}(t) \\ \boldsymbol{b_l}(t) = \boldsymbol{C}_{VF}\boldsymbol{x_l}(t) + \boldsymbol{D}_{VF}\boldsymbol{a_l}(t), \end{cases} \tag{5.9}$$

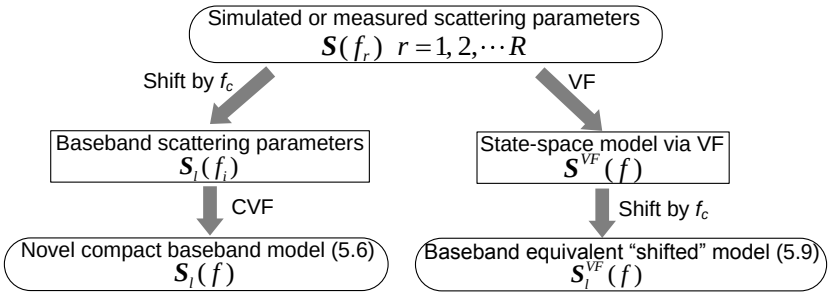

Figure 5.4: Flowchart of the CVF modeling approach (left branch) and the one presented in Chapter 4 (right branch).

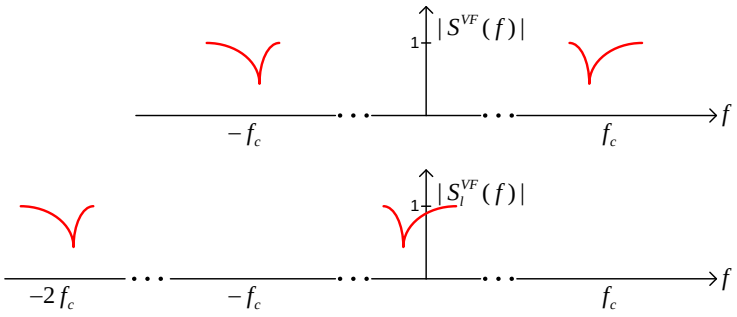

Figure 5.5: Spectrum of the model $\boldsymbol{S}^{VF}(f)$ (top) and the model $\boldsymbol{S}_l^{VF}(f)$ represented by (5.9) *(bottom).*

where $\boldsymbol{A}_{VF}, \boldsymbol{B}_{VF}, \boldsymbol{C}_{VF}, \boldsymbol{D}_{VF}$ are the state-space matrices of $\boldsymbol{S}^{VF}(f)$ computed via VF, starting from the bandpass scattering parameters $\boldsymbol{S}(f_r)$. In particular, $\boldsymbol{A}_{VF}$ is a diagonal matrix containing the poles identified by VF, $\boldsymbol{C}_{VF}$ is a matrix that contains residues, $\boldsymbol{B}_{VF}$ is a matrix containing only ones and zeros and $\boldsymbol{D}_{VF}$ is a real-valued matrix. Whereas the CVF model (5.6) and the one in the form (5.9) are somewhat similar, the different modeling strategies result in a major difference: the novel proposed approach allows one to build a model that can have half the size of the model (5.9) in terms of number of poles and state variables, thereby significantly decreasing the simulation time. The reason is clearly identified by considering the frequency-domain response $\boldsymbol{S}_l^{VF}(f)$ of model (5.9). Indeed, the frequency response $\boldsymbol{S}_l^{VF}(f)$ has also components around $-2f_c$, since it is computed by shifting the VF model $\boldsymbol{S}^{VF}(f)$ defined at bandpass frequency, as indicated in Fig. 5.5. In particular, by looking at equation (5.9), the poles of the VF model $\boldsymbol{S}^{VF}(f)$ collected in the matrix $\boldsymbol{A}_{VF}$ are shifted by the quantity $-j2\pi f_c$, as shown in the complex plane in Fig. 5.6. Clearly, the poles around $-j4\pi f_c$ do not contribute to the results of time-domain simulations performed with baseband signals $a_l(t)$ defined around 0 Hz (see Fig. 5.1). Intuitively, the frequency response around $-2f_c$ can be removed by simply discarding the corresponding poles and residues from the model (5.9), thereby achieving a half-size compact model. However, this brute-force operation can cause two problems: 1) slightly decreasing the accuracy of the desired frequency response around 0 Hz; 2) accidentally turning the model (5.9) from passive to non-passive. So calculation of the half-size model (5.6) using CVF technique is advised.

For time-domain simulations, solving the half-size model (5.6) requires less than half of the computational complexity with respect to (5.9). For example, the two main steps in the Matlab routine *lsim* to solve a linear system of ODEs have a computational complexity of $O(m^3)$ and $O(m^2 N_t)$ [6], respectively, where $m = nK$ is the size of $\boldsymbol{A}$ and N_t is the total number of time samples. Hence, the

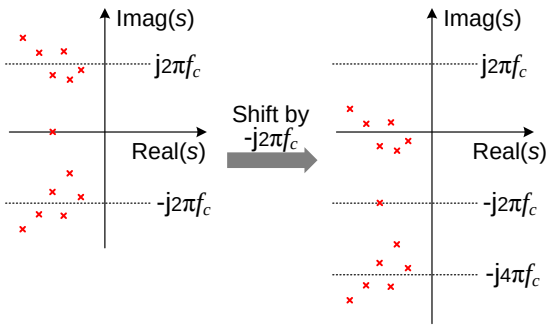

Figure 5.6: Poles of the model $\boldsymbol{S}^{VF}(f)$ (left) and the model $\boldsymbol{S}_l^{VF}(f)$ represented by (5.9) *(right).*

proposed technique offers a significant computational advantage, especially when the model size is large.

5.6 Real-valued baseband state-space models

Both the baseband CVF model represented by (5.6) and the VF-based model represented by (5.9) are complex-valued systems and can be simulated only in solvers that support complex-valued signals and matrices. However, in Chapter 4, the model (5.9) is analytically converted to a real-valued model that can be adopted in a wider range of simulators, such as SPICE and Verilog-A. In this section, we will demonstrate that a real-valued baseband state-space model can also be derived, starting from the modeling framework described in Section 5.3. Additionally, its stability and passivity properties are investigated.

5.6.1 Model derivation

Complex signals can be represented as a sum of their real and imaginary parts, such as for $\boldsymbol{a}_l(t)$

$$\boldsymbol{a}_l(t) = \boldsymbol{a}_{l\Re}(t) + j\boldsymbol{a}_{l\Im}(t). \tag{5.10}$$

Note that for a quadrature amplitude modulation (QAM) signal, $\boldsymbol{a}_{l\Re}(t)$ and $\boldsymbol{a}_{l\Im}(t)$ can be considered as in-phase and quadrature parts, respectively. By expressing all the complex signals and matrices in (5.6), namely $\boldsymbol{a}_l(t)$, $\boldsymbol{b}_l(t)$, $\boldsymbol{x}_l(t)$, $\boldsymbol{A}$ and $\boldsymbol{C}$, in the form of (5.10) and by solving separately with respect to the real and the

imaginary parts, leads to:

$$\begin{cases} \dfrac{\mathrm{d}\boldsymbol{x}_{l\Re}(t)}{\mathrm{d}t} = \boldsymbol{A}_{\Re}\boldsymbol{x}_{l\Re}(t) - \boldsymbol{A}_{\Im}\boldsymbol{x}_{l\Im}(t) + \boldsymbol{B}\boldsymbol{a}_{l\Re}(t) \\ \dfrac{\mathrm{d}\boldsymbol{x}_{l\Im}(t)}{\mathrm{d}t} = \boldsymbol{A}_{\Re}\boldsymbol{x}_{l\Im}(t) + \boldsymbol{A}_{\Im}\boldsymbol{x}_{l\Re}(t) + \boldsymbol{B}\boldsymbol{a}_{l\Im}(t) \\ \boldsymbol{b}_{l\Re}(t) = \boldsymbol{C}_{\Re}\boldsymbol{x}_{l\Re}(t) - \boldsymbol{C}_{\Im}\boldsymbol{x}_{l\Im}(t) + \boldsymbol{D}\boldsymbol{a}_{l\Re}(t) \\ \boldsymbol{b}_{l\Im}(t) = \boldsymbol{C}_{\Re}\boldsymbol{x}_{l\Im}(t) + \boldsymbol{C}_{\Im}\boldsymbol{x}_{l\Re}(t) + \boldsymbol{D}\boldsymbol{a}_{l\Im}(t), \end{cases} \tag{5.11}$$

where the indexes $\Re$ and $\Im$ indicate the real and imaginary part, respectively. Then, by defining

$$\hat{\boldsymbol{a}}(t) = \begin{bmatrix} \boldsymbol{a}_{l\Re}(t) \\ \boldsymbol{a}_{l\Im}(t) \end{bmatrix},\ \hat{\boldsymbol{b}}(t) = \begin{bmatrix} \boldsymbol{b}_{l\Re}(t) \\ \boldsymbol{b}_{l\Im}(t) \end{bmatrix},\ \hat{\boldsymbol{x}}(t) = \begin{bmatrix} \boldsymbol{x}_{l\Re}(t) \\ \boldsymbol{x}_{l\Im}(t) \end{bmatrix} \tag{5.12}$$

and

$$\begin{aligned} \hat{\boldsymbol{A}} &= \begin{bmatrix} \boldsymbol{A}_{\Re} & -\boldsymbol{A}_{\Im} \\ \boldsymbol{A}_{\Im} & \boldsymbol{A}_{\Re} \end{bmatrix}, \quad \hat{\boldsymbol{B}} = \begin{bmatrix} \boldsymbol{B} & \boldsymbol{0} \\ \boldsymbol{0} & \boldsymbol{B} \end{bmatrix}, \\ \hat{\boldsymbol{C}} &= \begin{bmatrix} \boldsymbol{C}_{\Re} & -\boldsymbol{C}_{\Im} \\ \boldsymbol{C}_{\Im} & \boldsymbol{C}_{\Re} \end{bmatrix}, \quad \hat{\boldsymbol{D}} = \begin{bmatrix} \boldsymbol{D} & \boldsymbol{0} \\ \boldsymbol{0} & \boldsymbol{D} \end{bmatrix}, \end{aligned} \tag{5.13}$$

where $\boldsymbol{0}$ represents the null matrix, equation (5.11) can be written as

$$\begin{cases} \dfrac{\mathrm{d}\hat{\boldsymbol{x}}(t)}{\mathrm{d}t} = \hat{\boldsymbol{A}}\hat{\boldsymbol{x}}(t) + \hat{\boldsymbol{B}}\hat{\boldsymbol{a}}(t) \\ \hat{\boldsymbol{b}}(t) = \hat{\boldsymbol{C}}\hat{\boldsymbol{x}}(t) + \hat{\boldsymbol{D}}\hat{\boldsymbol{a}}(t), \end{cases} \tag{5.14}$$

which is defined as *real-valued baseband state-space model*.

It is important to remark the main difference of the real-valued representation (5.14) with respect to the complex-valued one (5.6). The model (5.6) is a purely mathematical representation of the system under study, as described in Section 5.2. The novel model (5.14) has a symmetrical frequency response with respect to the positive and negative frequencies and its impulse response, input and output signals are real. Hence, it represents a physical linear system, while it can still be simulated at baseband. Furthermore, the novel model (5.14) is also a system of first order *real-valued ODEs*. Hence, it can be solved in a wider range of simulators than the complex-valued model (5.6).

5.6.2 Stability and passivity analysis

Since the model (5.14) can be considered as a physical, linear and time-invariant system, the stability and passivity conditions defined for physical linear systems [17], still hold for the new model (5.14).

The stability of a state-space model can be assessed from the eigenvalue of the matrix $\hat{\boldsymbol{A}}$: the model is stable if the real part of all the eigenvalues is negative [17].

First, a similarity transformation is applied to $\hat{\boldsymbol{A}}$:

$$\tilde{\boldsymbol{A}} = \boldsymbol{T}^{-1}\hat{\boldsymbol{A}}\boldsymbol{T} = \begin{bmatrix} \boldsymbol{A}_{\Re} - j\boldsymbol{A}_{\Im} & \boldsymbol{0} \\ \boldsymbol{0} & \boldsymbol{A}_{\Re} + j\boldsymbol{A}_{\Im} \end{bmatrix} = \begin{bmatrix} \boldsymbol{A}^* & \boldsymbol{0} \\ \boldsymbol{0} & \boldsymbol{A} \end{bmatrix}, \tag{5.15}$$

where $\boldsymbol{T} = [\boldsymbol{I}_m, \boldsymbol{I}_m; j\boldsymbol{I}_m, -j\boldsymbol{I}_m]$. If all the eigenvalues of $\boldsymbol{A}$ are in the vector $\boldsymbol{\lambda}$, then (5.15) indicates that the eigenvalues of $\tilde{\boldsymbol{A}}$ are $\boldsymbol{\lambda}$ and $\boldsymbol{\lambda}^*$ combined. Since similarity transformations do not change the eigenvalues, $\tilde{\boldsymbol{A}}$ and $\hat{\boldsymbol{A}}$ share the same set of eigenvalues. Therefore, when the model (5.6) is stable (all the elements in $\boldsymbol{\lambda}$ have negative parts), the real-valued model (5.14) is stable as well (all the eigenvalues of $\hat{\boldsymbol{A}}$ have negative real parts).

Then, as indicated in Section 5.4, the passivity of the model (5.14) can be verified by means of the Hamiltonian matrix for real-valued models [19]:

$$\hat{\boldsymbol{M}} = \begin{bmatrix} \hat{\boldsymbol{M}}_{11} & \hat{\boldsymbol{M}}_{12} \\ \hat{\boldsymbol{M}}_{21} & \hat{\boldsymbol{M}}_{22} \end{bmatrix}, \tag{5.16}$$

where

$$\begin{aligned} \hat{\boldsymbol{M}}_{11} &= \hat{\boldsymbol{A}} - \hat{\boldsymbol{B}}\hat{\boldsymbol{L}}^{-1}\hat{\boldsymbol{D}}^T\hat{\boldsymbol{C}}, \\ \hat{\boldsymbol{M}}_{12} &= -\hat{\boldsymbol{B}}\hat{\boldsymbol{L}}^{-1}\hat{\boldsymbol{B}}^T, \\ \hat{\boldsymbol{M}}_{21} &= \hat{\boldsymbol{C}}^T\hat{\boldsymbol{Q}}^{-1}\hat{\boldsymbol{C}}, \\ \hat{\boldsymbol{M}}_{22} &= -\hat{\boldsymbol{A}}^T + \hat{\boldsymbol{C}}^T\hat{\boldsymbol{D}}\hat{\boldsymbol{L}}^{-1}\hat{\boldsymbol{B}}^T, \\ \hat{\boldsymbol{L}} &= \hat{\boldsymbol{D}}^T\hat{\boldsymbol{D}} - \boldsymbol{I}_{2n}, \quad \hat{\boldsymbol{Q}} = \hat{\boldsymbol{D}}\hat{\boldsymbol{D}}^T - \boldsymbol{I}_{2n}. \end{aligned} \tag{5.17}$$

Starting from (5.13), (5.8) and (5.17), after some block matrices calculations described in Appendix 5.9.1, the following relations can be derived

$$\begin{aligned} \hat{\boldsymbol{M}}_{11} &= \begin{bmatrix} \boldsymbol{M}_{11}^{\Re} & -\boldsymbol{M}_{11}^{\Im} \\ \boldsymbol{M}_{11}^{\Im} & \boldsymbol{M}_{11}^{\Re} \end{bmatrix}, \quad \hat{\boldsymbol{M}}_{12} = \begin{bmatrix} \boldsymbol{M}_{12} & \boldsymbol{0} \\ \boldsymbol{0} & \boldsymbol{M}_{12} \end{bmatrix}, \\ \hat{\boldsymbol{M}}_{21} &= \begin{bmatrix} \boldsymbol{M}_{21}^{\Re} & -\boldsymbol{M}_{21}^{\Im} \\ \boldsymbol{M}_{21}^{\Im} & \boldsymbol{M}_{21}^{\Re} \end{bmatrix}, \quad \hat{\boldsymbol{M}}_{22} = \begin{bmatrix} \boldsymbol{M}_{22}^{\Re} & -\boldsymbol{M}_{22}^{\Im} \\ \boldsymbol{M}_{22}^{\Im} & \boldsymbol{M}_{22}^{\Re} \end{bmatrix}, \end{aligned} \tag{5.18}$$

where $\boldsymbol{M}_{11}^{\Re}$ and $\boldsymbol{M}_{11}^{\Im}$ are the real and imaginary parts of $\boldsymbol{M}_{11}$, respectively, and the same notation is also adopted for $\boldsymbol{M}_{12}$, $\boldsymbol{M}_{21}$, $\boldsymbol{M}_{22}$. It is important to remark that the relation (5.18) can only be derived thanks to the choice of computing $\boldsymbol{D}$ in (5.3) as real matrix, as indicated in Section 5.3.

By performing a similarity transformation on $\hat{\boldsymbol{M}}$, a new matrix $\bar{\boldsymbol{M}}$ can be obtained

$$\bar{\boldsymbol{M}} = \boldsymbol{P}^{-1}\hat{\boldsymbol{M}}\boldsymbol{P} = \begin{bmatrix} \boldsymbol{M}^* & \boldsymbol{0} \\ \boldsymbol{0} & \boldsymbol{M} \end{bmatrix}, \tag{5.19}$$

where

$$\boldsymbol{P} = \begin{bmatrix} \boldsymbol{I}_m & \boldsymbol{0} & \boldsymbol{I}_m & \boldsymbol{0} \\ j\boldsymbol{I}_m & \boldsymbol{0} & -j\boldsymbol{I}_m & \boldsymbol{0} \\ \boldsymbol{0} & \boldsymbol{I}_m & \boldsymbol{0} & \boldsymbol{I}_m \\ \boldsymbol{0} & j\boldsymbol{I}_m & \boldsymbol{0} & -j\boldsymbol{I}_m \end{bmatrix}, \tag{5.20}$$

and $\boldsymbol{M}$ is the Hamiltonian matrix of the CVF system (5.6), described in (5.7). Note that, the similarity transformation (5.19) can be derived by simple algebraic manipulations. Since similarity transformations do not change the eigenvalues, the eigenvalues of $\hat{\boldsymbol{M}}$ are the union set of the eigenvalues of $\boldsymbol{M}$ and their complex conjugate according to (5.19). This proves that, if the stable model (5.6) is passive ($\boldsymbol{M}$ does not have any purely imaginary eigenvalue), then the real-valued model (5.14) is passive by construction ($\hat{\boldsymbol{M}}$ has no purely imaginary eigenvalue either).

5.7 Examples on photonic circuits

This section presents three application examples of the proposed modeling and simulation techniques. The scattering parameters of the photonic circuits under study are evaluated via the *Caphe* circuit simulator (Luceda Photonics) and electromagnetic simulations in *FDTD Solutions* (Lumerical), while the time-domain simulations are carried out in Matlab on a personal computer with Intel Core i3 processor and 8 GB RAM.

5.7.1 Five-ring resonator filter

A five-ring resonator filter based on [20] is studied in this section. The filter comprises four directional couplers (DCs) and two multimode interferometers (MMIs), as shown in Fig. 5.7. The geometric parameters of the filter can be found in [20] and will not be repeated here.

A direct FDTD simulation of the entire five-ring filter is very time consuming, as the structure is very large, and because of the resonances a very long simulation time is needed to reach the termination condition where the residual fields have died out. Therefore, we only simulate the coupling structures, i.e. the MMI and two DCs (indicated in Fig. 5.7) given that the filter is symmetric, and evaluate the scattering parameters in the modeling frequency range $[187.37;\ 199.86]$ THz (corresponding to a wavelength of $[1.5;\ 1.6]$ μm) while considering a carrier frequency $f_c = 193.46$ THz. Then, the scattering parameters of the whole filter are calculated in the circuit simulator Caphe by connecting the MMI and DCs.

Following the CVF modeling procedure, the evaluated scattering parameters over optical frequency range are first shifted to the baseband $[-6.09;\ 6.40]$ THz by $f_c = 193.46$ THz. Next, a stable and passive baseband model in the form (5.6)

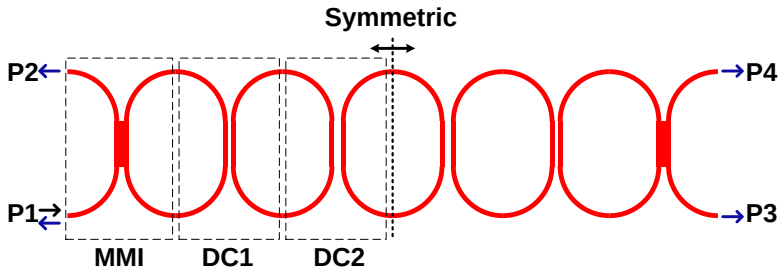

Figure 5.7: Example 5.7.1. The structure of the five-ring resonator filter.

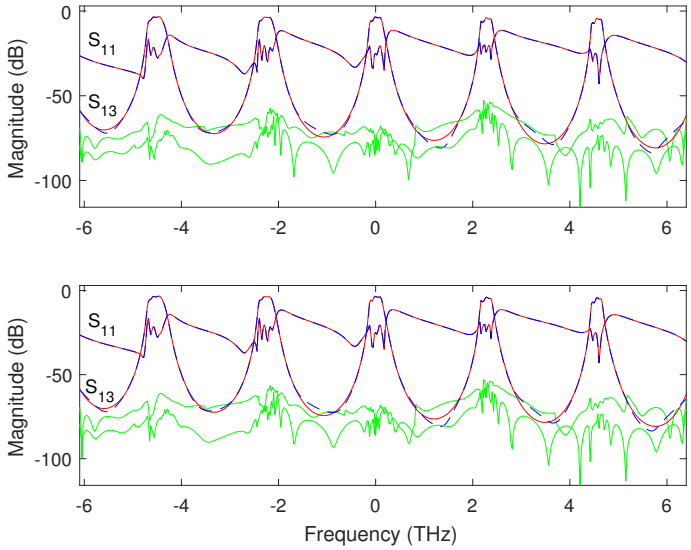

Figure 5.8: Example 5.7.1. The accuracy of the model (5.9) *(top) built via the technique in Chapter 4 and the model* (5.6) *(bottom) built via the newly proposed technique; the red solid lines represent the simulated scattering parameters, the blue dashed lines represent the models, while the green lines are the magnitude of the error between the two.*

is built with 54 poles. Then, a real-valued state-space model (5.14) for the filter is directly derived from (5.6) according to (5.13). Note that we deliberately considered a wide modeling frequency range in order to make the modeling process more challenging, even though RF signals with such large spectrum are rarely used. As a comparison, the model in the form (5.9) is also built via the VF algorithm with 108 poles. The magnitude of the maximum absolute error for both models is less than -52 dB, as shown in Fig. 5.8. Note that the calculated models are already passive, so no passivity enforcement is required in this example. The scattering parameters

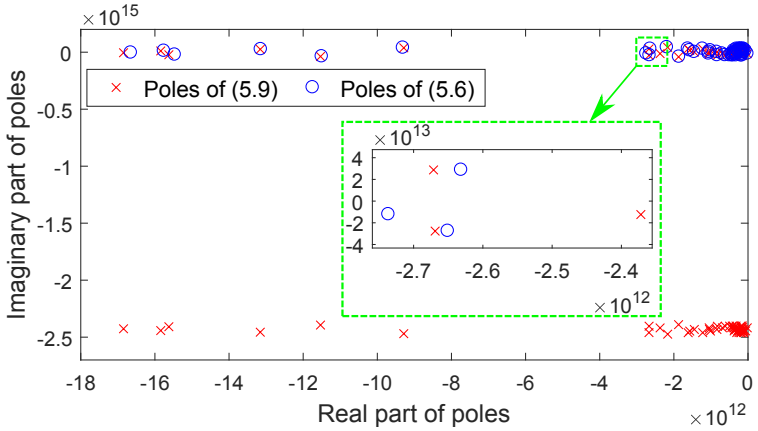

Figure 5.9: Example 5.7.1. The poles of the model (5.6) *from the proposed technique (represented by circles) and the model* (5.9) *from the technique in Chapter 4 (represented by crosses).*

of the filter are full matrices, since reflections are captured by the FDTD simulator. Hence, even though only S_{11} and S_{13} are shown in Fig. 5.8 for readability, the model is bidirectional, includes reflections and can be excited from any of the ports. The poles of the models (5.6) and (5.9) are illustrated in Fig. 5.9. It is clear that half of the poles of (5.9) are around $-j4\pi f_c$, while the other half cluster around 0 Hz, as explained in Section 5.5 (see Fig. 5.6). It is important to remark that the poles of the CVF model (5.6) and VF-based model (5.9) around 0 Hz are relatively close in the complex plane, but are different: the CVF model is not the same as first computing the VF-based model and then removing the poles around $-j4\pi f_c$.

To perform time-domain simulations, we applied a 16-QAM input signal at port P1. The corresponding in-phase $I(t)$ and quadrature component $Q(t)$ are RF bit sequence signals, with bit rate 80 Gbit/s and 1000 bits long. The first 25 bits of $I(t)$ and $Q(t)$ are shown in Fig. 5.10.

Note that $I(t)$ and $Q(t)$ can be considered as the real and imaginary parts of the baseband signals in the form (5.2), and can be directly adopted for baseband time-domain simulations with the models (5.6), (5.9), and (5.14) [1]. Relevant time-domain simulation results obtained by the three models are shown in Fig. 5.11. Additionally, the transmission signal at P3 (drop port of the filter) is plotted as a constellation diagram to better observe the influence of the filter on the input signal, as shown in Fig. 5.12. It is demonstrated by Figs. 5.8, 5.11, and 5.12 that the proposed technique is accurate in both frequency and time domain.

The model building time of the VF-based model (5.9) and the CVF model (5.6) is 3.4 s and 3.3 s, respectively. The simulation of the VF-based model (5.9), the

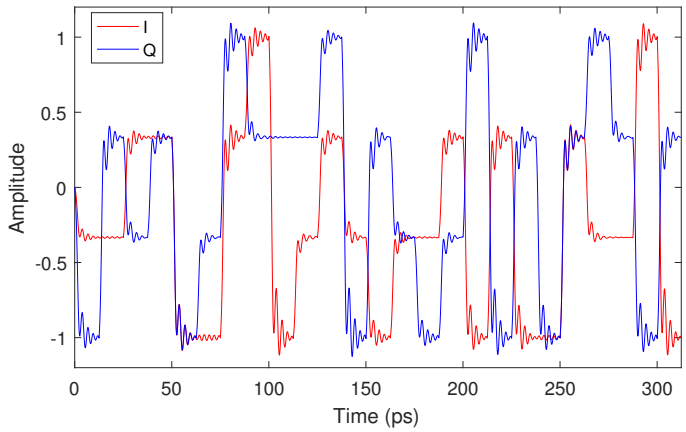

Figure 5.10: Example 5.7.1. The in-phase part $I(t)$ and quadrature part $Q(t)$ of the 16-QAM input signal.

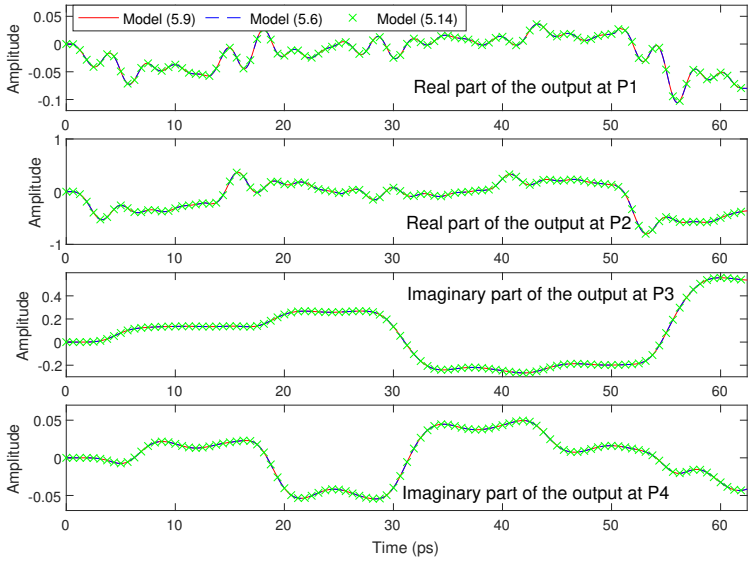

Figure 5.11: Example 5.7.1. The output signals at P1, P2, P3 and P4 obtained from base-band time-domain simulations of models (5.6)*,* (5.9) *and* (5.14)*.*

CVF model (5.6) and the real-valued state-space model (5.14) requires 132 s, 12 s, 12 s, respectively: the half-size CVF model (5.6) is superior to the full-sized VF-based model (5.9) in terms of computational speed, while achieving a comparable accuracy.

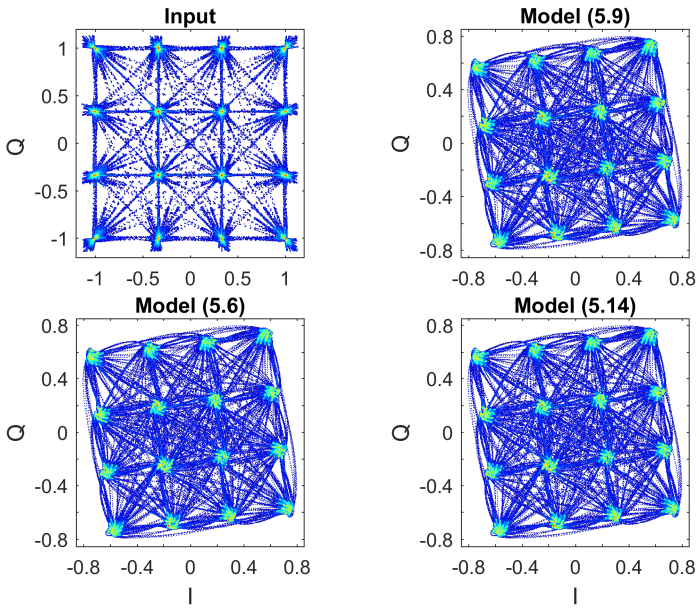

Figure 5.12: Example 5.7.1. Constellation diagrams of the transmission signal at P3 calculated from different models.

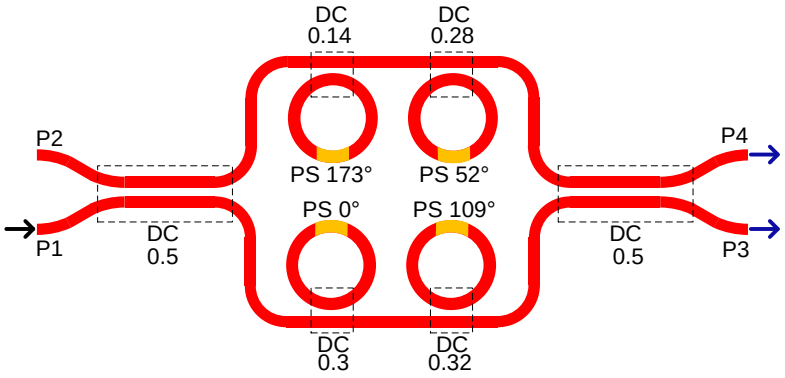

Figure 5.13: Example 5.7.2. The schematic circuit of the ring-loaded MZI filter.

5.7.2 Ring-loaded Mach-Zehnder filter

A ring-loaded MZI filter is designed according to the structure proposed in [21], as shown in Fig. 5.13. There are six directional couplers (DCs) and four ring resonators with a phase shifter (PS) in each ring. The power coupling coefficients and phase shifters parameters are indicated in Fig. 5.13. Once the phase shifters

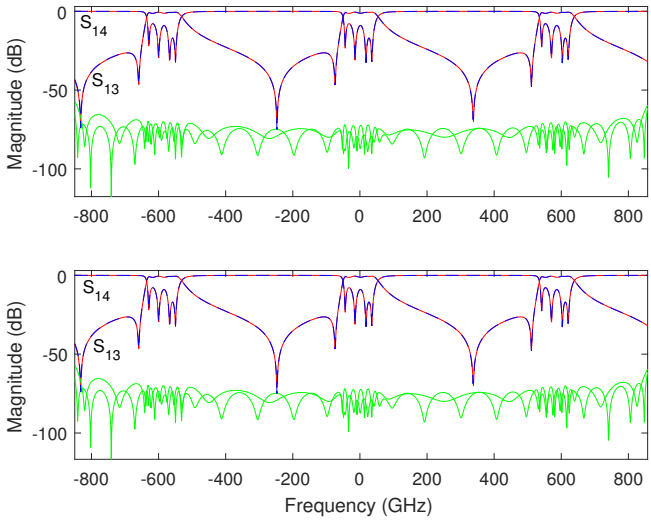

Figure 5.14: Example 5.7.2. The accuracy of the model (5.9) *(top) built via the VF-based technique in Chapter 4 and the model* (5.6) *(bottom) built via the new CVF-based technique; the red solid lines represent the simulated scattering parameters, the blue dashed lines represent the models, while the green lines are the magnitude of the error between the two.*

are tuned to the desired values, they are kept fixed and the filter can be considered as a linear time-invariant system. It is important to remark that the filter is designed intentionally to have an asymmetric passband feature as shown in Fig. 5.14, which can occur in practice due to variations of the manufacturing process or variations in the tuning of the phase shifters. In this example, we will demonstrate that the proposed modeling technique is robust with regard to this kind of imperfections as well.

The filter is simulated in the Caphe circuit simulator to extract the scattering parameters within the chosen frequency range $[190.34;\ 192.05]$ THz, which covers a bandwidth of 1710 GHz. The carrier frequency is set at the center of the passband of the filter: $f_c = 191.19$ THz. Note that reflections are not considered in the models of the waveguides and the couplers: the overall circuit has no reflections as well. As a result, the scattering matrices are sparse. The frequency range is chosen to be wide, in order to demonstrate the modeling power of the proposed technique. In practice, however, it can be chosen according the spectrum of the input signals according to Chapter 4. Then, a compact state-space model in the form (5.6) is built via the CVF technique with 21 poles over the corresponding baseband frequency range $[-850;\ 860]$ GHz. Finally, the real-valued state-space model (5.14) is analytically calculated as described in Section 5.6. For com-

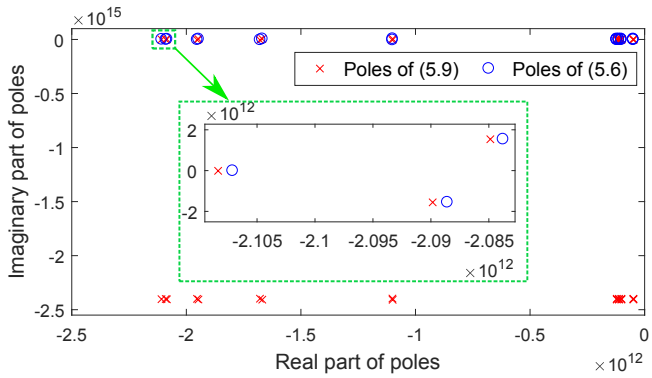

Figure 5.15: Example 5.7.2. The poles of the CVF model (5.6) *(represented by circles) and the model* (5.9) *from the VF-based technique in Chapter 4 (represented by crosses).*

parison, the VF-based model (5.9) of the filter is also built via the VF algorithm with 42 poles. The magnitude of the maximum absolute error for both the models (5.6) and (5.9) is less than -56 dB, as shown in Fig. 5.14. The poles of the CVF model (5.6) and the VF-based model (5.9) are illustrated in Fig. 5.15, which again demonstrates the poles from both models around 0 Hz are slightly different. The passivity assessment (see Section 5.4) reveals that all the models are passive and suitable for time-domain simulations.

In particular, the same 16-QAM signal in Fig. 5.10 is adopted as input for port P1, with one difference: the data rate is decreased from 80 Gbit/s to 20 Gbit/s, since the (single side) passband of the filter in this example is approximately 50 GHz. Time-domain simulations are conducted with the three models and the results for the first 250 ps are shown in Fig. 5.16.

For a better observation of the transmission signal at P3, constellation diagrams are plotted in Fig. 5.17, where the results from different models are compared to the input. It is evident that the constellation symbols are still clearly separated by safe gaps, but rotated by the total phase delay of the filter circuit at the carrier frequency f_c. The results shown in Figs. 5.14, 5.16 and 5.17 demonstrate the accuracy of the proposed modeling approach.

The model building time of the VF-based model (5.9) and the CVF model (5.6) is 2.7 s and 2.6 s, respectively. The simulation of the VF-based model (5.9), CVF model (5.6) and the real-valued model (5.14) requires 8.2 s, 2.5 s, 2.6 s, respectively. In this example, the simulation speed-up is less significant than the previous example in Section 5.7.1, because fewer poles are needed in the models. This result is consistent with the analysis in Section 5.5: the efficiency of the proposed technique with regard to the technique in Chapter 4 increases with respect to the size of the models [6].

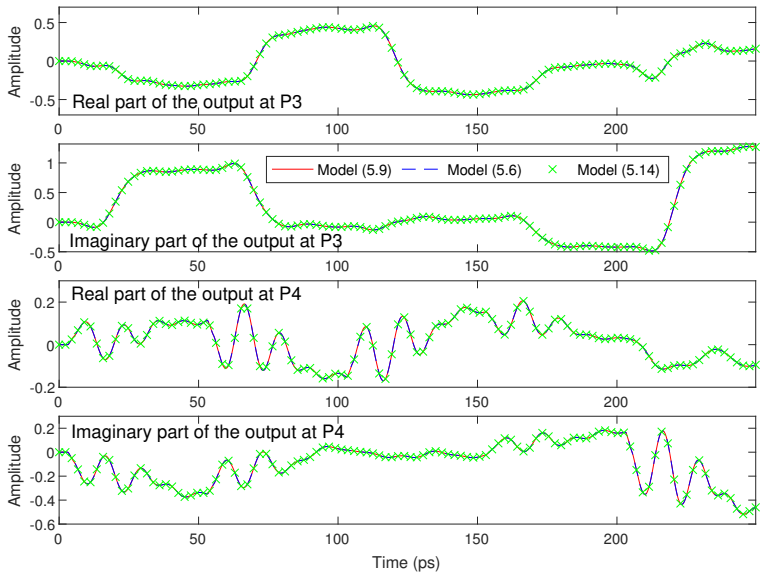

Figure 5.16: Example 5.7.2. The output signals at P3 and P4 obtained from baseband time-domain simulation of models (5.6), (5.9) *and* (5.14).

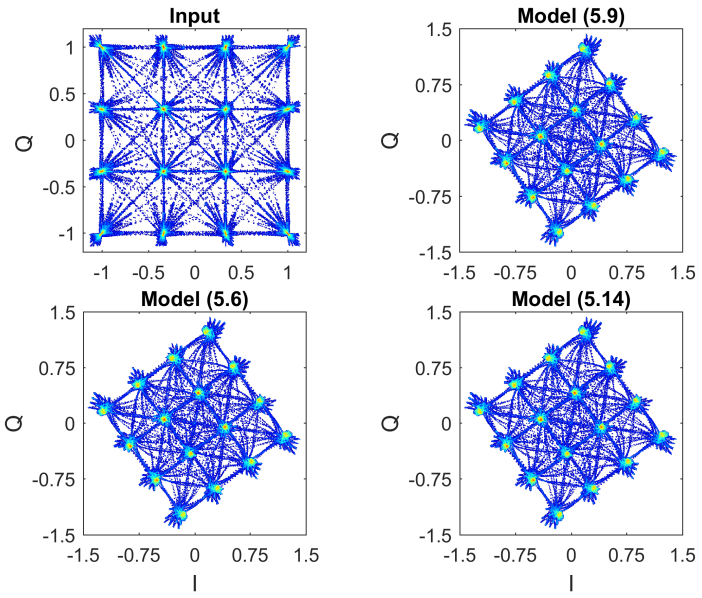

Figure 5.17: Example 5.7.2. Constellation diagram of the transmission signal at P3 calculated from different models.

In practice it is possible that the passband of the filter can shift due to fabrication variations. So, extra tests are conducted to study the influence of the passband shifting of the filter on the same input signal. We assume that the passband redshifts or blueshifts by 0.3 nm in wavelength (about 36 GHz in frequency). Then, the corresponding baseband model can be built in two ways: i) rebuild a CVF model at the new passband following the proposed technique; ii) directly shift the CVF model computed so far at the original passband to the new passband, by only shifting the poles in the matrix $\boldsymbol{A}$, which is represented by

$$\begin{cases} \dfrac{\mathrm{d}\boldsymbol{x_l}(t)}{\mathrm{d}t} = (\boldsymbol{A} - j2\pi\Delta f \boldsymbol{I}_m)\boldsymbol{x_l}(t) + \boldsymbol{B}\boldsymbol{a_l}(t) \\ \boldsymbol{b_l}(t) = \boldsymbol{C}\boldsymbol{x_l}(t) + \boldsymbol{D}\boldsymbol{a_l}(t), \end{cases} \tag{5.21}$$

where Δf is the amount that the passband shifts, which is very different from the model (5.9), where the shifted value is the optical carrier frequency. In this example, Δf is 36 GHz for the redshift, and -36 GHz for the blueshift.

This approach can be adopted since it is proven in Chapter 4 that shifting the poles of state-space models is equivalent to shifting the frequency response. It is also studied in Chapter 4 that shifting poles along the imaginary axis in the complex plane does not affect the model stability and passivity. Therefore, the shifted CVF model (5.21) is still stable and passive. It is important to remark that

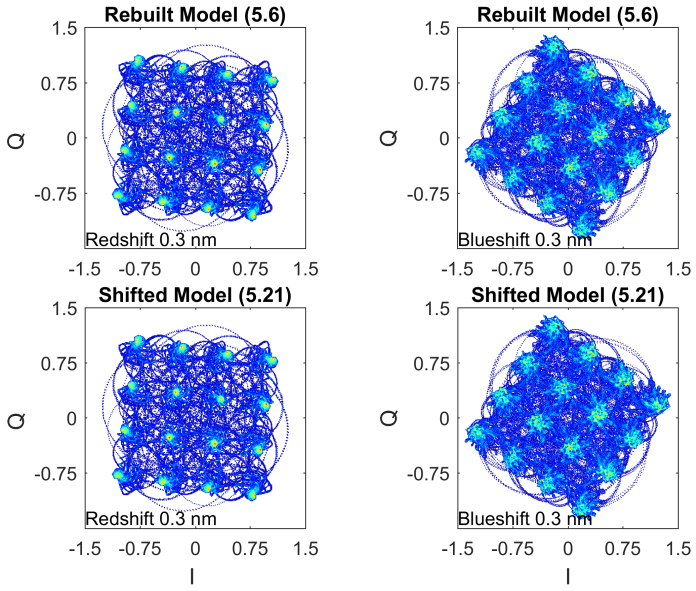

Figure 5.18: Example 5.7.2. Constellation diagram of the transmission signal at P3 calculated from the rebuilt CVF model in the form (5.6) *and the shifted one in the form* (5.21)*, when the passband of the filter redshifts and blueshifts by 0.3 nm.*

the maximum absolute error of the shifted CVF model with regard to the scattering parameters is the same as the original CVF model, but only if the shifted modeling frequency range still covers the entire spectrum of the input signal [1]. The wider the spectral range of the original CVF model, the more it can be shifted to perform a tolerance analysis without the need to rebuild the model. The results from the models generated by the two methods at red- and blueshifted passbands are shown in Fig. 5.18. Due to the asymmetric passband of the filter, it is understandable that the blueshifted passband makes the constellation symbols more fuzzy than the redshifted case.

5.7.3 Mach-Zehnder lattice filter

The baseband models based on the VF and CVF techniques in the previous two examples are passive by construction. In this example, the passivity enforcement of the CVF algorithm will be demonstrated via modeling the Mach-Zehnder-based lattice filter presented in Chapter 4, whose structure is shown in Fig. 5.19.

First, the scattering parameters of the filter are simulated in Caphe in the frequency range $[f_c - \Delta;\ f_c + \Delta]$, where $\Delta = 760$ GHz and $f_c = 195.11$ THz. Then, a compact state-space model is built via the CVF technique with 34 poles and a magnitude of the maximum absolute error of -51 dB. The passivity of the model is assessed with the method presented in Section 5.4, and small but multiple passivity violations are found. The passivity enforcement algorithm is then applied to the non-passive model, as shown in Fig. 5.20. Before passivity enforcement, the singular values of the CVF model are plotted with solid blue lines, where small passivity violations can be observed (singular values are larger than unity). After passivity enforcement, all the singular values are forced below unity, at the expense of a slight increase in the maximum absolute error (-48 dB). For comparison, a model in the form (5.9) is also built with 68 poles by first obtaining an VF model according to Chapter 4. Passivity enforcement of the VF model is

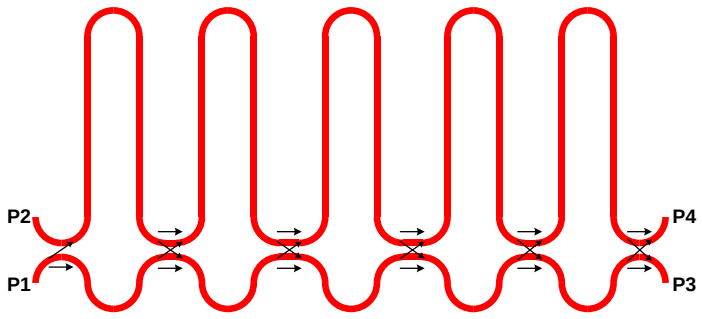

Figure 5.19: Example 5.7.3. The structure of the Mach-Zehnder interferometer lattice filter.

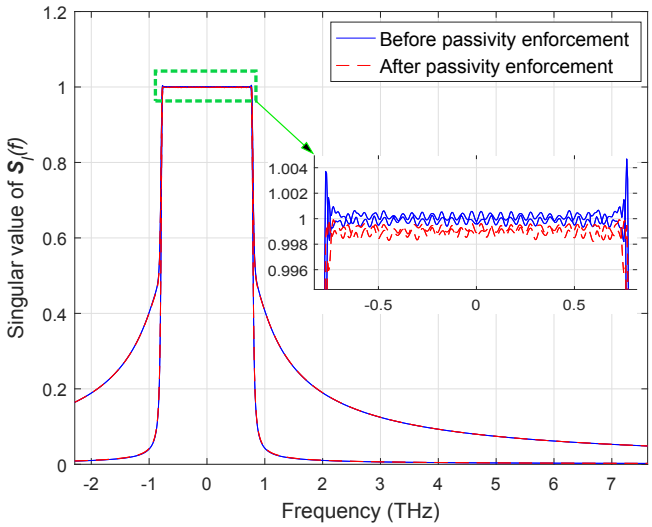

Figure 5.20: Example 5.7.3. The singular values of the scattering matrices calculated from the model (5.6) *before and after passivity enforcement.*

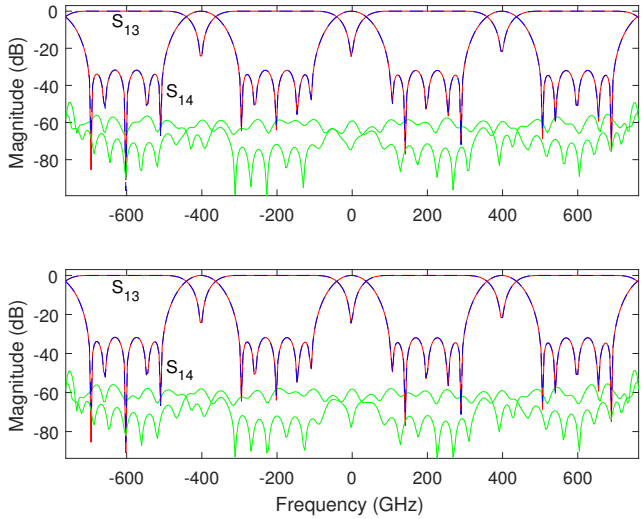

Figure 5.21: Example 5.7.3. The accuracy of the VF-based model (5.9) *(top) built via the technique in Chapter 4 and the new CVF model* (5.6) *(bottom); the red solid lines represent the simulated scattering parameters, the blue dash lines represent the models while the green lines show the error between them.*

also required in the modeling process, leading to an increase in the maximum absolute error from -51 dB to -49 dB. The modeling accuracy of the two techniques is illustrated in Fig. 5.21.

The modeling time (including passivity enforcement) of the VF-based model (5.9) and the CVF model (5.6) for the lattice filter are 6.3 s and 6.2 s, respectively. Since the accuracy and efficiency of the time-domain simulation with the proposed models is demonstrated in Sections 5.7.1 and 5.7.2, and the filter was studied in Chapter 4, time-domain results are not presented in this chapter.

5.8 Conclusion

This chapter presented a novel compact modeling approach for linear photonic circuits that is based on the scattering parameters and the proposed CVF technique. The new CVF models offer significant advantages in terms of compactness and simulation speed, as compared to the VF-based models derived from previous work. In order to extend the compatibility of the proposed approach to simulators that only support real-valued signals (such as many EDA simulators), equivalent real-valued baseband models were analytically derived and their stability and passivity is rigorously studied. Three photonic circuits examples were provided to validate the proposed approach.

5.9 Appendix

5.9.1 Transformation of Hamiltonian matrix

By means of (5.13), the following relation between $\hat{\boldsymbol{L}}^{-1}$ in (5.17) and $\boldsymbol{L}^{-1}$ in (5.8) can be derived:

$$\begin{aligned}\hat{\boldsymbol{L}}^{-1} &= \left(\begin{bmatrix}\boldsymbol{D}^T & \boldsymbol{0}\\ \boldsymbol{0} & \boldsymbol{D}^T\end{bmatrix}\begin{bmatrix}\boldsymbol{D} & \boldsymbol{0}\\ \boldsymbol{0} & \boldsymbol{D}\end{bmatrix} - \begin{bmatrix}\boldsymbol{I}_n & \boldsymbol{0}\\ \boldsymbol{0} & \boldsymbol{I}_n\end{bmatrix}\right)^{-1}\\ &= \left(\begin{bmatrix}\boldsymbol{D}^T\boldsymbol{D}-\boldsymbol{I}_n & \boldsymbol{0}\\ \boldsymbol{0} & \boldsymbol{D}^T\boldsymbol{D}-\boldsymbol{I}_n\end{bmatrix}\right)^{-1}\\ &= \begin{bmatrix}\boldsymbol{L}^{-1} & \boldsymbol{0}\\ \boldsymbol{0} & \boldsymbol{L}^{-1}\end{bmatrix}.\end{aligned} \tag{5.22}$$

In a similar way, there is

$$\hat{\boldsymbol{Q}}^{-1} = \begin{bmatrix}\boldsymbol{Q}^{-1} & \boldsymbol{0}\\ \boldsymbol{0} & \boldsymbol{Q}^{-1}\end{bmatrix}. \tag{5.23}$$

Thanks to the relations between $\boldsymbol{A}$, $\boldsymbol{B}$, $\boldsymbol{C}$, $\boldsymbol{D}$ and $\hat{\boldsymbol{A}}$, $\hat{\boldsymbol{B}}$, $\hat{\boldsymbol{C}}$, $\hat{\boldsymbol{D}}$ in (5.13), the following results can be derived by simple block matrices calculations:

$$\begin{aligned}\hat{\boldsymbol{M}}_{11} &= \begin{bmatrix}\boldsymbol{A}_{\Re} & -\boldsymbol{A}_{\Im}\\ \boldsymbol{A}_{\Im} & \boldsymbol{A}_{\Re}\end{bmatrix} - \begin{bmatrix}\boldsymbol{B} & \boldsymbol{0}\\ \boldsymbol{0} & \boldsymbol{B}\end{bmatrix}\begin{bmatrix}\boldsymbol{L}^{-1} & \boldsymbol{0}\\ \boldsymbol{0} & \boldsymbol{L}^{-1}\end{bmatrix}\begin{bmatrix}\boldsymbol{D}^T & \boldsymbol{0}\\ \boldsymbol{0} & \boldsymbol{D}^T\end{bmatrix}\begin{bmatrix}\boldsymbol{C}_{\Re} & -\boldsymbol{C}_{\Im}\\ \boldsymbol{C}_{\Im} & \boldsymbol{C}_{\Re}\end{bmatrix}\\ &= \begin{bmatrix}\boldsymbol{A}_{\Re} - \boldsymbol{B}\boldsymbol{L}^{-1}\boldsymbol{D}^T\boldsymbol{C}_{\Re} & -\boldsymbol{A}_{\Im} + \boldsymbol{B}\boldsymbol{L}^{-1}\boldsymbol{D}^T\boldsymbol{C}_{\Im}\\ \boldsymbol{A}_{\Im} - \boldsymbol{B}\boldsymbol{L}^{-1}\boldsymbol{D}^T\boldsymbol{C}_{\Im} & \boldsymbol{A}_{\Re} - \boldsymbol{B}\boldsymbol{L}^{-1}\boldsymbol{D}^T\boldsymbol{C}_{\Re}\end{bmatrix}\\ &= \begin{bmatrix}\boldsymbol{M}_{11}^{\Re} & -\boldsymbol{M}_{11}^{\Im}\\ \boldsymbol{M}_{11}^{\Im} & \boldsymbol{M}_{11}^{\Re}\end{bmatrix}\end{aligned} \tag{5.24}$$

$$\begin{aligned}\hat{\boldsymbol{M}}_{12} &= -\begin{bmatrix}\boldsymbol{B} & \boldsymbol{0}\\ \boldsymbol{0} & \boldsymbol{B}\end{bmatrix}\begin{bmatrix}\boldsymbol{L}^{-1} & \boldsymbol{0}\\ \boldsymbol{0} & \boldsymbol{L}^{-1}\end{bmatrix}\begin{bmatrix}\boldsymbol{B}^T & \boldsymbol{0}\\ \boldsymbol{0} & \boldsymbol{B}^T\end{bmatrix}\\ &= \begin{bmatrix}-\boldsymbol{B}\boldsymbol{L}^{-1}\boldsymbol{B}^T & \boldsymbol{0}\\ \boldsymbol{0} & -\boldsymbol{B}\boldsymbol{L}^{-1}\boldsymbol{B}^T\end{bmatrix}\\ &= \begin{bmatrix}\boldsymbol{M}_{12} & \boldsymbol{0}\\ \boldsymbol{0} & \boldsymbol{M}_{12}\end{bmatrix}\end{aligned} \tag{5.25}$$

$$\begin{aligned}\hat{\boldsymbol{M}}_{21} &= \begin{bmatrix}\boldsymbol{C}_{\Re}^T & \boldsymbol{C}_{\Im}^T\\ -\boldsymbol{C}_{\Im}^T & \boldsymbol{C}_{\Re}^T\end{bmatrix}\begin{bmatrix}\boldsymbol{Q}^{-1} & \boldsymbol{0}\\ \boldsymbol{0} & \boldsymbol{Q}^{-1}\end{bmatrix}\begin{bmatrix}\boldsymbol{C}_{\Re} & -\boldsymbol{C}_{\Im}\\ \boldsymbol{C}_{\Im} & \boldsymbol{C}_{\Re}\end{bmatrix}\\ &= \begin{bmatrix}\boldsymbol{C}_{\Re}^T\boldsymbol{Q}^{-1}\boldsymbol{C}_{\Re}+\boldsymbol{C}_{\Im}^T\boldsymbol{Q}^{-1}\boldsymbol{C}_{\Im} & \boldsymbol{C}_{\Im}^T\boldsymbol{Q}^{-1}\boldsymbol{C}_{\Re}-\boldsymbol{C}_{\Re}^T\boldsymbol{Q}^{-1}\boldsymbol{C}_{\Im}\\ \boldsymbol{C}_{\Re}^T\boldsymbol{Q}^{-1}\boldsymbol{C}_{\Im}-\boldsymbol{C}_{\Im}^T\boldsymbol{Q}^{-1}\boldsymbol{C}_{\Re} & \boldsymbol{C}_{\Im}^T\boldsymbol{Q}^{-1}\boldsymbol{C}_{\Im}+\boldsymbol{C}_{\Re}^T\boldsymbol{Q}^{-1}\boldsymbol{C}_{\Re}\end{bmatrix}\\ &= \begin{bmatrix}\boldsymbol{M}_{21}^{\Re} & -\boldsymbol{M}_{21}^{\Im}\\ \boldsymbol{M}_{21}^{\Im} & \boldsymbol{M}_{21}^{\Re}\end{bmatrix}\end{aligned} \tag{5.26}$$

$$\begin{aligned}\hat{\boldsymbol{M}}_{22} &= -\begin{bmatrix}\boldsymbol{A}_{\Re}^T & \boldsymbol{A}_{\Im}^T\\ -\boldsymbol{A}_{\Im}^T & \boldsymbol{A}_{\Re}^T\end{bmatrix} + \begin{bmatrix}\boldsymbol{C}_{\Re}^T & \boldsymbol{C}_{\Im}^T\\ -\boldsymbol{C}_{\Im}^T & \boldsymbol{C}_{\Re}^T\end{bmatrix}\begin{bmatrix}\boldsymbol{D} & \boldsymbol{0}\\ \boldsymbol{0} & \boldsymbol{D}\end{bmatrix}\begin{bmatrix}\boldsymbol{L}^{-1} & \boldsymbol{0}\\ \boldsymbol{0} & \boldsymbol{L}^{-1}\end{bmatrix}\begin{bmatrix}\boldsymbol{B}^T & \boldsymbol{0}\\ \boldsymbol{0} & \boldsymbol{B}^T\end{bmatrix}\\ &= \begin{bmatrix}-\boldsymbol{A}_{\Re}^T + \boldsymbol{C}_{\Re}^T\boldsymbol{D}\boldsymbol{L}^{-1}\boldsymbol{B} & -\boldsymbol{A}_{\Im}^T + \boldsymbol{C}_{\Im}^T\boldsymbol{D}\boldsymbol{L}^{-1}\boldsymbol{B}\\ \boldsymbol{A}_{\Im}^T - \boldsymbol{C}_{\Im}^T\boldsymbol{D}\boldsymbol{L}^{-1}\boldsymbol{B} & -\boldsymbol{A}_{\Re}^T + \boldsymbol{C}_{\Re}^T\boldsymbol{D}\boldsymbol{L}^{-1}\boldsymbol{B}\end{bmatrix}\\ &= \begin{bmatrix}\boldsymbol{M}_{22}^{\Re} & -\boldsymbol{M}_{22}^{\Im}\\ \boldsymbol{M}_{22}^{\Im} & \boldsymbol{M}_{22}^{\Re}\end{bmatrix},\end{aligned} \tag{5.27}$$

where $\boldsymbol{M}_{11}^{\Re}$ and $\boldsymbol{M}_{11}^{\Im}$ are the real and imaginary parts of $\boldsymbol{M}_{11}$, respectively, and the same notation is also used for $\boldsymbol{M}_{21}$ and $\boldsymbol{M}_{22}$, while $\boldsymbol{M}_{12}$ is a real-valued matrix.

It is important to note that equations (5.24) $-$ (5.27) hold because $\hat{\boldsymbol{B}}$ and $\hat{\boldsymbol{D}}$ are block diagonal matrices, while $\boldsymbol{B}$ and $\boldsymbol{D}$ are real matrices.

References

[1] Y. Ye, D. Spina, Y. Xing, W. Bogaerts, and T. Dhaene. *Numerical modeling of Linear Photonic System for Accurate and Efficient Time-Domain Simulations*. Photon. Res., 6(6):560–573, Jun. 2018.

[2] Y. Ye, D. Spina, W. Bogaerts, and T. Dhaene. *Baseband Macromodeling of Linear Photonic Circuits for Time-Domain Simulations*. J. Lightw. Technol., 37(4):1364–1373, Feb. 2019.

[3] B. Gustavsen and A. Semlyen. *Rational approximation of frequency domain responses by Vector Fitting*. IEEE Trans. Power Del., 14(3):1052–1061, Jul. 1999.

[4] D. Deschrijver, M. Mrozowski, T. Dhaene, and D. De Zutter. *Macromodeling of Multiport Systems Using a Fast Implementation of the Vector Fitting Method*. IEEE Microw. Compon. Lett., 18(6):383–385, Jun. 2008.

[5] B. Gustavsen. *Fast Passivity Enforcement for S-Parameter Models by Perturbation of Residue Matrix Eigenvalues*. IEEE Trans. Adv. Packag., 33(1):257–265, Feb. 2010.

[6] K. C. Sou and O. L. De Weck. *Fast time-domain simulation for large-order linear time-invariant state space systems*. Int. J. Numer. Meth. Engng., 63(5):681–708, Mar. 2005.

[7] C. Sorace-Agaskar, J. Leu, M. R. Watts, and V. Stojanovic. *Electro-optical co-simulation for integrated CMOS photonic circuits with VerilogA*. Opt. Exp., 23(21):27180–27203, Oct. 2015.

[8] M. C Jeruchim, P. Balaban, and K. S. Shanmugan. *Simulation of communication systems: modeling, methodology and techniques*. Springer, 2006.

[9] D. Deschrijver, B. Haegeman, and T. Dhaene. *Orthonormal Vector Fitting: A Robust Macromodeling Tool for Rational Approximation of Frequency Domain Responses*. IEEE Trans. Adv. Packag., 30(2):216–225, May 2007.

[10] S. Grivet-Talocia, M. Bandinu, and F. G. Canavero. *An automatic algorithm for equivalent circuit extraction from noisy frequency responses*. In 2005 International Symposium on Electromagnetic Compatibility, volume 1, pages 163–168 Vol. 1, Aug. 2005.

[11] S. Grivet-Talocia. *Passivity enforcement via perturbation of Hamiltonian matrices*. IEEE Trans. Circuits Syst. I, Reg. Paper, 51(9):1755–1769, Sep. 2004.

[12] D. Saraswat, R. Achar, and M. S. Nakhla. *A fast algorithm and practical considerations for passive macromodeling of measured/simulated data*. IEEE Trans. Adv. Packag., 27(1):57–70, Feb. 2004.

[13] D. Deschrijver, and T. Dhaene. *Fast Passivity Enforcement of S-Parameter Macromodels by Pole Perturbation*. IEEE Trans. Microw. Theory Techn., 57(3):620–626, Mar. 2009.

[14] T. Dhaene, D. Deschrijver, and N. Stevens. *Efficient Algorithm for Passivity Enforcement of S-Parameter-Based Macromodels*. IEEE Trans. Microw. Theory Techn., 57(2):415–420, Feb. 2009.

[15] `www.sintef.no/projectweb/vectfit/`.

[16] B. Gustavsen. *Improving the pole relocating properties of vector fitting*. IEEE Trans. Power Del., 21(3):1587–1592, Jul. 2006.

[17] S. Grivet-Talocia and B. Gustavsen. *Passive Macromodeling: Theory and Applications*. John Wiley and Sons, 2016.

[18] C. Lei, C. Cheung, H. Kwan, and N. Wong. *Efficient Complex Continuous-Time IIR Filter Design via Generalized Vector Fitting*. In Proceedings of the International MultiConference of Engineers and Computer Scientists, volume 2, Hongkong, China, 2008.

[19] B. Gustavsen and A. Semlyen. *Fast Passivity Assessment for S-Parameter Rational Models Via a Half-Size Test Matrix*. IEEE Trans. Microw. Theory Techn., 56(12):2701–2708, Dec. 2008.

[20] F. Xia, M. Rooks, L. Sekaric, and Y. Vlasov. *Ultra-compact high order ring resonator filters using submicron silicon photonic wires for on-chip optical interconnects*. Opt. Express, 15(19):11934–11941, Sep. 2007.

[21] S. Akiyama, T. Kurahashi, K. Morito, T. Yamamoto, T. Usuki, and S. Nomura. *Cascaded-ring-resonator-loaded Mach–Zehnder modulator for enhanced modulation efficiency in wide optical bandwidth*. Opt. Express, 20(15):16321–16338, Jul. 2012.

6

Time-Domain Characterization of Linear Photonic Circuits Subject to Fabrication Variations

Y. Ye, M. Wang, D. Spina, W. Bogaerts, and T. Dhaene, "Time-domain characterization of photonic integrated filters subject to fabrication variations," Under review.

Abstract

Fabrication variations are a key factor to degrade the performance of photonic integrated circuits (PICs), and especially wavelength filters. We propose an efficient modeling approach to quantify the effects of fabrication variations on the time-domain performance of linear passive photonic integrated circuits (including the wavelength filters) in the design stage, before fabrication. In particular, this novel approach conjugates the accuracy of the Polynomial Chaos (PC) expansion in describing stochastic variations and the efficiency of a Vector Fitting (VF)-based baseband modeling technique in performing time-domain simulations. A suitable example validates the performance of the proposed method.

6.1 Introduction

Fabrication variations pose a considerable design challenge for silicon-on-insulator based *photonic integrated circuits* (PICs), since the high material index contrast makes photonic devices very sensitive to the geometry variations [1, 2]. Such variations normally lead to performance degradation of PICs after manufacturing and can even cause considerable yield loss. Hence, it is very important to quantify the performance variations of PICs before they are fabricated, which is often referred to as variability analysis. In this scenario, the Monte Carlo (MC) method is a robust, accurate and easy to implement solution. However, it is also very time consuming due to its slow convergence rate [3]. The Polynomial Chaos (PC) expansion is considered as an efficient alternative approach for variability analysis in electronic applications, for example in [4–8], and in recent years it has also been demonstrated on PICs [9–13]. In the latter case, however, the proposed techniques focus mainly on the variability analysis of suitable performance indicators defined in the wavelength/frequency domain, such as coupling coefficients [9, 10], 3-dB bandwidth [11, 12], transmission or scattering matrices [13]. The time-domain variability analysis of linear and passive PICs, such as filters, has not been studied in the literature yet, due to the challenge of building accurate and efficient time-domain models of complex PICs [2]. In fact, from a system performance point of view, the time-domain performance for a given input signal, expressed as an eye diagram or constellation diagram, is a more direct and intuitive measure of the effect of the variations on signal integrity [14].

In this chapter, we propose a time-domain variability analysis approach for passive photonic circuits under uncertainty effects, which is based on two recent techniques: PC-based macromodeling for characterizing the variations in Chapter 2 and [7, 13], and baseband modeling for efficient time-domain simulations in Chapter 4. In particular, the PC-based macromodeling approach leverages on the PC expansion of the scattering parameters of the circuits under stochastic effects, and employs the Galerkin projection method and the Vector Fitting (VF) algorithm to compute a deterministic, stable and passive state-space model describing the relation between the PC coefficients of the input and output signals of the circuits [7]. This model is usually called “augmented”, since it has an higher number of ports than the original circuit under study [7]. Since a direct time-domain simulation of a state-space model computed at optical frequencies is time and memory consuming [15, 16], the augmented model is converted into an equivalent baseband representation, according to the technique introduced in Chapter 4, thereby obtaining a baseband augmented model which can be efficiently simulated. Furthermore, pertinent time-domain statistical information of the circuit input/output signals can be computed by means of only one time-domain simulation of such model. In this work we especially focus on wavelength filters, as they represent

an important category of passive photonic circuits and their performance suffers severely from fabrication variations when they are not designed to be robust [17].

The chapter is organized as follows. Section 6.2 describes the problem statement. Section 6.3 presents the standard MC approach for time-domain variability analysis, while Section 6.4 proposes the novel PC-based approach. A relevant application example is presented in Section 6.5, where the proposed technique is compared to the MC analysis in terms of accuracy and efficiency. Conclusions are drawn in Section 6.6.

6.2 Photonic filters subject to fabrication variations

Photonic filters are often studied in the frequency (or wavelength) domain, as their transfer function depends on suitable (geometrical or optical) design parameters and the frequency. Hence, it is straightforward to describe a photonic filter subject to fabrication variation via a scattering matrix $\boldsymbol{S}(f, \boldsymbol{\xi})$, where f is the frequency and the vector $\boldsymbol{\xi}$ collects all the normalized random variables of the problem at hand, which represent the design parameters affected by fabrication variations (e.g. width and thickness of a waveguide, coupling coefficients, effective index). The port signals of the scattering matrix of the filter are incident and reflected waves, which have the relation

$$\boldsymbol{b}(f, \boldsymbol{\xi}) = \boldsymbol{S}(f, \boldsymbol{\xi})\boldsymbol{a}(f, \boldsymbol{\xi}). \tag{6.1}$$

$\boldsymbol{S}(f, \boldsymbol{\xi})$ is a $N \times N$ matrix when the filter under study has N ports. Note that, due to the variability of the filter, no matter whether the incident waves are deterministic or stochastic, the reflected waves $\boldsymbol{b}(f, \boldsymbol{\xi})$ will always depend on $\boldsymbol{\xi}$ and can be considered stochastic quantities. In general, the incident waves $\boldsymbol{a}(f, \boldsymbol{\xi})$ can also be considered stochastic quantities when the filter connects to other photonic components and there are stochastic reflections at joints. If the reflections at the terminations can be neglected, the incident waves can be assumed deterministic.

The challenge addressed in this chapter is to quantify the impact of the random parameters $\boldsymbol{\xi}$ on the port signals in the time domain.

6.3 MC approach for time-domain variability analysis

The MC method is the standard approach for such variability analysis. In our problem formulation, it requires the following three steps: 1) computing a large number of samples of the random variables $\boldsymbol{\xi}_i$ for $i = 1, \cdots, N_{MC}$, according to their distribution. For each sample, the scattering parameters of the filter are calculated, representing N_{MC} different filters; 2) building models for all the N_{MC}

filters and performing N_{MC} time-domain simulations to obtain the port signals; 3) computing the relevant statistics, such as mean, standard deviation, probability density function (PDF) or any other stochastic information of interest, based on the data collected so far.

In this framework, it is crucial to choose a suitable modeling approach for time-domain simulations, considering that a large number N_{MC} is required to accurately estimate the stochastic information [3]. In this work, we adopt the baseband modeling technique proposed in Chapter 4 for time-domain modeling and simulations, which is elaborated as follows.

For each filter with parameters $\boldsymbol{\xi}_i$, the scattering matrix has to be evaluated at a set of frequencies in the range of interest, denoted by $\boldsymbol{S}(f_r, \boldsymbol{\xi}_i)$ for $r = 1, \cdots, R$. Then, a continuous VF model can be built [18]

$$\boldsymbol{S}(f, \boldsymbol{\xi}_i) = \sum_{k=1}^{K} \frac{\boldsymbol{R}_k}{j2\pi f - p_k} + \boldsymbol{D}, \tag{6.2}$$

where $\boldsymbol{R}_k$ are $N \times N$ matrices containing the residues and p_k are the corresponding poles, which can be either real or complex conjugate pairs, while $\boldsymbol{D}$ is a real matrix. Note that the model (6.2) is stable and passive: its stability is preserved by a pole-flipping scheme, while passivity assessment and enforcement can be accomplished by using robust standard techniques [19]. Next, a time-domain state-space model can be analytically derived from (6.2) [20]:

$$\begin{cases} \dot{\boldsymbol{x}}(t, \boldsymbol{\xi}_i) = \boldsymbol{A}\boldsymbol{x}(t, \boldsymbol{\xi}_i) + \boldsymbol{B}\boldsymbol{a}(t, \boldsymbol{\xi}_i) \\ \boldsymbol{b}(t, \boldsymbol{\xi}_i) = \boldsymbol{C}\boldsymbol{x}(t, \boldsymbol{\xi}_i) + \boldsymbol{D}\boldsymbol{a}(t, \boldsymbol{\xi}_i), \end{cases} \tag{6.3}$$

where $\boldsymbol{a}(t, \boldsymbol{\xi}_i)$ and $\boldsymbol{b}(t, \boldsymbol{\xi}_i)$ are the time-domain counterparts of $\boldsymbol{a}(f, \boldsymbol{\xi}_i)$ and $\boldsymbol{b}(f, \boldsymbol{\xi}_i)$, respectively. $\boldsymbol{A}$, $\boldsymbol{B}$, $\boldsymbol{C}$, $\boldsymbol{D}$ are the state-space matrices of $\boldsymbol{S}(f, \boldsymbol{\xi}_i)$. In particular, $\boldsymbol{A}$ is a diagonal matrix with all the poles p_k as diagonal entries, $\boldsymbol{B}$ is a matrix containing only ones and zeros, $\boldsymbol{C}$ contains all the residues $\boldsymbol{R}_k$, while $\boldsymbol{D}$ is the same as in (6.2).

The model (6.3) represents a system of first-order ordinary differential equations (ODE) that can be solved via robust numerical methods with respect to the incident waves $\boldsymbol{a}(t, \boldsymbol{\xi}_i)$. However, the port signals $\boldsymbol{a}(t, \boldsymbol{\xi}_i)$ and $\boldsymbol{b}(t, \boldsymbol{\xi}_i)$ are modulated optical waves defined at the Terahertz frequency range, and a time-step on femtosecond-scale is needed to solve (6.3), which is impractical in terms of memory requirements and computational time [15, 16]. To address this challenge, baseband equivalents $\boldsymbol{a}_B(t, \boldsymbol{\xi}_i)$ for the optical waves $\boldsymbol{a}(t, \boldsymbol{\xi}_i)$ are defined in Chapter 4:

$$\boldsymbol{a}(t, \boldsymbol{\xi}_i) = \Re[\boldsymbol{a}_B(t, \boldsymbol{\xi}_i) e^{j2\pi f_c t}], \tag{6.4}$$

$$\mathcal{H}[\boldsymbol{a}(t, \boldsymbol{\xi}_i)] = \Im[\boldsymbol{a}_B(t, \boldsymbol{\xi}_i) e^{j2\pi f_c t}], \tag{6.5}$$

where $\Re(\cdot)$ and $\Im(\cdot)$ stand for the real and imaginary part, respectively, and $\mathcal{H}(\cdot)$ represents the Hilbert transform. The signals $\boldsymbol{a}_B(t, \boldsymbol{\xi}_i)$ are called baseband equivalents since they no longer contain the fast oscillation of the optical carrier. Note that, to avoid any confusion (with the notation $\boldsymbol{a}_m$ in (6.7) and $\boldsymbol{a}_{Bm}$ in (6.12)), the subscript $_B$ is used to represent baseband equivalent signals in this chapter while the subscript $_l$ is used in Chapters 4 and 5. Correspondingly, a baseband equivalent system for (6.3) was proposed in Chapter 4

$$\begin{cases} \dot{\boldsymbol{x}}_B(t, \boldsymbol{\xi}_i) = (\boldsymbol{A} - j2\pi f_c \boldsymbol{I})\boldsymbol{x}_B(t, \boldsymbol{\xi}_i) + \boldsymbol{B}\boldsymbol{a}_B(t, \boldsymbol{\xi}_i) \\ \boldsymbol{b}_B(t, \boldsymbol{\xi}_i) = \boldsymbol{C}\boldsymbol{x}_B(t, \boldsymbol{\xi}_i) + \boldsymbol{D}\boldsymbol{a}_B(t, \boldsymbol{\xi}_i), \end{cases} \tag{6.6}$$

where $\boldsymbol{a}_B(t, \boldsymbol{\xi}_i)$, $\boldsymbol{b}_B(t, \boldsymbol{\xi}_i)$, and $\boldsymbol{x}_B(t, \boldsymbol{\xi}_i)$ are the baseband equivalents of $\boldsymbol{a}(t, \boldsymbol{\xi}_i)$, $\boldsymbol{b}(t, \boldsymbol{\xi}_i)$, and $\boldsymbol{x}(t, \boldsymbol{\xi}_i)$, respectively.

Then, the system of ODE (6.6) can be solved efficiently with a much larger time step compared to (6.3), since the baseband equivalent signals have spectrum in the radio frequency (RF) band [15]. Note that for photonic circuits we are only interested in the baseband equivalent signals $a_B(t, \boldsymbol{\xi}_i)$ rather than the fast oscillating modulated optical signals $a(t, \boldsymbol{\xi}_i)$, since $a_B(t, \boldsymbol{\xi}_i)$ represents the useful information that $a(t, \boldsymbol{\xi}_i)$ carries [15, 21]. Furthermore, the optical signals can be analytically calculated from their baseband counterpart, as shown in (6.4). Interested readers are referred to Chapter 4 for more details about the baseband signals and models.

The MC analysis is completed by repeating this procedure for each sample $\boldsymbol{\xi}_i$ of the random variables and pertinent statistical analyses can be performed based on the large number of time-domain simulations performed.

6.4 PC-based time-domain variability analysis

In contrast with the MC method, the technique described in this section is able to compute a statistical model of the input/output signals of the filter under study via a single time-domain simulation, which can be used to efficiently and accurately perform time-domain variability analysis, as described in the following.

6.4.1 PC-based augmented systems

The PC expansion is an efficient modeling method to quantify stochastic variations. The main properties of the PC expansion and the procedure to build PC-based augmented systems are described in this section.

According to the PC theory, the stochastic quantities in (6.1) can be represented

as [22, 23]:

$$\begin{aligned}\boldsymbol{S}(f_r,\boldsymbol{\xi}) &\approx \sum_{m=0}^{M} \boldsymbol{S}_m(f_r)\varphi_m(\boldsymbol{\xi}),\\ \boldsymbol{a}(f_r,\boldsymbol{\xi}) &\approx \sum_{m=0}^{M} \boldsymbol{a}_m(f_r)\varphi_m(\boldsymbol{\xi}),\\ \boldsymbol{b}(f_r,\boldsymbol{\xi}) &\approx \sum_{m=0}^{M} \boldsymbol{b}_m(f_r)\varphi_m(\boldsymbol{\xi}),\end{aligned} \tag{6.7}$$

where $\varphi_m(\boldsymbol{\xi})$ are called basis functions, while $\boldsymbol{S}_m(f_r)$, $\boldsymbol{a}_m(f_r)$ and $\boldsymbol{b}_m(f_r)$ for $m = 0, \ldots, M$ are suitable coefficients, referred to as PC coefficients. In particular, the basis functions $\varphi_m(\boldsymbol{\xi})$ are orthonormal and depend on the joint distribution of the random variables $\boldsymbol{\xi}$ as

$$\langle \varphi_i(\boldsymbol{\xi}), \varphi_m(\boldsymbol{\xi}) \rangle = \int_{\boldsymbol{\Omega}} \varphi_i(\boldsymbol{\xi})\varphi_m(\boldsymbol{\xi}) W(\boldsymbol{\xi}) d\boldsymbol{\xi} = \delta_{im}, \tag{6.8}$$

where δ_{im} is the Kronecker delta and $\boldsymbol{\Omega}$ represents the stochastic space where the random variables $\boldsymbol{\xi}$ are defined, while $W(\boldsymbol{\xi})$ is a weight factor corresponding to the normalized joint probability density function of $\boldsymbol{\xi}$.

Given (6.8), several techniques exist to estimate the basis functions [23]. It is important to note that, if the random variables $\boldsymbol{\xi}$ are independent, the basis functions are defined as product combination of the orthonormal polynomials corresponding to each *individual* random variable in $\boldsymbol{\xi}$, which are *known* for certain distributions. For example, $\varphi_m(\boldsymbol{\xi})$ are product of Hermite polynomials if the random variables $\boldsymbol{\xi}$ follow a Gaussian distribution, while for Uniform distribution they can be computed as product of Legendre polynomials [22, 23]. The accuracy of the approximations in (6.7) can be improved by increasing the number of basis functions $M + 1$, which depends on the number Q of random variables in $\boldsymbol{\xi}$ and the PC order P: $M + 1 = (Q + P)!/(Q!P!)$ [22]. Since the basis functions are typically polynomials, the PC order P is defined as the maximum degree of the elements $\varphi_m(\boldsymbol{\xi})$, for $m = 0, \ldots, M$ [22, 23].

In this framework, only the PC coefficients must be estimated to obtain the models (6.7). Several non-intrusive techniques can be adopted to reach this goal, based on linear regression [13], numerical integration [22], or stochastic testing (ST) [4, 6]. Similar to the MC method, these approaches require to evaluate the filter scattering parameters for a set of samples N_{PC} of the random variables, with one main difference: $N_{PC} << N_{MC}$. Hence, computing the PC models (6.7) is much more efficient than performing a MC analysis.

Mathematically, the PC expansion process in (6.7) can be considered as projecting a stochastic quantity onto $M + 1$ known orthonormal bases. Once the PC coefficients are calculated, the variability analysis can be performed with great accuracy and efficiency:

- the mean and standard deviation of the stochastic quantity under study, for example $\boldsymbol{S}(f_r, \boldsymbol{\xi})$, can be directly calculated from the corresponding PC coefficients [22, 23];
- more complex stochastic moments, such as the probability density or the cumulative distribution function, can be estimated via a MC analysis based on the *analytical* models (6.7), which can be evaluated very efficiently.

The interested reader is referred to [4–13, 22, 23] for a complete description of the properties of the PC expansion, including its application to problems involving correlated random variables.

Now, by following the procedure described in Chapter 2 and [7, 13], it is possible to describe the relationship between the PC coefficients of the incident and reflected waves as:

$$\boldsymbol{b}_{PC}(f_r) = \boldsymbol{S}_{PC}(f_r)\boldsymbol{a}_{PC}(f_r), \tag{6.9}$$

where the vectors $\boldsymbol{a}_{PC}(f_r)$ and $\boldsymbol{b}_{PC}(f_r)$ are formed by the PC coefficients of the incident and reflected wave, respectively: they have a total of $(M+1)N$ elements. Note that equation (6.9) is *deterministic*, since $\boldsymbol{S}_{PC}(f_r)$ with size $(M+1)N \times (M+1)N$ is obtained by a suitable combination of the PC coefficients $\boldsymbol{S}_m(f_r)$ in (6.7). It is important to remark that (6.9) describes a new system represented by $\boldsymbol{S}_{PC}(f_r)$, whose port signals are the PC coefficients of the incident and reflected waves of the original stochastic filter. In particular, $\boldsymbol{S}_{PC}(f_r)$ is $M+1$ times larger than the original system under study in terms of ports number, and is often referred to as "augmented system" in the PC jargon. It is demonstrated in [7] that $\boldsymbol{S}_{PC}(f_r)$ can be considered as a scattering matrix of a physical linear and passive system: it can be modeled with the same approaches that are used for modeling the filter (see (6.2)), as it will be described in the next section. Furthermore, an augmented matrix representation $\boldsymbol{S}_{PC}(f_r)$ is adopted in [13] to model stochastic building blocks in PICs for efficient frequency-domain variability analysis.

Note that, when the incident waves do not depend on the random variables considered ($\boldsymbol{a}(f_r, \boldsymbol{\xi}) = \boldsymbol{a}(f_r)$), (6.9) still holds and $\boldsymbol{a}_{PC}(f_r) = [\boldsymbol{a}(f_r), \boldsymbol{0}, \boldsymbol{0}, \cdots]^T$, due to the properties of the PC expansion [22, 23].

6.4.2 Time-domain augmented model

Let us assume that $\boldsymbol{S}_{PC}(f_r)$ has been computed for a discrete set of frequency values f_r for $r = 1, \cdots, R$. Then, as it can be done for $\boldsymbol{S}(f_r, \boldsymbol{\xi}_i)$, a continuous frequency-dependent pole-residue model for $\boldsymbol{S}_{PC}(f_r)$ can be built by means of the VF technique [18]

$$\boldsymbol{S}_{PC}(f) = \sum_{l=1}^{L} \frac{\boldsymbol{R}_l^{PC}}{j2\pi f - p_l^{PC}} + \boldsymbol{D}_{PC}, \tag{6.10}$$

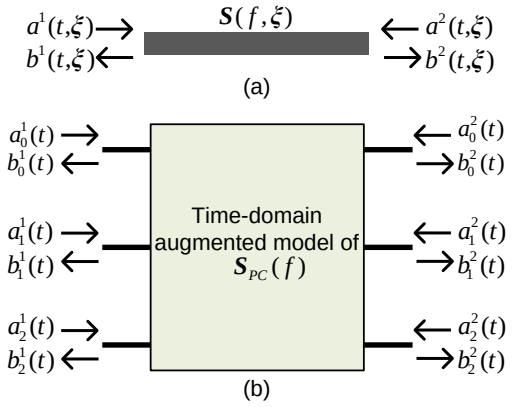

Figure 6.1: (a) Waveguide under stochastic effects; (b) the corresponding time-domain augmented model.

where $\boldsymbol{R}_l^{PC}$ are $(M+1)N \times (M+1)N$ matrices containing the residues and p_l^{PC} are the poles, while $\boldsymbol{D}_{PC}$ is a real matrix. Next, it is straightforward to convert (6.10) into a corresponding time-domain state-space representation [20]

$$\begin{cases} \dot{\boldsymbol{x}}_{PC}(t) = \boldsymbol{A}_{PC}\boldsymbol{x}_{PC}(t) + \boldsymbol{B}_{PC}\boldsymbol{a}_{PC}(t) \\ \boldsymbol{b}_{PC}(t) = \boldsymbol{C}_{PC}\boldsymbol{x}_{PC}(t) + \boldsymbol{D}_{PC}\boldsymbol{a}_{PC}(t), \end{cases} \tag{6.11}$$

where $\boldsymbol{A}_{PC}$, $\boldsymbol{B}_{PC}$, $\boldsymbol{C}_{PC}$, $\boldsymbol{D}_{PC}$ are the state-space matrices of $\boldsymbol{S}_{PC}(s)$ and can be directly calculated from (6.10) according to [20]. Note that $\boldsymbol{x}_{PC}(t)$ is the corresponding state-vector, while $\boldsymbol{a}_{PC}(t)$ and $\boldsymbol{b}_{PC}(t)$ are the time-domain counterparts of $\boldsymbol{a}_{PC}(f)$ and $\boldsymbol{b}_{PC}(f)$, respectively, which collect all the PC coefficients $\boldsymbol{a}_m(t)$ of $\boldsymbol{a}(t,\boldsymbol{\xi})$ and $\boldsymbol{b}_m(t)$ of $\boldsymbol{b}(t,\boldsymbol{\xi})$.

To better understand this model, let us consider a waveguide in Fig. 6.1(a), which depends on one random variable (such as the width of the waveguide). If three basis functions are used for the PC expansion (PC order $P = 2$), then the corresponding time-domain augmented model is shown in Fig. 6.1(b). In this case, $\boldsymbol{a}_{PC}(t) = [a_0^1(t), a_0^2(t), a_1^1(t), a_1^2(t), a_2^1(t), a_2^2(t)]^T$, where $a_0^1(t)$ represents the first PC coefficient of the stochastic signal at port one and so on.

Now, time-domain simulations can be performed by solving the system of first-order ODE (6.11) with input signals $\boldsymbol{a}_{PC}(t)$. However, the PC coefficients collected in $\boldsymbol{a}_{PC}(t)$ have spectrum in the terahertz frequency range, considering that the optical signals $\boldsymbol{a}(t,\boldsymbol{\xi})$ are defined at such frequencies and the PC basis functions are time independent. As a result, similar to (6.3), time-domain simulations of (6.11) would have to adopt time steps of the order of the femtoseconds and would be very time and memory consuming [15]. This issue is addressed in the following by defining a baseband augmented model.

6.4.3 Time-domain baseband augmented model

The PC expansion of $\boldsymbol{a}(t,\boldsymbol{\xi})$ and its baseband equivalent $\boldsymbol{a}_B(t,\boldsymbol{\xi})$ are

$$\begin{aligned}\boldsymbol{a}(t,\boldsymbol{\xi}) &\approx \sum_{m=0}^{M} \boldsymbol{a}_m(t)\varphi_m(\boldsymbol{\xi}),\\ \boldsymbol{a}_B(t,\boldsymbol{\xi}) &\approx \sum_{m=0}^{M} \boldsymbol{a}_{Bm}(t)\varphi_m(\boldsymbol{\xi}).\end{aligned} \tag{6.12}$$

Combining (6.4) and (6.12), there is

$$\sum_{m=0}^{M} \boldsymbol{a}_m(t)\varphi_m(\boldsymbol{\xi}) = \Re[\sum_{m=0}^{M} \boldsymbol{a}_{Bm}(t)\varphi_m(\boldsymbol{\xi})e^{j2\pi f_c t}]. \tag{6.13}$$

Thanks to (6.8), projecting (6.13) on the $i-$th PC basis function via Galerkin projection gives [22]

$$\boldsymbol{a}_i(t) = \Re[\boldsymbol{a}_{Bi}(t)e^{j2\pi f_c t}], \tag{6.14}$$

which indicates that the PC coefficients $\boldsymbol{a}_i(t)$ of the optical signals $\boldsymbol{a}(t,\boldsymbol{\xi})$ can be analytically recovered from the PC coefficients $\boldsymbol{a}_{Bi}(t)$ of the corresponding baseband equivalents $\boldsymbol{a}_B(t,\boldsymbol{\xi})$. Then, by collecting all the elements $\boldsymbol{a}_i(t)$ and $\boldsymbol{a}_{Bi}(t)$ in vectors, it leads to:

$$\boldsymbol{a}_{PC}(t) = \Re[\boldsymbol{a}_{BPC}(t)e^{j2\pi f_c t}]. \tag{6.15}$$

Starting from (6.5) and (6.12), the following relation can be obtained in the same way

$$\mathcal{H}[\boldsymbol{a}_{PC}(t)] = \Im[\boldsymbol{a}_{BPC}(t)e^{j2\pi f_c t}]. \tag{6.16}$$

It is easy to prove that similar relations also hold for $\boldsymbol{b}_{PC}(t)$ and $\boldsymbol{x}_{PC}(t)$ in (6.11).

Hence, considering the relations (6.15) and (6.16), a baseband augmented model for (6.11) can be derived by following the same procedure used for the filter (see (6.3) and (6.6)), which leads to:

$$\begin{cases}\dot{\boldsymbol{x}}_{BPC}(t) = (\boldsymbol{A}_{PC} - j2\pi f_c \boldsymbol{I})\boldsymbol{x}_{BPC}(t) + \boldsymbol{B}_{PC}\boldsymbol{a}_{BPC}(t)\\ \boldsymbol{b}_{BPC}(t) = \boldsymbol{C}_{PC}\boldsymbol{x}_{BPC}(t) + \boldsymbol{D}_{PC}\boldsymbol{a}_{BPC}(t).\end{cases} \tag{6.17}$$

Now, all the PC coefficients $\boldsymbol{b}_{BPC}(t)$ of the stochastic baseband equivalent signals $\boldsymbol{b}_B(t,\boldsymbol{\xi})$ can be obtained by performing only a *single* time-domain simulation of (6.17) in the baseband with efficiency and accuracy. With these PC coefficients, the mean and standard deviation of the baseband port signals can be immediately calculated, while a cheap MC analysis based on the obtained PC model can also be

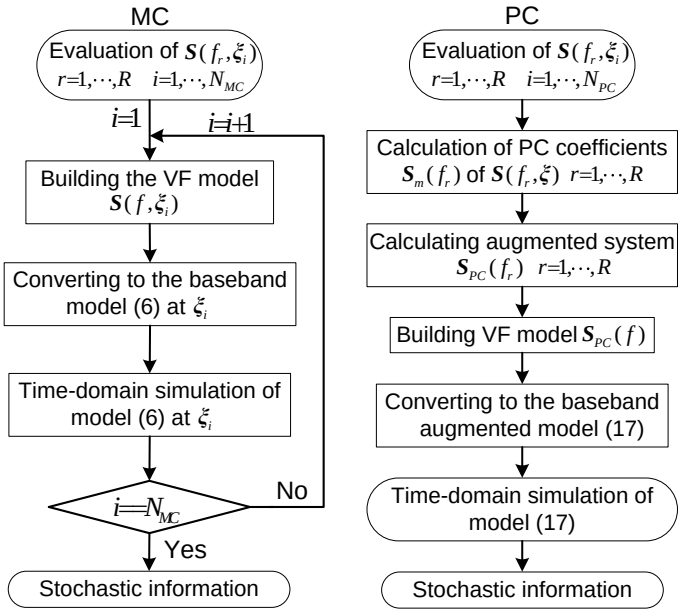

Figure 6.2: Flowchart of the MC approach (left) and the proposed PC-based method (right).

performed to estimate more complex quantities, such as the PDF, eye or constellation diagrams [22, 23]. Note that, starting from the PC coefficients of the baseband signals, it is possible to analytically estimate the corresponding PC coefficients of the signals at optical frequencies, see (6.15): the variations of the optical signals are fully characterized by the PC model of their baseband counterpart.

The key steps of the MC method presented in Section 6.3 and of the novel PC-based approach are illustrated in Fig. 6.2. It is important to remark that both techniques start with evaluating scattering matrices, whereas the MC and PC-based approach require N_{MC} and N_{PC} samples respectively, and N_{PC} is much smaller than N_{MC}, as will be demonstrated in Section 6.5. Note that several steps in the MC approach have to be repeated N_{MC} times, while those in PC-based approach need to be carried out only once. These differences make the proposed method far superior in terms of efficiency.

6.5 Study of a ring-loaded MZI filter under stochastic effects

The proposed technique is applied to a compact silicon-on-insulator bandpass filter presented in [24], whose structure is shown in Fig. 6.3. The filter is designed based

on unbalanced Mach-Zehnder interferometer (MZI) loaded with a pair of ring resonators (RR). The length of the unloaded arm is set in such a way that the free spectral range of the RR matches that of the MZI. The characteristics of the filter, such as 3 dB bandwidth, off-band rejection and shape factor, are mainly determined by three phase shifters PS_0, PS_1, PS_2, and two power coupling coefficients K_1, K_2 as indicated in Fig. 6.3. In particular, K_1 and K_2 affect the bandwidth tunability and off-band rejection; the phase difference between PS_0 and PS_1 has an impact on the 3 dB bandwidth; the condition $PS_2 = m\pi + (PS_0 + PS_1)/2$ has to be satisfied in order to achieve a symmetric passband with regard to the center frequency, where m is an integer [24]. In our design, these parameters are chosen as $PS_0 = 0$, $PS_1 = \pi$, $PS_2 = \pi/2$, $K_1 = 0.67$, $K_2 = 0.67$.

We assume that, due to fabrication variations, the coupling coefficients K_1 and K_2 vary independently from chip to chip and can be represented as Gaussian random variables with standard variation of 0.02. Furthermore, while the phase shifter PS_0 is switched off since it is zero, the phase shifters PS_1 and PS_2 on different chips are sensitive to fabrication variations. For example, when the phase shifter is implemented by diode-loaded heaters, the shifted phase obtained from temperature changes could be different due to the post-processing of the heaters, or the slight difference of the applied voltage and current. Hence, PS_1 and PS_2 are assumed as independent and Gaussian distributed random variables with a standard deviation of two degrees. Hence, the filter scattering parameters depend on $Q = 4$ random variables.

To build the baseband augmented model, first a suitable modeling frequency range around the carrier frequency $f_c = 190.77$ THz must be defined: [190.29; 191.25] THz. This choice depends on the spectrum of the modulated input signals: a bandwidth of ± 480 GHz is sufficient for our application. In particular, 260 frequency samples that are uniformly distributed over the modeling frequency range are adopted. Then, a PC order $P = 2$ is chosen, leading to 15 basis functions, which is sufficient to obtain an accurate PC expansion of the scattering parameters in this case. According to the ST approach [4, 6], the PC coefficients of the scattering matrices $\boldsymbol{S}(f_r, \boldsymbol{\xi})$ can be calculated by evaluating $\boldsymbol{S}(f_r, \boldsymbol{\xi}_i)$ at only $N_{PC} = 15$

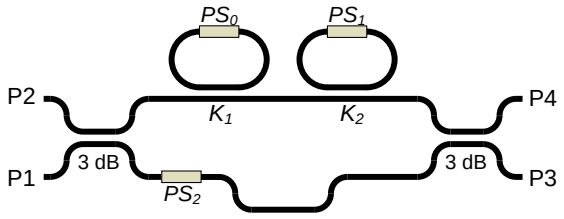

Figure 6.3: Structure of the ring-loaded MZI filter under study.

samples of $\boldsymbol{\xi}$, which is equal to the number of basis functions. Finally, the obtained PC coefficients $\boldsymbol{S}_m(f_r)$ for $r = 1, \ldots, 260$ can be used to calculate $\boldsymbol{S}_{PC}(f_r)$, as described in Section 6.4.1.

With the VF technique [18–20], a stable, passive, and continuous state-space model $\boldsymbol{S}_{PC}(f)$ in the form (6.11) is built with 34 poles [7, 8]. The magnitude of the maximum absolute error between the VF model and the data is less than -55 dB. It is important to remark that the PC coefficients $\boldsymbol{S}_m(f)$ can always be estimated from the corresponding augmented system $\boldsymbol{S}_{PC}(f)$ [7, 8]. Since a continuous frequency-domain model of $\boldsymbol{S}_{PC}(f)$ has been computed via the VF technique, the PC coefficients of the filter scattering matrix can be evaluated at any frequency point in the frequency range considered, which is $[190.29;\ 191.25]$ THz in this case. Hence, a cheap MC analysis based on the PC model of the scattering parameters is conducted to calculate $\boldsymbol{S}(f_k, \boldsymbol{\xi}_i)$ for $i = 1, \cdots, 10000$ and $k = 1, \cdots, 800$, as shown in Fig. 6.4. The blue and red curve are the frequency response with the intended design parameters (also called nominal design), while the gray lines represent the variations in the frequency response of the filter under stochastic effects. Note that the carrier frequency is chosen at the passband center of the filter as indicated in Fig. 6.4. Finally, the baseband stochastic model can be built according to (6.17) for efficient time-domain variability analysis.

We assume that the filter is excited at port P1 with quadrature amplitude modulated (QAM) source signal, then the incident waves are $\boldsymbol{a}(t, \boldsymbol{\xi}) = \boldsymbol{a}(t)$, while

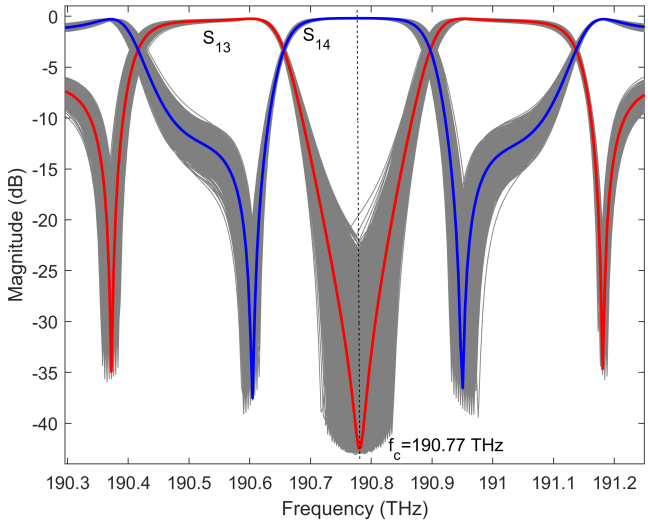

Figure 6.4: The variation (gray lines) in frequency response of the filter due to stochastic effects and the nominal design (red S_{13} and blue S_{14}).

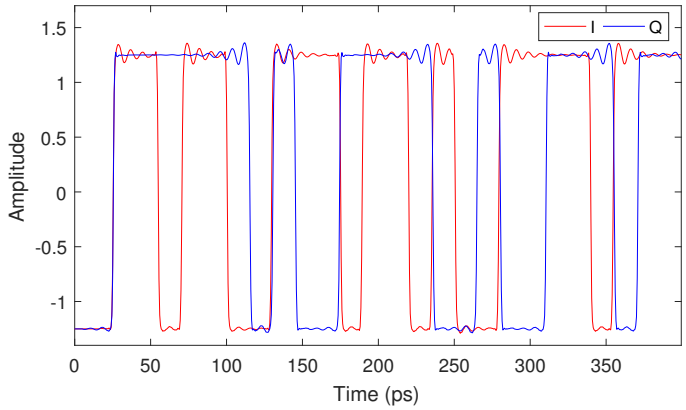

Figure 6.5: The in-phase part (I) and quadrature part (Q) of the input QAM signal.

the outputs $\boldsymbol{b}(t, \boldsymbol{\xi})$ will vary from chip to chip due to the variations of PS_1, PS_2, K_1 and K_2. The in-phase part $I(t)$ and quadrature part $Q(t)$ of the QAM input signal are pseudo-random sequence of 1000 bits with a bit time of 15 ps, whose first 25 bits are plotted in Fig. 6.5. Note that $I(t)$ and $Q(t)$ correspond to the real and imaginary parts of the baseband equivalent of the QAM modulated signal, respectively [15]. Furthermore, any input signal with a generic shape can be adopted here as the filter excitation, as long as the chosen modeling frequency range covers the spectrum of the signal.

Considering that the incident waves at port P1 is a deterministic source signal, its first PC coefficient is equal to the source signal itself, while all the others are zeros (see Section 6.4.1). Similarly, we assume that the other ports have no incident waves, so their PC coefficients are all zeros. In this framework, the input signal for the built baseband model (6.17) can be easily calculated: $\boldsymbol{a}_{BPC}(t) = [I(t) + jQ(t), 0, 0, \cdots]$. It is important to remark that in this example only the port P1 is excited for an easier demonstration of the simulation results. In fact, the proposed modeling and simulation technique allows that all the ports are excited at the same time with different input signals. Once we have the baseband augmented model and its input $\boldsymbol{a}_{BPC}(t)$, time-domain simulations can be conducted by solving the first-order ODE (6.17) by robust ODE solvers. In this work, the Matlab linear system simulator *lsim* is adopted. Finally, all the PC coefficients of the baseband reflected wave $\boldsymbol{b}_B(t, \boldsymbol{\xi})$ are obtained, which are collected in the output $\boldsymbol{b}_{BPC}(t)$. The mean and standard deviation (sigma) of the output signal $\boldsymbol{b}_B(t, \boldsymbol{\xi})$ are readily calculated from $\boldsymbol{b}_{BPC}(t)$ [7, 8].

As a benchmark, a time-domain MC analysis is also performed with $N_{MC} = 10000$ samples of PS_1, PS_2, K_1 and K_2, by following the procedure outlined in

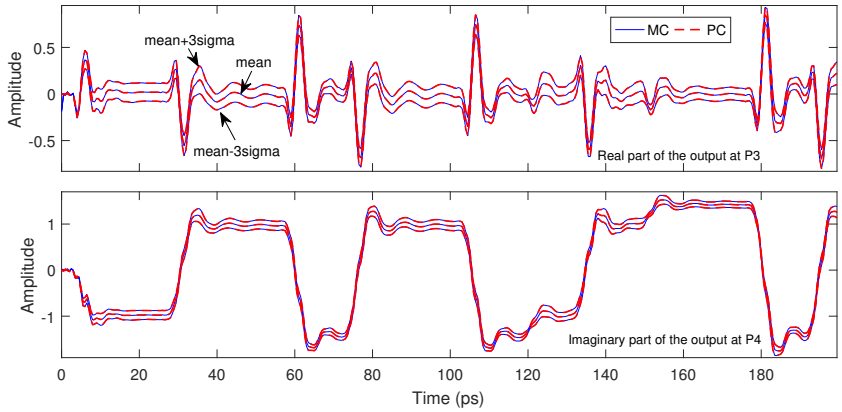

Figure 6.6: Variations of the output at port P3 and P4 obtained from the proposed technique (red dash line) and MC analysis (blue line).

Section 6.3. Figure 6.6 shows the $mean$ and $mean \pm 3sigma$ of the output at P3 and P4 at the first 200 ps, computed via the proposed PC-based approach and via the MC analysis: an excellent agreement can be observed.

Furthermore, $\boldsymbol{b}_{BPC}(t)$ is a cheap but accurate PC model, from which $\boldsymbol{b}_B(t, \boldsymbol{\xi})$ at any point in the stochastic space can be efficiently computed. So if the PDF and CDF of $\boldsymbol{b}_B(t, \boldsymbol{\xi})$ are desired, a cheap MC analysis based on the obtained PC model can be immediately conducted [7, 8, 13]. In this example, a MC analysis of the constellation diagrams of the output at port P4 is carried out by computing $\boldsymbol{b}_B(t, \boldsymbol{\xi}_i)$ of the filters at 10000 samples of $\boldsymbol{\xi}$. Note that the real and imaginary parts of $\boldsymbol{b}_B(t, \boldsymbol{\xi}_i)$ are the in-phase part $I(t)$ and quadrature part $Q(t)$, respectively, and the constellation diagram can be immediately plotted with $I(t)$ and $Q(t)$. Figure 6.7 shows the 10000 diagrams computed from the cheap PC model and MC analysis, and the diagrams for input signal and output signal of the nominal design for comparison. Again, the results demonstrate the accuracy of the proposed method.

The computational time for the proposed technique and MC analysis are compared in Table 6.1 in term of three phases: evaluating scattering matrices, building the models with the VF technique, and time-domain simulations. It demonstrates that the proposed technique is much more efficient than the MC method, while achieving a comparable accuracy. Note that all the operations are carried out on a personal computer with Intel Core i3 processor and 8 GB RAM. However, the efficiency of the proposed technique is sensitive to the number of random variables. More random variables leads to more basis functions for the same PC order (see Section 6.4.1), which has two effects: not only the the number N_{PC} of samples required to calculate the PC coefficients of the filter scattering parameters increases,

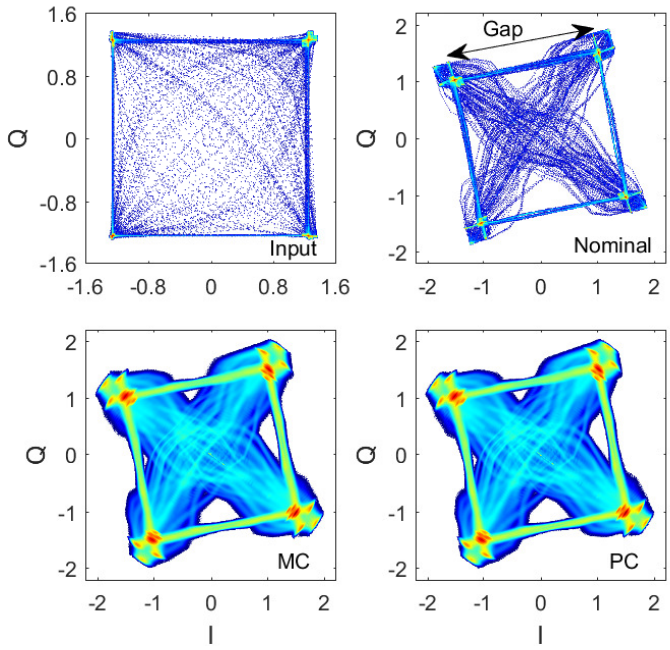

Figure 6.7: Constellation diagrams of: input (top left), the output at P4 of nominal design (top right), 10000 filters from MC analysis described in Section 6.3 (bottom left), and 10000 filters from the computed PC model (bottom right).

Technique	Steps	Computational time
Proposed technique	Extract scattering matrices at 15 (PS_1, PS_2, K_1, K_2) samples	1 min 2 s
	Build baseband augmented model (6.17)	1 min 52 s
	Time-domain simulation	9 min 22 s
	Total time	12 min 16 s
MC	Extract scattering matrices at 10000 (PS_1, PS_2, K_1, K_2) samples	11 h 35 min
	Build 10000 baseband models (6.6)	1 h 54 min
	10000 time-domain simulations	1 h 56 min
	Total time	15 h 25 min

Table 6.1: Efficiency of the proposed technique

but also the size of $\boldsymbol{S}_{PC}(f)$ and its corresponding baseband model increase as well, which can reduce the efficiency of the proposed method both in the model

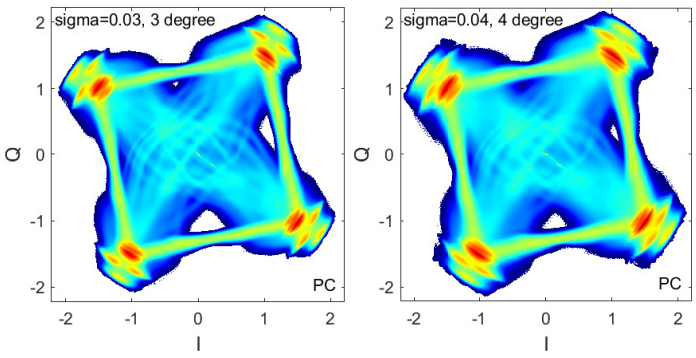

Figure 6.8: Constellation diagrams of 10000 filters from the proposed PC-based technique when different variations are considered.

building and simulation phase. This is a de facto challenge for PC-based techniques: their efficiency is high if the number of random variables is (relatively) limited [23].

To study how the variations in PS_1, PS_2, K_1 and K_2 impact the output signal at port P4, the standard deviation for (K_1, K_2) and (PS_1, PS_2) is first increased to 0.03 and 3 degrees, respectively, then to 0.04 and 4 degrees, respectively. Performing the variability analysis via the MC approach outlined in Section 6.3 is particularly expensive, since a new set of $N_{MC} = 10000$ samples must be evaluated each time the standard deviation of the random variables changes. With the proposed technique, only $N_{PC} = 15$ samples of the random parameters need to be computed anew for the chosen standard deviation values, which leads to a great efficiency gain. The effect of the change in the standard deviation on the constellation diagrams by means of the proposed method is shown in Fig. 6.8.

Furthermore, the PDF of the constellation symbol gap can also be calculated from both the MC analysis and the proposed PC-based technique, as illustrated in Fig. 6.9. Note that the gap is defined as the distance between the centers of two constellation symbols, as indicated in Fig. 6.7. It is evident that the PDF of the gap obtained from both techniques show an excellent agreement for the original assumption of the standard deviations. When the standard deviations increase, a clear larger spread of the gap distribution can be observed from the PDF computed via the efficient PC-based technique.

6.6 Conclusion

In this work, we presented an efficient baseband augmented modeling technique for time-domain variability analysis of photonic filters under stochastic effects.

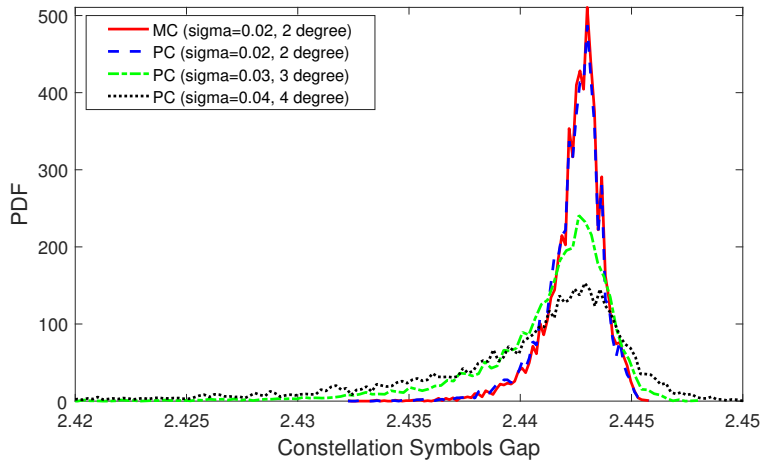

Figure 6.9: PDF of the constellation symbols gap calculated from MC analysis and the proposed PC-based technique while considering different variations.

The proposed approach is applicable to general linear passive photonic devices and circuits, since it is based on the scattering parameters representation, and allows for an efficient characterization of the impact of random variables on the time-domain performance of photonic circuits. The accuracy and efficiency of the proposed method was validated by means of a comparison with the time-domain MC approach for a pertinent example of a photonic integrated filter circuit.

References

[1] A. Waqas, D. Melati, and A. Melloni. *Sensitivity Analysis and Uncertainty Mitigation of Photonic Integrated Circuits*. J. Lightw. Technol., 35(17):3713–3721, Sep. 2017.

[2] W. Bogaerts and L. Chrostowski. *Silicon photonics circuit design: methods, tools and challenges*. Laser Photon Rev., 12(4):1700237, Mar. 2018.

[3] G. Fishman. *Monte Carlo: concepts, algorithms, and applications*. Springer Science & Business Media, 2013.

[4] Z. Zhang, T. A. El-Moselhy, I. M. Elfadel and L. Daniel. *Stochastic Testing Method for Transistor-Level Uncertainty Quantification Based on Generalized Polynomial Chaos*. IEEE Trans. Comput.-Aided Design Integr. Circuits Syst., 32(10):1533–1545, Oct. 2013.

[5] P. Manfredi and F. G. Canavero. *Efficient statistical simulation of microwave devices via stochastic testing-based circuit equivalents of nonlinear components*. IEEE Trans. Microw. Theory Techn., 63(5):1502–1511, May 2015.

[6] P. Manfredi, D. Vande Ginste, D. De Zutter, and F. G. Canavero. *Generalized Decoupled Polynomial Chaos for Nonlinear Circuits With Many Random Parameters*. IEEE Microw. Wireless Compon. Lett, 25(8):505–507, Aug. 2015.

[7] D. Spina, T. Dhaene, L. Knockaert, and G. Antonini. *Polynomial Chaos-Based Macromodeling of General Linear Multiport Systems for Time-Domain Analysis*. IEEE Trans. Microw. Theory Techn., 65(5):1422–1433, May 2017.

[8] Y. Ye, D. Spina, P. Manfredi, D. Vande Ginste, and T. Dhaene. *A Comprehensive and Modular Stochastic Modeling Framework for the Variability-Aware Assessment of Signal Integrity in High-Speed Links*. IEEE Trans. Electromagn. Compat., 60(2):459–467, Apr. 2018.

[9] T. W. Weng, Z. Zhang, Z. Su, Y. Marzouk, A. Melloni, and L. Daniel. *Uncertainty quantification of silicon photonic devices with correlated and non-Gaussian random parameters*. Opt. Express, 23(4):4242–4254, Feb. 2015.

[10] Y. Xing, D. Spina, A. Li, T. Dhaene, and W. Bogaerts. *Stochastic collocation for device-level variability analysis in integrated photonics*. Photon. Res., 4(2):93–100, Apr. 2016.

[11] T. W. Weng, D. Melati, A. Melloni, and L. Daniel. *Stochastic simulation and robust design optimization of integrated photonic filters*. Nanophotonics, 6(1):299–308, 2017.

[12] C. Cui and Z. Zhang. *Uncertainty Quantification of Electronic and Photonic ICs with Non-Gaussian Correlated Process Variations*. In IEEE/ACM International Conference on Computer-Aided Design (ICCAD), pages 1–8, San Diego, USA, Nov. 2018.

[13] A. Waqas, D. Melati, P. Manfredi, and A. Melloni. *Stochastic process design kits for photonic circuits based on polynomial chaos augmented macromodelling*. Opt. Express, 26(5):5894–5907, Mar. 2018.

[14] M. Heins, C. Cone, J. Ferguson, et al. *Design Flow Automation for Silicon Photonics: Challenges, Collaboration, and Standardization*. In Silicon Photonics III: Systems and Applications, pages 99–156. Springer Berlin Heidelberg, Berlin, Heidelberg, 2016.

[15] Y. Ye, D. Spina, Y. Xing, W. Bogaerts, and T. Dhaene. *Numerical modeling of Linear Photonic System for Accurate and Efficient Time-Domain Simulations*. Photon. Res., 6(6):560–573, Jun. 2018.

[16] Y. Ye, D. Spina, W. Bogaerts, and T. Dhaene. *Baseband Macromodeling of Linear Photonic Circuits for Time-Domain Simulations*. J. Lightw. Technol., 37(4):1364–1373, Feb. 2019.

[17] P. De Heyn, J. De Coster, P. Verheyen, G. Lepage, M. Pantouvaki, P. Absil, W. Bogaerts, J. Van Campenhout, and D. Van Thourhout. *Fabrication-Tolerant Four-Channel Wavelength-Division-Multiplexing Filter Based on Collectively Tuned Si Microrings*. J. Lightw. Technol., 31(16):2785–2792, Aug. 2013.

[18] B. Gustavsen and A. Semlyen. *Rational approximation of frequency domain responses by Vector Fitting*. IEEE Trans. Power Del., 14(3):1052–1061, Jul. 1999.

[19] D. Deschrijver, and T. Dhaene. *Fast Passivity Enforcement of S-Parameter Macromodels by Pole Perturbation*. IEEE Trans. Microw. Theory Techn., 57(3):620–626, Mar. 2009.

[20] B. Gustavsen and A. Semlyen. *Fast Passivity Assessment for S-Parameter Rational Models Via a Half-Size Test Matrix*. IEEE Trans. Microw. Theory Techn., 56(12):2701–2708, Dec. 2008.

[21] C. Sorace-Agaskar, J. Leu, M. R. Watts, and V. Stojanovic. *Electro-optical co-simulation for integrated CMOS photonic circuits with VerilogA*. Opt. Exp., 23(21):27180–27203, Oct. 2015.

[22] M. S. Eldred. *Recent advances in non-intrusive polynomial-chaos and stochastic collocation methods for uncertainty analysis and design*. In Proc. 50th AIAA/ASME/ASCE/AHS/ASC Struct., Structural Dynam., Mat. Conf., AIAA-2009-2274, Palm Springs, California, May 2009.

[23] A. Kaintura, T. Dhaene, and D. Spina. *Review of Polynomial Chaos-Based Methods for Uncertainty Quantification in Modern Integrated Circuits*. Electronics, 7(3), 2018.

[24] P. Orlandi, F. Morichetti, M. J. Strain, M. Sorel, P. Bassi, and A. Melloni. *Photonic Integrated Filter With Widely Tunable Bandwidth*. J. Lightw. Technol., 32(5):897–907, Mar. 2014.

7 Conclusion

7.1 Summary and results

The purpose of this PhD was to develop modeling techniques for the design and analysis of electronic and photonic circuits.

In the early phase of my PhD research, the main focus was on quantifying the effects of the variations of the manufacturing process on the performances of modern ICs. Since this problem can be studied in a probabilistic framework, I developed stochastic macromodeling approaches to characterize the behaviour of electronic circuits under stochastic effects. In this PhD thesis, stochastic macromodels are defined as mathematical models describing the behaviour of the stochastic system under study as seen from the system input/output ports. Given the large variety of devices and components in modern ICs, I first focused on a specific class of systems, namely linear and passive multiport electronic circuits (such as transmission lines, distributed filters, connectors, etc.). These systems can be described both in the frequency- and time-domain by means of their transfer function, which can be expressed by different representations, such as impedance, admittance and scattering parameters. Hence, Chapter 2 presented an extensive study of stochastic macromodeling of general passive multiport electronic circuits based on their transfer function representation. It is important to remark that the proposed stochastic macromodeling approaches preserve relevant physical properties of the system under study, namely causality, stability and passivity, allowing one to perform variability analysis both in the frequency and time domain with accuracy

and efficiency with respect to traditional MC-based approaches. Finally, a unique modeling framework for passive circuits depending on both deterministic design parameters and stochastic random parameters was developed.

Chapter 3 extended the proposed stochastic macromodeling framework to general electronic circuits consisting of both linear and nonlinear devices. The main feature of the proposed approach is that the stochastic macromodels for linear and nonlinear elements under stochastic effects can be built separately, and then connected and simulated in SPICE-like simulators. The simulation results can be used not only to calculate simple stochastic information, such as mean and standard deviation, but also complex statistics like the PDF and the CDF. The proposed technique is much more efficient than MC-based approaches and is widely applicable to general electronic circuits.

Then my research gradually shifted towards photonic integrated circuits (PICs), which represent a promising solution to overcome the bottleneck in data transmission speed and volume of electronic circuits. However, unlike electronic circuits, which are highly sophisticated in terms of design and manufacturing, there are many challenges to design highly integrated silicon photonic circuits for mass production. In particular, modeling and simulation techniques for photonic circuits are still not well established. Hence, I first developed robust modeling and simulation techniques, then focused on efficient variability analysis methods able to quantify the impact of the fabrication variations.

In particular, Chapter 4 proposed a baseband modeling technique for general linear and passive photonic circuits, which allows to perform time-domain simulations with accuracy and efficiency. The modeling process starts with the scattering parameters, which contain both transmission and refection information and are able to characterize nonideal behaviours, such as higher-order dispersion and wavelength-dependent losses. The proposed technique is widely applicable, since any linear passive photonic circuit can be described by its scattering parameters. Furthermore, the modeling process is very robust since it leverages on the VF technique, which has been extensively studied in the last two decades. Chapter 5 presented a novel modeling technique based on the CVF algorithm, which inherits all the advantages of the approach described in Chapter 4 and offers a reduced modeling complexity: for the same application, the model built via the technique in Chapter 5 has half the size of the model built via the technique in Chapter 4. This characteristic is crucial when simulating circuits with a large number of components, since compact models lead to more efficient simulations.

Finally, Chapter 6 introduced a stochastic baseband modeling technique for general linear and passive photonic circuits. To the best of my knowledge, it is the first PC-based approach presented in the literature allowing for the efficient characterization of stochastic photonic circuits directly in the time domain. This novel approach leverages on the PC expansion, a state-of-the-art stochastic method

for variability analysis, and the baseband modeling approach defined in this thesis for efficient and accurate time-domain simulations.

7.2 Future work

7.2.1 Compact modeling of linear photonic circuits via delayed vector fitting

General linear and passive photonic circuits can be accurately modeled by the Vector Fitting (VF) technique, as demonstrated in Chapter 4. One of the main advantages is that only the scattering parameters of a linear device or circuit are required to compute the desired model: the approach in Chapter 4 can be applied to a large class of devices (couplers, filters, ring resonators, etc.). In particular, the VF algorithm adopts a set of poles and residues to approximate the scattering parameters, so the built models are also called pole-residue models. Mathematically, the pole-residue models can also be expressed as pole-zero models. Therefore, the VF technique is inherently good at modeling the oscillations in the frequency response that are caused by resonances.

However, many photonic devices, such as waveguides and directional couplers, are characterized by smooth frequency responses (without resonances) over a wide frequency range and have a large wavelength dependent phase rotation, and the VF technique normally requires a relatively high amount of poles and residues to approximate such smooth frequency responses. If we consider an extreme case: a nondispersive waveguide can be modeled by a single delay, but it is challenging to compute a compact VF model over a wide bandwidth, since the magnitude of its frequency response is constant with respect to the frequency (no resonances).

Hence, a large increase in modeling power can be expected by adding delays to the VF pole-residue model. In this framework, a modeling technique has been proposed in the electronic field, called Delayed Vector Fitting (DVF) [1]. Researching approaches based on DVF to describe linear photonic circuits seems very promising, since it could lead to more compact models than the VF technique, especially for optically long systems (where the physical length is much larger than the wavelength). Unfortunately, the DVF has two main challenges: 1) the accurate estimation of multiple delays; 2) the development of robust and efficient passivity assessment and enforcement strategies. Even though some successful applications were demonstrated in literature, it is still a far less robust modeling technique and not widely used as compared to the VF algorithm. Hence, developing robust and accurate DVF-based modeling approaches for photonic circuits is a challenging task.

7.2.2 SPICE-compatible models of linear photonic circuits

As mentioned in Chapter 1, for electronic and photonic circuits co-simulation, it is promising to build models of photonic devices which are compatible with electronic simulators, such as SPICE and Verilog-A. Several techniques have been published in the literature for building SPICE or Verilog-A compatible models for nonlinear photonic devices (e.g. lasers [2, 3], modulators [4–6], photodetectors [7–10]), but there are still challenges to build SPICE or Verilog-A compatible models for general linear and passive photonic elements. In Chapters 4 and 5, it is demonstrated that complex-valued state-space models of linear photonic circuits can be converted into real-valued ones. Real-valued state-space models represent physical systems and have the potential to be converted into suitable equivalent circuits (netlists) which are SPICE-compatible [11].

However, there is a fundamental issue that must be addressed. In SPICE, signals are node voltages and branch currents, while the port signals of photonic circuits are incident and reflected waves. Therefore, a suitable transformation of waves into voltages and currents must be performed to simulate photonic circuits in electronic circuit simulators. The definition of such transformation is the main research challenge to overcome [12]. A possible solution is to directly interpret the magnitude/phase or real/imaginary parts of the forward and backward waves to voltage and/or current. This approach is accurate from a mathematical point of view in some cases [13, 14]; however, the voltages and currents in electronic circuit simulators always comply with the Kirchhoff's voltage law (KVL) and Kirchhoff's current law (KVL), respectively, whereas the optical waves never follow these rules. For microwave systems, the non-conservative electromagnetic waves are converted to voltages and currents through the definition of the characteristic impedance in waveguide circuit theory [15]. It would be very useful to define a suitable optical equivalent counterpart of the characteristic impedance, which could physically map optical waves to voltages and currents.

7.2.3 Variability analysis of linear and nonlinear photonic circuits

A general photonic system always contains linear and nonlinear devices. When it comes to manufacturing, both kinds of devices are subject to fabrication variations. Therefore, it is meaningful to develop variability analysis techniques applicable to circuits with both linear and nonlinear devices.

To this end, a possible approach is to define a methodology allowing to model the stochastic variations of linear and nonlinear devices separately: the computed models can then be suitably connected to estimate the variability of the entire circuit. Such methodology has been presented in Chapter 3 for electronic circuits and its applicability in the photonic domain could be investigated in the future.

Furthermore, the variability analysis techniques described in this thesis (Chapters 2, 3 and 6) are based on the PC expansion: one of the main challenges is to extend the proposed methodologies to circuits with a large number of random parameters. Indeed, the number of PC coefficients increases rapidly with the number of random parameters, leading to very large augmented models which are computationally expensive to simulate. Developing efficient PC-based variability analysis techniques for circuits depending on a large numbers of random parameters is still an open problem.

It is also interesting if the variability analysis can take into account both the systematic and random variations and the correlations among the random variables, which is often the case in practice [16].

References

[1] A. Chinea, P. Triverio, and S. Grivet-Talocia. *Delay-Based Macromodeling of Long Interconnects From Frequency-Domain Terminal Responses*. IEEE Trans. Adv. Packag., 33(1):246–256, Feb. 2010.

[2] P. V. Mena, J. J. Morikuni, S. M. Kang, A. V. Harton, and K. W. Wyatt. *A comprehensive circuit-level model of vertical-cavity surface-emitting lasers*. J. Lightw. Technol., 17(12):2612–2632, Dec. 1999.

[3] Z. Zhang, R. Wu, Y. Wang, C. Zhang, E. J. Stanton, C. L. Schow, K. T. Cheng, and J. E. Bowers. *Compact Modeling for Silicon Photonic Heterogeneously Integrated Circuits*. J. Lightw. Technol., 35(14):2973–2980, July 2017.

[4] S. Tanaka, T. Usuki, and Y. Tanaka. *Accurate SPICE Model of Forward-Biased Silicon PIN Mach-Zehnder Modulator for an Energy-Efficient Multi-level Transmitter*. J. Lightw. Technol., 36(10):1959–1969, May 2018.

[5] B. Wang, C. Li, C. Chen, K. Yu, M. Fiorentino, R. G. Beausoleil, and S. Palermo. *A Compact Verilog-A Model of Silicon Carrier-Injection Ring Modulators for Optical Interconnect Transceiver Circuit Design*. J. Lightw. Technol., 34(12):2996–3005, Jun. 2016.

[6] H. Bahrami, H. Sepehrian, C. S. Park, L. A. Rusch, and W. Shi. *Time-Domain Large-Signal Modeling of Traveling-Wave Modulators on SOI*. J. Lightw. Technol., 34(11):2812–2823, Jun. 2016.

[7] Y. M. El-Batawy and M. J. Deen. *Analysis, circuit modeling, and optimization of mushroom waveguide photodetector (mushroom-WGPD)*. J. Lightw. Technol., 23(1):423–431, Jan. 2005.

[8] M. Jalali, M. K. Moravvej-Farshi, S. Masudy-Panah, and A. Nabavi. *An Equivalent Lumped Circuit Model for Thin Avalanche Photodiodes With Nonuniform Electric Field Profile*. J. Lightw. Technol., 28(23):3395–3402, Dec. 2010.

[9] M. Piels, A. Ramaswamy, and J. E. Bowers. *Nonlinear modeling of waveguide photodetectors*. Opt. Express, 21(13):15634–15644, Jul. 2013.

[10] D. Dai, M. Piels, and J. E. Bowers. *Monolithic Germanium/Silicon Photodetectors With Decoupled Structures: Resonant APDs and UTC Photodiodes*. IEEE J. Sel. Topics Quantum Electron, 20(6):43–56, Nov. 2014.

[11] J. F. Villena and L. M. Silveira. *Circuit synthesis for guaranteed positive sparse realization of passive state-space models*. IEEE Trans. Circuits Syst. I, Reg. Papers, 64(6):1576–1587, Jun. 2017.

[12] R. G. Longoria. *Wave-scattering formalisms for multiport energetic systems*. J. Franklin Inst., 333(4):539 – 564, Jul. 1996.

[13] P. Gunupudi, T. Smy, J. Klein, and Z. J. Jakubczyk. *Self-Consistent Simulation of Opto-Electronic Circuits Using a Modified Nodal Analysis Formulation*. IEEE Trans. Adv. Packag., 33(4):979–993, Nov. 2010.

[14] C. Sorace-Agaskar, J. Leu, M. R. Watts, and V. Stojanovic. *Electro-optical co-simulation for integrated CMOS photonic circuits with VerilogA*. Opt. Express, 23(21):27180–27203, Oct. 2015.

[15] R. B. Marks and D. F. Williams. *A general waveguide circuit theory*. J. Res. Natl. Inst. Stand. Technol., 97(5):533, 1992.

[16] Y. Xing, J. Dong, S. Dwivedi, U. Khan, and W. Bogaerts. *Accurate extraction of fabricated geometry using optical measurement*. Photon. Res., 6(11):1008–1020, Nov. 2018.